The Pennsylvania State University

The Graduate School

Department of Materials Science and Engineering

PROBING HEAT TRANSFER, FLUID FLOW AND MICROSTRUCTURAL EVOLUTION DURING FUSION WELDING OF ALLOYS

A Thesis in

Materials Science and Engineering

by

Wei Zhang

Submitted in Partial Fulfillment
of the Requirements
for the Degree of

Doctor of Philosophy

August 2004

The thesis of Wei Zhang was reviewed and approved* by the following:

Tarasankar DebRoy
Professor of Materials Science and Engineering
Thesis Advisor
Chair of Committee

Long-Qing Chen
Professor of Materials Science and Engineering

John W. Elmer
Adjunct Professor of Materials Science and Engineering
Group Leader Materials Joining
Chemistry and Materials Science Department
Lawrence Livermore National Laboratory
Special Member

Panagiotis Michaleris
Associate Professor of Mechanical Engineering

Judith A. Todd
Professor of Engineering Science and Mechanics
P. B. Breneman Department Head Chair

Gary L. Messing
Professor of Ceramic Science and Engineering
Head of the Department of Materials Science and Engineering

*Signatures are on file in the Graduate School

ABSTRACT

The composition, geometry, structure and properties of the welded joints are affected by the various physical processes that take place during fusion welding. Understanding these processes has been an important goal in the contemporary welding research to achieve structurally sound and reliable welds. In the present thesis research, several important physical processes including the heat transfer, fluid flow and microstructural evolution in fusion welding were modeled based on the fundamentals of transport phenomena and phase transformation theory. The heat transfer and fluid flow calculation is focused on the predictions of the liquid metal convection in the weld pool, the temperature distribution in the entire weldment, and the shape and size of the fusion zone (FZ) and heat affected zone (HAZ). The modeling of microstructural evolution is focused on the quantitative understanding of phase transformation kinetics during welding of several important alloys under both low and high heating and cooling conditions.

Three numerical models were developed in the present thesis work: (1) a three-dimensional heat transfer and free surface flow model for the gas metal arc (GMA) fillet welding considering the complex weld joint geometry, (2) a phase transformation model based on the Johnson-Mehl-Avrami (JMA) theory, and (3) a one-dimensional numerical diffusion model considering multiple moving interfaces.

To check the capabilities of the developed models, several cases were investigated, in which the predictions from the models were compared with the experimental results. The cases studied are the follows. For the modeling of heat transfer and fluid flow, the welding processes studied included gas tungsten arc (GTA) linear welding, GTA transient spot welding, and GMA fillet welding. The calculated weldment geometry and thermal cycles was validated against the experimental data under various welding conditions. For the modeling of microstructural evolution, the welded materials investigated included AISI 1005 low-carbon steel, 1045 medium-carbon steel, 2205 duplex stainless steel (DSS) and Ti-6Al-4V alloy. The calculated phase transformation

kinetics were compared with the experimental results obtained using an x-ray diffraction technique by Dr. John W. Elmer of Lawrence Livermore National Laboratory.

Accurate knowledge of the heat transfer and fluid flow in the weld pool is important for the quantitative modeling of weldment geometry and microstructure. An existing weld thermo-fluid model at Penn State was used to investigate the transient heat transfer and fluid flow during GTA spot welding of the 1005 steel. The calculated FZ geometry and cooling rates were compared with those measured experimentally. The role of liquid convection in the weld pool heat transfer, the relative importance of driving forces in the weld pool liquid flow, and the resulting weld pool geometry were examined using the dimensional analysis. The transient melting and solidification processes and the behavior of the mushy zone were investigated, which were useful in understanding the weld microstructure.

Since the existing weld thermo-fluid model solves governing conservation equations in a rectangular solution domain with a flat surface, it cannot be applied to systems with complex joint geometry such as the GMA fillet welding. In the present study, a three-dimensional numerical heat transfer and free surface flow model was developed to study the temperature profile, velocity field, weld pool shape and size, and nature of the solidified weld bead geometry during GMA fillet welding. The special features of the numerical model are the following. (a) A boundary fitted curvilinear coordinate is used to calculate temperature and velocity fields in fillet welds with significant free surface deformation. (b) The model takes into accounts various complex physical processes such as metal transfer from droplets, heat transfer from the arc and droplets, the effect of arc pressure, and liquid convection in the deformed weld pool. (c) The predictions are checked against experimental data. In particular, the calculated weld zone geometric characteristics and cooling rates were in fairly good agreement with those measured experimentally for various welding conditions.

The computed thermal cycles were used in conjunction with phase transformation models to study the microstructural evolution during welding. A phase transformation

model based on the JMA theory was developed to study the kinetics of phase transformations controlled by the nucleation and growth mechanism. The JMA method was used to study the kinetics of α-ferrite→γ-austenite transformation in the 1005 and 1045 steels, and the α-Ti→β-Ti transformation in Ti-6Al-4V alloy. The calculated transformation kinetics were compared with those measured using the x-ray diffraction technique and the correlations were reasonable. A set of kinetic parameters in the JMA equation were developed, allowing the predictions of phase transformation kinetics under various heating conditions.

A complete microstructural evolution map in the HAZ of the 1005 steel arc welds was developed by combing three existing kinetic models. The α→γ transformation during heating was studied using a JMA equation, the γ grain growth was examined using a Monte Carlo simulation, and the γ→α transformation during cooling was calculated using an austenite decomposition model. These three kinetic models and computed thermal cycles were coupled together to provide the spatial variation of final microstructure in the HAZ.

The γ-austenite→δ-ferrite transformation in the 2205 DSS arc welds was studied using a numerical diffusion model, which considers the diffusion of nitrogen in both γ and δ phases and the movements of multiple δ/γ interfaces. A moving grid technique was used to trace the interfaces. The calculated transformation kinetics were compared with the x-ray diffraction results. The effect of starting microstructure on the phase transformation rates was investigated using the numerical diffusion model.

The results presented in this thesis, taken as a whole, indicated that the heat transfer, fluid flow and microstructural evolution during fusion welding can be quantitatively predicted from fundamentals of transport phenomena and phase transformation theory. The thesis research work represents a contribution to the growing quantitative knowledge base in welding. Expansion of this knowledge base is necessary, if not essential, to achieve structurally sound and reliable welds during fusion welding of important engineering materials.

TABLE OF CONTENTS

LIST OF FIGURES

LIST OF TABLES

ACKNOWLEDGEMENTS

Over the course of four years at Penn State, I have met many people that have helped to make the undertaking of this magnitude possible. I would first like to express my sincere gratitude and deep appreciation to my advisor, Dr. Tarasankar DebRoy. His guidance of the research effort, professional expertise, demand for excellence and encouragement brought the best from all involved. He gave me many opportunities to advance my research as well as my professional development. I am grateful to the invaluable contributions of Dr. John W. Elmer at Lawrence Livermore National Laboratory. I consider myself fortunate to have had the opportunity to work with him. He has added valuable phase transformation expertise to my work.

I would like to acknowledge Drs. Long-Qing Chen, John W. Elmer, Panagiotis Michaleris, and Judith A. Todd for their valuable advice and suggestions on my work while serving on my thesis committee. I am very appreciative to them for giving their time to review and comment on this thesis.

I would also like to express my thanks to Dr. Todd A. Palmer at Lawrence Livermore National Laboratory for his help in the microstructural modeling, Drs. Stan A. David and Sudarsanam S. Babu at Oak Ridge National Laboratory for their helpful discussions, and Dr. Harshad K. D. H. Bhadeshia at Cambridge University for allowing me to use his phase transformation model.

Many thanks to my colleagues, Drs. Amitava De, Tao Hong, Cheolhee Kim, Gour G. Roy, Zhishang Yang, Hailiang Zhao, Mrs. Xiuli He, Mr. Amit Kumar, and Mr. Saurabh Mishra, for their outstanding research and great help. They have made my study at Penn State a rewarding and memorable experience. Special thanks to Saurabh Mishra for his help in the grain growth calculations.

I am grateful to my parents and parents-in-law for their love and support. I am deeply indebted to my wife, Min Wang, who has always supported me with her love, understanding, encouragement and faith.

Finally, I would like to acknowledge a grant from the U.S. Department of Energy, Office of Basic Energy Sciences, Division of Materials Sciences, for supporting this research work, under grant number DE-FGO2-01ER45900. I am also grateful to the American Welding Society Foundation, which provided me with a graduate fellowship to further my education at Penn State.

Chapter 1

INTRODUCTION

1.1 General Background

Fusion welding is a process in which an intense heat source is applied to join components. The material is rapidly heated and it melts to form a weld pool. Once the liquid pool solidifies, two parts are jointed together. The interaction between the base material and the heat source leads to a series of physical and chemical processes [1-7], which culminate in the final weld composition, geometry, structure and properties. In the weld pool, the liquid undergoes strong circulation, which is driven by the buoyancy, surface tension gradient, jet impingement or friction, and, when electric arc is used, electromagnetic forces. Depending on the shielding gas used, partitioning of nitrogen, oxygen and/or hydrogen into the melt pool may take place. In the solid region around the weld pool, the variation of temperature with time, often referred to as the thermal cycle, may lead to various solid-state phase transformations and changes in the grain structure. Since the composition, geometry, structure and properties of the welded joints are affected by the forementioned processes, understanding these component processes has been an important goal in the contemporary welding research [1-7].

In the present thesis research, the heat transfer, fluid flow and microstructural evolution in fusion welding were modeled based on the fundamentals of transport phenomena and phase transformation theory [8-21]. The heat transfer and fluid flow calculation is focused on the predictions of the liquid metal convection in the weld pool, the temperature distribution in the entire weldment, and the shape and size of the fusion zone (FZ) and heat affected zone (HAZ). On the other hand, the modeling of microstructural evolution is focused on the quantitative understanding of phase transformation kinetics during welding of several important alloys under both low and high heating and cooling conditions. Since the integrity and properties of a weldment are

directly related with its geometry and microstructure, understanding the heat transfer, fluid flow and microstructural evolution is very important.

Knowledge of the temperature distribution and thermal cycles in the weldment is a prerequisite to understand the development of geometry, microstructures, residual stresses and the extent of the distortions in the weldment [1-7]. Due to the high temperatures, the steep temperature gradients, the presence of the plasma in the vicinity of the weld pool, and small size of the weld area, the experimental measurement of weld temperature fields and thermal cycles still remains a major challenge today. Temperature measurements in the solid regions, which commonly involve the placement of thermocouples, are cumbersome and expensive [1,6,7]. Furthermore, no reliable technique is currently available to accurately measure the temperature within the molten weld pool. A practical recourse is to utilize transport phenomena based numerical models. In the past two decades, application of heat transfer and fluid flow has resulted in improved understanding of complex fusion welding processes and welded materials [22-40]. Examples include quantitative calculations of weld thermal cycles and the FZ geometry [22-26]. In many simple systems, the computed thermal cycles have been used to quantitatively understand weldment microstructures and grain structure [8,14,29-32], inclusion characteristics [33-35], vaporization of alloying elements from the weld pool [36-38], and concentrations of dissolved gases in the weld metal [39,40].

Accurate prediction of the weld geometry and the thermal cycles in the weldment requires a comprehensive understanding of heat transfer and fluid flow in the weld pool. In the recent years, the importance of convective heat transfer in the weld pool has been recognized and the different driving forces responsible for the fluid motion, such as surface tension gradient, electromagnetic, and buoyancy forces have been investigated in detail by utilizing mathematical modeling [22-26]. Most of the previous research has been focused mainly on simple systems with a rectangular workpiece and ignoring any deformation of the weld pool top surface (i.e. flat top surface). These models worked well for gas tungsten arc (GTA) or laser conduction mode welding of butt joints. However, such simple models are not readily applicable to widely used gas metal arc (GMA) fillet

welding process because of the complexities in the weld geometry and welding process [15-17]. Therefore, a thermo-fluid model considering complex joint geometry is essential for achieving realistic simulation of heat transfer and fluid flow in the weld pool as well as microstructural evolution in the weldment during GMA fillet welding.

The welding-induced microstructural changes such as annealing, grain growth, and phase transformation alter the grain size, phase ratios and microstructural morphologies in the welded region [1-7]. The degree to which the microstructure is altered depends on the weld thermal cycle and the kinetics of the various transformations that are taking place. If the microstructure of the base material is significantly altered, the loss of material properties can be acute. Understanding the evolution of microstructure during welding is crucial for obtaining structurally sound welds.

With the knowledge of the thermal cycle, the ability to model weldment microstructure relies on a deep understanding of phase transformation theory governing the phase changes. In the past decades, considerable progress has been made in the prediction of weldment microstructure in both the FZ and the HAZ. Some phase transformation models have been established in an effort to predict microstructures in steel welds for a variety of compositions [41,42]. Most of these models have been focused on the phase transformations during cooling, which directly determine the final microstructure in the weldment. Only a few studies have been reported on the phase transformations during heating.

Understanding the kinetics of phase transformations during heating is important, since the transformed phases during heating affect the kinetics of subsequent grain growth and phase transformations during cooling. Phase transformations during heating have not been extensively studied experimentally and theoretically because of the following reasons [43,44]. Firstly, the transformed phase during heating is destroyed by subsequent transformations during cooling. The conventional methods such as dilatometry and calorimetry are indirect in that they measure certain changes in the welded sample (e.g. change in length) and cannot directly determine the amount of phases present during the test. Direct observation of phase transformations during heating

is still evolving. Secondly, the transformation kinetics during heating normally becomes more rapid as the temperature is increased. As a result, application of traditional experimental techniques to measure the transformation kinetics is difficult. Finally, the extent of phase changes during heating depends on the composition, size and distribution of the base material as well as the weld thermal cycle. It means that separate experiments are needed for different starting microstructures and welding conditions. Therefore, experimental study of phase transformation kinetics is time consuming and expensive. Because of these problems, progress in the field of weld microstructural evolution has been slow, and quantitative kinetic data pertaining to phase transformations in important alloy systems under the conditions of welding still remain scarce.

A recently developed X-ray diffraction technique [**44**-**46**] can provide the real-time phase mapping of the weldment surface during welding. This technique has been used to successfully measure phase transformation kinetic data at both low and high heating and cooling rates during welding of a variety of steels and other alloys [**14**,**31**,**44**-**46**]. Since the kinetic data collected by the X-ray diffraction technique vary from run to run, analysis of the data to obtain kinetics and mechanisms of phase transformations requires the combination of phase transformation models and thermal cycles at various locations in the weldment.

In summary, the composition, structure and properties of the welded joints are affected by the various physical processes. In order to obtain accurate predictions of the weld geometry and thermal cycles during the practical welding production, heat transfer and fluid flow in complex joint geometry should be considered in the development of a comprehensive thermo-fluid model. Accurate knowledge of the thermal cycles at various locations of the weldment is a prerequisite for modeling welding-induced phase transformations. The unique data collected using the X-ray diffraction technique can be analyzed using phase transformation models to obtain the kinetics and mechanisms of various transformations that are taking place during welding.

1.2 Research Objectives and Methodology

The overall objective of this study is to seek a quantitative understanding of the heat transfer, fluid flow and microstructural evolution during fusion welding, based on the fundamentals of transport phenomena and phase transformation theories. The predictions are focused on the liquid metal convection in the weld pool, the temperature distribution in the entire weldment, the shapes and sizes of the FZ and HAZ, the phase transformation kinetics, and the microstructure of the weldment. To achieve this objective, comprehensive mathematical models were developed and the models were validated by comparing the computed results with the experimental data.

The methodology used in the present thesis research is depicted in Fig. **1.1**. As shown in this figure, a three-dimensional heat transfer and fluid flow model considering complex joint geometry was developed to calculate the weld bead geometry, temperature and velocity fields in the weld pool, and the thermal cycles in the entire weldment. The phase transformation kinetics was then simulated by coupling the phase transformation models with the computed temperature history information in the weldment.

To check the capabilities of the research methodology and the developed models, several cases were investigated. Figure **1.2** summarizes the various cases studies and their relationship. For the modeling of heat transfer and fluid flow, the welding processes studied included GTA linear [**8**-**11**,**14**], GTA spot [**13**] and GMA welding [**12**,**15**-**17**]. The temperature distribution in the weldment is at quasi-steady during GTA linear welding, whereas it varies with time during spot welding. The GMA fillet welding is characterized by complex joint geometry containing a deformable weld pool free surface. The calculated weldment geometry was validated against the experimental data under various welding conditions. For the modeling of microstructural evolution, the welded materials investigated included AISI 1005 steel [**8**-**11**,**14**], 1045 steel [**20**], 2205 duplex stainless steel (DSS) [**47**] and Ti-6Al-4V alloy [**19**,**21**]. The heating and cooling rates in 1045 steel and Ti-6Al-4V spot welds are much higher than those in 1005 steel and 2205 DSS linear welds. The calculated phase transformation kinetics were compared with those obtained using the spatially and temporally resolved x-ray diffraction techniques.

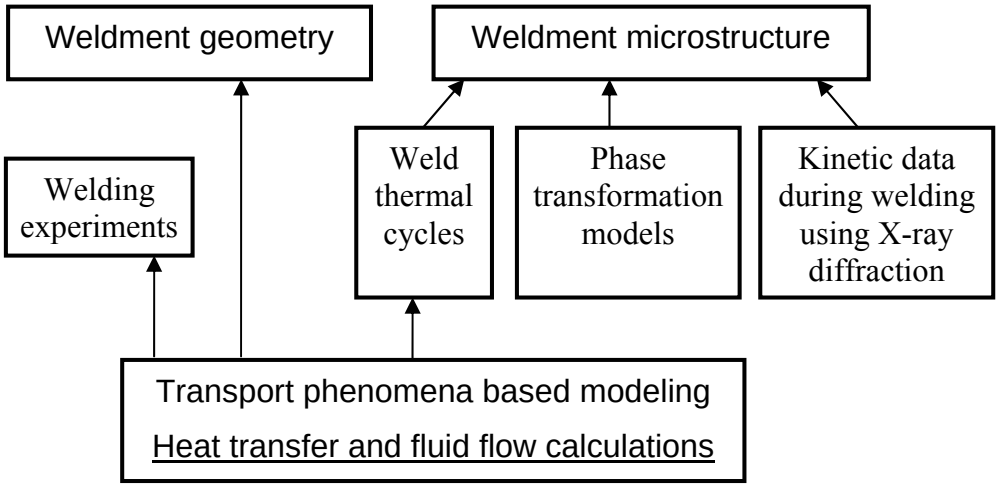

Fig. **1.1**: Research methodology used in the present thesis study.

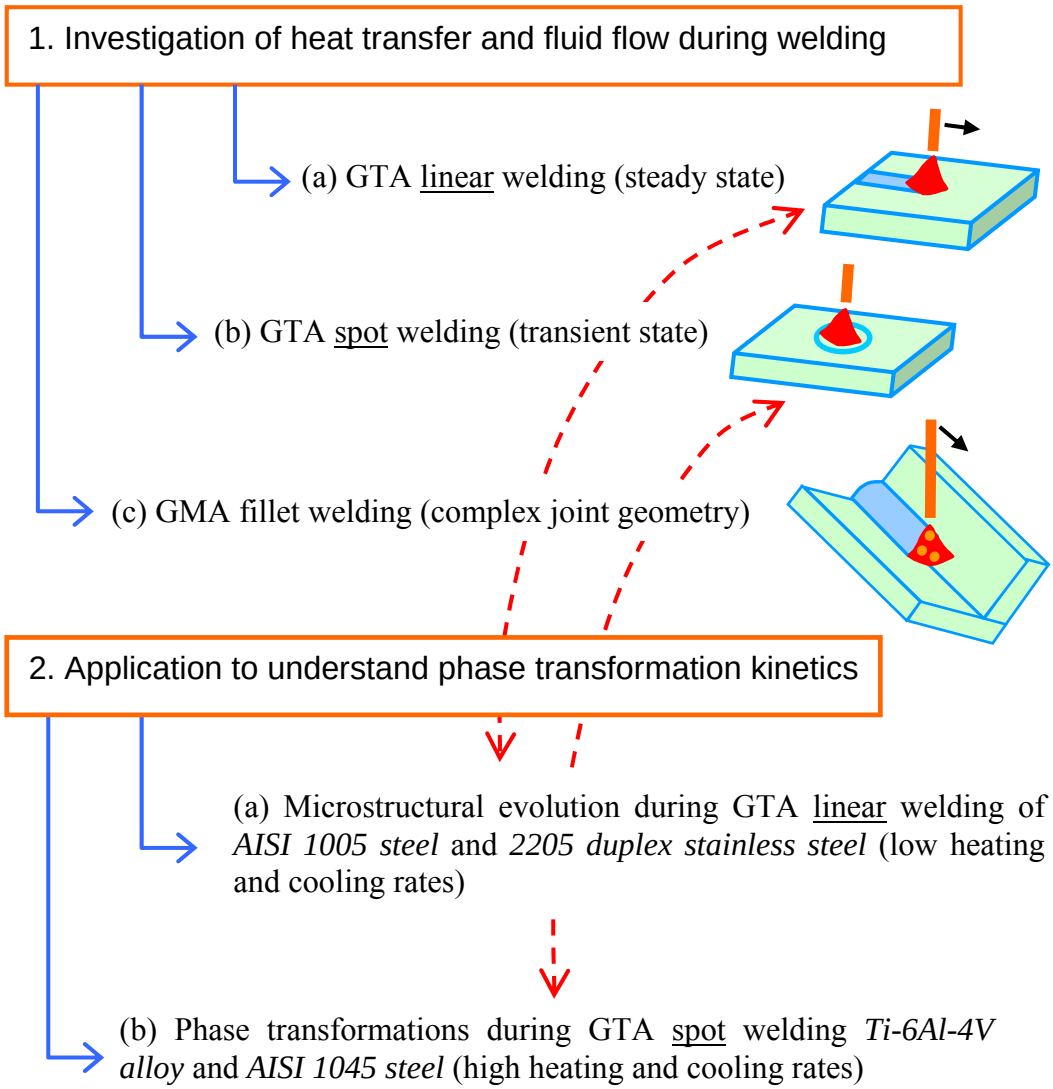

Fig. **1.2**: Various cases investigated in the present thesis research and their relationship.

1.3 Thesis structure

The thesis consists of seven chapters. Chapter 1 describes the subject matter, the research objectives and methodology, and the thesis contents.

In chapter 2, the background materials necessary for simulating heat transfer, fluid flow and microstructural evolution in fusion welding are critically reviewed. At first, the current understanding of transport processes including energy absorption, liquid convection and driving forces, turbulence and free surface flow is examined. Secondly, the modeling of heat transfer and fluid flow in two specific welding processes, i.e., GTA transient stationary welding and GMA fillet welding, are examined. Finally, several phase transformation models for predicting the microstructure evolution in the weldment are evaluated.

Chapter 3 presents the results of modeling transient heat transfer and fluid flow during GTA spot welding. The evolution of temperature and velocity fields in the GTA spot welds was studied using a transient numerical model. Verification of the model was performed through comparing the calculated results with metallographic weld cross sections and measured thermal cycles. Dimensionless analysis was carried out to understand the heat transfer mechanism in the weld pool, and the significance of the various driving forces for the liquid convection. The behavior of the mushy zone, i.e., the solid + liquid two phase region, during heating and cooling were investigated. Results also revealed information about the important solidification parameters, i.e., the solidification rate and the temperature gradient at the solid/liquid front, as a function of time. These data are useful for determining the solidification morphology and the scale of the solidification substructure.

In chapter 4, the heat transfer and free surface flow in complex weld joints was modeled. A three-dimensional numerical heat transfer and fluid flow model was developed to study the temperature profile, velocity field, weld pool shape and size, and nature of the solidified weld bead geometry during GMA fillet welding. A boundary fitted curvilinear coordinate was used to calculate temperature and velocity fields in fillet welds with significant free surface deformation. The model took into accounts various

complex physical processes such as metal transfer from droplets, heat transfer from the arc and droplets and the effect of arc pressure. The predictions were compared against experimental data. In particular, the calculated weld zone geometric characteristics and cooling rates were in fairly good agreement with those measured experimentally for various welding conditions.

In chapter 5, the research work on applying phase transformation models in conjunction with computed thermal cycles to study the weld microstructural evolution is described. A phase transformation model based on the Johnson-Mehl-Avrami (JMA) theory was developed to study the kinetics of phase transformations controlled by nucleation and growth mechanism. The JMA method was used to study the kinetics of the α-ferrite$\rightarrow\gamma$-austenite transformation in 1005 and 1045 steels, as well as the α-Ti$\rightarrow\beta$-Ti transformation in Ti-6Al-4V alloy. A set of JMA kinetic parameters were determined from the experimental data obtained using the X-ray diffraction techniques. These kinetic parameters allow the calculation of phase transformation rates under different heating conditions.

In chapter 6, a numerical diffusion model considering moving interfaces was developed to investigate the γ-austenite$\rightarrow\delta$-ferrite transformation during GTA welding of 2205 duplex stainless steel. The calculated transformation kinetics were compared with the experimental data. The effect of the starting microstructure on the transformation rate was investigated using the numerical diffusion model.

Summary and conclusions of the present study are presented in chapter 7. The results of the case studies presented here indicate the heat transfer, fluid flow and microstructural evolution during fusion welding can be quantitatively predicted from fundamentals of transport phenomena and phase transformation theory. The thesis research work represents a contribution to the growing quantitative knowledge base in fusion welding.

1.4 References

1. T. DebRoy and S. Kou: *Heat Flow in Welding*, Chapter 3, Welding Handbook, vol. 1, 9th Edition, American Welding Society, 2001, pp. 87-113.

2. J. F. Lancaster: *The Physics of Welding* 2nd Edition, Pergamon, Oxford, 1986.

3. K. Easterling: *Introduction to the Physical Metallurgy of Welding*, 2nd Edition, Butterworth-Heinemann, Oxford, 1992.

4. S. A. David and T. DebRoy: *Science*, **257**, 497 (1992).

5. T. DebRoy and S. A. David: *Rev. Mod. Phys.*, **67**, 85 (1995).

6. Ø. Grong: *Metallurgical Modeling of Welding*, 2nd edition, The Institute of Materials, London, 1997.

7. S. Kou: *Welding Metallurgy*, 2nd edition, John Wiley & Sons, Hoboken, New Jersey, 2003.

8. W. Zhang, J. W. Elmer and T. DebRoy: *Mater. Sci. Eng. A*, **333**, 320 (2002).

9. W. Zhang, J. W. Elmer and T. DebRoy: *Scripta Mater.*, **46**, 753 (2002).

10. T. DebRoy, H. Zhao, W. Zhang and G. G. Roy: *Proceedings of 6th Mathematical Modeling of Weld Phenomena*, edited by H. Cerjak et. al., Maney, London, p. 21 (2002).

11. W. Zhang, J. W. Elmer and T. DebRoy: *Proceedings of 6th Trends in Welding Research*, edited by S. A. David et. al., ASM International, Materials Park, OH, p. 180 (2002).

12. W. Zhang and T. DebRoy: *Proceedings of Mathematical Modeling and Information Technologies in Welding and Related Processes*, edited by V. I. Makhnenko, Criema, Ukraine, p. 24 (2002).

13. W. Zhang, G. G. Roy, J. W. Elmer and T. DebRoy: *J. Appl. Phys.*, **93**, 3022 (2003).

14. J. W. Elmer, T. A. Palmer, W. Zhang, B. Wood and T. DebRoy: *Acta Mater.*, **51**, 3333 (2003).

15. C.-H. Kim, W. Zhang and T. DebRoy: *J. Appl. Phys.*, **94**, 2667 (2003).

16. W. Zhang, C.-H. Kim and T. DebRoy: *J. Appl. Phy.*, **95**, 5210 (2004).

17. W. Zhang, C.-H. Kim and T. DebRoy: *J. Appl. Phy.*, **95**, 5220 (2004).

18. A. Kumar, W. Zhang, C.-H. Kim and T. DebRoy: *A Smart Bi-directional Model of Heat Transfer and Free Surface Flow in Gas Metal Arc Fillet Welding for Practicing Engineers*, Proceedings of the 7th Numerical Analysis of Weldability, Graz, Austria, in press (2003).

19. J. W. Elmer, T. A. Palmer, S. S. Babu, W. Zhang and T. DebRoy: *In-Situ Observations of Phase Transformations in the Fusion Zone of Ti-6Al-4V Alloy Transient Welds Using Synchrotron Radiation*, Proceedings of the 7th Numerical Analysis of Weldability, Graz, Austria, in press (2003).

20. J. W. Elmer, T. A. Palmer, S. S. Babu, W. Zhang and T. DebRoy: *Direct Observations of Austenite, Bainite and Martensite Formation During Arc Welding of 1045 Steel using Time Resolved X-Ray Diffraction*, submitted to Welding Journal (February 2004).

21. J. W. Elmer, T. A. Palmer, S. S. Babu, W. Zhang and T. DebRoy: *Direct Observations of Phase Transitions in Ti-6Al-4V Alloy Transient Welds using Time Resolved X-Ray Diffraction*, accepted for publication in Journal of Applied Physics (February 2004).

22. K. Mundra, T. DebRoy and K. M. Kelkar: *Numer. Heat Transfer A*, **29**, 115 (1996).

23. M. C. Tsai and S. Kou: *Weld. J.*, **69**, 241s (1990).

24. G. M. Oreper and J. Szekely: *Metall. Trans. A*, **18A**, 1325 (1987).

25. W. H. Kim and S. J. Na: *Int. J. Heat Mass Transfer*, **41**, 3213 (1998).

26. W. Pitscheneder, T. DebRoy, K. Mundra, and R. Ebner: *Welding J.*, **75**, 71s (1996).

27. K. Hong, D. C. Weckmann, A. B. Strong and W. Zheng: *Sci. Technol. Weld. Joining*, **7**, 125 (2002).

28. T. Zacharia, S. A. David, J. M. Vitek, and T. DebRoy: *Welding J.*, **68**, 510s (1989).

29. Z. Yang and T. DebRoy: *Metall. Mater. Trans. B*, **30B**, 483 (1999).

30. Z. Yang, J. W. Elmer, J. Wong, and T. DebRoy: *Weld. J.*, **79**, 97s (2000).

31. Z. Yang, S. Sista, J. W. Elmer, and T. DebRoy: *Acta Mater.*, **48**, 4813 (2000).

32. S. Mishra and T. DebRoy: *Acta Mater.*, **52,** 1183 (2004).

33. T. Hong and T. DebRoy: *Metall. Mater. Trans. B*, **34**, 267 (2003).

34. T. Hong and T. DebRoy: *Ironmak. Steelmak.*, **28**, 450 (2001).

35. T. Hong, W. Pitscheneder and T. DebRoy, *Sci. Technol. Weld. Joining*, **3**, 33 (1998).

36. X. He, P. W. Fuerschbach and T. DebRoy: *J. Phys. D: Appl. Phys.*, **36**, 1388 (2003).

37. X. He, T. DebRoy and P. W. Fuerschbach: *J. Appl. Phys.*, **94**, 6949 (2003).

38. H. Zhao and T. DebRoy: *J. Appl. Phys.*, **93**, 10089 (2003).

39. T. A. Palmer and T. DebRoy: *Sci. Technol. Weld. Joining*, **3**, 190 (1998).

40. T. A. Palmer and T. DebRoy: *Metall. Mater. Trans. B*, **31B**, 1371 (2000).

41. H. K. D. H. Bhadeshia and L. E. Svensson: *Proceedings of Mathematical Modeling of Weld Phenomena*, edited by Cerjak et. al., Institute of Materials, London, p. 109 (1993).

42. J. C. Ion, K. E. Easterling and M. F. Ashby: *Acta Metall.*, **36**, 1949 (1984).

43. T. Akbay, R. C. Reed and C. Atkinson: *Acta Metall. Mater.*, **47**, 1469 (1994).

44. J. W. Elmer, J. Wong, M. Fröba, P. A. Waide and E. M. Larson: *Metall. Mater. Trans. A*, **27A**, 775 (1996).

45. T. A. Palmer, J. W. Elmer and J. Wang: *Sci. Technol. Weld. Joining*, **7**, 159 (2002).

46. J. W. Elmer, J. Wong and T. Ressler: *Metall. Trans. A*, **32A**, 1175 (2001).

47. W. Zhang, T. DebRoy, T. A. Palmer and J. W. Elmer: *Unpublished Documentation*, The Pennsylvania State University (March 2004).

Chapter 2

BACKGROUND

The objective of the present thesis research is to understand heat transfer, fluid flow and microstructural evolution during fusion welding based on the fundamentals of transport phenomena and phase transformation theory. In particular, the research work seeks to quantitatively predict the liquid convection in the weld pool, temperature distribution in the weldment, thermal cycles, weld bead shape and size, and phase transformation kinetics. Since the subject of heat transfer, fluid flow and microstructural evolution covers a wide range of topics, it is not possible to review all the topics in this chapter. Therefore, important problems and issues pertinent to the subject of this study are selected to be reviewed here. The intention of this chapter is to examine some of the numerical methods for modeling heat transfer, fluid flow and microstructural evolution during fusion welding.

The following topics are covered in this chapter.

(1) The current understanding of the important transport processes during fusion welding, which includes energy absorption, liquid convection and driving forces, turbulence, free surface deformation, and governing conservation equations and their numerical solutions, is examined. This section reviews some of the general yet important issues in the calculation of heat transfer and fluid flow in the weld pool. In the next two sections, the simulation of heat transfer and fluid flow in two specific welding processes are examined.

(2) Transient spot welds behave differently than their moving weld counterparts because the thermal profiles never reach a steady state value. The heating and cooling rates for these welds are often much higher than that of steady state welds, and can lead to solidification cracking and formation of non-equilibrium phases. Accurate calculation of the evolution of temperature and velocity fields during transient spot welding requires

very fine grids and very small time steps. The modeling of heat transfer and fluid flow during transient spot welding is critically evaluated in this section.

(3) Much of previous study to understand welding processes and welded materials through numerical thermo-fluid calculations has considered mainly on simple rectangular workpiece with a flat weld pool top surface. A fundamental understanding of heat transfer and fluid flow considering free surface deformation and complex joint geometry is still evolving. In this section, the simulation of heat transfer and free surface flow during welding of joints with complex geometry particularly during gas metal arc (GMA) fillet welding is reviewed.

(4) Recently, several comprehensive phase transformation models have been developed to predict weldment microstructural evolution by taking into account the characteristics of phase transformations in welding. Coupling these phase transformation models with computed thermal cycles has been an important approach to quantitatively predict the weldment microstructure. This section critically reviews some of these phase transformation models and the current understanding of microstructural evolution during welding.

At the end of this chapter, a selection of important unanswered questions in the field of heat transfer, fluid flow and microstructural evolution during welding are identified. Solving these unanswered questions is an important goal of the present thesis study, and details of the solution are presented in subsequent chapters.

2.1 Transport Processes during Fusion Welding

The fusion welding process is schematically illustrated in Fig. 2.1 [2-6]. As shown in this figure, there are three distinct regions in the weldment: the fusion zone (FZ), the heat affected zone (HAZ) and the base material. During fusion welding, the interaction of the heat source with the base material leads to a serials of complex physical processes [2-6]. The FZ undergoes melting and solidification. In the weld pool, the liquid metal circulates vigorously driven by electromagnetic, surface tension gradient and buoyancy forces. It is well known that the convective heat flow affect the FZ geometry

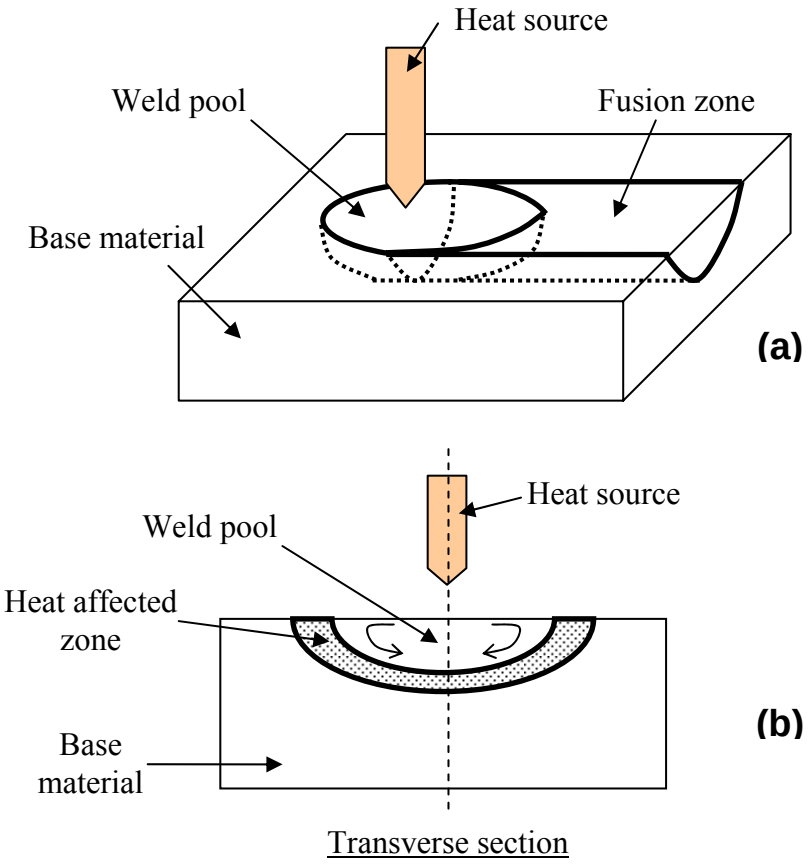

Fig. **2.1**: Schematic plot depicting the fusion welding process: (a) interaction between the heat source and the base material; and (b) the transverse section directly under the heat source [5].

and the temperature distribution in the HAZ. The HAZ, which experiences significant thermal exposure, may undergo various solid-state transformations. The base material region is the region unaffected by the welding process. During fusion welding, the complex physical processes are taking place in a rather small area, usually of the order of a few millimeters. The spatial variation of temperature in the weldment is quite high, generally up to several hundreds to thousands of degrees. The small welded area, where various physical processes are occurring, and the high spatial temperature gradients are the two characteristics of the welding process [2,3].

Since the number of processes occurring simultaneously during welding is rather large, it is often necessary to divide the complex welding process into a number of simple constituent parts. These parts include the interaction of the heat source and the weld pool, the heat transfer and fluid flow in the weld pool, the evolution of microstructure of the FZ and HAZ, and the development of residual stress and distortion in the weldment. The heat transfer and fluid flow is of particular interest, since it provides the knowledge of temperatures in the weldment, which is essential for understanding other physical processes such as the microstructural evolution and residual stress [2-6].

Experimental observation of the heat transfer and fluid flow in the weld pool is very difficult. Direct measurement of the temperatures in the weld pool by placing thermocouples is cumbersome and inaccurate because of the small size of the weld pool and very high liquid temperatures [7-14]. Indirect measurement methods such as infrared thermographic cameras [9,13] entail a high degree of uncertainty due to many assumptions need to be made with respect to the dependency of emissivity on the temperature, the associated angle, and the wavelength [11,12]. In addition, the intense arc and plasma environment associated with the arc welding process can further result in some extra errors. Currently, no reliable technique exists with respect to the measurement of temperature within the molten pool. On the other hand, the measurement of liquid flow velocities in the small and intensely heated weld pool is even more difficult than that of temperatures. Very few data have been reported on the measurement of velocities in the weld pool [15,16]. Therefore, a practical recourse is to utilize quantitative calculations to gain insights into the phenomena of heat transfer and fluid flow during welding [14].

In this section, the current understanding of heat transfer and fluid flow in the weld pool is examined. In fusion welding, only a fraction of heat energy is actually absorbed by the base material. The energy absorption efficiency is an important parameter. Thus, the factors affecting energy absorption efficiency is discussed at first. In the weld pool, the absorbed heat is transported by means of both convection and conduction. Therefore, the liquid convection and its driving forces are also discussed. The turbulence and the weld pool free surface deformation may affect the weld pool heat transfer, and they are also reviewed. The conservation equations governing heat transfer and fluid flow are then presented. Because of the complexities of these conservation equations, numerical solution is generally required. Therefore, several numerical methods for solving these conservation equations are discussed. This section ends with a summary of the previous work in the field of heat transfer and fluid flow in simple systems.

2.1.1 Energy absorption efficiency

During welding, only a fraction of energy is transferred from the heat source to the workpiece. The amount of energy transferred is importance since it directly affects the shape and size of the weld pool and the temperature distribution in the HAZ. The physical phenomena that influence the energy absorption are unique to each welding process [2,7].

2.1.1.1 Arc welding

For arc welding, the arc efficiency (η), which defines the fraction of the arc energy that is transferred to the workpiece, is given as [2]:

$$\eta = 1 - \frac{q_e + (1-n)q_p + mq_w}{VI} \qquad (2.1)$$

where q_e is the rate of heat transferred to the electrode from the welding arc, q_p is the rate of heat radiated and convected from the arc column, n is the proportion of heat output form the arc column that is transferred into the workpiece, q_w is the rate of heat absorbed by the workpiece, m is the fraction of absorbed energy that is radiated away and lost, and V and I are welding voltage and current, respectively.

When a consumable electrode is used, such as in GMA welding, q_e is also transferred to the workpiece and therefore the arc efficiency is thus given as [2]:

$$\eta = 1 - \frac{(1-n)q_p + mq_w}{VI} \qquad (2.2)$$

It should be noted that although Eqs. 2.1 and 2.2 are useful in explaining the manner in which various types of heat loss affect arc efficiency. However, evaluation of the values of q_e, q_p, q_w, n and m from theoretical considerations is very difficult. Therefore, a common practice is to experimentally determine the arc efficiency under various welding conditions. In the literature, experimentally measured arc efficiency is available for various arc welding processes including shielded metal arc welding (SMAW), submerged arc welding (SAW) and gas tungsten arc welding (GTAW) as well as gas metal arc welding (GMAW). The reported measured arc efficiency varies from 20% to over 95% depending on the welding process used [7,14].

Tsai and Eagar [17] experimentally measured the distribution of heat flux and the arc efficiency for a gas tungsten arc on a water-cooled copper anode as a function of various welding parameters. These welding parameters included the welding current, arc length, electrode tip angle, and shielding gas. In their experiments, the current changed from 100 to 280 A, the arc length varied from 2.0 to 9 mm, the electrode trip angel changed from 30° to 120°, and three different shielding gases were used: pure argon, 25% of helium + 75% of argon, and 50% of helium + 50% of argon. It was found that the arc energy distribution parameter (r_b) depended strongly on the welding current, arc length and shielding gas, whereas it did not change significantly with the electrode tip angle. The value of r_b varied from 1.5 to 3.6 mm for the welding conditions used in their experiments.

Based on the experimental data of Tsai and Eagar [17] for a pure argon arc, Arenas et al. [18,19] proposed the following simple approximation for estimating the arc efficiency.

$$\eta = 7.48 \frac{I^{0.63} R_c^2}{L^{0.8} IV} \qquad (2.3)$$

where L is the arc length (mm), and R_c is the arc radius (mm), which is related to the arc energy distribution parameter by $R_c = 2.13 r_b$ [18,19], I is the arc current (ampere) and V is the arc voltage (volt). It should be noted that Eq. 2.3 was derived by fitting the experimental data of Tsai and Eagar. Strictly speaking, this equation is valid only for the welding conditions used in Tsai and Eagar's experiments [17], as described in the previous paragraph.

The arc efficiency is usually higher for GMAW than for GTAW, since a fraction of energy lost to the electrode is transferred into the workpiece in the form of superheating metal droplets. The droplet transfer is a unique feature in GMAW where a consumable electrode is used, and it is often responsible for the finger penetration observed in the GMA welds. The droplet heat transfer will be reviewed in a later section.

2.1.1.2 Laser welding

There are usually two modes of laser welding: conduction and keyhole modes. During conduction mode laser welding, the absorption efficiency is equivalent to the absorptivity of the workpiece material. Bramson [20] related the absorptivity to the substrate resistivity and the wavelength of the laser radiation by the following equation:

$$\eta_\lambda(T) = 0.365\left(\frac{r}{\lambda}\right)^{1/2} - 0.0667\left(\frac{r}{\lambda}\right) + 0.006\left(\frac{r}{\lambda}\right)^{3/2} \qquad (2.4)$$

where η_λ is the laser absorptivity at temperature T and wavelength λ (cm), and r is the resistivity (Ω cm). Eq. 2.4 is accurate when the metal surface is clean and no plasma plume is formed or the plume is not affecting the absorption of the laser beam. Eq. 2.4

indicates the absorption of laser energy becomes more efficient as the laser wavelength decreases. It should be noted that several other factors such as the nature of the surface, the joint geometry, the concentration of volatile alloying elements in the base material also affect the absorption efficiency of laser beam energy [20].

If a keyhole is formed during laser welding, the laser absorption efficiency can be much higher than the material absorptivity due to multiple reflections of the beam in the cavity. Fuerschbach measured the absorption efficiency during CO_2 laser welding of 1018 steel, 304 stainless steel and tin [21]. It was found that the absorption efficiency is almost independent of the composition and physical properties of the substrate material in the keyhole mode.

Two excellent surveys of the absorption efficiency during laser welding can be found in references [14] and [22].

2.1.1.3 Deposition of heat energy at weld top surface

It is important to know how the heat energy is distributed over the weld top surface, since the distribution of heat input has a direct influence on the weld pool geometry. For GTA welding, the following Gaussian distribution has been widely used to account for the heat flux at the weld top surface [23-25].

$$q(r) = \frac{f_d \, VI \, \eta}{\pi \, r_b^2} \exp\left(- f_d \frac{r^2}{r_b^2} \right) \qquad (2.5)$$

where q is the heat flux at a given location at the weld top surface, r is the distance between the specific location and the heat source, f_d is a distribution factor, V and I are welding voltage and current, respectively, η is the arc efficiency and r_b is a characteristic energy distribution parameter. In the literature, two typical values of f_d have been reported: 3 and 0.5. The f_d value of 0.5 was proposed by Tsai et al. [17] and Smartt et al. [26] based on experimental measurements. On the other hand, several weld models [23-25,27-29] used the f_d value of 3. Depending on the electrode tip angle, arc length and current, the distribution parameter (r_b) is reported to vary in the range between 1.0 and

4.0 mm [17,26]. Eq. 2.5 indicates that the heat flux at the weld top surface can be computed if the values of f_d, η and r_b are known. The knowledge of heat input flux is a prerequisite to calculate the heat dissipation in the weldment.

It should be noted that although Eq. 2.5 was originally proposed for GTA welding, similar expressions have also been used to describe the heat flux at the weld top surface for GMA [30,31] as well as laser conduction welding processes [32-34]. It should be noted that for laser welding, the VI term in Eq. 2.5 should be replaced by the power of the laser beam.

2.1.2 Convective heat transfer in weld pool

Convective heat transfer is very important because in many cases it determines the shape and size of the weld pool and the temperature distribution in the entire weldment [2,4-7]. The liquid convection is driven by the surface tension gradient, buoyancy, jet impingement, and when electric current is used, electromagnetic forces [2,4-7]. Since the calculation of convective heat transfer involves the solution of the equations of conservations of mass, momentum and heat and is highly complicated, numerical solution is often utilized. The effect of various driving forces must be properly incorporated into the momentum equation in order to accurately predict the convective heat transfer in the weld pool.

2.1.2.1 Electromagnetic force

Figure 2.2 is a schematic plot showing the various driving forces in the weld pool and the resulting liquid flow pattern. The electromagnetic force, also called Lorentz Force, is caused by the electric current field together with the magnetic field it induces in the metal workpiece. Figure 2.2(a) shows the electromagnetic force with direct current electrode negative. As shown in this figure, the direction of the electromagnetic force is downward and inward. As a result, in the center of the weld pool, the liquid metal is

driven downwards, whereas at the top surface the melt flows from the periphery to the center of the pool. The electromagnetic force ($\vec{F}_{emf}$) can be expressed as [35]:

$$\vec{F}_{emf} = \vec{J} \times \vec{B} \qquad (2.6)$$

where $\vec{J}$ is the current density vector and $\vec{B}$ is the magnetic flux vector in the weld pool.

Comprehensive three-dimensional calculations of $\vec{J}$ and $\vec{B}$ fields are needed for the accurate determination of the electromagnetic force in the weld pool. Kou and Sun [36] developed the following analytical expressions for $\vec{J}$ and $\vec{B}$ fields by solving Maxwell's equations in an axis-symmetric system with Magneto-hydrodynamics (MHD) approximation.

$$J_z = \frac{I}{2\pi}\int_0^{\infty} \lambda J_o(\lambda r)\exp\left(-\lambda^2\sigma_j^{\,2}/12\right)\frac{\sinh[\lambda(c-z)]}{\sinh(\lambda c)}d\lambda \qquad (2.7a)$$

$$J_r = \frac{I}{2\pi}\int_0^{\infty} \lambda J_1(\lambda r)\exp\left(-\lambda^2\sigma_j^{\,2}/12\right)\frac{\cosh[\lambda(c-z)]}{\sinh(\lambda c)}d\lambda \qquad (2.7b)$$

$$B_\theta = \frac{\mu_m I}{2\pi}\int_0^{\infty} J_1(\lambda r)\exp\left(-\lambda^2\sigma_j^{\,2}/12\right)\frac{\sinh[\lambda(c-z)]}{\sinh(\lambda c)}d\lambda \qquad (2.7c)$$

where J_z is the vertical component of the current density, I is the current, J_0 is the Bessel function of zero order and first kind, r is the radial distance from the arc center, σ_j is the effective current radius of the arc, c is the thickness of the workpiece, z is the vertical distance from the top surface, J_r is the radial component of current density, J_1 is the first kind of Bessel function of first order, B_θ is the angular component of the magnetic field, and μ_m is the magnetic permeability of the material. The radial and the axial components of the magnetic flux, B_r and B_z, are assumed to be zero. With the knowledge of $\vec{J}$ and $\vec{B}$ fields, the electromagnetic force in the weld pool can be computed using Eq. 2.6.

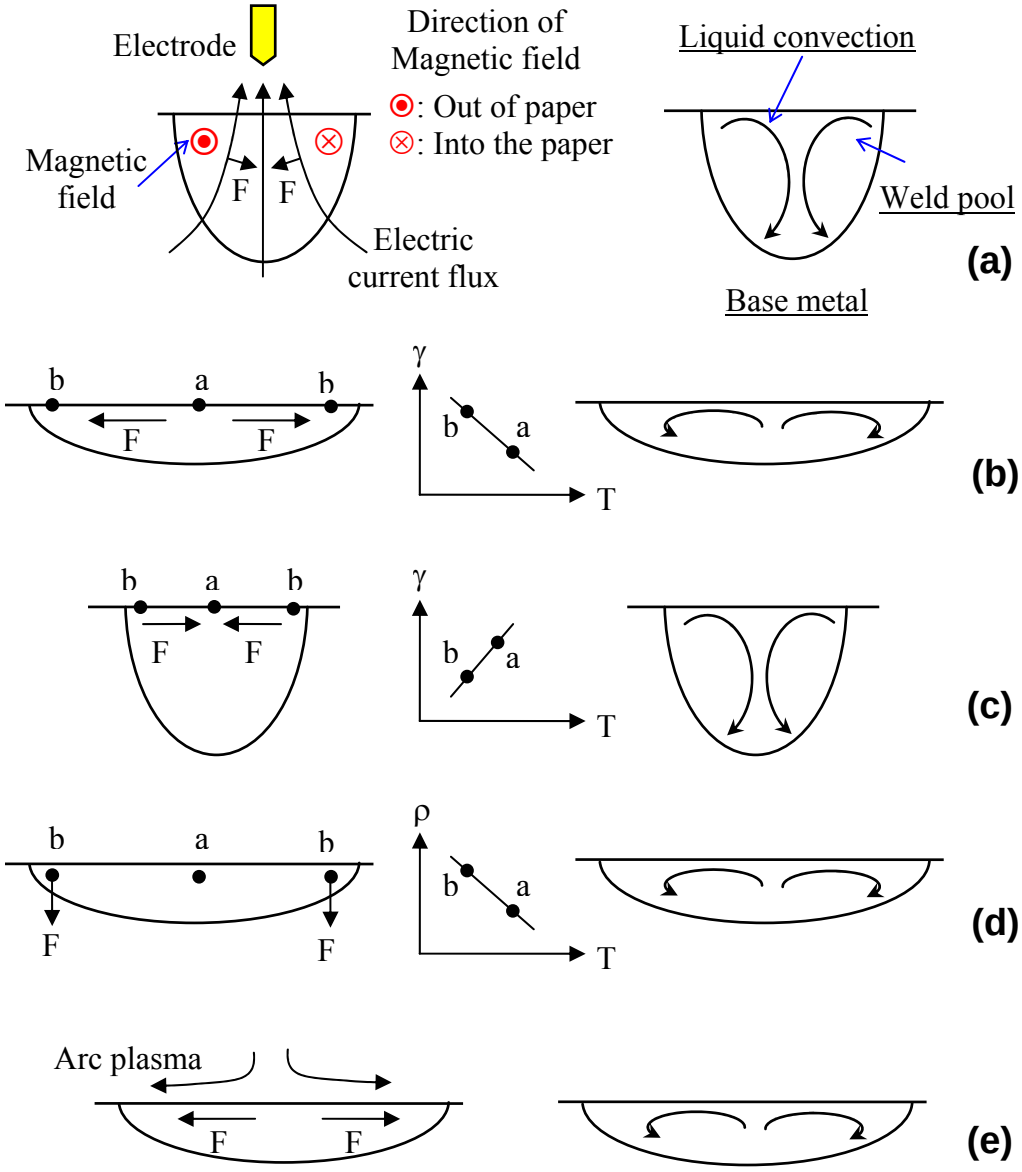

Fig. **2.2**: Various driving forces and the resulting liquid convection in the weld pool [7]: (a) electromagnetic force, (b) surface tension gradient force with negative $\partial\gamma/\partial T$, (c) surface tension gradient force with positive $\partial\gamma/\partial T$, (d) buoyancy force, and (e) plasma jet impingement force. Symbol γ is the surface tension, $\partial\gamma/\partial T$ is the temperature coefficient of surface tension, T is the temperature, ρ is the density, a and b are two locations in the weld pool, and F is the driving force.

More recently, Kumar and DebRoy [37] developed a numerical model to accurately calculate the $\vec{J}$ and $\vec{B}$ fields and the resulting electromagnetic force field in three dimensions in the entire weldment. Contributions of the electrode current, arc plasma and current distribution inside the three-dimensional workpiece to the magnetic field and the electromagnetic force field were determined. They evaluated the effects of different arc locations and work piece geometry on the electromagnetic force field. Figure 2.3 shows the computed electromagnetic force distribution inside the workpiece for two different arc locations. They concluded that the accuracy of the computed electromagnetic force field can be significantly improved by considering the contributions of electrode current, arc plasma and the current distribution within the workpiece.

2.1.2.2 Marangoni shear stress

Surface tension (γ) of is a thermo-physical property of the liquid metal, which may generate a shear stress at the liquid/gas interface. The spatial gradient of surface tension is a stress, which is known as the Marangoni shear stress. This stress arises due to spatial variation of temperature and composition, which can be expressed as:

$$\tau = \frac{\partial \gamma}{\partial T}\frac{\partial T}{\partial r} + \frac{\partial \gamma}{\partial C}\frac{\partial C}{\partial r} \qquad (2.8)$$

where τ is the shear stress due to surface tension, T is the temperature, r is the distance along the surface from the heat source, and C is the concentration of surface active element. In most cases, the difference in surface tension is due to the spatial temperature variation. In other words, the $\partial\gamma/\partial C$ term in Eq. 2.8 is zero, and the shear stress depends only on $\partial\gamma/\partial T$ and the spatial temperature gradient $\partial T/\partial r$ at the pool surface.

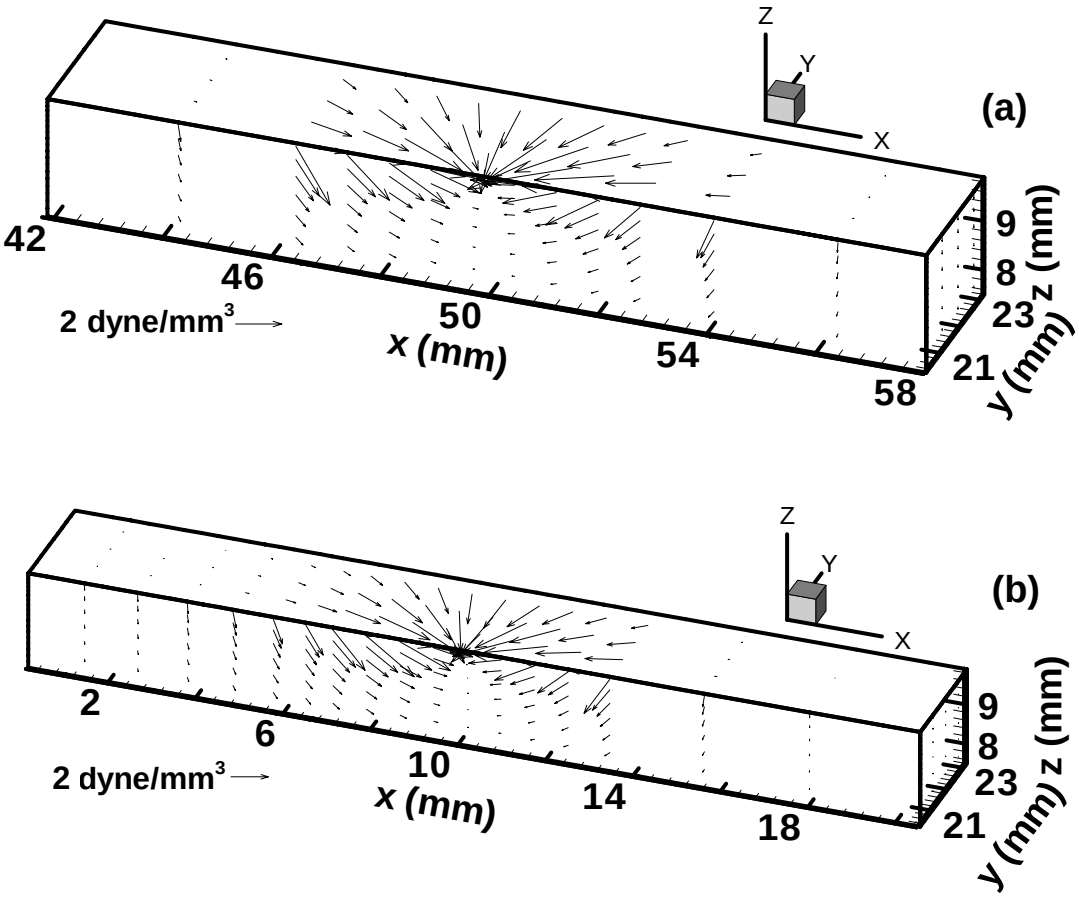

Fig. **2.3**: Electromagnetic force distribution inside the work piece: (a) the arc is located at x = 50 mm and y = 20 mm, and (b) the arc is located at x = 10 mm and y = 20 mm. Adapted from Kumar and DebRoy [**37**].

In the absence of a surface active element, the temperature coefficient of surface tension ($\partial\gamma/\partial T$) for many materials is less than zero. In other words, the higher the temperature, the lower the surface tension. Hence, at the weld pool top surface, the liquid metal flows radically outward, since the warmer liquid metal of lower surface tension near the center of the pool is pulled outward by the cooler metal of higher surface tension at the pool edge [7]. Pushed by the strong outward flow at the top surface, the liquid metal is transported outwards from the middle of the weld pool and arises at the center of the pool, as shown in Fig. **2.2(b)**.

If a small amount yet significant surface active elements such as sulfur and oxygen are presented in the weld pool, the value of $\partial\gamma/\partial T$ can be dramatically altered. For liquid material with a positive value of $\partial\gamma/\partial T$, the direction of the Marangoni shear stress and the resulting flow pattern are shown in Fig. **2.2(c)**. This flow pattern is expected, since the cooler metal of lower surface tension at the pool edge is pulled inward by the warmer liquid metal of higher surface tension near the center of the pool. If the value of $\partial\gamma/\partial T$ in the weld pool is not always positive or negative, the resulting flow pattern in even more complicated than those shown in Figs. **2.2(b)** and **(c)**, and four circulation loops may exist in the weld pool.

The Marangoni stress driven flow in the weld pool has been experimentally observed by Limmaneevichitr and Kou [38]. In their experiments, the Marangoni convection was introduced in a transparent pool of $NaNO_3$ with a defocused CO_2 laser beam. Figure **2.4(a)** shows the Marangoni convection with an outward surface flow in the $NaNO_3$ molten pool, which has a $\partial\gamma/\partial T$ value of 5.6×10^{-5} N m^{-1} K^{-1}. The outward surface flow is much faster than the inward return flow due to the following reason. The outward flow, driven by the Marangoni shear stress, drags the liquid underneath the surface to move outwards. However, such outward flow decays rapidly in the depth direction due to the liquid viscous friction. Therefore, only a thin layer of outward flow is formed in the vicinity of the molten pool surface, as shown in Fig. **2.4(a)**. The liquid mass continuity indicates that the amount of liquid flowing in outward and inward directions should be the same. Hence, the return inward flow, which occupies a much larger area than the surface outward flow, has a lower velocity than the outward flow.

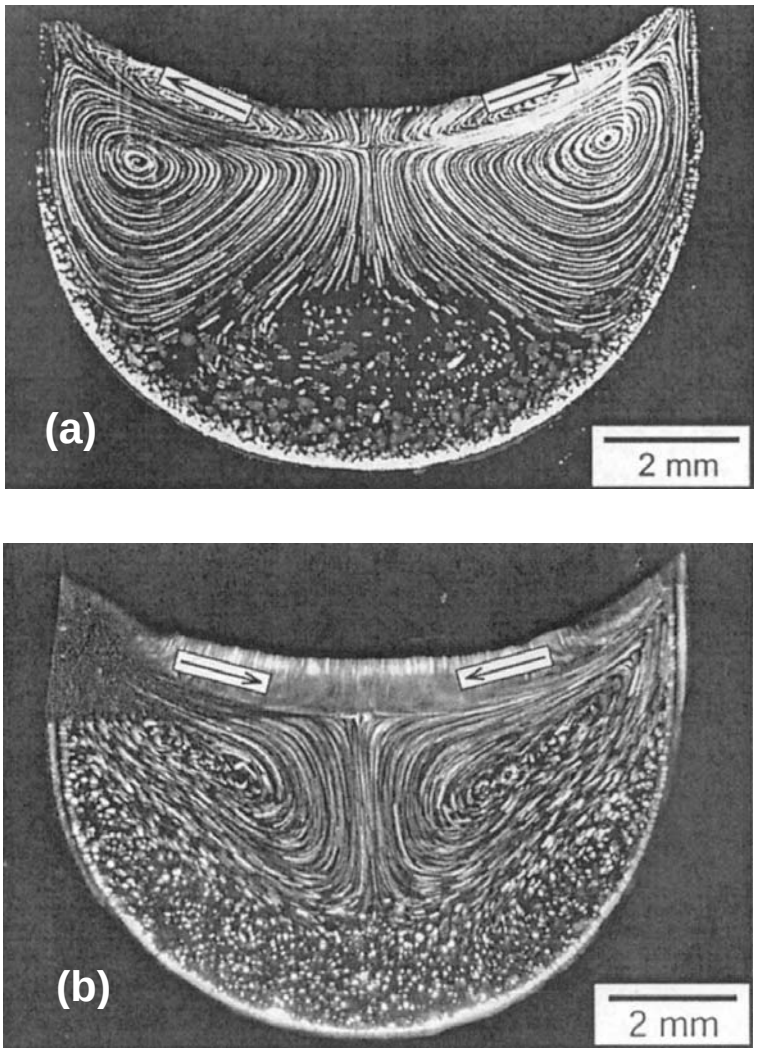

Fig. **2.4**: Marangoni convection in a $NaNO_3$ molten pool: (a) outward flow; and (b) inward flow when 2 mol% of C_2H_5COOK was added. Adapted from Limmaneevichitr and Kou [**38**,**39**].

To study the effect of surface active elements on the liquid convection, Limmaneevichitr and Kou [39] added C_2H_5COOK into the $NaNO_3$ molten pool, and they found the direction of Marangoni convection was reversed. Figure 2.4(b) shows the inward surface flow when 2 mol% of C_2H_5COOK was added into the pool. This inward flow is due to the following reason. The C_2H_5COOK is a surface active compound in $NaNO_3$, and it can reduce the surface tension of $NaNO_3$, just as S reduces the surface tension of liquid steel. The value of $\partial\gamma/\partial C$ for C_2H_5COOK is 2.2×10^{-2} N m^{-1} $mol\%^{-1}$. At the center of the pool surface, C_2H_5COOK was present at a lower concentration because it decomposed during the heating by the CO_2 laser beam. The surface tension at the center of the pool surface was now higher than that at the pool periphery. Hence, the liquid was pulled inward by the shear stress. In this particular case, the spatial variation of temperature did not play dominant role in changing the surface tension, since the magnitude of $\frac{\partial\gamma}{\partial T}\frac{\partial T}{\partial r}$ was much smaller than that of $\frac{\partial\gamma}{\partial C}\frac{\partial C}{\partial r}$ [39].

Sahoo et al. [41] determined the $\partial\gamma/\partial T$ as a function of both temperature and composition, which is expressed as:

$$\frac{\partial\gamma}{\partial T} = A - R\Gamma_s \ln\left(1 + Ka_i\right) - \frac{Ka_i}{\left(1 + Ka_i\right)}\frac{\Gamma_s\left(\Delta H^o - \Delta\overline{H}_i^M\right)}{T} \qquad (2.9)$$

where A is the $\partial\gamma/\partial T$ value for pure metal, Γ_s is the surface excess at saturation, K is the adsorption coefficient, a_i is the activity of species i in the solution, ΔH^o is the standard heat of adsorption, and $\Delta\overline{H}_i^M$ is the partial molar enthalpy of mixing of species i in the solution.

Pitscheneder et al. [26] applied Eq. 2.9 and a thermo-fluid model to study the effect of sulfur content and heat input on the weld pool geometry. Figure 2.5 shows the comparison between the predicted and measured cross sections of steel welds containing 20 and 150 parts per million (ppm) of sulfur, which were laser welded under different powers. As shown in this figure, at a laser power of 1.9 kW, the pool geometries in two steels were similar. In contrast, when the laser power increased to 5.2 kW, the weld containing 150 ppm sulfur had a much deeper penetration than that containing 20 ppm

sulfur. They explained the observed phenomena based on the direction of the convection dominant heat transport in the weld pool. At the laser power of 1.9 kW, the resulting weld pool was small and so were the liquid velocities. The maximum values of the Peclet number for the steel weld pools with 20 and 150 ppm sulfur0 were 0.18 and 0.91. Such low Peclet number indicated that conduction was the dominant mechanism in dissipating the heat in the weld pool. In other words, the direction of the liquid flow was not important in determining the weld pool shape. Consequently, there were no significant difference between the weld pool geometries for steels containing 20 and 150 ppm sulfur. On the other hand, at the laser power of 5.2 kW, the values of Peclet number were greater than 200. Such high Peclet number indicated that convection was dominant in transporting the heat in the weld pool. As a result, the weld pool geometry was largely determined by the direction of the liquid flow. For the sulfur content of 20 ppm, the value of $\partial\gamma/\partial T$ was negative, which resulted in an outward flow and consequently a shallow and wide pool. For the sulfur content of 150 ppm, the value of $\partial\gamma/\partial T$ was positive in the majority part of the weld pool, and the convection pattern is radially inward. Hence, the convective heat transport in the downward direction resulted in a deep weld penetration. As shown in Fig. **2.5**, the good agreement between the calculated and measured weld pool geometries indicated that the role of sulfur on the weld pool geometry could be reasonable predicted using Eq. **2.9** and the heat transfer and fluid flow model.

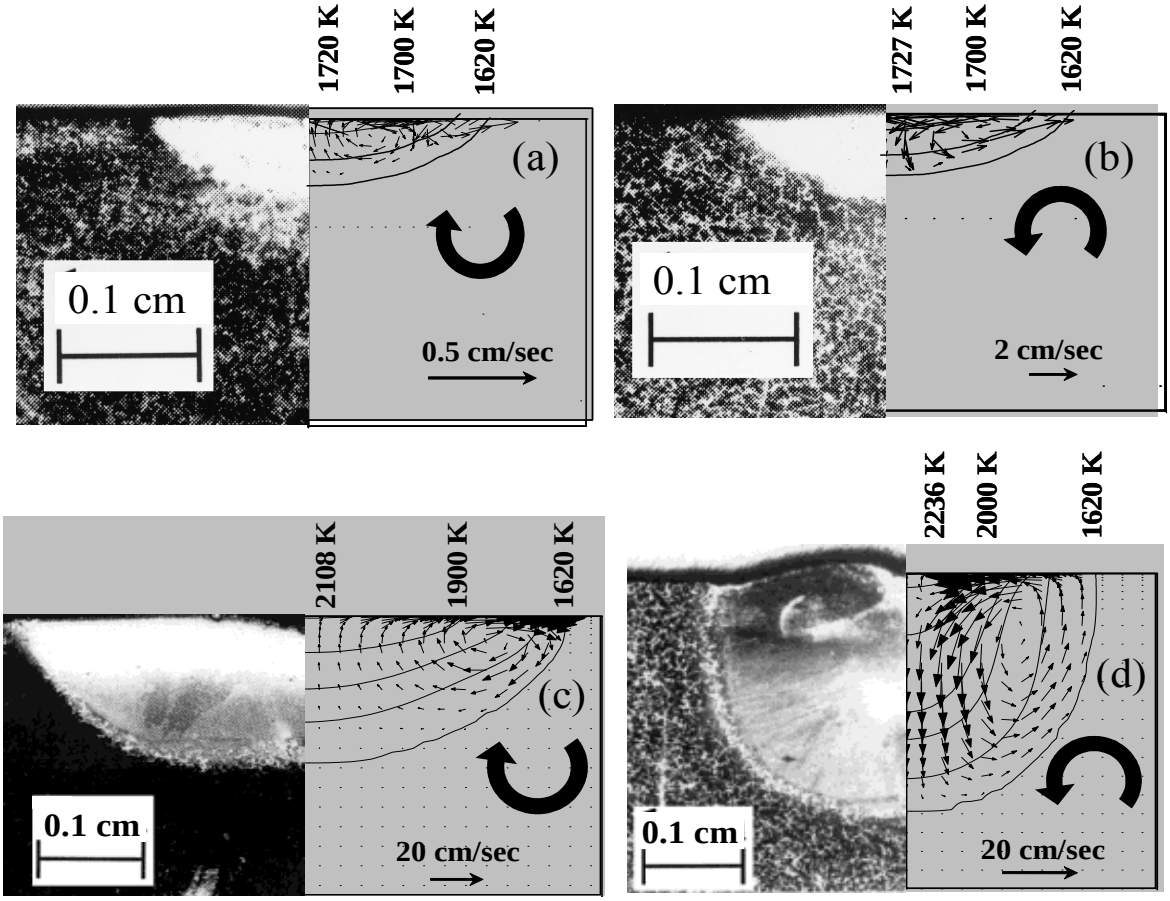

Fig. 2.5: Comparison between calculated and measured weld pool geometry for various sulfur contents and heat inputs: (a) 20 ppm and 1.9 kW, (b) 150 ppm and 1.9 kW, (c) 20 ppm and 5.2 kW, and (d) 150 ppm and 5.2 kW. Adapted from Pitscheneder et al. [26].

2.1.2.3 Buoyancy force

The Boussinesq approximation was used in the calculation of buoyancy force driven flow. In other words, the variation in the density of the liquid metal is ignored, except insofar as it gives rise to a buoyancy force, which is also termed as the gravitational force. Figure **2.2(d)** shows the buoyancy force direction and the buoyancy driven convection. As shown in this figure, the liquid metal rises along the pool center with low magnitude and fall along the pool boundary due to the local variation of density. This flow pattern is expected because the liquid metal near the heat source is at a relatively high temperature. It moves upwards because of its relatively low density. On the other hand, the liquid metal near the pool boundary has relatively low temperature and it flows downward because of its high density [7].

The buoyancy force can be expressed as [32]:

$$F_b = \rho g \beta (T - T_{ref}) \qquad (2.10)$$

where ρ is the density of liquid metal, g is the acceleration due to gravity, β is the thermal expansion coefficient, T is the temperature of the liquid metal, and T_{ref} is an arbitrarily selected reference temperature.

2.1.2.4 Shear stress induced by plasma jet

When an electric arc is used during welding, the arc plasma moves outward at high speeds along the weld pool surface, which can exert an outward shear stress at the pool surface, as shown in Fig. **2.2(e)**. The direction of the shear stress is similar to that resulting form the surface tension gradient with negative $\partial\gamma/\partial T$ value. The liquid metal flows from the center of the pool surface to the pool periphery, and then returns below the pool surface in the middle of the molten pool.

Matsunawa and Shinichiro [42,43] experimentally studied the importance of the plasma shear stress during GTA welding. They found that the plasma shear stress may outweigh both electromagnetic and surface tension gradient forces and become the

dominant driving force for the liquid convection when a long arc was used. They studied two series of stationary GTA welds in mild steel, one with a 2-mm-long arc and the other with an 8-mm-long arc. The 8-mm-long arc welds were much wider and shallower than the 2-mm-long arc welds. This was because for a longer and thus wider arc, the electric current and heat input flux were distributed over a larger area at the weld top surface. Hence, the electromagnetic force was largely reduced due to the flatter and wider current distribution. The surface tension gradient force was also reduced, since the temperature gradient at the weld pool surface decreased.

Matsunawa and shinichiro [42,43] also experimentally measured the FZ shape and size in the 304 stainless steel with two difference levels of sulfur: 18 ppm and 77 ppm. It was found that when a 2-mm-long arc was used, the FZ was much deeper in the 304 stainless steel with 77 ppm than that with 18 ppm. On the other hand, when an 8-mm-long arc was used, the FZ were shallow regardless the sulfur level presented in the base metal. This further indicated that the surface tension gradient force dominated in case of the 2-mm-long arc, whereas the plasma shear stress was primarily responsible for driving the liquid convection in case of the 8-mm-long arc.

2.1.2.5 Relative importance of driving forces

In order to understand the heat transfer and fluid flow behavior in the weld pool, it is useful to check some dimensionless numbers, which characterize the relative importance of the driving forces responsible for the motion of the fluid flow. Such dimensionless numbers can be used to predict the size and shape of the FZ and HAZ. For instance, if the electromagnetic force is the dominant driving force, a deep and narrow pool shape is expected. In contrast, if the surface tension gradient force with negative $\partial\gamma/\partial T$ is largely responsible for the liquid motion, the resulting weld pool is expected to be wide and shallow. The following dimensionless numbers are used to evaluate the relative importance of the driving forces, as indicated in Eqs. 2.11 through 2.13.

The ratio of buoyancy to viscous force is determined by Grashof number, Gr [44]:

$$Gr = \frac{g \beta L_B^3 \Delta T \rho^2}{\mu^2} \quad (2.11)$$

where g is the acceleration due to gravity, β is the thermal expansion coefficient, ΔT is the difference between the pool peak temperature and the solidus temperature of the material, L_B is a characteristic length for the buoyancy force in the liquid pool, which is approximated by one eighth of the pool width, and μ is the liquid viscosity.

Magnetic Reynolds number (Rm) defines the ratio of electromagnetic force to viscous force, and is expressed as [45,46]:

$$Rm = \frac{\rho \mu_m I^2}{4\pi^2 \mu^2} \quad (2.12)$$

where ρ is the density, I is the arc current, and μ_m is the magnetic permeability.

Surface tension Reynolds number (Ma) is used to describe the ratio of surface tension gradient force to viscous force, and is calculated as [45,46]:

$$Ma = \frac{\rho L_R \Delta T \left| \partial \gamma / \partial T \right|}{\mu^2} \quad (2.13)$$

where L_R is the characteristic length of the weld pool and is assumed to be equal to a half of the weld pool width, and $\partial\gamma/\partial T$ is the temperature coefficient of surface tension.

Once the values of Gr, Rm and Ma are determined, the relative importance of the driving forces, i.e., surface tension gradient, electromagnetic, and buoyancy forces, can then be judged by the combination of these dimensionless numbers. For example, the ratio of the electromagnetic force to the buoyancy force is given by:

$$R_{M/B} = \frac{Rm}{Gr} \quad (2.14)$$

The ratio of the surface tension gradient to the buoyancy force is expressed as:

$$R_{S/B} = \frac{Ma}{Gr} \quad (2.15)$$

To demonstrate the usefulness of the forementioned approach, a GTA welding of 1005 steel case [8] is considered here. The welding conditions, material properties and

other data needed for the calculation of the relative importance of driving forces are listed in Table 2.1. The calculated dimensionless numbers using Eqs. 2.11 through 2.15 are summarized in Table 2.2. As shown in this table, the buoyancy force is negligible comparing to the electromagnetic and surface tension gradient forces. On the other hand, the surface tension gradient force plays more important role than the electromagnetic force, since $R_{S/B}$ is greater than $R_{M/B}$. Therefore, a wide and shallow pool shape is expected, which is consistent with the experimental observation [8].

2.1.2.6 Estimation of order of maximum velocity in weld pool

If buoyancy force is the only driving force for the liquid convection, an order of magnitude of the maximum velocity (u_{grv}) under buoyancy driven flow is given by [45]:

$$u_{grv} = \sqrt{g \beta \Delta T \, D} \tag{2.16}$$

where D is the pool depth.

For electromagnetic force driven flow, an order of magnitude calculation of the maximum velocity (u_{emf}) under electromagnetic convection can be estimated from the following expression [45]:

$$u_{emf} = \frac{DI}{2\pi r_b^2}\sqrt{\frac{10\mu_m D}{\rho L_w}} \tag{2.17}$$

where L_w is the thickness of the workpiece, and r_b is the arc distribution parameter.

An order of magnitude of the maximum velocity (u_{st}) under Marangoni convection can be estimated by from following expression [5]:

$$u_{st}^{3/2} = \frac{\Delta T}{0.664\left(\rho \mu W\right)^{1/2}}\left|\frac{\partial \gamma}{\partial T}\right| \tag{2.18}$$

where W is the half width of the weld pool.

For the GTA welding of 1005 steel case considered in the previous section, the order of the maximum liquid velocity under different driving forces were estimated using the data given in Table 2.1. Table 2.3 shows the computed maximum velocities in the

GTA weld pool. As shown in this table, the maximum velocity for the buoyancy driven flow is much smaller than those for the electromagnetic and Marangoni driven flows. The magnitude of the maximum velocity for Marangoni driven flow was comparable with the computed maximum velocity in the weld pool, i.e., 120 mm/s [**8**]. This further indicates the Marangoni shear stress is the dominant driving force in the GTA weld pool under the conditions of the welding.

It should be noted that for the particular GTA welding case examined here, the electromagnetic force is smaller than the surface tension gradient force because of the low current (110 A) used. It has been reported that when the current is high (>250 A), the electromagnetic force becomes the dominant driving force in the weld pool convection, which can result in a weld pool with deep penetration [**48**,**49**].

As shown in the above discussion, the different driving forces play important role in dissipating the heat in the weld pool and determine the temperature distribution in both the weld pool and the HAZ. Therefore, to accurately simulate the weld heat transfer and fluid flow, the various driving forces need to be incorporated in the governing conservation equations and corresponding boundary conditions. Details on incorporating the driving forces in the governing equations will be presented in later sections.

2.1.2.7 Convection versus conduction on weld pool heat transfer

During welding, the arc energy is transported from the top surface of the weld pool to the surrounding solid region by both heat conduction and convection. The rate of the heat flow determines not only the peak temperature and shape of the weld pool but also the temperature distribution in the HAZ. Therefore, it is important to understand the effects of conduction and convection on the heat dissipation in the weld pool. The relative importance of convection versus conduction in transferring heat in the molten pool can be evaluated using the Peclet number (Pe), which is given by [**44**]:

Table 2.1: Welding conditions, material properties and other data of AISI 1005 steel welds [8].

Data	Value
Arc current, I, (A)	110
Arc voltage, V, (V)	17.5
Welding speed, U_w, (mm/s)	0.6
Arc energy distribution parameter, r_b, (mm)	2.7
Gravitational acceleration, g, (m/s^2)	9.8
Coefficient of thermal expansion, β, (K^{-1})	1.7×10^{-6}
Density of liquid metal, ρ, (kg/m^3)	7.2×10^{3}
Solidus temperature, T_s, (K)	1779
Effective viscosity of liquid, μ, (kg/m-s)	6.3×10^{-3}
Specific heat of liquid, C_{pl}, (J/kg-K)	754
Effective thermal conductivity of liquid, k_l, (J/m-s-K)	36.4
Magnetic permeability, μ_m, (N/A^2)	1.26×10^{-6}
Temperature coefficient of surface tension, $\partial\gamma/\partial T$, (N/m-K)	-0.49×10^{-3}
Width of the weld pool, (mm)	8.8
Depth of the weld pool, (mm)	1.8
Maximum velocity at the weld pool top surface, (mm/s)	120
Peak temperature of the weld pool, (K)	2020
Temperature variation at the pool surface, ΔT, (K)	240
Thickness of the workpiece, L_w, (mm)	10

Table 2.2: Dimensionless numbers in the GTA weld pool for the conditions of welding indicated in Table 2.1.

Dimensionless number	Description	Value
Gr	Ratio of buoyancy to viscous force	30
Rm	Ratio of electromagnetic to viscous force	7.0×10^{4}
Ma	Ratio of surface tension to viscous force	9.4×10^{4}
$R_{M/B}$	Ratio of electromagnetic to buoyancy force	2.3×10^{3}
$R_{S/B}$	Ratio of surface tension to buoyancy force	3.1×10^{3}

Table 2.3: Order of the maximum velocity in the GTA weld pool for the conditions of welding indicated in Table 2.1.

Maximum velocity	Description	Value (mm/s)
u_{grv}	Buoyancy driven flow	2.7
u_{emf}	Electromagnetic force driven flow	21
u_{st}	Marangoni driven flow	140

$$Pe = \frac{u_R \rho C_{pl} L_R}{k_l} \qquad (2.19)$$

where u_R and L_R are the characteristic velocity and length in the weld pool, respectively, ρ is the density, and C_{pl} and k_l are the specific heat and thermal conductivity of liquid metal, respectively. When Pe is large, which in physical terms means large liquid metal velocity, large weld pool, and poor thermal diffusivity (i.e. $k_l/(\rho C_{pl})$), the liquid metal convection significantly affects the heat transfer in the weld pool. In contrast, when Pe is small, say much less than unity, the conduction plays an important role in the heat dissipation in the weld pool [4,5].

For the GTA welding of 1005 steel case considered in the previous section, the Marangoni shear stress is the dominant driving force for the liquid convection in the weld

pool. A strong outward flow is formed at the weld pool top surface, and the resulting weld pool is wide and shallow. Therefore, the half width of the weld pool and the maximum velocity at the pool top surface can be assumed to represent the characteristic velocity and length of the pool, respectively. The physical property data of the 1005 steel and several characteristic parameters of the 1005 weld pool are listed in Table **2.1**. Using these data and Eq. **2.19**, the computed Peclet number is about 40. Since the Peclet number is much larger than unity, the liquid metal convection plays a dominant role in dissipating the heat in the weld pool. In other words, a model, which takes into account only the conduction heat transfer in the pool, is not able to accurately describe the heat transport process in the GTA weld pool.

The foregoing dimensional analysis provides insights about the heat transport process in the weld pool. The relative importance of driving forces for liquid metal convection, the order of magnitude of the velocity driven by the different forces and the role of conduction and convection on heat transfer in the weld pool could be evaluated using several dimensionless numbers. It should be noted that the order of magnitude analysis cannot provide accurate and detailed information on the temperature and velocity fields in the weldment, which requires numerical solution of the complex governing conservation equations.

2.1.3 Turbulence in weld pool

The liquid flow can be classified into the following two types according to its stability: laminar flow and turbulent flow. In a laminar flow, the flow velocity in any location is deterministic, whereas in a turbulent flow, the flow velocity is fluctuating in a random manner. Laminar flow is often observed at low flow velocity and high viscosity. As the flow velocity increases, the laminar flow may change to the turbulent flow, which can greatly enhance the mixing of mass, momentum and energy. The following Reynolds number is used to describe the flow behavior [**44**].

$$\mathrm{Re} = \frac{\rho u_R L_R}{\nu} \qquad (2.20)$$

where ρ is the liquid density, u_R and L_R are the characteristic velocity and length of the flow, respectively, and ν is the kinematic (molecular) viscosity of the liquid. For flow through pipes, the critical transition Reynolds number from laminar to turbulent is determined to be about 2100 [44].

In order to accurately simulate the heat transfer and fluid flow in the weld pool, it is important to understand the turbulent behavior of the liquid metal. It is not yet completely clear whether the flow in the weld pool is turbulent in nature. However, there are evidences that suggest the existence of turbulence in the weld pool. Malinowski-Brodnicka et al. [50] measured the flow velocity in AISI 310 stainless steel weld pools and found that the Reynolds number was about 3000. Comparing this value to the classical critical Reynolds number of 2100, they concluded that the flow in the weld pool was most likely turbulent.

Choo and Szekely [51] first considered turbulence in GTA weld pools. They developed a two-dimensional model based on the two-equation K-ε turbulence model [52]. The liquid flow in 304 stainless steel weld pools during stationary GTA welding was simulated using their turbulence model. The calculated geometry from both laminar and turbulence models was compared with the experimental data. They found that turbulence affected the pool depth significantly, and the calculated weld pool geometry from turbulence model was in much better agreement with measurements than that from laminar model.

Hong et al. [53,54] also developed a K-ε turbulence thermo-fluid model, where the free surface of the weld pool and the wall function boundary for the solid-liquid interface were considered by using a dynamic grid-remapping technique. It was found that the depth of the weld pool, the peak temperature, and the maximum velocity were reduced due to consideration of turbulent heat transfer and fluid flow. The predicted results from the turbulent model were also found in much better agreement with the observed results than those obtained from the laminar model. They concluded that the turbulence had significant influence on the final weld pool shape and size in GTA welding processes.

More recently, Yang and DebRoy [55] studied the turbulent heat transfer and fluid flow during GMA welding of HSLA-100 steels. Figure 2.6 shows the distribution of turbulent viscosity, thermal conductivity, kinetic energy and dissipation rate in the weld pool from their calculations [55]. It was observed that the maximum values of these variables lay in the middle of the weld pool, and the values decreased progressively from the center to the periphery. The high computed values of turbulent viscosity and thermal conductivity suggested that the transport of heat and momentum in the weld pool was significantly aided by turbulence. Their computed FZ geometry was in good agreement with the experimental data.

Although the two-equation K-ε turbulence model [51-55] has been successfully used to predict the weld pool geometry, they have the following two limitations. First, application of the semi-empirical two-equation K-ε turbulence model requires the knowledge of several empirical constants. These constants were originally developed to model liquid flow in large systems such as pipes. The use of these constants to model strong circulation flow in small weld pools is open to question. Second, the turbulence model requires the solution of two extra equations (turbulence kinetic energy and its dissipation rate) in addition to the three governing conservation equations. Therefore, the solution process is very complex and a converged solution may not always be obtained.

Due to the difficulties in applying the K-ε turbulence model, a more widely used approach is to use an effective viscosity and an effective thermal conductivity in the weld pool [32-34,26,56]. The effective viscosity and thermal conductivity are often 5 to 20 times higher than their molecular values [32-34,57]. Such high values are necessary to account for the enhanced mixing of momentum and energy caused by turbulence. The predicted shape and size of the weld pool by adopting appropriate effective viscosity and thermal conductivity values were found to be quite close to experimental results, whereas no extra solution of the K-ε equations were needed. However, in these calculations the values of the effective viscosity and thermal conductivity were often taken based on experience and not from fundamental principles. To overcome this difficulty, De and DebRoy [58] recently proposed a procedure combining a heat transfer and fluid flow model and an optimization algorithm to estimate the effective viscosity and thermal

conductivity. Their model could determine the effective viscosity and thermal conductivity as a function of power input from a limited volume of experimental data, and the computed weld pool geometry were in good agreement with the experimental results.

2.1.4 Weld pool free surface flow and surface deformation

In many of the previous numerical simulations of heat transfer and fluid flow in the weld pool, the weld pool top surface is assumed to be flat and not deformable. This is a reasonable assumption when the arc current is low and the arc pressure exerted on the top surface is small. However, when the arc current is high, the weld pool surface can be severely deformed. For example, Lin and Eagar [59] experimentally measured the depression of the pool top surface during GTA stationary welding of 304 stainless steel. Their measurement indicated that the surface depression at currents below 200 A was negligible. However, when current increased to about 300 A, the surface depression can be as high as 4.5 mm in the stainless steel weld pools. During GMA welding, the use of consumable electrode and the droplet transfer further displace the weld pool. Such deformed pool surface may affect the heat transfer and fluid flow in the weld pool, the weld pool geometry and the temperature distribution in the HAZ [49]. In the worst case, the severely deformed surface may result in the formation of several weld defects such as humped bead and undercutting [7,49]. Hence, understanding the weld pool top surface profile and its effect on the heat transfer and fluid flow is very important.

It should be noted that the weld pool top surface, i.e., the liquid/gas interface, is a free surface. This is because the densities of the gas and liquid metal are largely different (e.g., the ratio for liquid metal and air is about 7000). A low gas density means that its inertia can generally be ignored compared to that of the liquid. Therefore, the liquid moves freely with respect to the gas. The only influence of the gas is the pressure it exerts on the liquid surface. In other words, the weld pool top surface is not constrained, but free. Free surface flow means the liquid flow which contains a free surface.

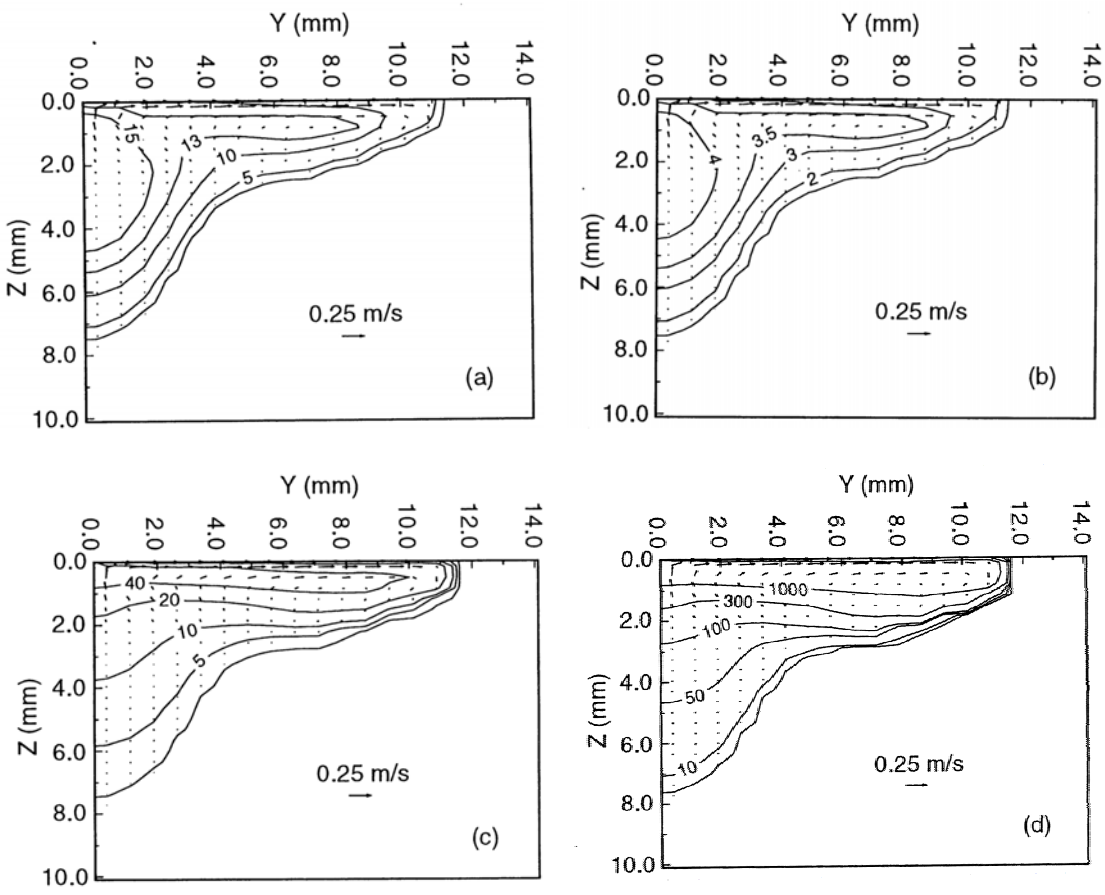

Fig. **2.6**: Distribution of turbulent variables in the weld pool: (a) dimensionless viscosity, μ_t/μ, (b) dimensionless thermal conductivity, k_t/k, (c) turbulent kinetic energy ($m^2\ s^{-2} \times 10^{-4}$), and (d) dissipation rate of turbulent kinetic energy ($m^2\ s^{-3} \times 10^{-4}$). Welding conditions: GMA, 405 A, 31.3 V, 3.22 mm s^{-1}. Adapted from Yang and DebRoy [**55**].

Accurate calculation of heat transfer and fluid flow in a deformable weld pool requires the knowledge of the free surface profile. Since such information is often unknown, it has to be included as a part of the solution process. There are three essential features needed to properly model free surfaces [60]:

(1) A scheme is needed to describe the shape and location of a surface,

(2) An algorithm is required to evolve the shape and location with time, and

(3) Free surface boundary conditions must be applied at the surface.

Recently, significant progress has been made in modeling the weld pool surface depression and the liquid flow in the deformed pool. These models shall be examined in detail in the later section, where the simulation of heat transfer and free surface flow in complex weld joints are reviewed.

2.1.5 General governing equations for transport processes

As discussed previously, direct experimental measurement of various physical processes during welding is very difficult. A practical recourse is to utilize transport phenomena based models to accurately calculate the temperature and velocity fields in the weld pool. These transport phenomena based models involve the numerical solution of governing conservation equations including the mass, momentum and energy conservation equations. In this section, the governing conservation equations are presented in a general form. Several numerical methods for solving the governing equations are reviewed in the following section.

The numerical solution of heat transfer, fluid flow and other related processes can begin with the mathematical forms in which the physical laws governing these processes have been expressed. The mathematical forms of the transport processes are often expressed as differential equations, which define certain conservation principles. Each equation employs a certain physical quantity as its dependent variable and implies that there must be a balance among the various factors that influence the variable [61].

Examples of the physical quantity are mass, velocity and enthalpy. If the dependent variable is denoted by ϕ, the general differential equation is given as:

$$\frac{\partial(\rho\phi)}{\partial t} + \nabla(\rho\vec{u}\phi) = \nabla(\Gamma\nabla\phi) + S \qquad (2.21)$$

where t is the time, ρ is the density, $\vec{u}$ is the convective velocity, Γ is the general diffusion coefficient, and S is the source term. The quantities Γ and S are specific to a particular meaning of ϕ. For instance, if ϕ denotes a velocity component, Γ is then the viscosity of the liquid, and S has the unit of force per unit volume. The four terms in Eq. **2.21** are the unsteady term, the convection term, the diffusion term and the source term [**61**].

The physical meaning of Eq. **2.21** is the quantity of ϕ is conserved. Figure **2.7** shows an infinitesimal control volume. For the clarity of the following discussion, only the flux across x direction is considered. As shown in Fig. **2.7**, the net flux across the control volume is equal to $\frac{\partial J_x}{\partial x}dx$. The change of ϕ in a small time period induced by the net flux will be compensated by the source S, and the difference between these two will result in the net change of ϕ in the control volume. Mathematically, the above relationship is expressed as:

$$\frac{\partial(\rho\phi)}{\partial t} = \frac{\partial J_x}{\partial x} + S \qquad (2.22)$$

The flux J_x has two components: one from the convection and the other from diffusion. In other words, $J_x = \rho u_x \phi - \Gamma\frac{\partial\phi}{\partial x}$, where u_x is the velocity component along the x direction. Substituting this equation into Eq. **2.22** and re-writing it in the vector form, Eq. **2.21** is obtained.

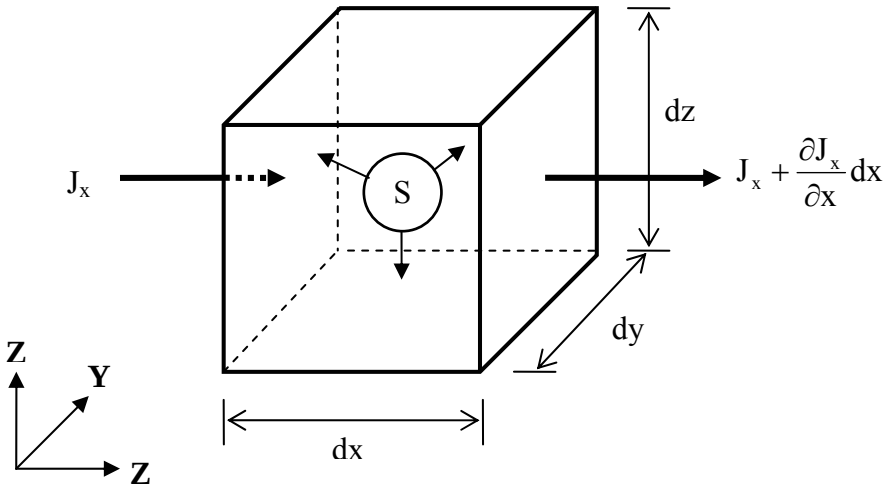

Fig. **2.7**: Conservation of quantity ϕ over an infinitesimal control volume.

Generally, in order to describe the heat transfer and fluid flow in the weld pool, the following three governing conservation equations [61], which are presented in the Cartesian-tensor form for clarity, are needed.

$$\frac{\partial \rho}{\partial t} + \frac{\partial (\rho u_j)}{\partial x_j} = 0 \qquad (2.23)$$

$$\frac{\partial (\rho u_i)}{\partial t} + \frac{\partial (\rho u_j u_i)}{\partial x_j} = \frac{\partial}{\partial x_j}\left(\mu \frac{\partial u_i}{\partial x_j}\right) + S_{ui} \qquad (2.24)$$

$$\frac{\partial (\rho h)}{\partial t} + \frac{\partial (\rho u_j h)}{\partial x_j} = \frac{\partial}{\partial x_j}\left(\frac{k}{C_p}\frac{\partial h}{\partial x_j}\right) + S_h \qquad (2.25)$$

where the subscripts i and j can take the values 1, 2, 3, denoting the three space coordinates, μ is the melt viscosity, h is the enthalpy, k is the thermal conductivity, C_p is the specific heat, S_{ui} and S_h are corresponding source terms.

Eqs. 2.23, 2.24 and 2.25 are the mass conservation or the continuity equation, momentum conservation equation and energy conservation equation, respectively. Numerical solution of these governing equations is needed due to their complexities.

2.1.6 Numerical solution of governing differential equations

There are traditionally three main approaches for solving the governing conservation equations like the one shown in Eq. 2.21: (1) the control volume (CV)/finite difference (FD) method [61-63], (2) the finite element (FE) method [64-67], and (3) the boundary element (BE) method [68,69]. Each method has found its extensive applications in solving engineering problems. The FE and BE methods are well established in the analysis of solid mechanics [65,66], where CV/FD method is extensively used in computational fluid dynamics problems [61-63], such as the heat transfer and fluid flow during fusion welding. In this section, the key features of each method are summarized and compared.

The comparison of the three numerical methods is illustrated in Fig. 2.8. As shown in this figure, the major differences among the three numerical methods lie in the

way the solution domain is discretized and consequently the way the discretized equations are formulated [66].

For FE method, the entire solution domain is divided into small finite elements. The elements shown in Fig. 2.8(a) have triangular or quadrilateral geometries represented by the solid lines. The intersections of these elements are the nodes, indicated by the solid dots, where the unknown ϕ values are stored. The variation of the ϕ in an element is represented using some predetermined interpolation functions and the ϕ values at the nodes. The discretized equation for a given element is formulated by integrating the governing differential equation using the interpolation function [65,66]. The discretized equations are then assembled and solved to obtain the ϕ field in the entire solution domain. The main advantage of FE method is the elements can have very flexible shapes, which make the FE method suitable for modeling systems with complex geometry.

For BE method, only the surface (boundary) of the domain is divided into small boundary segments [68,69], as shown in Fig. 2.8(b). The governing differential equations are transformed from volume integrals into surface or boundary integrals, which are numerically integrated over each surface segment. The distinguished feature of BE method among the three methods is that the solution at internal points are optional. The BE method can easily accommodate geometrically complex boundaries and the accuracy in regions with rapidly changing variables is better than that in the FE method [65].

For CV/FD method, the entire solution domain is divided into a grid of small volumes [61-63], which boundaries are indicated by dashed lines. The unknown ϕ values are stored in the grid points (solid dots) located in the center of the control volumes. The ϕ value in a control volume is assumed to be constant and is equal to the value of ϕ at the grid point of that control volume. The partial derivates are then numerical approximated using the ϕ values at adjacent grid points, and the discretized equations are obtained. Unlike FE or BE method, application of CV/FD method to systems with complex geometry may require special treatments, since the control volume usually has a regular shape such as a rectangle. These special treatments include the coordinate transformation [60] and the grid blocking method [61], and are reviewed in a later section.

Although FE and BE methods are flexible in modeling systems with complex geometry, they are primarily used in solid mechanical analysis. Applications of FE and BE methods to study coupled heat transfer and fluid flow problems are still evolving, since the FE and BE formulation of mass, momentum and energy conservation equations are very difficult and cumbersome, to say the least. On the other hand, CV/FD method has been extensive used in solving the heat transfer and fluid flow problems. In the present thesis, the CV method is used to develop thermo-fluid models for calculating the heat transfer and fluid flow during fusion welding.

In summary, this section examines the current issues and problems in modeling transport processes in fusion welds. In particular, the energy absorption efficiency, liquid convection and driving forces, turbulence, free surface deformation, governing conservation equations and numerical techniques for solving governing differential equations, are discussed.

It is well known that accurate prediction of temperature and velocity fields, weld bead geometry, and the thermal cycles in the weldment needs to consider convective heat transfer in the weld pool. Appropriate modeling of liquid metal motion in the weld pool needs to account for the combination of driving forces such as surface tension gradient, electromagnetic, and buoyancy forces. The modeling should also take into account the weld pool free surface deformation, since it have a profound effect on the heat transfer, fluid flow and the weld geometry.

The topics covered in this section are rather general, not related to any specific welding processes. In the following two sections, the modeling of heat transfer and fluid flow in transient spot welding and GMA fillet welding processes is critically reviewed.

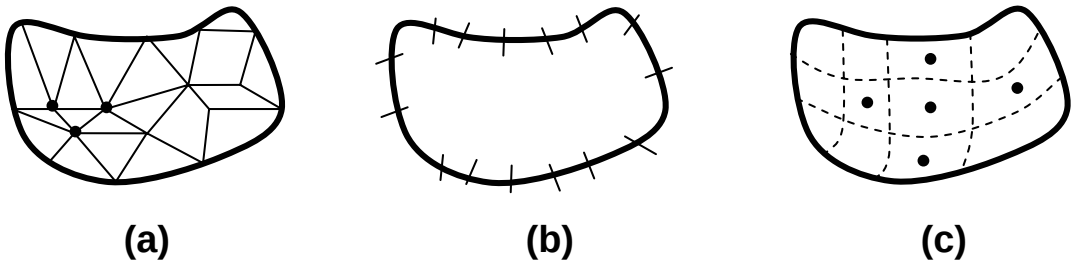

Fig. **2.8**: Overview of numerical methods for solving governing differential equations [**65**]: (a) finite element method, (b) boundary element method, and (c) control volume / finite difference method.

2.2 Modeling of Heat and Fluid Flow during Transient Spot Welding

Transient welding conditions are encountered in many everyday welding situations such as weld starts and stops, tack-welding routines, stationary spot welds, and solidifying weld craters [2,6]. These types of welds behave differently than their moving weld counterparts because the thermal profiles never reach a steady state value. The heating and cooling rates for these welds are often much higher than that of steady state welds, and can lead to solidification cracking and formation of non-equilibrium phases. Therefore, it is important to understand how the weld thermal profiles change as a function of time.

A typical example of transient welding situations is the spot welding, where the heat source is stationary in space and the weld is done is a very short time period. Figure 2.9 shows the GTA spot welding process. During heating, the base material absorbs arc energy and its temperature increases rapidly. A small liquid weld pool soon forms after the arc is on, and the liquid metal undergoes strong circulation inside the weld pool. When the arc extinguishes, the solidification of the weld pool takes place. Because of the limited amount of heat input in the short period of spot welding, the entire weld can be quickly "quenched" to low temperatures. The cooling rates are often more than thousands of Kelvin per second in arc welds and even much higher in laser welds. Under such high cooling conditions, the various solid-state transformations in the weldment may result in the formation of non-equilibrium phases [2,6].

Because of the small size of the weld pool, the presence of plasma in the vicinity of the weld pool and the rapid changes of temperature in arc spot welds, physical measurements of important parameters such as temperature and velocity fields, solidification rate and thermal gradient in the weld pool are extremely difficult [7-16]. Therefore, in recent decades, numerical calculations of heat transfer and fluid flow have been utilized to understand various weld characteristics that cannot be obtained otherwise.

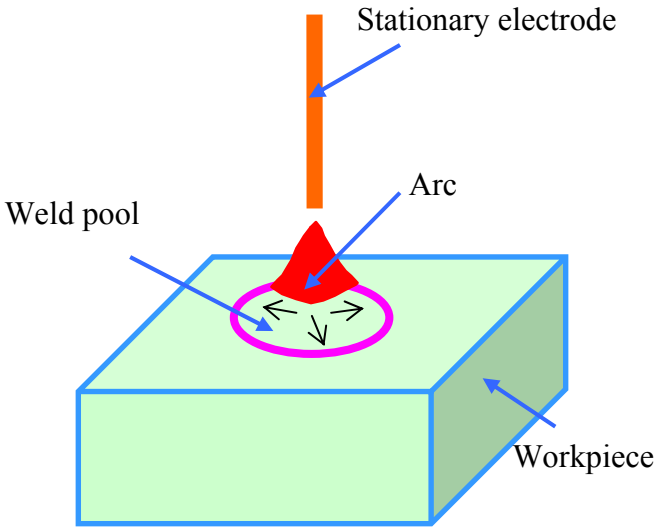

Fig. **2.9**: Schematic plot showing the GTA spot welding process.

In a first attempt to model the transient welding processes, Oreper et al. [70] studied the evolution of temperature and velocity fields, solidification rate and thermal gradient using a two-dimensional model. Due to the hardware limitation at that time, a rather crude grid system (typically 18×20) was used, but the calculations provided useful temperature and velocity fields. Oreper and Szekely [45] also used dimensionless analysis and numerical modeling to understand the role of conduction and convection in the weld pool heat transfer for materials with different thermal physical properties. It was found that the convection played a major role in affecting the weld pool shape, and the convection was often dominated by the surface tension gradient force.

Zacharia et al. [28,71] carried out computational and experimental study to investigate the effect of the surface active element on the weld pool geometry. They examined the weld pool development during GTA and laser welding of 304 stainless steel. The numerically predicted and experimentally observed FZ size and shape were compared to validate their model. They found that the temperature coefficient of surface tension ($\partial\gamma/\partial T$) significantly affected the FZ geometry. In particular, shallow welds were obtained for low sulfur contents. Increasing the sulfur content increased the weld penetration in 304 stainless steel arc welds.

Betram [72] examined the role of heat and liquid flow on the final solidification microstructure considering the mushy zone behavior. It was found in the GTA spot weld pool, the solidification events consisted of three stages. At the initial stage, the FZ boundary was smoothed out and the superheat in the weld pool was removed. The initial stage followed by the quasi-steady stage, where weld pool dimensions (i.e., radius and depth) decreased nearly linearly with time. In other words, the solidification velocity was near constant at the quasi-steady stage. In the final stage, the solidification process accelerated and the solidification velocity increased.

Katayama et al. [73] developed a heat conduction and solidification model considering the effects of microsegregation and latent heat to simulate the rapid melting

and solidification behavior in laser spot welds. It was shown that the latent heat of fusion greatly affected the thermal histories and growth rates during solidification. Liquid convection was not considered in their calculations.

More recently, Kim and Na [74] investigated the heat transfer and fluid flow in the weld pool with deformable free surface during pulsed current stationary GTA welding. Various driving forces for the transient liquid convection in the weld pool were considered, which included the electromagnetic, surface tension gradient, and buoyancy forces. The effect of deformed weld pool free surface due to the arc pressure was also considered. A boundary fitted coordinate system was used to fit the deformed pool surface. They showed that the increase of pulse duration resulted in a deeper penetration. Their work was mainly focused on the calculation of FZ geometry and thermal cycles in the weldment.

In summary, the transport phenomena based numerical models have been successful in revealing special features in transient spot welding processes such as the transient nature of the solidification rate [45,72]. However, a detailed analysis of the transient heating and solidification behavior still remains to be undertaken to investigate the important unanswered questions such as how the mushy zone region behaves during heating and solidification and how the solidification front velocity changes with time during spot welding. Such a computationally intensive investigation, requiring use of very fine grids and very small time steps, have now become practical because of recent advances in the computational hardware and software.

2.3 Simulation of Heat Transfer and Free Surface Flow in Complex Joints

GMA welding is an arc welding process joining metals by heating them with an electric arc that is established between a consumable electrode and the workpiece [75]. The main advantages of GMA welding include high deposition rates which allow thick workpiece to be welded at high welding speeds, suitability for all position welding, and

deep penetration in spray transfer mode. Fillet weld, which joins two pieces of metals approximately at right angle to each other in a lap joint, T-joint, or corner joint, is one of the most important joint types used in shipbuilding and other heavy industries. GMA welding is particularly well suited for welding of fillet joints due to its high productivity and amiability to automation [75]. Therefore, GMA fillet welding has become the predominant process choice in manufacturing industries.

Performance of structurally sound fillet welds is determined by the geometrical features of the weld bead. Figure **2.10** shows cross sections of two fillet weld beads. The weld bead profile shown in Fig. **2.10(a)** is certainly less desirable than that shown in Fig. **2.10(b)**, since the presence of any sharp notch in the weldment is detrimental to its fatigue property. Various factors such as the weld pool convective flow, arc pressure, droplet transfer, weldment thermal history and physical properties of the weld metal affect the weld bead profile [2,75]. At present, the control of weld bead shape is often achieved through trial and error. This approach has three main disadvantages. Fist, the trial and error procedure is inherently expensive because of the large number of welding variables. Second, the chosen ranges of variables do not always produce optimum results. Finally, the approach ignores the potential competitive technological advantage that is attainable based on fundamental understanding of welding science. A practical recourse is to guide experiments with advanced numerical modeling of the welding processes so that the desired weldment features can be tailored based on scientific principles.

Previous computer simulation efforts to understand welding processes and welded materials through numerical heat transfer and fluid flow calculations have focused mainly on simple systems. Most of the studies considered butt welding of rectangular workpiece and ignored any deformation of the weld pool top surface. However, such simple systems may not be readily applicable to more complicated and useful welding processes such as the GMA fillet welding process.

Figure **2.11** is a schematic plot showing the important physical processes that are taking place during GMA fillet welding. As shown in this figure, heat is transported from the arc to the workpiece, and superheated liquid metal droplets formed from the consumable electrode wire also carry heat and mass into the weld pool [2,75]. Depending

on the current and the voltage, the arc can exert significant pressure on the top surface of the pool. The deformation of the weld pool surface can affect heat transfer and the eventual solidified surface profile of the weld bead. The welding parameters affect droplet diameter, transfer frequency, acceleration, impingement velocity, and the arc length. All these parameters, in turn, affect the resulting temperature field, thermal cycles, and the structure and properties of the weldment. The complexity of the welding process is further augmented by the complicated V-shaped joint geometry containing curved weld pool surface. All these complexities must be taken into account to accurately model GMA fillet welding processes.

One of the major challenges in modeling GMA welding process is the simulation of heat transfer and free surface flow in a domain with irregular geometry. As discussed in a previous section, although FE methods are well suited for modeling systems with complex geometry, application of FE methods to study coupled heat transfer and fluid flow problems are very difficult [**65**,**66**]. Over the past two decades, several numerical techniques have been developed to treat the free surface flow in complex geometry based on the CV/FD methods. These techniques can be roughly divided into two categories: methods based moving (Lagrangian) grid and those based on fixed (Eulerian) grid.

In this section, the general numerical techniques used for modeling free surface flow in complex geometry are reviewed at first. In particular, the volume of fluid method and the boundary fitted grid method are examined. Secondly, recent development in modeling heat transfer and free surface flow in weld joints with complex geometry is discussed. Finally, some current issues and problem in this subject are summarized.

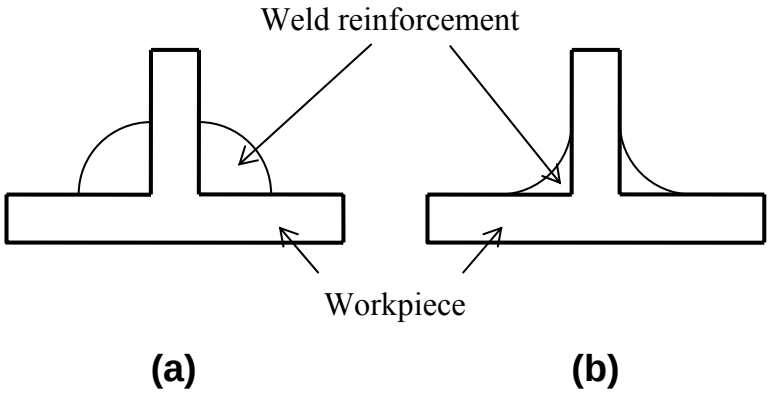

Fig. **2.10**: Weld bead shape control based on science is important, since properties of structurally sound welds are significantly affected by their geometry: (a) undesirable bead profile, and (b) target shape.

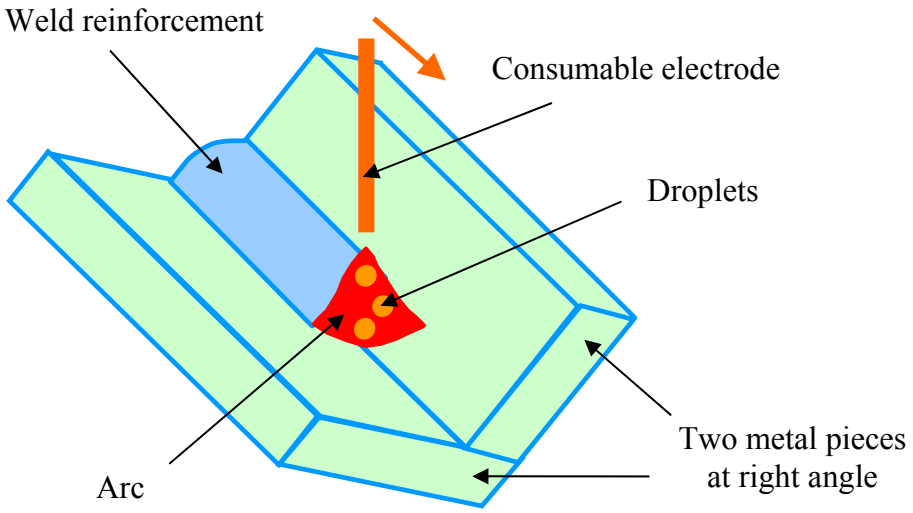

Fig. **2.11**: Schematic plot showing the GMA welding process.

2.3.1 Volume of fluid method

The use of a fixed grid as the basis for calculating complicated surface motions is sometimes referred as the Eulerian grid method, in comparison with the Lagrangian grid methods where a grid is imbedded in and moves with the fluid. Various numerical techniques based on the fixed grid method have been developed over the past few decades. Here, a particular algorithm, namely the volume of fluid (VOF) method [76,77], for tracking free surface flow is examined. The VOF method is a popular interface tracking algorithm, which has proven to be a useful, effective and robust tool for solving practical engineering problems involving free surface flow.

One of the key features of the VOF method is the introducing of a new scalar quantity, i.e., the fluid volume fraction (F), in the discretized equations. The fluid volume fraction defines the extent of a cell (control volume) filled with fluid. As shown Fig. 2.12, F is equal to zero when the cell is empty of liquid, whereas F is equal to unity when the cell is completely filled with liquid. For a cell contains the free surface, it is partly filled with fluid, and F for the interface cells has a value between zero and unity. If the amount of fluid in each cell is known, it is possible to locate surfaces, as well as determine surface slopes and surface curvatures. Surfaces can thus be easily located because they lie in cells partially filled with fluid or between cells full of fluid and cells that have no fluid.

The fluid volume fraction (F) is evolving based on the following volume conservation equation.

$$\frac{\partial F}{\partial t} + \frac{\partial \left(u_j F\right)}{\partial x_j} = 0 \qquad (2.26)$$

where t is the time, and u_j and x_j are velocity component and distance along the j-th direction, respectively. A straightforward numerical approximation cannot be used to model Eq. 2.26, because numerical diffusion and dispersion errors destroy the sharp, step-function nature of the F distribution [77]. A donor-acceptor flux method [77] is often employed to discretize Eq. 2.26 and update F values. This donor-acceptor flux together with the bookkeeping adjustments usually ensures the stability of the solution process.

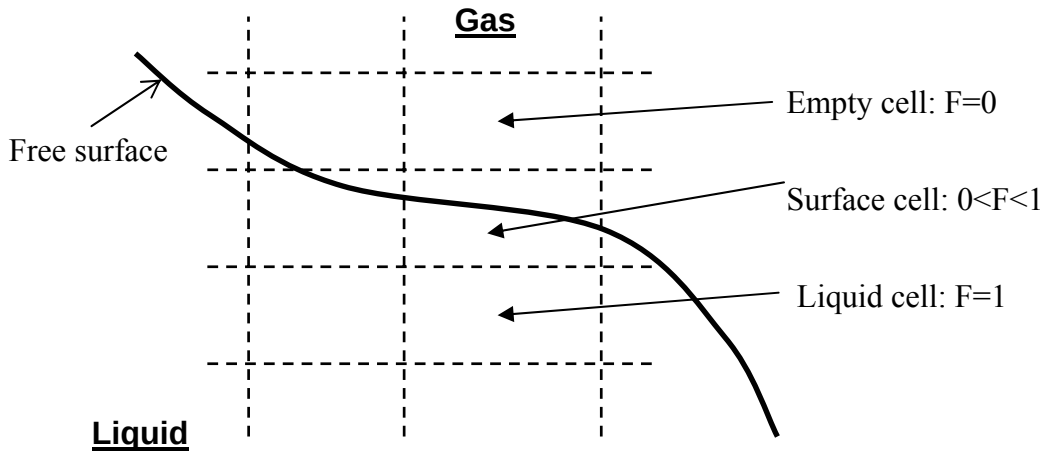

Fig. **2.12**: Schematic plotting showing the grid used in the VOF method [**77**].

With the knowledge of F values in the surface cells, the interface location within a surface cell can be determined. Such knowledge of the interface location is necessary for the accurate application of free surface boundary conditions. Several algorithms [77-79] have been developed to compute slopes and curvatures of the interface by using the fluid volume fractions in neighboring cells.

Once the interface location is determined within a cell, free surface boundary conditions must be applied to the interface. That is, assigning the proper gas pressure, surface tension condition as well as determining what velocity components outside the surface should be used to satisfy a zero shear-stress condition at the surface [77].

The VOF method has lived up to its goal as a powerful and efficient tool for solving free surface flow problems. It is particularly useful in handling the breakup and coalescence of fluid masses [77], because of the use of a volume tracking function. It should be noted that the exact location of the interface within a cell is not known in the VOF method. The accuracy of the interface location largely depends on the algorithm used for interpolating and reconstructing the interface and the grid size. Such drawbacks limit the application of the VOF method in some practical problems, particulary where the exact location of the interface needs to be accurately determined.

2.3.2 Boundary fitted grid

Comparing to the Eulerian grid based VOF methods, the boundary fitted grid methods utilizes a Lagrangian grid, which moves with and exactly fits the interface [60,80,81]. Therefore, these methods determine the location of the free surface with higher accuracy than the interface capturing methods. The boundary conditions at the free surface can thus be applied accurately. The main limitation of the boundary fitted grid method is that it is difficult to include the breakup and coalescence of fluid masses.

Figure 2.13 shows the grid system used in the boundary fitted grid method. As shown in this figure, the interface is exactly fitted using the grid system, and unlike in the VOF method, no new variable is needed to interpolate the interface location.

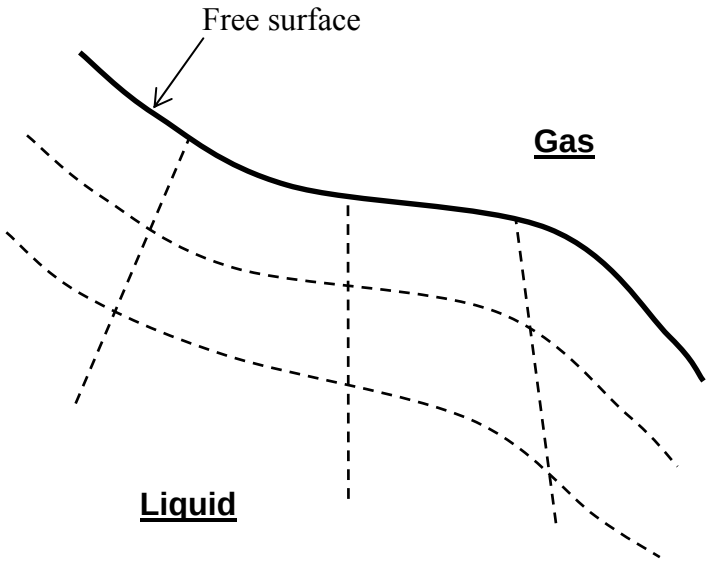

Fig. **2.13**: Schematic plot showing the grid used in the boundary fitted grid method [**60**].

Although no new conservation equation is introduced in the boundary fitted grid method, the governing conservation equations (Eqs. **2.23**, **2.24** and **2.25**) need to be transformed into forms in the general curvilinear coordinate. The transformed equations are often fairly complex, containing many extra terms to account for the geometrical transformation [**60**,**80**,**81**].

In the present study, we are mostly interested in the quasi-steady state heat transfer and free surface flow in the fillet welds. The boundary fitted grid based method is well suited for our purpose, since our model does not emphasis the dynamic breakup and coalescence of liquid mass such as the metal droplet transfer. Furthermore, for our case, the boundary fitted grid method is more efficient and robust, since no solution of additional equation is needed. Therefore, the boundary fitted grid method is used to model the heat transfer and free surface flow during GMA fillet welding. Details of the GMA fillet heat transfer and fluid flow model using the boundary fitted grid are presented in Chapter 4.

2.3.3 Recent development in modeling free surface flow in weld pool

A fundamental understanding of heat transfer and fluid flow considering free surface deformation is still evolving. Tsai and Kou [**24**] considered Marangoni convection in weld pools with a free surface using a two-dimensional model. An orthogonal curvilinear coordinate was used to fit the weld pool top surface. It was found that the liquid metal moved outwards at the pool surface, when the temperature coefficient of surface tension ($\partial\gamma/\partial T$) was negative; and vice versa. The outward flow resulted in a slight depression in the center of the pool surface, while the outer portion of the pool surface was elevated. The reverse was true when the liquid metal flowed inwards. Their results showed that in case of positive $\partial\gamma/\partial T$, the pool depth could be significantly over-estimated if the pool surface was assumed to be flat.

Choo, Szekely and Westhoff [49] simulated the heat transfer and fluid flow in both the welding arc and the weld pool using a two-dimensional model. Their results on the welding arc simulation showed that when the free surface of the weld pool was significantly deformed, the resultant heat and current flux falling on the anode may be markedly modified. In other words, the widely-used Gaussian heat flux distribution may not be applicable for significantly deformed weld pools. Their results on the heat flow and melt circulation in the weld pool indicated that the melt circulation may be markedly affected by the shape of the free surface. In their study, the weld pool surface profile was not computed but was predefined to fit the measured pool shape.

Wu and Dorn [30] studied heat transfer and fluid flow in fully-penetrated GTA weld pools with surface depression. Since the workpiece was fully penetrated, two free surfaces were considered: the weld pool top and bottom surfaces. Both surface profiles were computed by minimizing the total surface energy, which included the surface tension energy, gravitational potential energy and, for the pool top surface, the work done by the arc pressure displacing the pool surface. They showed that weld pool depression increased significantly with increasing welding current and, to a lesser extent, with decreasing welding speed.

Kim and Na [31] developed a three-dimensional model to study the heat and fluid flow in GMA butt welds. Their model was based on the boundary fitted coordinate and the weld top surface profile was obtained by minimizing the total surface energy. The electromagnetic, surface tension gradient and buoyancy force were considered in the weld pool convection. It was found that the size and profile of the weld pool were strongly influenced by the volume of molten electrode wire, impingement force of the arc plasma and surface tension of the liquid metal.

Cao and Dong [82] investigated GMA weld pools with consideration of droplet impact. They developed a three-dimensional heat transfer and fluid flow model using boundary fitted coordinate. The heat content of droplets was modeled by considering a

Gaussian distribution at the weld top surface. The impact force of droplets, which was also assumed as a Gaussian function, was incorporated in the calculation of the free surface profile. They applied their model to study both partial and full penetration welding conditions. They showed that the droplet heat and impact force contributed to the finger-type penetration characteristics in GMA welds, and an adequate prediction of penetration profile required consideration of both the sensible heat and the impact force of the droplet.

Yang and DebRoy [**55**] developed a three-dimensional turbulence model to study the heat transfer and fluid flow in GMA steel welds. The turbulence in the weld pool was considered using the two-equation K-ε model. The weld top surface was assumed to be flat ant the droplet transfer was not considered. A time-averaged volumetric heat source was used to simulate the additional heat from the superheating metal droplets. Figure **2.14** shows the comparison between the calculated and measured FZ geometry. As shown in this figure, their model could reasonable predict the shape and size of the GMA welds. Particularly, the finger penetration in the FZ of the GMA weld could be reasonably predicted using the volumetric heat source method.

Fan and Kovacevic [**83**] studied the globular metal droplet transfer during stationary GMA welding using a two-dimensional VOF model. The model could capture the dynamic processes of melt droplets impinging the molten pool, arc striking and solidification after the arc extinguished. It was found that the droplet transfer frequency has a major influence on the weld pool configuration. If the droplet impinged the molten pool at widely scattered locations, the resulting pool was wide and shallow. In contrast, a finger penetration was formed in the FZ when droplet impinged a small area. A higher transfer frequency led to a deeper penetration.

Wang and Tsai [**84**] also simulated the impingement of droplets to the weld pool during GMA welding. Their model was based on a two-dimensional VOF method, similar to the one Fan and Kovacevic [**83**] used. The metal droplets were driven by gravity, electromagnetic and plasma drag forces.

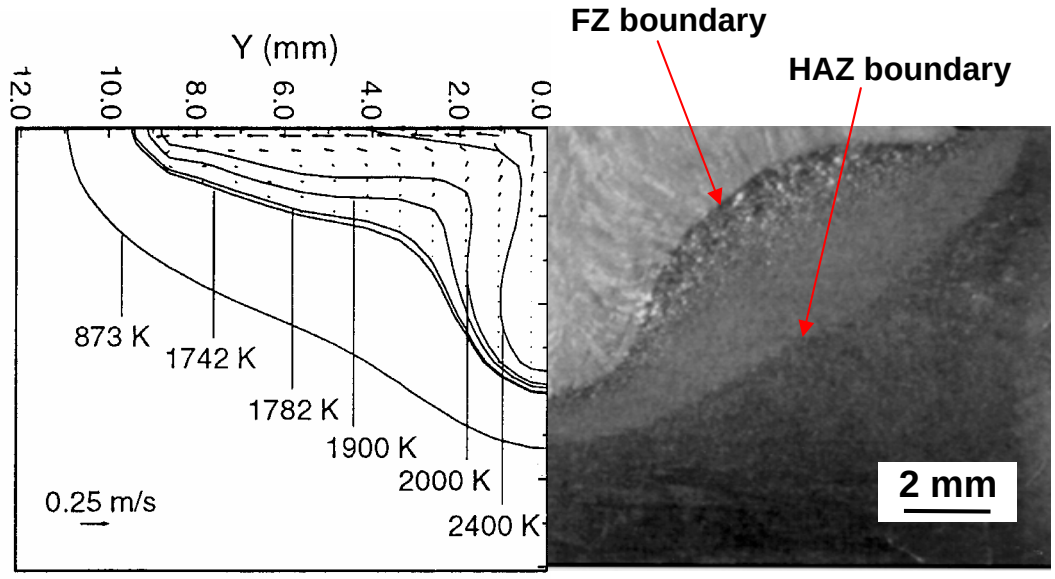

Fig. **2.14**: Comparison of the calculated and experimental geometry of the FZ and the HAZ. Adapted from Yang and DebRoy [**55**].

In summary, although significant progresses have been made in modeling of GMA welding of butt joints with free surface deformation [30,31,82], a three-dimensional framework for understanding of heat transfer and fluid flow based on scientific principles still remains to be undertaken for GMA welding of fillet joints due to its complexities. These complexities include irregular weldment geometry, significant deformation of the weld pool top surface, and filler metal addition. These physical processes are difficult to represent adequately by orthogonal rectangular grids. Use of boundary fitted deformable grids requires special transformation of the governing equations and the boundary conditions. The transport of the metal drops into the weld pool is largely responsible for the finger penetration commonly observed in the FZ. Thus, the model must take into account how the droplet size, acceleration, impingement velocity, and arc length affect heat transfer. With the advancement of computational hardware and software, it has now become practical to relax some of the simplifying assumptions of the previous research and address more realistic situations.

2.4 Modeling of Weld Microstructural Evolution

During fusion welding, the rates of the phase transformations vary across the weldment because of local variations of thermal cycles. For instance, in the FZ, the temperature is high enough to melt the material during heating, and the liquid material solidifies during cooling. On the other hand, in the HAZ, only various solid-state transformations occur, and the extent of these transformations depends on the local temperatures. These welding induced spatial variations of microstructure significantly affect weldment properties such as strength, ductility, toughness, and corrosion resistance [3,7]. Thus, control of the microstructure is important in achieving structurally sound welds. The main task to achieve this goal is to understand phase transformation kinetics under rapid heating and cooling conditions encountered during welding.

Modeling of weld microstructure requires understanding of the phase transformation kinetics and the knowledge of thermal cycles in the weldment. The thermal cycles can be obtained from reliable mathematical models by comprehensive

modeling of heat transfer and fluid flow during welding, which has been discussed in detail in the previous section. In recent years, significant progress has been made in understanding the microstructural evolution during welding [6]. Several phase transformation models have been developed for modeling the microstructure in both FZ and HAZ of steel welds [85-91]. Coupling these phase transformation models with the computed thermal cycles has proved to be an effective approach for quantitative understanding of weldment microstructure [55,30].

Microstructural evolution in the weldment is very complex. Depending on the material composition and thermal cycles, the mechanism of a phase transformation may be different, which results in different morphology and property of the product phase. For instance, in steel welds, γ-austenite decomposes into α-ferrite during cooling. The austenite may transform into various microconstituents such as allotriomorphic ferrite, Widmanstatten ferrite, pearlite, bainite (non-lamellar ferrite plus Fe_3C) and martensite, depending on the composition of the parent austenite phase and cooling rates [85-87]. Addition of alloy elements in the base material even further complicates the problem. Therefore, considering the complexities of phase transformations, the review given here is not intended to cover all the topics. Instead, several important subjects related to the microstructural evolution during fusion welding are chosen. These subjects include (1) direct observation of microstructural evolution during fusion welding using a recently developed X-ray diffraction technique, (2) phase transformations during heating, (3) grain growth, and (4) phase transformation during cooling.

2.4.1 Direct observation of microstructural evolution

Much of the previous research in understanding microstructural evolution has focused on the post-weld microstructural characterization. However, the traditional characterization of weldments only provides a snapshot of the very last stage of a series of phase transformations that culminate in the eventual microstructure. As a result, the post-weld microstructural characterization cannot provide information about how the

microstructure evolves or at what rate various phase transformations occur during weld heating and cooling. The use of conventional experimental methods such as dilatometry to study phase transformation kinetics under realistic welding conditions is inherently difficult, since these methods are indirect in that they measure certain changes in the welded sample (e.g. change in length). Furthermore, the conventional methods cannot resolve the spatial distribution of phases during welding [93]. Because of these problems, progress in this field has been slow and quantitative kinetic data pertaining to phase transformations in important alloy systems under welding conditions still remain scarce.

A recently developed X-ray diffraction technique can largely overcome the difficulties in traditional methods and provide direct observation of microstructural evolution in the weldment. Figure 2.15 schematically shows the experimental setup for the X-ray diffraction technique [94-99]. A focused synchrotron beam was passed through a 260 μm tungsten pinhole to render a sub-millimeter beam on the sample at an incident angle of around 25 degree. The spatially resolved X-ray diffraction patterns were recorded behind the weld using a 50-mm-long 2048-element position-sensitive Si photodiode array detector. The welding assembly was integrally mounted to a translation stage driven by a stepper motor with 10 μm precision and placed inside an environmentally controlled chamber to minimize oxidation during welding. Diffraction data were taken while the beam was at a fixed location with respect to the welding electrode and collected for 10 s while the bar rotated under the stationary torch at a constant speed [94-99].

The X-ray diffraction based technique has been successfully used to directly observe the phase transformations during welding of several alloys systems under both low and high heating and cooling rates [94-99]. These systems include AISI 1005 steel [97], 304 Stainless steel [98], commercially pure titanium [30], and 2205 duplex stainless steel [99]. The X-ray diffraction data not only identify the spatial distribution of phases but also provided relative fractions of phases during phase transformations. Such unique kinetic data are valuable in that they can be analyzed to understand the kinetics and mechanisms of the phase transformations [30,98].

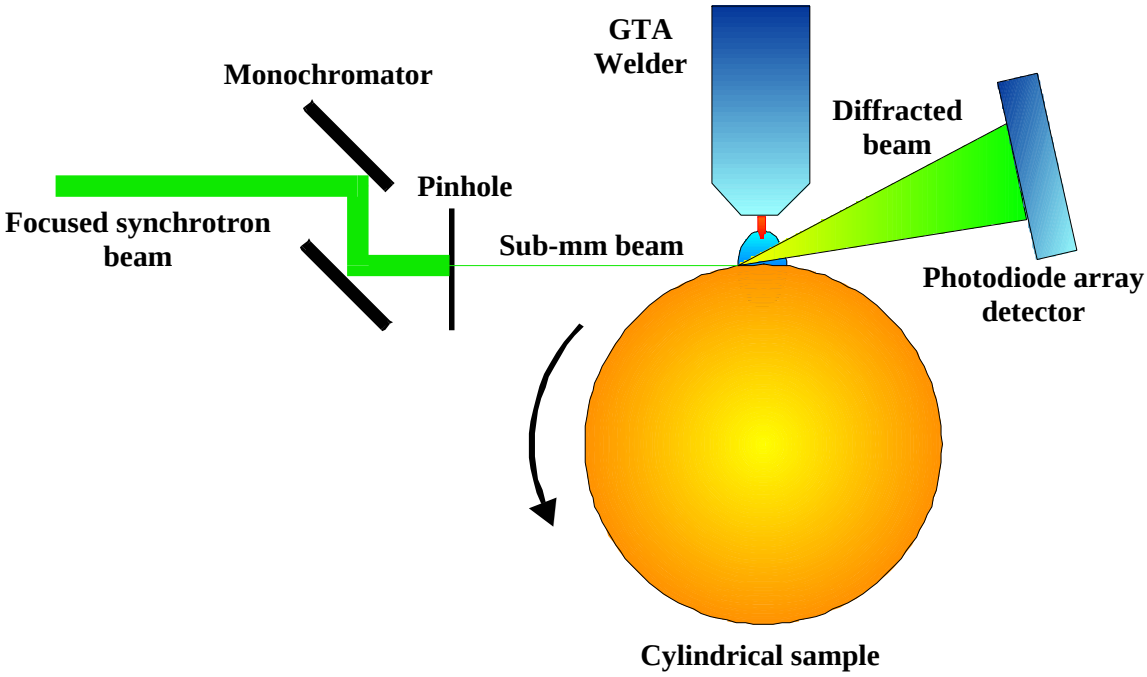

Fig. **2.15**: Experimental setup used in the X-ray diffraction technique. Adapted from Elmer et al. [**94**-**99**].

2.4.2 Phase transformations during weld heating

Much of previous research on understanding the microstructural evolution during welding is focused on the phase transformation during weld cooling, since the final microstructure in the weldment is the direct product of these transformations. However, phase transformations during weld heating are also important in that the transformed phases during heating affect the kinetics of subsequent grain growth and phase transformations during cooling. The reasons that phase transformations during heating have not been extensively studied experimentally and theoretically are the following. First, observation of phase transformations during heating is difficult, since the transformed phase during heating is destroyed by subsequent transformations during cooling, and the transformation kinetics becomes more rapid with increasing temperatures [**93**,**100**]. Second, the kinetics of phase transformations during heating depends on the starting composition, size and distribution of the base material as well as the weld thermal cycle. Experimental study of phase transformation kinetics is time consuming and expensive. Recently, several models have been developed to study the phase transformation kinetics [**100**-**104**], and they have been used to provide useful insights into the kinetics and mechanisms of transformations during heating. This section examines some of the recently-developed phase transformation models during heating.

Hillert et al. [**105**] systematically examined the α-ferrite to γ-austenite during heating (austenitization) in steels. The basic reaction of austenitization is α + cementite (θ) $\rightarrow \gamma$. However, depending upon temperature, carbon and alloy contents, the process of austenitization may take various forms. They proposed five possible mechanisms for the dissolution of cementite, which are schematically shown in Fig. **2.16**. Type I of the reaction is encountered when the carbon content is low. In this case, the cementite particles are far way from each other in the base metal. The main reaction is the diffusion of carbon through a shell of γ nucleated around the cementite particle. At realistic carbon contents, the distance between the cementite particles is not very large. Therefore, carbon could diffuse from a cementite particle through α matrix to the neighboring γ shell, as

demonstrated in Fig. **2.16** (type II). This reaction may control the overall rate of the transformation if the nucleation rate of γ is low. The dissolution of cementite may take the form of type III, when the carbon contents are sufficiently high. In this case, the cementite particles are so close to each other that a γ grain may impinge with neighboring γ grains before the cementite in its center is completely dissolved. If the carbon contents are very high, the austenite region can continue to grow with the cementite particles being partially dissolved, as shown in Fig. **2.16** (type IV). At sufficient high temperature, the α phase may transform to γ without any cementite being dissolved at the same time. The dissolution of cementite will then take place completely inside the γ-matrix, as demonstrated in Fig. **2.16** (type V). Hillert et al. studied the austenitization under these five different mechanisms, and their results suggested that the reaction of austenitization was governed by the rate of diffusion rather than interface control [**105**].

Akbay, Reed and Atkinson [**100-102**] carried out a series of studies to investigate the austenitization from ferrite/cementite mixtures in Fe-C binary and Fe-C-X ternary steel systems, where X stands for a substitutional solute such as Mn, Si or Cr. They developed a one-dimensional finite difference based diffusion model to calculate the carbon diffusion rates during austenitization. The model utilized a moving grid technique to trace two moving interfaces: cementite/austenite (θ/γ) and austenite/ferrite (γ/α) interfaces. Local equilibrium was assumed to apply at the two interfaces. Kinetics of austenitization was calculated for different starting microstructure and at different temperatures. In particular, the austenitization kinetics in Fe-0.4C steel was measured using dilatometry and neutron diffraction techniques [**102**]. The measured kinetic data was in good agreement with that predicted using their model. Nucleation kinetics was not considered in their austenitization model.

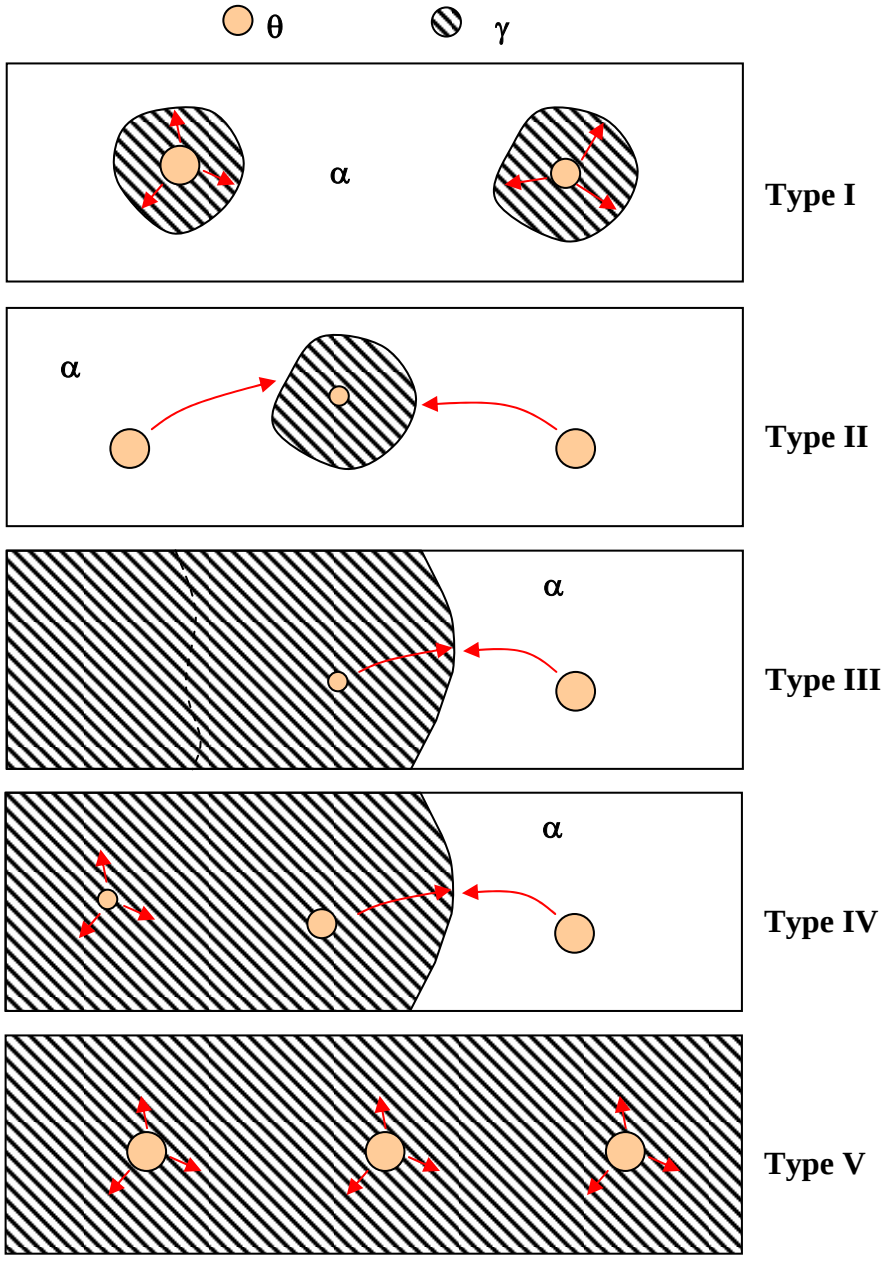

Fig. **2.16**: Different mechanisms of dissolution of cementite. Adapted from Hillert et al. [**105**].

In an effort to understand the importance of both nucleation and growth during austenitization, Roósz et al. [**103**] used quantitative metallographic methods to examine the isothermal formation of austenite in a eutectoid carbon steel. An Avrami type of equation was used to describe the kinetics involving nucleation and growth. The activation energies for nucleation and growth as well as the nucleation and growth rates were determined from the experimental data. They established the dependence of nucleation and growth rates on the initial microstructure, particularly the characteristic parameters of pearlite such as the lamellar spacing of pearlite. It was found that the austenite nuclei were formed at the edges of pearlite colonies and the growth of the austenite nuclei was controlled by the interface diffusion.

Caballero et al. [**104**] applied the Avrami equation proposed by Roósz et al. [**103**] to study the influence of pearlite morphology and heating rate on the kinetics of austenitization in a Eutectoid steel. It was found that the coarser the initial microstructure, the slower the transformation kinetics. Experimental results for austenite volume fraction were in good agreement with the predicted values using their model.

Phase transformations during heating are also important in titanium alloys. Recently, Yang et al. [**30**] used a modified Johnson-Mehl-Avrami (JMA) equation to study the α-Ti to β-Ti phase transformation in a commercially pure titanium. The modification was needed to take into account the non-isothermal heating conditions encountered during welding. The modified JMA equation was derived by approximating the continuous temperature-time curves by many small isothermal steps. The final expression for the transformed fraction obtained from m subsequent isothermal steps can be expressed as:

$$f\big(t(T)\big) = 1 - \exp\left\{-\left[\sum_{i=0}^{m-1} k(T_0 + i\Delta T)\Delta t\right]^n\right\} \qquad (2.27)$$

where f(t(T)) stands for the transformed phase fraction under non-isothermal conditions, Δt is the time step, ΔT is the temperature change corresponding to each Δt, T_0 is the

initial temperature, k is a temperature dependent constant, n is a numerical exponent which value is determined by the nucleation mode and the growth dimensions, and m is the total number of the subsequent isothermal steps.

They examined three possible mechanisms of the $\alpha \rightarrow \beta$ phase transformation during heating: (I) Ti short-range diffusion (interface controlled), (II) O short-range diffusion (interface controlled), and (III) O long range diffusion. For each mechanism, the corresponding kinetic constants including the activation energy and the exponent were used in Eq. **2.27** to calculate the times required for the completion of the $\alpha \rightarrow \beta$ transition. These calculated times for each mechanism were then compared with the times determined from an experimental phase distribution map, as shown in Fig. **2.17**. It was found that the times taken from the phase distribution map were in good agreement with those calculated assuming mechanism (I). Through the comparison of the calculated times with those determined experimentally, they concluded that the $\alpha \rightarrow \beta$ transformation is most likely controlled by the transport of Ti atoms across the interface.

It should be noted that modified JMA equation, i.e. Eq. **2.27**, is valid for describing the transformation which path involves $\alpha \rightarrow \gamma$ (eutectoid), and not valid for transformation which path involves $\alpha \rightarrow (\alpha+\gamma) \rightarrow \gamma$ [**106**].

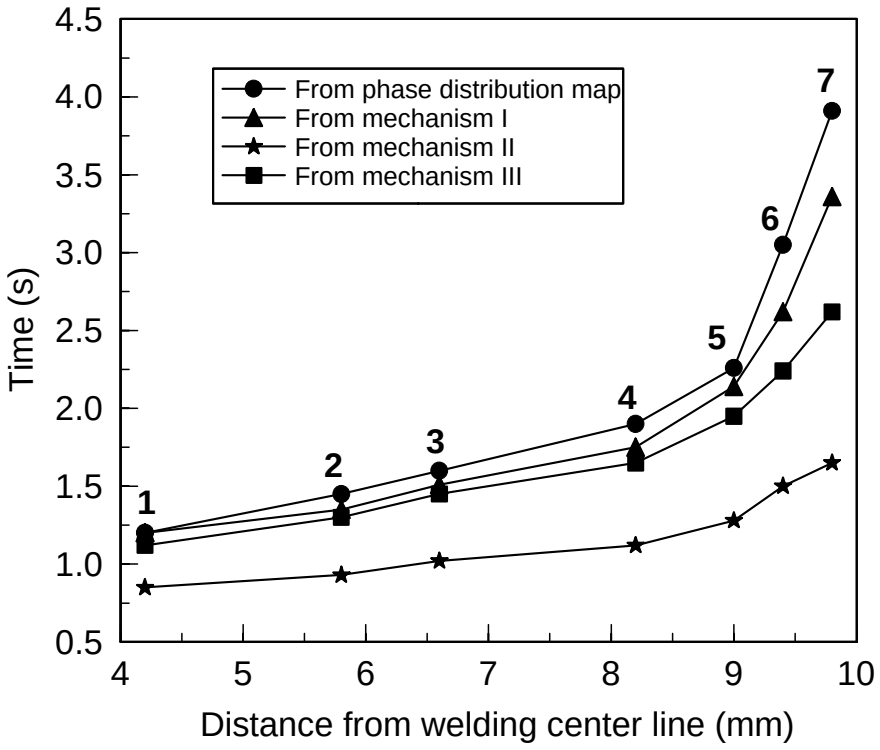

Fig. **2.17**: Comparison of times needed for the completion of the α→β transformation from JMA equation and from phase distribution map. Distances from welding center line: 1 - 4.2 mm; 2 - 5.8 mm; 3 - 6.6 mm; 4 - 8.2 mm; 5 - 8.8 mm; 6 - 9.2 mm; 7 - 9.6 mm. Adapted from Yang et al. [**30**].

2.4.3 Grain growth

During welding, the interaction between the heat source and the base material not only leads to various phase transformations but also grain growth. Severe grain growth may adversely affect the strength and toughness of the weldment. For example, in GTA welding of Ti-6Al-4V alloy, the α-Ti first transforms into β-Ti during heating. The further exposure of the transformed β grains to elevated temperatures may lead to extensive β grain growth. It has been reported that the maximum β grain size can be as high as twelve times larger than the starting β grain size [**107**]. The resulting coarse prior-β grain significantly lowers the strength of the weld [**108**]. Therefore, understanding grain growth kinetics is crucial to obtaining structurally sound welds.

It is well known that the driving force for grain growth is the reduction of the total grain boundary energy. There are usually two types of grain growth phenomena: normal and abnormal growth. The abnormal grain growth is characterized by the growth of just few grains to very large sizes. In contrast, in the normal grain growth, the microstructure exhibits a uniform increase in grain size and the normalized grain size distribution function is invariant with time [**109**,**110**]. Most instances of grain growth during welding are the normal grain growth.

The following parabolic relation, proposed by Burke and Turnbull [**111**], has been widely used to describe the normal grain growth kinetics in various materials.

$$\overline{D}^{n} - \overline{D}_{0}^{n} = Kt \qquad (2.28)$$

where $\overline{D}$ is the mean grain size at time t, $\overline{D}_0$ is the initial mean grain size, n is the growth constant, and K is a kinetic constant. According to Burke and Turnbull [**111**], the growth constant is equal to 2 for ideal systems. However, the experimentally determined grain growth exponent values have been reported to vary from 2 to 4 for pure metals.

It should be noted that although Eq. **2.28** allows the mean grain size at a given time to be predicted, it cannot be easily applied to calculate the grain growth kinetics during welding. Eq. **2.28** or similar analytical models cannot take into account the high spatial temperature gradient present in the weldment (the so called “thermal pinning”

effect). Furthermore, the effects of topological features are not considered in the analytical models. On the other hand, numerical mathematical models based on the basic principles of grain growth phenomena, such as Monte Carlo (MC) based grain simulation techniques, have been used to model the grain growth kinetics in welds [**112**].

Recently, Mishra and DebRoy [**107**] experimentally and theoretically studied the grain growth in the HAZ of Ti-6Al-4V arc welds. They used a heat transfer and fluid flow model to calculate the thermal cycles at various locations in the HAZ. The computed temperature history data were then incorporated into a three-dimensional MC model to calculate the grain growth kinetics in the entire HAZ. Figure **2.18** shows the simulated final grain structure in the HAZ, where significant spatial grain size gradients were observed. At locations closer to the fusion line, the grains were coarse; and vice versa. It was found the extent of grain growth in the HAZ strongly depended on the heat input. Depending on the heat input used, the average grain size near the fusion plane was about four to twelve times larger than that in the base plate. The computed grain size for various heat inputs was in good agreement with the corresponding experimental data.

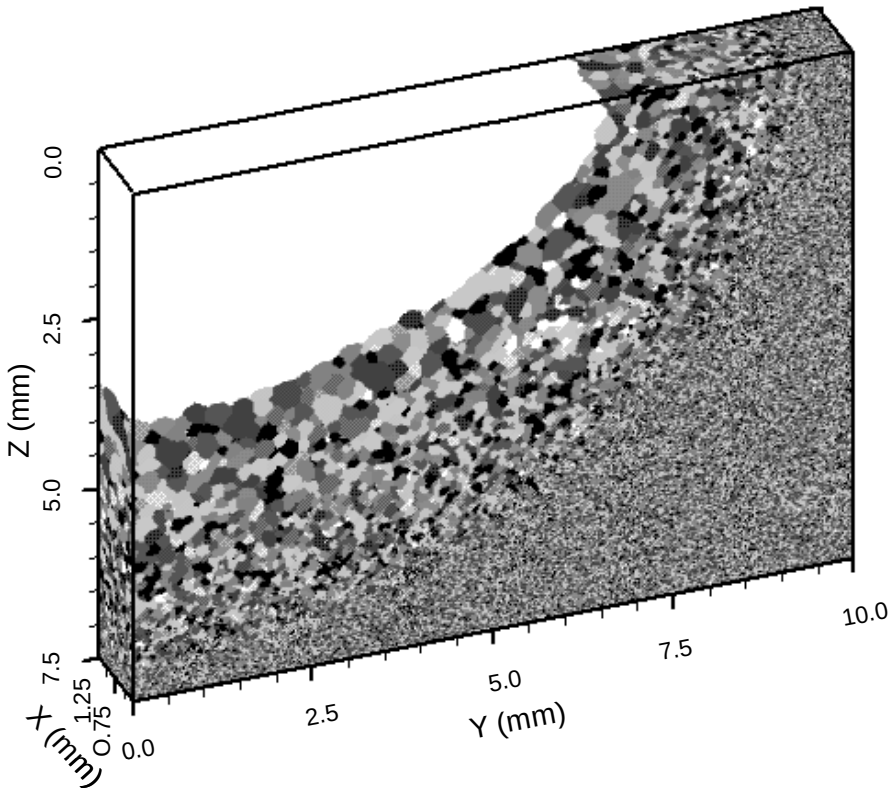

Fig. **2.18**: Simulated final grain structure in the HAZ of Ti-6Al-4V arc weld. Adapted from Mishra and DebRoy [**107**].

2.4.4 Phase transformations during weld cooling

The phase transformations during cooling have been extensively investigated both experimentally and theoretically. In the literature, there exist a wealth of time-temperature-transformation (TTT) and continuous-cooling-transformation (CCT) diagrams for describing the phase transformations during cooling of a variety of materials. These diagrams are usually constructed based on extensive metallographic experiments and are useful in understanding the phase transformations during cooling. On the other hand, several phase transformation models based on fundamentals of thermodynamics and kinetics have been developed to model the microstructure in the weldment. These phase transformation models include the model developed by Ion et al. [88,89], the model developed by Watt et al. [90,91] for prediction of microstructure in the HAZ, and the model developed by Bhadeshia et al. [85-87] for the simulation of microstructure in the FZ. In this section, the phase transformation model developed by Bhadeshia et al. is described in detail for the following two reasons. First, this model has been extensively tested and widely used in predicting the FZ microstructure. Second, this model is used in the present study to predict the microstructural evolution in 1005 steel GTA welds.

2.4.4.1 Austenite decomposition during cooling

Figure 2.19 schematically shows the various phase changes during cooling of the weld metal in low alloy steels. The δ-ferrite first solidifies from the liquid metal and quickly transforms into γ-austenite. Upon further cooling, austenite decomposes into various ferrite microconstituents, which consist of the final weld metal microstructure. The decomposition of austenite normally takes place within the temperature range from 1073 to 773 K (800 to 500 ^{o}C). During cooling of the austenite in low alloy steels, allotriomorphic ferrite is the first ferrite phase to form. It nucleates at the austenite grain boundaries and then grows along the boundaries by a diffusional mechanism. As the temperature decreases, diffusion becomes sluggish and displacive transformation is then

kinetically favored. At relatively low undercoolings, plates of Widmanstatten ferrite forms by a displacive mechanism. At further undercoolings, bainite nucleates and grows in the form of sheaves of small platelets. Acicular ferrite may also nucleate intragranularly around inclusions inside the austenite grains. If the cooling rate is high enough, the diffusionless martensite transformation may occur.

2.4.4.2 Assumptions used in the phase transformation model

In low alloy steel welds, solidification involves the epitaxial growth of δ at the fusion boundary. The final δ grains have an anisotropic columnar morphology, with their major axes lying along the direction of maximum heat flow [**113**]. On further cooling, γ grains nucleate at the δ grain boundaries and grow along these boundaries. The resulting γ grains closely resemble the original δ grain morphology. As shown in Fig. **2.20**, the morphology of the γ grains in the FZ is assumed to be represented as a honeycomb of hexagonal prisms with a cross-section side length h and major axis of the prism parallel to the direction of the maximum heat flow. The knowledge of the side length, h, is necessary to calculate the kinetics of austenite decomposition. It can be either determined metallographically from the welded specimen or estimated using some semi-empirical relationships [**114**].

It is also assumed that paraequilibrium exists at the γ/α interface during the transformation. Paraequilibrium is a constrained phase equilibrium when a phase change is so rapid that one or more components cannot redistribute within the phase in the available time scale [**85**-**87**]. The paraequilibrium condition implies that the ratio of substitutional solute over iron atoms remains constant everywhere, allowing the transformation to be controlled by the diffusion of carbon. The substitutional alloying elements can only influence kinetics through their effect on the carbon concentration and activity at the α/γ interface [**85**-**87**].

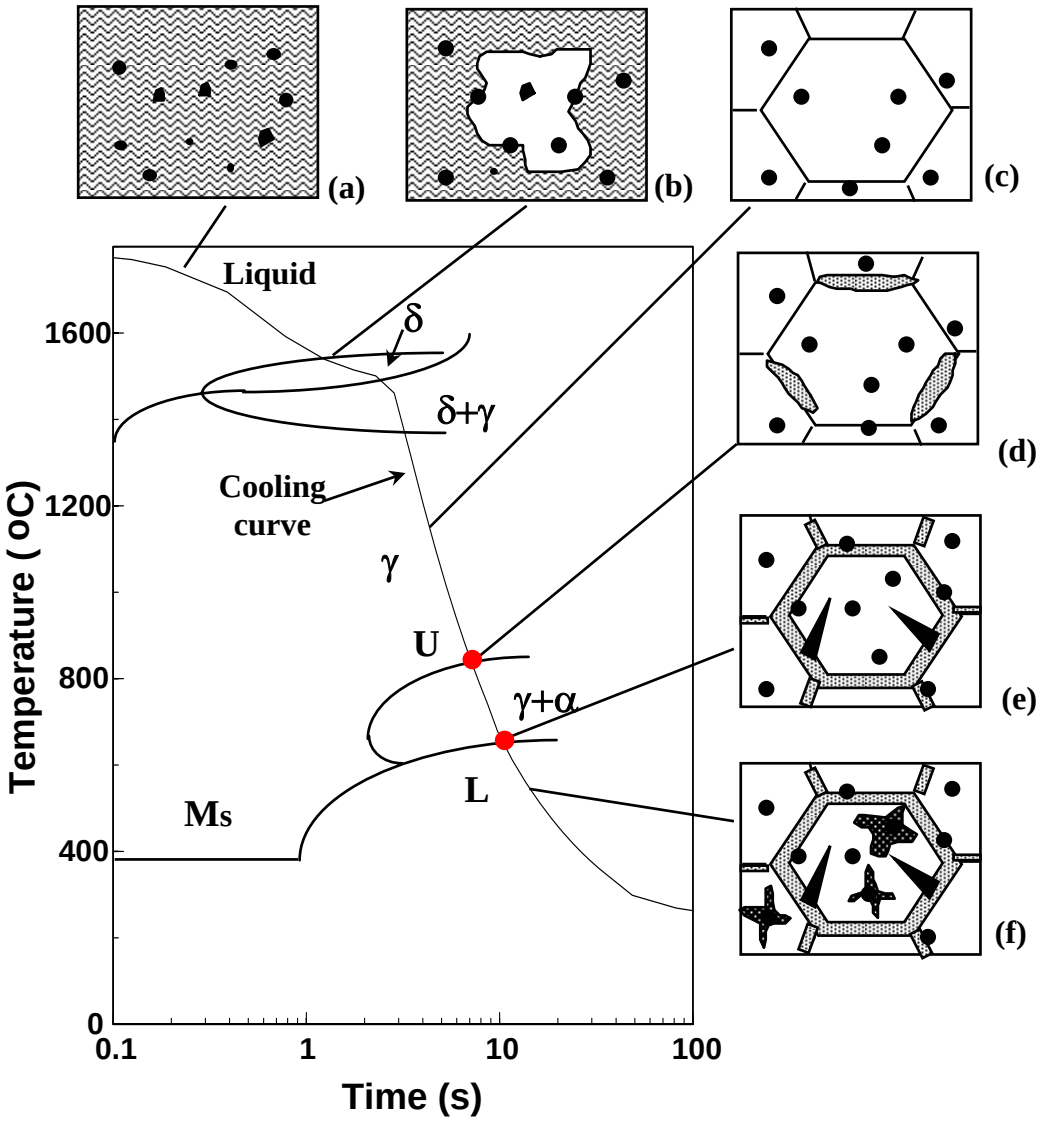

Fig. **2.19**: Schematic diagram showing the phase evolution during cooling of the weld metal in low alloy steels: (a) inclusion formation, (b) δ-ferrite formation, (c) γ-austenite formation, (d) allotriomorphic ferrite formation, (e) Widmanstatten ferrite formation, and (f) acicular ferrite/bainite formation. Points U and L represent the interception between the cooling curve and upper and lower C curves, respectively. Adapted from Bhadeshia [**85**].

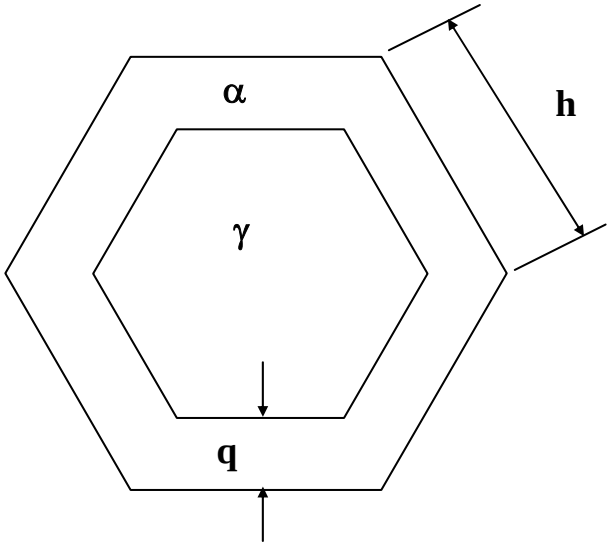

Fig. **2.20**: Assumed shape of an austenite grain [**114**], where γ is the austenite grain, α is an allotriomorphic ferrite layer, and q is its thickness, and h is the side length of prior hexagonal austenite grain.

2.4.4.3 Calculation of TTT and CCT diagrams

The TTT curves in the model are classified into two C curves, the one at higher temperatures representing replacive transformations, and that at lower temperatures representing displacive transformations. The incubation times for both replacive and displacive transformations are calculated by Russell's expression [115,116]:

$$\tau = T^{a} \times (\Delta G_{max})^{b} \times \exp(\frac{c}{T}) \times d \qquad (2.29)$$

where τ is the incubation time for a transformation, T is the temperature, ΔG_{max} is the maximum driving force for nucleation and a, b, c and d are constants. The details of calculation of ΔG_{max} and determination of constants a, b, c, and d are given in reference [117].

The CCT diagram can be calculated from the corresponding TTT diagram based on Scheil additive rule [118]:

$$\int_{0}^{t} \frac{dt}{t_a(T)} = 1 \qquad (2.30)$$

where $t_a(T)$ is the incubation time to a specified stage on a TTT diagram for isothermal reactions, t is the time to that stage for the non-isothermal reactions, and dt is the time interval at temperature T. In this procedure, the total time to reach a specified stage of transformation for non-isothermal reactions is obtained by adding the fractions of the time to reach this stage isothermally until the sum reaches unity.

2.4.4.4 Estimation of phase volume fractions

When the weld metal cools to a temperature below Ae_3, austenite begins to transform into a layer of allotriomorphic ferrite that grows from the prior austenite grain boundary by diffusion. The start temperature for this transformation is determined from the interception temperature of the cooling curve and upper C curve in the CCT diagram (i.e., point U). The completion temperature for the allotriomorphic ferrite transformation

is taken from the interception temperature of the cooling curve with the lower C curve (i.e., point L), because below this temperature displacive transformations are assumed to be kinetically favored. At this point, the growth of allotriomorphic ferrite ceases and gives way to displacive transformations. Under the paraequilibrium assumption, the growth rate of allotriomorphic ferrite is controlled by the diffusion of carbon in the austenite ahead of the moving allotriomorphic ferrite/austenite interface. The thickness of the allotriomorphic ferrite layer can be calculated by the following parabolic thickening relationship [**85**-**87**]:

$$q = \int_{T_l}^{T_h} 0.5\,\alpha_1\, t^{-0.5}\,dt \qquad (2.31)$$

where q is the thickness of the allotriomorphic layer, t is the time, T_h and T_l are the start and finish temperatures of the transformation, respectively, and α_l is the one-dimensional parabolic thickening rate constant. Based on the area that allotriomorphic ferrite occupies in the hexagonal cross section of austenite grain, as shown in Fig. **2.20**, the volume fraction of allotriomorphic ferrite (V_α) can be calculated as [**85**-**87**]:

$$V_\alpha = [2q\tan(30^o)(2h - 2q\tan(30^o))]/h^2 \qquad (2.32)$$

where V_α is the volume fraction of allotriomorphic ferrite, q is the thickness of allotriomorphic ferrite, and h is the side length of austenite.

The austenite to Widmanstatten ferrite transformation is a paraequilibrium displacive transformation with the growth rate controlled by the combination of carbon diffusion and an invariant-plane strain change [**119**,**120**]. Based on the area that Widmanstatten ferrite occupied in the hexagonal cross section of austenite grain after the formation of the allotriomorphic ferrite, the volume fraction of Widmanstatten ferrite (V_w) is calculated by [**85**-**87**]:

$$V_w = C_4 G[2h - 4q\tan(30^o)t_2^2/(2h)^2] \qquad (2.33)$$

where C_4 is a constant independent of alloy composition, G is the lengthening rate of Widmanstatten ferrite, h is the side length of austenite, q is the thickness of the

allotriomorphic ferrite layer, and t_2 is the time available for the formation of Widmanstatten ferrite. Details on determining these parameters are available in the literature [**85-87**].

The volume fraction of microconstituents other than allotriomorphic and Widmanstatten ferrites, V_o, is calculated from the mass conservation equation:

$$V_o = 1 - V_\alpha - V_w \qquad (2.34)$$

where V_α and V_w are volume fractions of allotriomorphic ferrite and Widmanstatten ferrite, respectively.

In summary, a series of transformations taking place during both weld heating and cooling culminate in the final weldment microstructure. The ability to model microstructural evolution during welding relies on a deep understanding of phase transformation theory governing the phase changes and the thermal cycle that the material experiences. Thus, coupling of phase transformation models with the calculated thermal cycles from a comprehensive thermo-fluid model is attractive for the prediction of the microstructural evolution during fusion welding.

2.5 Selection of Important Unanswered Questions

Achieving structurally sound and defect free weld joints requires the understanding of heat transfer, fluid flow and microstructural evolution during welding. Transport phenomena based numerical models have provided significant insights into the various physical processes taking place during welding. Due to the complexity of the welding process, assumptions and simplifications are often used to make the simulation work tractable, and many important questions still remain unanswered. The following is a selection of important unanswered questions that are addressed in the present thesis study.

(A) Heat transfer and fluid flow during transient spot welding

In transient spot welding, the weld is rapidly heated and cooled. It is important to understand the following questions: (1) how the welding conditions affect the heating and cooling rates, (2) how the weld thermal profiles change as a function of time, (3) the role of convection in a rapid growing and shrinking weld pool, (4) how the mushy zone behaves during heating and solidification, and (5) how the solidification front velocity and temperature gradient changes with time during spot welding.

In order to address these questions, a transient numerical model is used to provide detailed insight about the nature of heat transfer and fluid flow during GTA stationary spot welding. Very fine grid system and small time step are used for the accuracy of the transient calculations.

(B) Heat transfer and free surface flow in complex weld joints

Performance of structurally sound fillet welds is determined by the geometrical features of the weld bead. A three-dimensional framework for understanding of heat transfer and fluid flow based on transport phenomena was developed to address the following questions: (1) how the complex fillet joint geometry affects the heat transfer and fluid flow, (2) what influence the liquid convection has on the weld pool heat transfer, (3) how the arc pressure and droplet addition affect the weld pool free surface profile, and (4) how the droplet heat transfer affects the temperature distribution in the weldment.

(C) Microstructural evolution in the weldment

Phase transformation models that consider the characteristics of welding process are now available to quantitatively predict welding-induced phase transformations. In order to apply these phase transformation models to understand weldment microstructure, accurate knowledge of the thermal cycles at various locations of the weldment is needed. Coupling the available phase transformation models with thermal cycles calculated from a well-tested heat transfer and fluid flow model is an effective approach for quantitative calculation of phase transformations during welding. In the present thesis study, by

combing weld experiments and models based on transport phenomena and phase transformation theory, the kinetics and mechanism of several important phase transformations under welding conditions are studied.

The welded materials investigated in this thesis included AISI 1005 steel, 1045 steel, 2205 duplex stainless steel (DSS) and Ti-6Al-4V alloy. The heating and cooling rates in 1045 steel and Ti-6Al-4V spot welds are much higher than those in 1005 steel and 2205 DSS linear welds. A phase transformation model based on the JMA theory was developed to study the kinetics of phase transformations controlled by nucleation and growth. The JMA method was then used to quantitatively study the rates of α-ferrite→γ-austenite transformation in 1005 and 1045 steels, and α-Ti→β-Ti transformation in Ti-6Al-4V alloy under the conditions of welding. A numerical diffusion model considering moving interfaces was developed to investigate the γ-austenite→δ-ferrite transformation during GTA welding of 2205 DSS. The calculated transformation kinetics in the four systems were compared with those measured using spatially or temporally resolved X-ray diffraction techniques.

2.6 References

1. J. F. Lancaster: *The Physics of Welding*, 2nd Edition, Pergamon, Oxford, 1986.
2. K. Easterling: *Introduction to the Physical Metallurgy of Welding*, 2nd Edition, Butterworth-Heinemann, Oxford, 1992.
3. S. A. David and T. DebRoy: *Science*, **257**, 497 (1992).
4. T. DebRoy and S. A. David: *Rev. Mod. Phys.*, **67**, 85 (1995).
5. S. Kou: *Welding Metallurgy*, 2nd edition, John Wiley & Sons, Hoboken, New Jersey, 2003.
6. Ø. Grong: *Metallurgical Modeling of Welding*, 2nd edition, The Institute of Materials, London, 1997.
7. D. A. Schauer, W. H. Giedt and S. M. Shintaku: *Weld. J.*, **57**, 127s (1978).
8. W. H. Giedt, X. Wei and S. Wei: *Weld. J.*, **63**, 376s (1984).

9. W. E. Lukens and R. A. Morris: *Weld. J.*, **61**, 27s (1982).

10. J. D. Boillot, P. Cielo, G. Begin, C. Michel and M. Lessard: *Weld. J.*, **64**, 209s (1985).

11. H. G. Kraus: *Weld. J.*, **66**, 353s (1987).

12. H. G. Kraus: *Weld. J.*, **68**, 84s (1989).

13. W. Pitscheneder, R. Ebner, T. Hong, T. DebRoy, K. Mundra and R. Benes: in *Mathematical Modelling of Weld Phenomena 4*, edited by H. Cerjak, p. 4, 1998.

14. T. DebRoy and S. Kou: *Heat Flow in Welding*, Chapter 3, Welding Handbook, vol. 1, 9th Edition, American Welding Society, p. 87, 2001.

15. C. R. Heiple and J. R. Roper: *Weld. J.*, **60**, 143s (1981).

16. C. R. Heiple and J. R. Roper: *Weld. J.*, **61**, 97s (1982).

17. N. S. Tsai and T. W. Eager: *Metall. Trans. B*, **16B**, 841 (1985).

18. M. Arenas, V. L. Acoff and N. El-Kaddah: in *Joining of advanced and specialty materials III*, edited by M. Singh et al., ASM International, Materials Park, OH, p. 142, 2001.

19. M. Arenas, V. L. Acoff and N. El-Kaddah: in *Mathematical Modelling of Weld Phenomena 5*, IOM Communications, edited by H. Cerjak, London, UK, p. 39, 2001.

20. M. A. Bramson: *Infrared Radiation: A Handbook for Applications*, Plenum Press, New York, 1968.

21. P. W. Fuerschbach: *Weld. J.*, **75**, 24s (1996).

22. H. Zhao, D. R. White and T. DebRoy: *Int. Mater. Rev.*, **44**, 238 (1999).

23. M. C. Tsai and S. Kou: *Numer. Heat Transfer A*, **17**, 73 (1990).

24. M. C. Tsai and S. Kou: *Weld. J.*, **69**, 241s (1990).

25. M. C. Tsai and S. Kou: *Int. J. Numer. Meth. Fl.*, **9**, 1503 (1989).

26. H. B. Smartt, J. A. Stewart and C. J. Einerson: in *85 ASM International Welding Congress*, edited by E. F. Nippes et al., paper no. 8511-011, ASM International, Materials Park, OH, 1985.

27. S. Kou and Y. H. Wang: *Metall. Trans. B*, **17B**, 2271 (1986).

28. T. Zacharia, S. A. David, J. M. Vitek and T. DebRoy: *Weld. J.*, **68**, 499s (1989).

29. K. Mundra, T. DebRoy, T. Zacharia and S. A. David: *Weld. J.*, **71**, 313s (1992).

30. C. S. Wu and L. Dorn: *Comput. Mater. Sci.*, **2**, 341 (1994).

31. J. W. Kim and S. J. Na: *Weld. J.*, **74**, 141s (1995).

32. K. Mundra, T. DebRoy and K. Kelkar: *Numer. Heat Transfer A*, **29**, 115 (1996).

33. X. He, P. W. Fuerschbach and T. DebRoy: *J. Phys. D: Appl. Phys.*, **36**, 1388 (2003).

34. X. He, T. DebRoy and P. W. Fuerschbach: *J. Appl. Phys.*, **94**, 6949 (2003).

35. J. D. Jackson: *Classical Electrodynamics*, 3rd edition, Wiley, New York, 1998.

36. S. Kou and D. K. Sun: *Metall. Trans. A*, **16A**, 203 (1985).

37. A. Kumar and T. DebRoy: *J. Appl. Phys.*, **94**, 1267 (2003).

38. C. Limmaneevichitr and S. Kou: *Weld. J.*, **79**, 126s (2000).

39. C. Limmaneevichitr and S. Kou: *Weld. J.*, **79**, 324s (2000).

40. W. Pitscheneder, T. DebRoy, K. Mundra and R. Ebner: *Welding J.*, **75**, 71s (1996).

41. P. Sahoo, T. DebRoy and M. J. McNallan: *Metall. Trans. B*, **19B**, 483 (1988).

42. A. Matsunawa and Y. Shinichiro: in *Recent Trends in Welding Science and Technology*, edited by S. A. David et al., ASM International, Materials Park, OH, p. 31, 1990.

43. A. Matsunawa and Y. Shinichiro: in *International Trends in Welding Science and Technology*, edited by S. A. David et al., ASM International, Materials Park, OH, p. 3, 1993.

44. R. B. Bird, W. E. Stewart and E. N. Lightfoot: *Transport Phenomena*, John Wiley & Sons, New York, 1960.

45. G. M. Oreper and J. Szekely: *Metall. Trans. A*, **18A**, 1325 (1987).

46. W. Zhang, G. G. Roy, J. W. Elmer and T. DebRoy: *J. Appl. Phys.*, **93**, 3022 (2003).

47. W. Zhang, J. W. Elmer and T. DebRoy: *Mater. Sci. Eng. A*, **333**, 320 (2002).

48. W. G. Essers and R. Walter*: Weld. J.*, **60**, 38s (1981).

49. R. T. C. Choo, J. Szekely and R. C. Westhoff: *Weld. J.*, **69**, 360s (1990).

50. M. Malinowski-Brodnicka, G. denOuden, and W. J. P. Vink: *Weld. J.*, **69**, 52s (1990).

51. R. T. C. Choo and J. Szekely: *Weld. J.*, **73**, 25s (1994).

52. B. E. Launder and B. D. Spalding: *Mathematical Models of Turbulence*, Academic Press, New York, 1972.

53. K. Hong, D. C. Weckman and A. B. Strong: in *Trends in Welding Research*, edited by H. B. Smartt et al., ASM International, Materials Park, OH, p. 399, 1996.

54. K. Hong, D. D. Weckman, A. B. Strong and W. Zheng: *Sci. Technol. Weld. Joining*, **3**, 125 (2002).

55. Z. Yang and T. DebRoy: *Metall. Mater. Trans. B*, **30B**, 483 (1999).

56. K. Mundra, J. M. Blackburn and T. DebRoy: *Sci. Technol. Weld. Joining*, **2**, 174 (1997).

57. H. Davis: *Numerical Modelling of Weld Pool Convection in Gas Metal Arc Welding*, Ph.D. Thesis, University of Adelaide, Australia, September, 1995.

58. A. De and T. DebRoy: *J. Phys. D: Appl. Phys.*, **37**, 140 (2004).

59. M. L. Lin and T. W. Eagar: *Weld. J.*, **64**, 163s (1985).

60. W. Shyy: *Computational Fluid Dynamics with Moving Boundaries*, Taylor & Francis, Washington D. C., 1996.

61. S. V. Patankar: *Numerical Heat Transfer and Fluid Flow*, Hemisphere Publishing Corp., New York, 1982.

62. H. K. Versteeg and W. Malalasekera: *An Introduction to Computational Fluid Dynamics: The Finite Volume Method*, Addison-Wesley, New York, 1996.

63. W. Shyy, H. Ouyang, E. Blosch, S. S. Thakur and J. Liu: *Computational Techniques for Complex Transport Phenomena*, Cambridge University Press, London, 1997.

64. J. Donea and A. Huerta: *Finite Element Methods for Flow Problems*, John Wiley and Sons, New York, 2002.

65. A. A. Becker, *An Introductory Guide to Finite Element Analysis*, ASME Press, New York, 2004.

66. D. V. Hutton: *Fundamentals of Finite Element Analysis*, McGraw-Hill, Boston, 2004.

67. T. J. Chung: *Finite Elements in Fluids*, Hemisphere Publishing, New York, 1992.

68. C. A. Brebbia and P. W. Partridge: *Boundary Elements in Fluid Dynamics*, Elsevier Science, New York, 1992.

69. C. Pozrikidis: *Boundary Integral and Singularity Methods for Linearized Viscous Flow*, Cambridge University Press, London, 1992.

70. G. M. Oreper, J. Szekely, and T. W. Eager: *Metall. Trans. B*, **17B**, 735 (1986).

71. T. Zacharia, S. A. David, J. M. Vitek and T. DebRoy: *Welding J.*, **68**, 510s (1989).

72. L. A. Betram: *J. Eng. Mater. Technol.*, **115**, 24 (1993).

73. S. Katayama, M. Mizutani and A. Matsunawa: *Sci. Technol. Weld. Joining*, **2**, 1, 1997.

74. W. H. Kim and S. J. Na: *Int. J. Heat Mass Transfer*, **41**, 3213 (1998).

75. ASM Handbook: *Welding, Brazing and Soldering*, Volume 6, ASM International, Materials Park, OH, 1993.

76. B. D. Nichols and C. W. Hirt: *Nucl. Sci. Eng.*, **73**, 196 (1980).

77. C. W. Hirt and B. D. Nichols: *J. Comp. Phys.*, **39**, 201 (1981).

78. D. L. Youngs: in *Numerical Methods for Fluid Dynamics*, edited by K. W. Morton et al., p. 273, 1982.

79. M. J. Berger and P. Colella: *J Comput. Phys.*, **82**, 64 (1989).

80. K. A. Hoffmann and S. T. Chiang, *Computational Fluid Dynamics for Engineering – Volume II*, Engineering Education System, Wichita, KS, USA, 1993.

81. J. F. Thompson, Z. U. A. Warsi and C. Wayne Mastin, *Numerical Grid Generation: Fundamentals and Applications*, Elsevier Science, New York, 1985.

82. Z. N. Cao and P. Dong: *J. Eng. Mater. Technol.*, Trans. ASME, **120**, 313 (1998).

83. H. G. Fan and R. Kovacevic*: J. Phys. D: Appl. Phys.*, **31**, 2929 (1998).

84. Y. Wang and H. L. Tsai: *Metall. Mater. Trans. B*, **32B**, 501 (2001).

85. H. K. D. H. Bhadeshia and L. E. Svensson: in *Mathematical Modeling of Weld Phenomena*, edited by H. Cerjak et al., Institute of Materials, London, p. 109, 1993.

86. H. K. D. H. Bhadeshia, L. -E. Svensson and B. Gretoft: *Acta metall.*, **33**, 1271 (1985).

87. H. K. D. H. Bhadeshia: *Bainite in Steels*, Institute of Materials, London, 1992.

88. M. F. Ashby and K. E. Easterling: *Acta metall.*, **30**, 1969 (1982).

89. J. C. Ion, K. E. Easterling and M. F. Ashby: *Acta Metall.*, **36**, 1949 (1984).

90. D. F. Watt, L. Coon, M. Bibby, J. Goldak and C. Henwood: *Acta metall.*, **36**, 3029 (1988).

91. L. Coon and D. F. Watt: in *Computer Modeling of Fabrication Processes and Constitutive Behaviour of Materials*, edited by J. Too, p. 467, Ottawa (1987).

92. Z. Yang, J. W. Elmer, J. Wong and T. DebRoy: *Weld. J.*, **79**, 97s (2000).

93. J. W. Elmer, J. Wong, M. Fröba, P. A. Waide and E. M. Larson: *Metall. Mater. Trans. A*, **27A**, 775 (1996).

94. J. Wong, M. Fröba, J. W. Elmer, P. A. Waide and E. M. Larson: *J. Mat. Sci.*, **32**, 1493, (1997).

95. J. W. Elmer, J. Wong and T. Ressler: *Metall. Mater. Trans. A*, **29A**, 2761, (1998).

96. T. Ressler, J. Wong and J. W. Elmer: *J. Phys. Chem. B*, **102**, 10724 (1998).

97. J. W. Elmer, J. Wong and T. Ressler: *Metall. Mater. Trans. A*, **32A**, 175 (2001).

98. J. W. Elmer, J. Wong and T. Ressler: *Scripta Mater.*, **43**, 751 (2000).

99. T. A. Palmer, J. W. Elmer and J. Wong: *Sci. Technol. Weld. Joining*, **7**, 159 (2002).

100. T. Akbay, R. C. Reed and C. Atkinson: *Acta Metall. Mater.*, **47**, 1469 (1994).

101. C. Atkinson, T. Akbay and R. C. Reed: *Acta Metall. Mater.*, **43**, 2013 (1995).

102. R. C. Reed, T. Akbay, Z. Shen, J. M. Robinson and J. H. Root: *Mater. Sci. Eng. A*, **256**, 152 (1998).

103. A. Roósz, Z. Gácsi and E. G. Fuchs: *Acta Metall.*, **31**, 509 (1983).

104. F. G. Caballero, C. Capdevila and C. García de Andrés: *Metall. Mater. Trans. A*, **32A**, 1283 (2001).

105. M. Hillert, K. Nilsson and L.-E. Törndahl: *J. Iron Steel Inst.*, **209**, 49 (1971).

106. J. W. Elmer, T. A. Palmer, W. Zhang, B. Wood and T. DebRoy: *Acta Mater*, **51**, p. 3333 (2003).

107. S. Mishra and T. DebRoy: *Acta Mater.*, **52**, 1183 (2004).

108. M. J. Donachie, Jr.: *Titanium: A Technical Guide*, 2nd edition, ASM International, Materials Park, OH, 2000.

109. M. Hillert: *Acta metall.*, **13**, 227 (1965).

110. P. Feltham: *Acta metall.*, **5**, 97 (1957).

111. J. E. Burke and D. Turnbull: *Prog. Met. Phys.*, **3**, 220 (1952).

112. Z. Yang, S. Sista, J. W. Elmer and T. DebRoy: *Acta Mater.*, **48**, 4813 (2000).

113. G. J. Davies and J. G. Garland: *Int. Metall. Rev.*, **20**, 83 (1975).

114. H. K. D. H. Bhadeshia, L. -E. Svensson and B. Gretoft: *J. Mater. Sci.*, **21**, 3947 (1986).

115. K. C. Russell: *Acta Metall.*, **16**, 761 (1968).

116. K. C. Russell: *Acta Metall.*, **17**, 1123 (1969).

117. H. K. D. H. Bhadeshia: *Metal Sci.*, **16**, 159 (1982).

118. J. W. Christian: *The Theory of Transformations in Metals and Alloys*, 1st Edition, Pergamon, Oxford (1965).

119. L. -E. Svensson: *Control of Microstructures and Properties in Steel Arc Welds*, CRC Press, London, 1994.

120. S. J. Jones and H. K. D. H. Bhadeshia: *Acta Mater.*, **45**, 2911 (1997).

Chapter 3

MODELING OF HEAT TRANSFER AND FLUID FLOW DURING GAS TUNGSTEN ARC SPOT WELDING OF 1005 STEEL

In this chapter, the evolution of temperature and velocity fields during gas tungsten arc (GTA) spot welding of AISI 1005 carbon manganese steel was studied. Transient welding conditions encountered in many everyday welding situations, such as the spot welds, are examined here. These types of welds are characterized by transient temperature fields and high heating and cooling rates, which can lead to solidification cracking and formation of non-equilibrium phases [1]. The purpose of the present study is to investigate how the weld thermal profiles and the liquid convection in the molten pool change as a function of time. Such information is useful to further understand the characteristics of the spot welds such as composition and microstructure [2-6].

Since experimental measurements of the weld thermal profiles and the liquid flow in the weld pool are cumbersome and unreliable [9,10], a practical recourse is to utilize numerical modeling based on the fundamentals of transport phenomena. However, most of previous studies on the simulation of weld heat transfer and fluid flow are focused on steady-state temperature distribution. In the few studies on the transient temperature distribution, rather crude grid systems and large time steps [11,12] were used due to the hardware limitation at that time. As a result, a detailed analysis of the transient heating and solidification behavior still remains to be undertaken to investigate how the mushy zone region behaves during heating and solidification and how the solidification front velocity changes with time in spot welds. Such a computationally intensive investigation, requiring use of very fine grids and very small time steps, have now become practical because of recent advances in the computational hardware and software.

In the present study, an existing transient numerical model developed at Penn State was used to provide detailed insight about the nature of heat transfer and fluid flow in arc spot welds. The equations of conservation of mass, momentum and energy were discretized using the control volume (CV) method in a Cartesian coordinate system.

Electromagnetic, surface tension gradient and buoyancy driving forces were considered for the calculation of transient weld pool convection. The weld pool boundary was traced using an enthalpy-porosity technique [13,14] in the fixed grid system. For the accuracy of the calculation, very fine grid spacing and small time step were used. The transient model was validated by comparing the calculated geometry of the weld fusion zone (FZ) and heat affected zone (HAZ) and the weld thermal cycles with the corresponding experimental results. Dimensionless analysis was carried out to understand the heat transfer mechanism in the weld pool and the significance of the various driving forces for the liquid pool convection. The calculated temperature distributions and heating and cooling rates are useful for understanding phase transformation kinetics. The behavior of the mushy zone, i.e. the solid + liquid two phase region, during heating and cooling were investigated. Results also revealed information about the important solidification parameters, i.e. the solidification rate and the temperature gradient at the mushy zone/solid front, as a function of time. These data are useful information for determining the solidification morphology and the scale of the solidification substructure.

3.1 Mathematical Formulation

During spot welding, the weld temperature and velocity fields are essentially axis-symmetric due to the nature of heat distribution [11,12]. This allows the governing equations to be solved in a two-dimensional system. However, the calculations presented here for spot welds are carried out in a three-dimensional Cartesian coordinate system, since the heat transfer and fluid flow model is also used for the calculation of moving heat source welding, which is a three-dimensional problem. Therefore, in the following formulation, all the governing equations are presented in their three-dimensional forms.

3.1.1 Governing equations

An incompressible, laminar and Newtonian liquid flow is assumed in the weld pool. Thus, the circulation of liquid metal in the weld pool can be represented by the following momentum equation:

$$\rho\frac{\partial u_j}{\partial t}+\rho\frac{\partial\left(u_i u_j\right)}{\partial x_i}=\frac{\partial}{\partial x_i}\left(\mu\frac{\partial u_j}{\partial x_i}\right)+S_j \qquad (3.1)$$

where ρ is the density, t is the time, x_i is the distance along the ith (i = 1, 2 and 3) direction, u_j is the velocity component along the jth direction, μ is the viscosity, and S_j is the source term for the jth momentum equation, which is given as:

$$S_j=-\frac{\partial p}{\partial x_j}+\frac{\partial}{\partial x_i}\left(\mu\frac{\partial u_i}{\partial x_j}\right)-C\left(\frac{(1-f_L)^2}{f_L{}^3+B}\right)u_j+Se_j+Sb_j \qquad (3.2)$$

where p represents pressure. In Eq. **3.2**, the first term on the right hand side (RHS) is the pressure gradient [**15**]. The second term is the viscosity term arising from casting the momentum equation into a general form. The third term represents the frictional dissipation in the mushy zone according to the Carman-Kozeny equation for flow through a porous media [**13**,**14**], where f_L is the liquid fraction, B is very small computational constant introduced to avoid division by zero, and C is a constant accounting for the mushy zone morphology. The fourth and fifth terms, Se_j and Sb_j, correspond to the electromagnetic and buoyancy source terms, respectively. As discussed in section **2.1.2.1**, the electromagnetic force term (Se_j) is calculated using Eq. **2.7** [**16**]. On the other hand, the buoyancy force term (Sb_j) is computed by using the Boussinesq approximation, as given by Eq. **2.10** [**17**].

The following continuity equation is solved in conjunction with the momentum equation to obtain the pressure field.

$$\frac{\partial u_i}{\partial x_i}=0 \qquad (3.3)$$

In order to trace the weld pool liquid/solid interface, i.e. the phase change, the total enthalpy H is represented by a sum of sensible heat h and latent heat content ΔH, i.e. $H = h + \Delta H$ [13,14]. The sensible heat h is expressed as $h = \int C_p dT$, where C_p is the specific heat, and T is the temperature. The latent heat content ΔH is given as $\Delta H = f_L L$, where L is the latent heat of fusion. The liquid fraction f_L is assumed to vary linearly with temperature [16]:

$$f_L = \begin{cases} 1 & T > T_L \\ \dfrac{T - T_S}{T_L - T_S} & T_S \le T \le T_L \\ 0 & T < T_S \end{cases} \qquad (3.4)$$

where T_L and T_S are the liquidus and solidus temperature, respectively. Thus, the thermal energy transportation in the weld workpiece can be expressed by the following modified energy equation:

$$\rho \frac{\partial h}{\partial t} + \rho \frac{\partial (u_i h)}{\partial x_i} = \frac{\partial}{\partial x_i}\left(\frac{k}{C_p} \frac{\partial h}{\partial x_i} \right) + S_h \qquad (3.5)$$

where k is the thermal conductivity. The source term S_h is due to the latent heat content and is given as:

$$S_h = -\rho \frac{\partial (\Delta H)}{\partial t} - \rho \frac{\partial (u_i \Delta H)}{\partial x_i} \qquad (3.6)$$

3.1.2 Boundary conditions

A three-dimensional Cartesian coordinate system is used in the calculation, while only half of the workpiece is considered since the weld is symmetrical about the weld center line. Figure 3.1 is a schematic plot showing the boundary conditions. These boundary conditions are further discussed as follows.

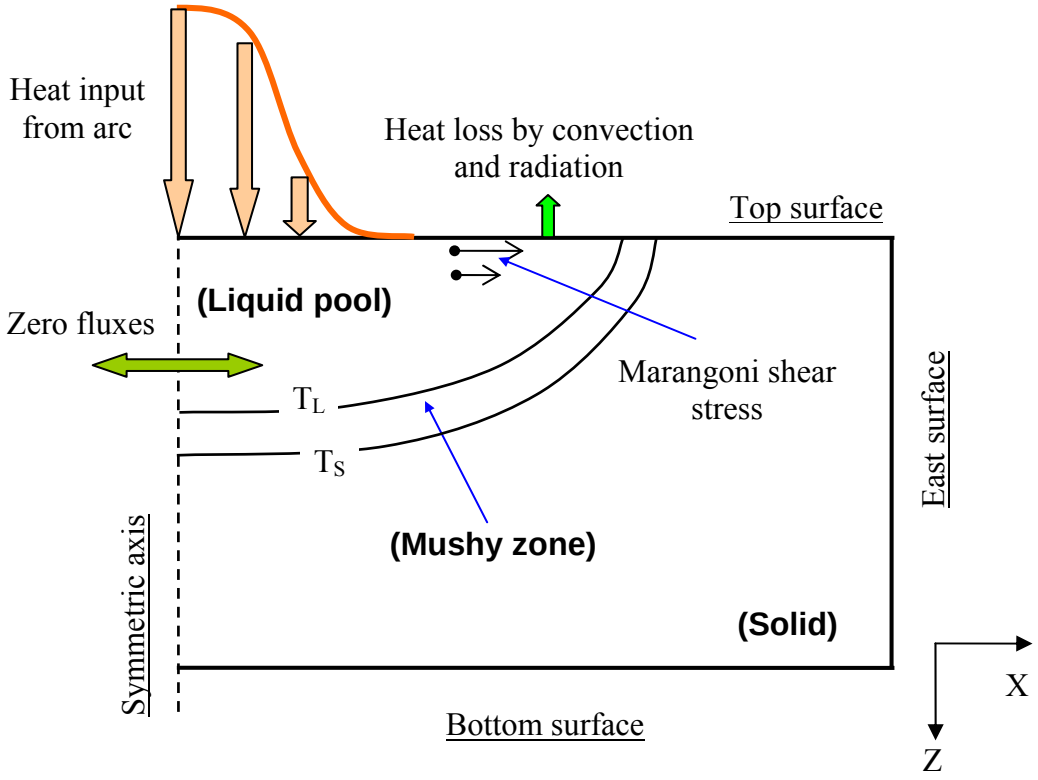

Fig. **3.1**: A schematic plot of the weld cross section showing boundary conditions used in the calculation.

3.1.2.1 Top surface

The weld top surface is assumed to be flat. The velocity boundary condition is given as [16]:

$$\mu\frac{\partial u}{\partial z} = f_L\frac{d\gamma}{dT}\frac{\partial T}{\partial x}$$
$$\mu\frac{\partial v}{\partial z} = f_L\frac{d\gamma}{dT}\frac{\partial T}{\partial y} \qquad (3.7)$$
$$w = 0$$

where u, v and w are the velocity components along the x, y and z directions, respectively, and $d\gamma/dT$ is the temperature coefficient of surface tension. As shown in this equation, the u and v velocities are determined from the Marangoni effect. The w velocity is equal to zero since there is no outward flow at the pool top surface.

The heat flux at the top surface is given as:

$$k\frac{\partial T}{\partial z}\bigg|_{top} = \frac{f_d Q\eta}{r_b^{\,2}}\exp\left(-\frac{f_d(x^2+y^2)}{r_b^{\,2}}\right) - \sigma\varepsilon\left(T^4 - T_a^{\,4}\right) - h_c(T - T_a) \qquad (3.8)$$

where r_b is the heat distribution parameter, f_d is the power distribution factor, Q is the total arc power, η is the arc efficiency, σ is the Stefan-Boltzmann constant, h_c is the heat transfer coefficient, and T_a is the ambient temperature. In Eq. 3.8, the first term on the RHS is the heat input from the heat source, defined by a Gaussian heat distribution. The second and third terms represent the heat loss by radiation and convection, respectively.

3.1.2.2 Symmetric surface

The boundary conditions are defined as zero flux across the symmetric surface as:

$$\frac{\partial u}{\partial y} = 0, \quad v = 0, \quad \frac{\partial w}{\partial y} = 0 \qquad (3.9)$$

$$\frac{\partial h}{\partial y} = 0 \qquad (3.10)$$

3.1.2.3 Other surfaces

At all other surfaces, temperatures are set at ambient temperature (T_a) and the velocities are set to be zero.

3.1.3 Discretization of governing conservation equations

Detailed method of discretizing the governing conservation equations is available in the literature [16]. A brief description is presented here to highlight the salient features. The governing equations are discretized using the control volume method [18], where the computational domain is divided into small rectangular control volumes. A scalar grid point is located at the center of each control volume, storing the values of scalar variables such as pressure and enthalpy. Velocity components are stored at separate locations, staggered with respect to scalar locations, to ensure the stability of numerical calculation. Thus, the control volumes for scalars are different from those for the vectors. Discretized equations for a variable are formulated by integrating the corresponding governing conservation equation over the control volumes. The final discretized equation takes the following form [18]:

$$a_P \phi_P = \sum_{nb} (a_{nb} \phi_{nb}) + a_P^0 \phi_P^0 + S_U \Delta V \qquad (3.11)$$

where subscript P represents a given grid point, while subscript nb represents the neighbors of the given grid point P, ϕ is a general variable such as velocity or enthalpy, a is the coefficient calculated based on the power law scheme [18], ΔV is the volume of the control volume, and a_P^0 and ϕ_P^0 are the coefficient and value of the general variable at the previous time step, respectively. The coefficient a_P is defined as:

$$a_P = \sum_{nb} a_{nb} + a_P^0 - S_P \Delta V \qquad (3.12)$$

The terms S_U and S_P are used in the source term linearization as:

$$S = S_U + S_P \phi_P \qquad (3.13)$$

3.1.4 Convergence criteria

At each time step, the discretized equations are solved using the Semi-Implicit Method for Pressure Linked Equation (SIMPLE) algorithm [18]. The calculation proceeds to the next time step if certain convergence criteria in the present step are satisfied. Two convergence criteria, i.e. residuals and heat balance, are used in the transient model. The residuals for velocities and enthalpy are defined as:

$$R = \frac{\sum_{\text{domain}} \left| \frac{\sum_{nb} (a_{nb}\phi_{nb}) + a_P^0\phi_P^0 + S_U\Delta V}{a_P} - \phi_P \right|}{\sum_{\text{domain}} |\phi_P|} \qquad (3.14)$$

The term inside the bracket defines the error in solving Eq. 3.13 for a control volume. This error is summed over the entire solution domain and then normalized to determine the residual for the variable ϕ. The residual values should be very small when a converged solution is obtained.

The following overall heat balance check provides another criterion for the convergence of the solution.

$$\theta = \left| \frac{\text{net heat input}}{\text{total heat out} + \text{heat accumulation}} \right| \qquad (3.15)$$

Upon convergence, heat balance ratio θ should be very close to 1.

In the present study, we define that the convergence is reached when $R \le 10^{-4}$ as well as $0.999 \le \theta \le 1.001$. More strict convergence conditions were found not to change the final results while increasing the computational time significantly.

3.1.5 Grid spacings and time steps

It is well accepted that as the grid spacing and time step approach zero, the numerical solution approaches to the true solution [18]. Such exercise is not practical due

to the limited computational power and the finite computer accuracy in representing floating numbers. In the present study, different grid systems and time steps were tested, and the calculated temperature and velocity fields and the geometry of the FZ under these conditions were compared. It was found the computed results converged to some fixed solution, as the grid spacing and time step reduced to a certain level. Further reducing of grid spacing and time step did not change the final results, while making the solution process much more computationally expensive. A typical grid system consisted of 130×65×60 grid points, and the corresponding computational domain had dimensions of 64 mm in length, 32 mm in width and 22 mm in depth. Spatially non-uniform grids were used for the maximum resolution of variables. Finer grid spacings were used near the heat source. The minimum grid spacings along the x and z directions were about 50 μm and 20 μm, respectively. The time step used in the cooling part was 1 ms to ensure the accurate calculation of solidification parameters, while the time step used in the heating part was 20 ms to reduce the computational time. Such fine grid spacing and small time step were necessary to obtain the accurate solution of the temperature and velocity fields under the rapid heating and cooling conditions encountered during spot welding.

3.2 Spot Welding Experiments

AISI 1005 carbon manganese steel in the form of 10.2 cm diameter cylindrical bar was used for the spot welding experiments. The composition of as-received bar was (by wt%): 0.05 C, 0.31 Mn, 0.18 Si, 0.11 Ni, 0.10 Cr, 0.009 P, 0.008 Cu, 0.005 S, <0.005 Al, <0.005 Nb, <0.005 Mo, <0.005 Ti and <0.005 V. GTA spot welds were made on steel bars placed in an environmental chamber filled with high purity helium (99.999%). A 225-ampere direct constant current welding power supply with electrode negative polarity was used. The welding electrode was made of W-2%Th measured 4.7 mm in diameter. High purity helium was used as both the welding and shielding gases. In the welding experiments, both the arc current an voltage were maintained constant at about 120 A and 17.5 V, respectively. Additional details about the welding procedure are

reported in the literature [19]. The physical properties for the 1005 steel and other data used in the calculations are listed in Table 3.1.

Table 3.1: Physical properties of 1005 steel and other data used in the calculations [20].

Name	Value
Liquidus Temperature, T_L, (K)	1802
Solidus temperature, T_S, (K)	1779
Latent heat of fusion, L, (J kg^{-1})	2.5×10^{5}
Density of liquid metal, ρ, (kg m^{-3})	7.2×10^{3}
Effective viscosity of liquid, μ, (kg m^{-1} s^{-1})	0.1
Thermal conductivity of solid, k_S, (W m^{-1} K^{-1})	36.4
Effective thermal conductivity of liquid, k_L, (W m^{-1} K^{-1})	109.2
Specific heat of solid, C_{PS}, (J kg^{-1} K^{-1})	754.0
Specific heat of liquid, C_{PL}, (J kg^{-1} K^{-1})	754.0
Temperature coefficient of surface tension, dγ/dT, (N m^{-1}·K^{-1})	-4.3×10^{-4}
Coefficient of thermal expansion, β, (K^{-1})	1.7×10^{-6}
Arc efficiency, η	72%
Arc radius, r_b, (mm)	2.7
Power distribution factor, f_d	0.5
Convective heat transfer coefficient, h_c, (W mm^{-2} K^{-1})	42.0
Emissivity, ε	0.7
Ambient temperature, T_a, (K)	298
Constant B in the Carman-Kozeny equation	1.0×10^{-7}
Constant C in the Carman-Kozeny equation	1.6×10^{4}

3.3 Results and Discussion

3.3.1 Validation of transient heat transfer and fluid flow model

In the spot welding experiments, the arc on time was set to more than 10 s, which was long enough to ensure that the weld pool was fully developed. Figures **3.2(a)** and **3.2(b)** show the comparison between the measured and calculated geometry of the FZ at the weld top surface and vertical cross section, respectively. In these figures, the weld pool boundary, represented by the solidus isotherm (1779 K), was calculated just before the arc was extinguished at time = 16 s. The dashed line in Fig. **3.2(b)** corresponds to the experimentally measured fusion line at the weld cross section. As shown in these figures, the calculated geometry of the FZ agrees well with the experimental result.

Three microstructural sub-regions, namely, the partially transformed region (PTR), the fine grained region (FGR), and the coarse grained region (CGR) [**19**], were observed in the HAZ of the weld cross section, as shown in Fig. **3.2(b)**. The presence of these phase regions depends on both local thermal cycles and kinetics of phase transformations. In general, the PTR is the region where α-ferrite partially transforms into γ-austenite, while the FGR corresponds to the region where α-ferrite to γ-austenite transformation completes but has not had enough time for γ-austenite grain growth. The CGR is the region closest to the FZ, where the temperatures are high enough that α-ferrite to γ-austenite transformation completes, and the transformed γ-austenite grains grow significantly [**19**]. The A3 (1204 K) and A1 (991 K) equilibrium temperatures for the 1005 steel are normally used to represent FGR/PTR and PTR/Base Metal boundaries, respectively. However, the calculated isotherms at 1320 K and 1055 K, matched the size and location of the FGR/PTR and PTR/Base Metal boundaries better that the A3 and A1 isotherms. These two temperatures, 1320 K and 1055 K, are higher than the A3 and A1 temperatures for 1005 steel, indicating that superheating was required for the α-ferrite to γ-austenite transformation under the rapid heating conditions in spot welding.

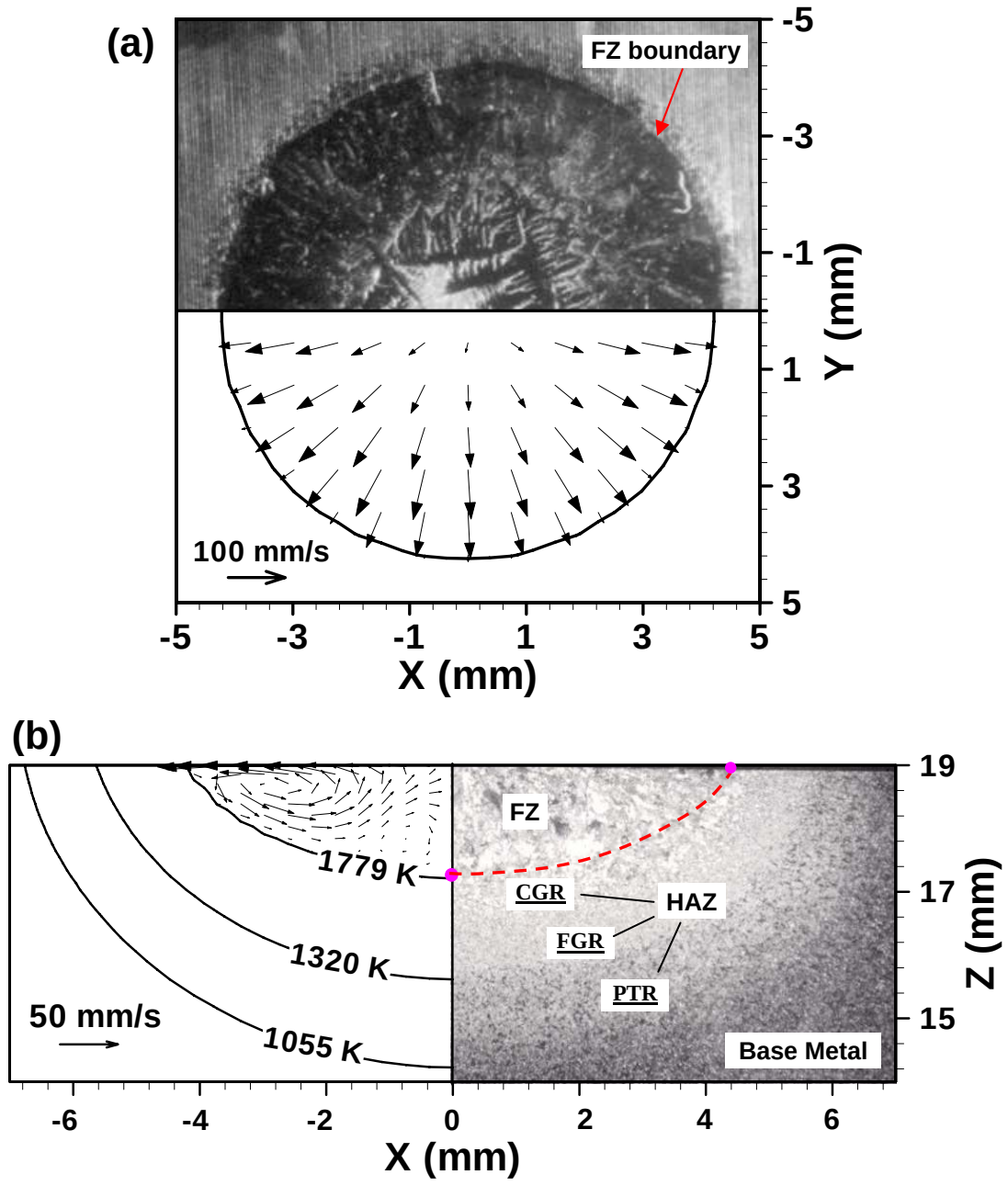

Fig. 3.2: Comparison between the calculated and measured weld pool geometry. (a): the top surface, and (b): the cross section. Welding conditions: arc current = 120 A, arc voltage = 17.5 V, and arc on time = 16 s. Symbols CGR, FGR and PTR represent the coarse grained region, fine grained region and partially transformed region, respectively. The HAZ consists of the CGR, FGR, and PTR regions.

Figure 3.3 shows the comparison between the measured and calculated cooling curves. The cooling curve was measured by plunging a thermocouple into the weld pool and switching off the arc at the same time. In this figure, the measured cooling curve is plotted as solid dots, while the calculated cooling curves at three different locations in the weld pool are represented by the lines. As shown in Fig. 3.3, there is a plateau in the calculated cooling curves. In other words, the cooling rate is rather small in this region. This is due to the release of the latent heat of fusion, as discussed in the next section. Although the thermocouple data doesn't capture the temperature plateau, the otherwise good agreement between the computed and the experimental weld pool geometry and cooling curves indicates the validity of the transient heat transfer and fluid flow model.

3.3.2 Evolution of temperature and velocity fields

Figure 3.4 shows the evolution of temperature and velocity fields in the weldment. For clarity, only a half of the weld is shown. As depicted in this figure, when the arc starts, the arc energy input leads to rapid heating, melting and the formation of the weld pool. In the weld pool, the liquid metal motion is driven mainly by the surface tension gradient and electromagnetic forces and, to a much lesser extent, by the buoyancy force. The relative importance of these driving forces is quantitatively examined in a subsequent section using the dimensionless analysis. Because the temperature coefficient of surface tension ($d\gamma/dT$) is negative, the surface tension gradient force drives the liquid metal to move from the center to the periphery at the top surface of the weld pool. This outward flow at the top surface causes the liquid to return from the edge to the center of pool below the surface. The strong outward flow driven by the surface tension gradient force carries a significant amount of arc energy from the center to the edge of the pool. As a result, the weld pool is wide and shallow.

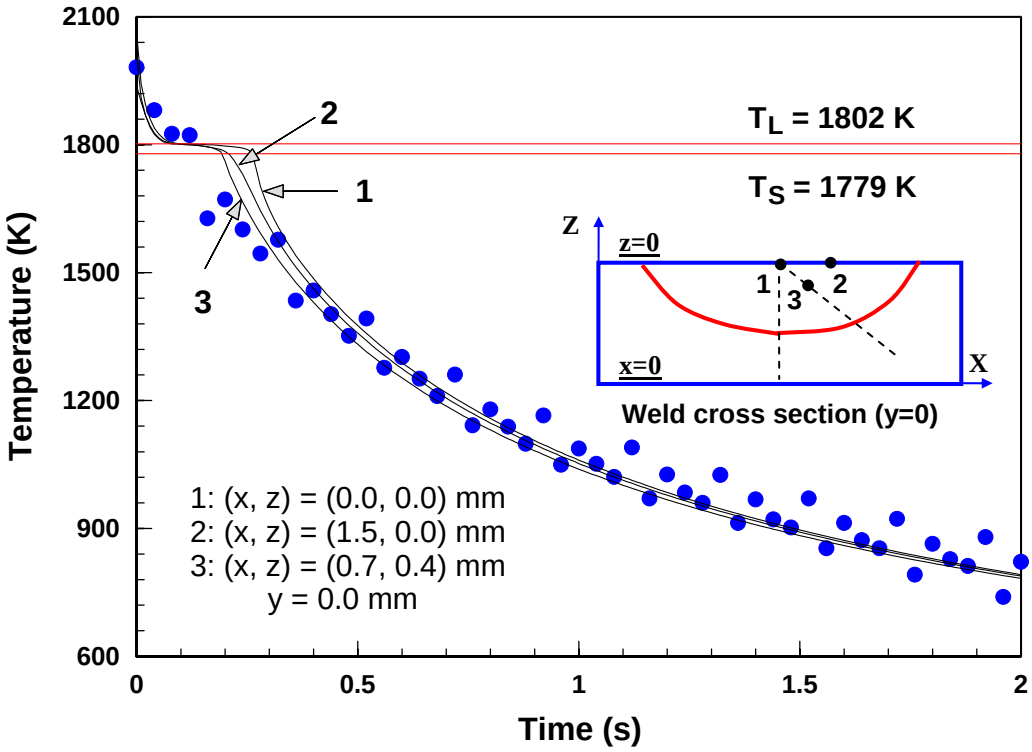

Fig. **3.3**: Comparison between the measured and calculated cooling curves. Welding conditions: arc current = 108 A, arc voltage = 18 V, and arc on time = 10 s. The time zero corresponds to the time when the arc is switched off at t = 10 s. The measured cooling curve is represented by the dots. Solid lines represent the computed cooling curves at several different locations in the weld pool, as shown in the inset figure.

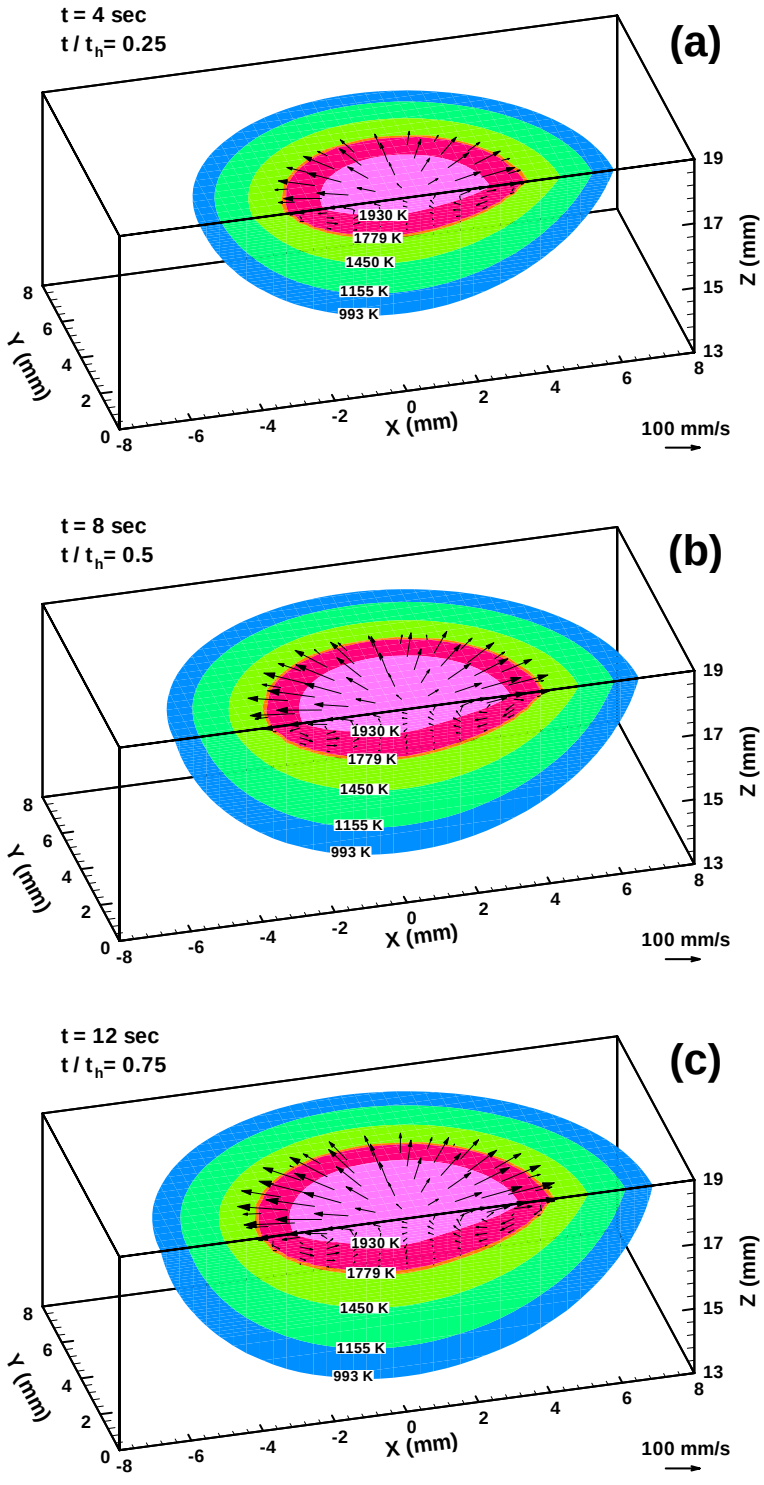
t = 4 sec
t / t_h= 0.25
(a)
1930 K
1779 K
1450 K
1155 K
993 K
Y (mm)
X (mm)
Z (mm)
100 mm/s
t = 8 sec
t / t_h= 0.5
(b)
1930 K
1779 K
1450 K
1155 K
993 K
Y (mm)
X (mm)
Z (mm)
100 mm/s
t = 12 sec
t / t_h= 0.75
(c)
1930 K
1779 K
1450 K
1155 K
993 K
Y (mm)
X (mm)
Z (mm)
100 mm/s

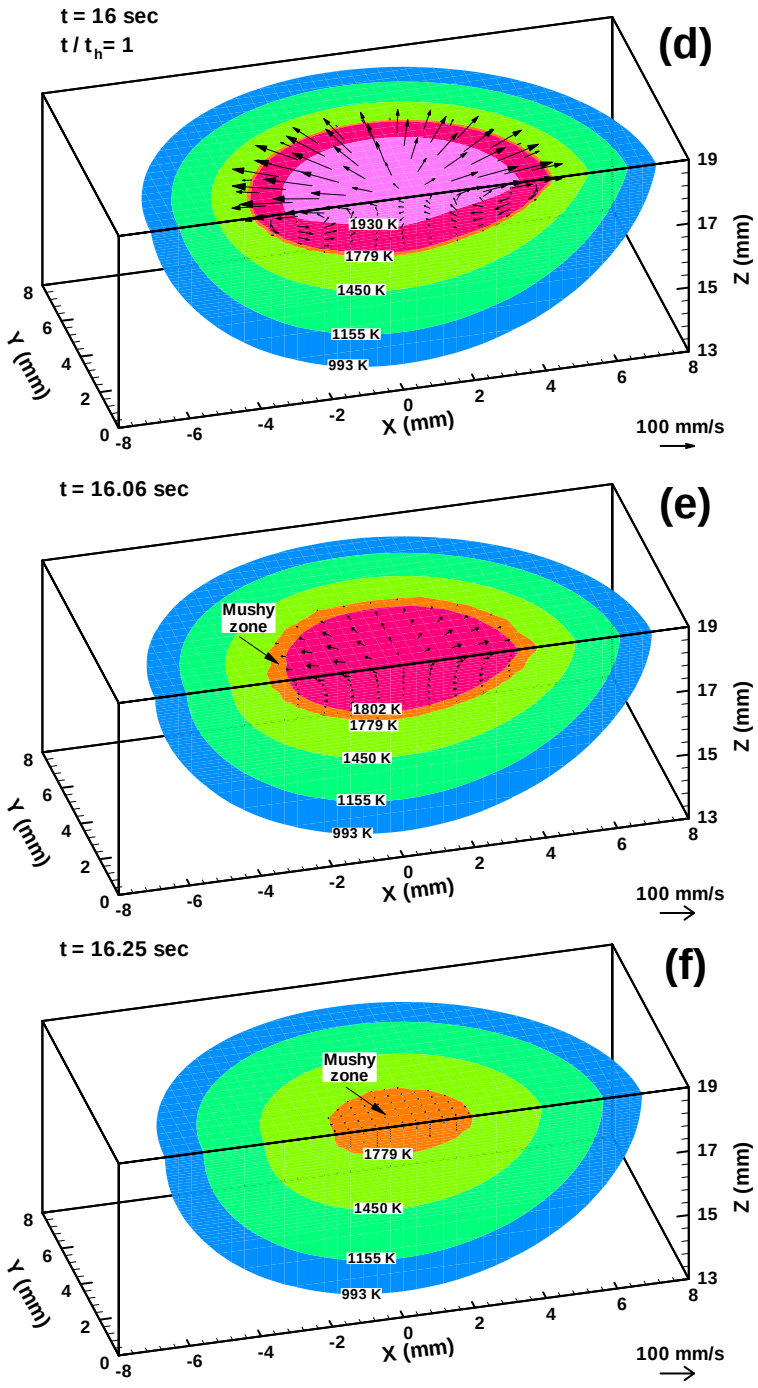

Fig. **3.4**: Evolution of temperature and velocity fields in the arc spot weld. (a): t = 4 s, (b): t = 8 s, (c) t = 12 s, (d): t = 16 s, (e): t = 16.06 s, and (f): t = 16.25 s. Welding conditions: arc current = 120 A, arc voltage = 17.5 V, and arc on time (t_h) = 16 s. Figures **3.4(a)** to **3.4(d)** are for weld heating, whereas Figs. **3.4(e)** and **3.4(f)** are for weld cooling. The velocities of the liquid convection are represented by the arrows, while the temperatures are indicated by the contours.

When the arc is switched off, the weld pool shrinks very rapidly, as shown in Figs. **3.4(e)** and **3.4(f)**. The calculations show that the entire weld pool solidifies in about 435 ms after the arc is turned off. Figures **3.4(e)** and **3.4(f)** show a dramatic drop in the liquid velocity as the pool solidifies. This is due to the fact that as the arc is turned off, the electromagnetic force is discontinued. The surface tension gradient force also decreases rapidly as the temperature gradient at the pool top surface drops significantly. Thus, the liquid motion is maintained mainly by inertia. Furthermore, the rapid shrinkage of the weld pool restricts the liquid flow. As a result, the flow diminishes rapidly during solidification. However, although the velocities decay quite rapidly, the average velocity at 350 ms after the starting of solidification is still about 1 mm/s. Therefore, most of the weld pool solidification takes place from an essentially circulating melt. However, the mixing of the liquid diminishes as solidification proceeds.

In the present study, the mushy zone, i.e. the solid + liquid two-phase region, is determined as the region having temperatures between the solidus and liquidus isotherms. As shown in Figs. **3.4(a)** through **3.4(d)**, the size of the mushy zone is very small during heating. This is due to the large temperature gradient in the weld. Figure **3.5** shows the evolution of the mushy zone size (S_m) during solidification. As shown in this figure, the mushy zone expands initially and the maximum size of the mushy zone is reached when the pure liquid region vanishes. The size of the mushy zone then decreases as solidification proceeds further. The initial expansion of the mushy zone size could be explained by considering the effect of the latent heat of fusion. The energy conservation equation for a cell containing both solid and liquid is expressed as:

$$H_{loss} = -C_P \frac{dT}{dt} - L \frac{df_L}{dt} \qquad (3.16)$$

where H_{loss} is the heat loss rate per unit mass, and C_P is the specific heat, T is the temperature, t is the time, L is the latent heat, and f_L is the liquid fraction.

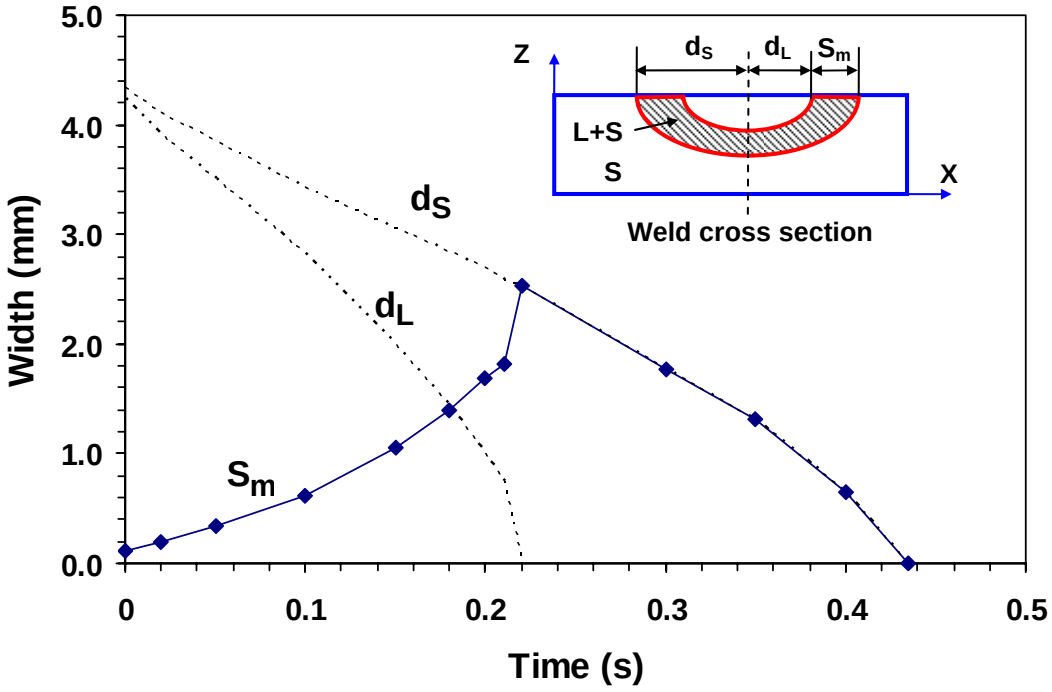

Fig. **3.5**: Evolution of the mushy zone width during solidification. Symbols d_L and d_S are the distances from the weld center to the liquid/mushy zone and mushy zone/solid interfaces at the pool top surface, respectively. The width of the mushy zone, S_m, is defined as the difference between d_S and d_L, i.e. $S_m = d_S - d_L$, as shown in the inset figure.

The first and second terms in the RHS of Eq. **3.16** account for the heat loss due to the decrease of temperature and latent heat content, respectively. When the temperature is higher than the liquidus temperature, the heat loss is accompanied by only the decrease in temperature. As the temperature drops between the liquidus and solidus temperatures, the heat loss now originates primarily from the release of the latent heat of fusion, and the temperature decreases slowly in this temperature range. In other words, the cooling rate defined by dT/dt is small between the liquidus and solidus temperature range, as indicated by the plateau in the calculated cooling curves in Fig. **3.3**. As a result of heat loss during the initial period of solidification, pure liquid region vanishes at the early stage of solidification, which leaves the weld pool occupied by the mushy region.

Figure **3.6** shows the evolution of the spatial temperature gradient and mushy zone at the weld pool top surface during solidification. As shown in this figure, both the peak temperature and temperature gradient in the liquid pool drop rapidly as the heat source is switched off. At t = 0.22 s, the peak temperature decreases just below the liquidus temperature, and the pure liquid region disappears completely. The mushy zone exists for less than another 0.22 s before the entire weld pool solidifies. The existence of a mushy pool is a unique feature of the solidification during spot welding and has significant effect on the final solidified microstructure [**21**].

3.3.3 Estimation of order of magnitude using dimensionless numbers

3.3.3.1 Relative importance of heat transfer by convection and conduction

The Peclet number (Pe), defined in Eq. 2.19, is used to evaluate the relative importance of heat transfer by convection versus conduction in the weld pool. As shown in Fig. **3.4**, the outward flow driven by the surface tension force is dominant in the liquid metal circulation and has significant effect on modifying the weld pool shape. Therefore, u_R is taken as the average u velocity at the pool top surface, and L_R is taken as the pool radius at the top surface.

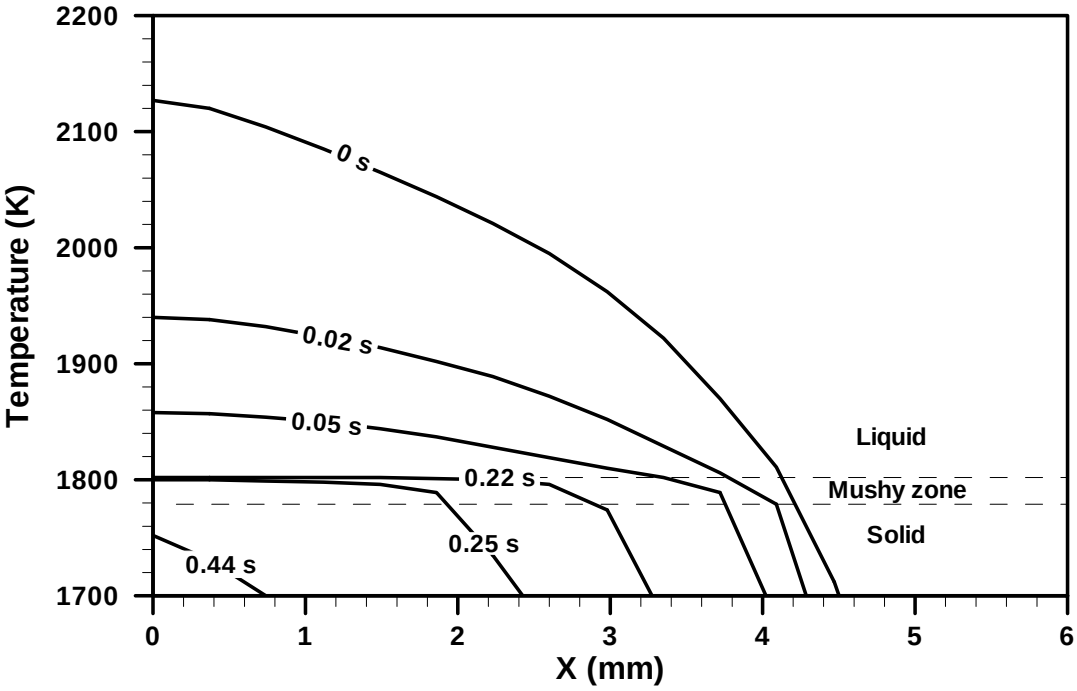

Fig. **3.6**: Distribution of temperature at the pool top surface at various solidification times. Time equal to zero corresponds to the time when the arc is switched off, i.e. the start of solidification.

For spot welding, the value of Peclet number is function of time since both u_R and L_R depend on time. Based on the dimensional analysis, two dimensionless times, t_1^* and t_2^*, are defined as:

$$t_1^* = \frac{t}{t_h} \tag{3.17}$$

$$t_2^* = \frac{\alpha t}{R_W^{\,2}} \tag{3.18}$$

where t_h is the arc duration, α is the thermal diffusivity of liquid metal ($\alpha = \rho/kC_P$), and R_W is the weld pool radius at steady state (a value of 4.5 mm used). As shown in Eq. **3.17** and **3.18**, t_1^* represents the ratio between the actual time and the heating time, while t_2^* defines the extent of heat transfer by conduction in the weld pool. Figure **3.7** shows the calculated Peclet number as a function of the two dimensionless times. As shown in this figure, the Peclet number progressively increases during the growth of the weld pool and decreases dramatically during the solidification of the weld pool. This behavior indicates that at the early stage of heating, the heat transfer by conduction is comparable to that by convection in the weld pool. As the weld pool grows, the heat transfer by convection becomes increasingly important in the weld pool. Thus, convection plays a dominant role in modifying the shape of the weld pool when the pool is fully developed. After the arc is switched off, the heat transfer by conduction soon becomes more important than that by convection during solidification due to the rapidly diminished velocity.

3.3.3.2 Relative importance of driving forces in weld pool

The driving forces for the flow in the weld pool considered in the present study include surface tension gradient, electromagnetic and buoyancy forces. As discussed in Chapter 2, the relative importance of these driving forces can be estimated using several dimensionless numbers defined in Eqs. 2.11 to 2.15.

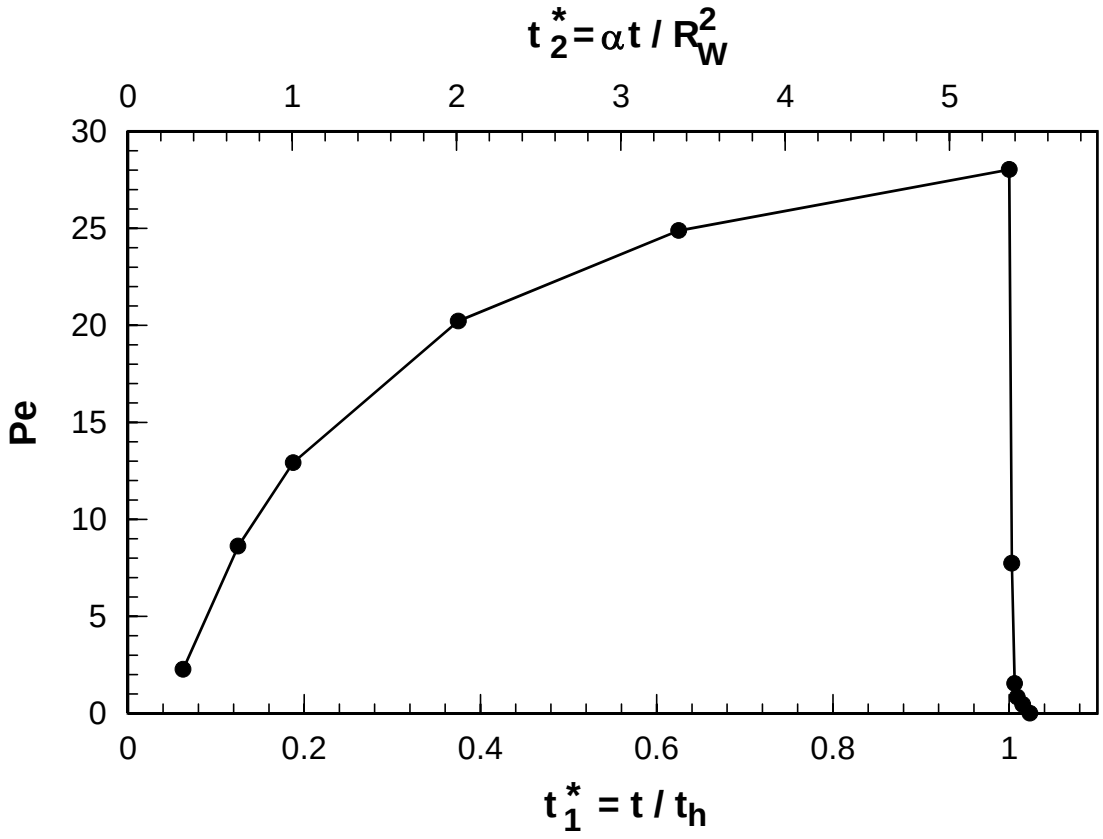

Fig. **3.7**: Peclet number as a function of two dimensionless times. Weld conditions are the same as those listed in Fig. **3.4**.

Using the physical properties given in Table 3.1, the calculated dimensionless numbers at t = 16 s (i.e. just before the arc is switched off) are listed in Table 3.2. It is expected that the liquid flow is mainly driven by the surface tension gradient and electromagnetic forces, and to a much less extent, by the buoyancy force. It should be noted that the dimensional numbers shown in Table 3.2 are fairly close to those in Table 2.2, indicating a similar effect of driving forces in both the GTA linear and spot 1005 steel weld pool. It is expected since the welding conditions such as arc current and voltage used in the two cases are similar.

Table 3.2: Dimensionless numbers calculated in the weld pool just before the arc is extinguished.

Dimensionless number	Description	Value
Gr	Ratio of buoyancy to viscous force	62.0
Rm	Ratio of electromagnetic to viscous force	7.4×10^{4}
Ma	Ratio of surface tension to viscous force	1.3×10^{5}
$R_{M/B}$	Ratio of electromagnetic to buoyancy force	1.2×10^{3}
$R_{S/B}$	Ratio of surface tension to buoyancy force	2.1×10^{3}

3.3.3.3 Order of magnitude of maximum velocity in weld pool

Since the surface tension force is the dominant driving force for convection in the weld pool, the order of magnitude of the maximum velocity can be approximated by using Eq. 2.18. The maximum velocity estimated using Eq. 2.18 is found to be of the order of 80 mm/s. This value is in good agreement with that calculated using transient heat transfer and fluid flow model, where the maximum velocity at t = 16 s was found to be about 100 mm/s.

The foregoing dimensional analysis provided insights about the weld pool behavior during transient spot welding. The role of conduction and convection on the weld pool heat transfer, and the relative importance of driving forces for liquid convection were estimated using several dimensionless numbers. It should be noted that these dimensional analysis cannot provide accurate and detailed information on the weld temperature and velocity fields, which requires numerical calculations with very fine grids and small time steps.

3.3.4 Weld thermal cycles during transient spot welding

Figure 3.8 shows the calculated thermal cycles at different locations in the weldment. Monitoring locations 2, 3 and 4 are of the same 1.5 mm distance from the weld center but along 0°, 45°, and 90° planes, respectively. Similarly, monitoring locations 5, 6 and 7 are located along 0°, 45°, and 90° planes, respectively, with a distance of 3 mm from the center. For locations of the same distance from the center, the temperatures at the 0° plane, such as curve 2, are the highest, while those at the 90° plane, such as curves 4, are the lowest. This variation is mainly due to the effect of the wide and shallow pool shape causing from the surface tension driven flow, and the resulting higher temperature gradient along the 90° plane than the 0° plane. As shown in Fig. 3.9 , the average temperature gradient ($\overline{G}_a$) of the weld pool along a given plane is defined as:

$$\overline{G}_a = \frac{T_P - T_S}{d} \qquad (3.19)$$

where T_P is the peak temperature, T_S is the solidus temperature, and d is the distance between the weld center and pool boundary at the given plane. Since d is maximum at 0° plane and minimum at 90° plane, the value of $\overline{G}_a$ at the 90° location is the highest while that at the 0° plane is the lowest. For locations of the same distance to the weld center, the higher the average temperature gradient, the lower the temperature. Therefore, the temperatures at the 0° plane are the highest and those at the 90^o plane are the lowest.

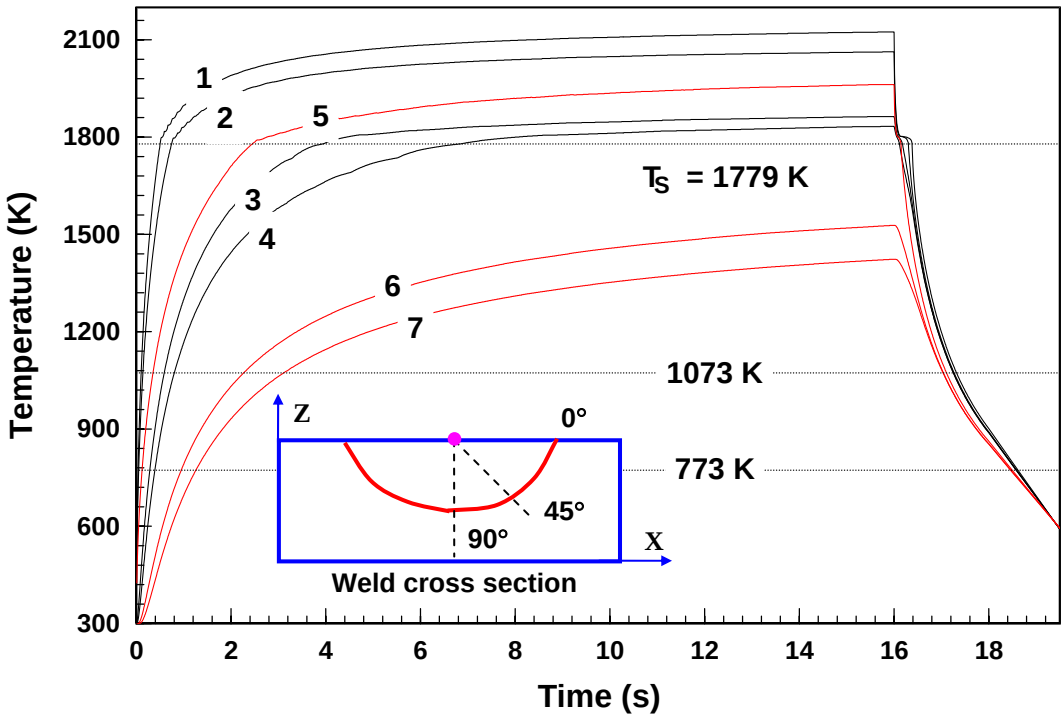

Fig. **3.8**: Computed weld thermal cycles at different locations in the 1005 steel weld. Distance from the weld center: 1: 0.0 mm, 2: 1.5 mm at 0°, 3: 1.5 mm at 45°, 4: 1.5 mm at 90°, 5: 3.0 mm at 0°, 6: 3.0 mm at 45°, and 7: 3.0 mm at 90°, as shown in the inset figure. Welding conditions are the same as those in Fig. **3.4**.

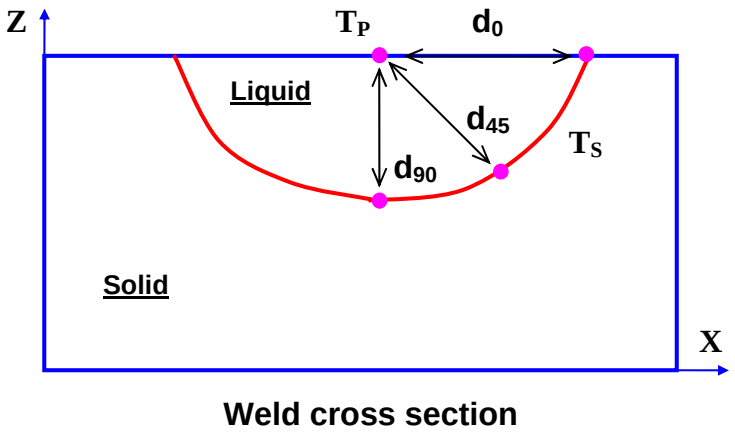

Fig. **3.9**: Schematic plot showing the calculation of average temperature gradient in the weld pool. The symbols d_0, d_{45} and d_{90} are the distances from the weld center to the pool boundary along 0°, 45° and 90° planes, respectively.

Figure 3.8 also indicates that the peak temperatures and heating rates at different locations vary significantly. Similarly, the cooling rates vary with position at high temperatures above the melting point. However, as the weld metal cools, the spatial variation of cooling rates decreases. In the 1073 K to 773 K (800 °C to 500 °C) range, the cooling rate is almost independent of position, as shown in Figs. 3.3 and 3.8. This is due to the nearly constant outward heat loss from all locations of the weld at this temperature range. Thus in steels, where much of the final microstructure is determined by the cooling rate through this temperature range, the spatial variation of microstructures is expected to be small. However, there are certain alloys where a small change in the cooling rate may result in significant difference in the final microstructure [22]. In such cases, the spatial variation of cooling rates should be considered carefully.

3.3.5 Solidification of weld pool

During rapid solidification of the weld pool, the undercooling of liquid metal is a critical parameter that controls the solidification microstructure and segregation effects. Since weld solidification proceeds from the preexisting solid substrate, only undercooling associated with growth is of importance, which is comprised of contributions from thermal, constitutional, kinetic and solid curvature effects [5]. An accurate modeling of the weld pool solidification requires coupling of a sophisticated solidification model with the heat transfer and fluid model. In the present study, in order to simplify the calculations, no undercooling is considered. In other words, the equilibrium liquidus isotherm is assumed to represent the liquid/mushy zone boundary, while the equilibrium solidus isotherm corresponds to the mushy zone/solid boundary. Therefore, the solidification parameters presented in this work were calculated by considering only the heat transfer and fluid flow in the weld pool.

Figure 3.10 shows distances of the mushy zone/solid interface to the weld center, d_0 and d_{90}, as a function of the solidification time. The subscripts 0 and 90 are used to represent the value measured at the 0° and 90° planes, respectively, as shown in the

figure. With the knowledge of the distance versus time data, the solidification rates, R_0 and R_{90}, are calculated as:

$$R_0 = \frac{d}{dt}(d_0), \qquad R_{90} = \frac{d}{dt}(d_{90}) \tag{3.20}$$

Figure 3.11 shows the calculated solidification rates as a function of the solidification time at the 0° and 90° planes, where the peak temperature of the weld pool is superimposed. As shown in this figure, the solidification rates at both planes increase with time while the peak temperature decreases. The maximum solidification rate is reached when the peak temperature drops below the solidus temperature, i.e., the weld pool solidifies completely. The increasing solidification rate, which has been experimentally observed [23], is reasonable on physical grounds. As shown in Fig. 3.9, a thin liquid shell with thickness of dr solidifies in a short time step dt. As dt approaches zero, we have $\lim_{dt\to 0}(A_S) = \lim_{dt\to 0}(A_L) = A$. Thus, the heat balance equation is given as:

$$A(k_S G_S - k_L G_L)dt = \overline{f_L} L A dr \tag{3.21}$$

where A is the surface area of the thin shell, k_S and k_L are the thermal conductivity of solid and liquid, respectively, G_S and G_L are the temperature gradient in solid and mushy zone at the mushy zone/solid interface, respectively, and $\overline{f_L}$ is the average liquid fraction of the thin shell. It should be noted that the convective heat flux in the liquid is neglected in order to simplify the discussion. Eq. 3.21 can be rewritten as:

$$R = \frac{dr}{dt} = \frac{k_S G_S - k_L G_L}{\overline{f_L} L} \tag{3.22}$$

where R is the solidification rate. As shown in Fig. 3.6, G_L drops more rapidly than G_S during solidification. Furthermore, $\overline{f_L}$ decreases with time due to the release of the latent heat of fusion. As a result, the solidification rate increases with time.

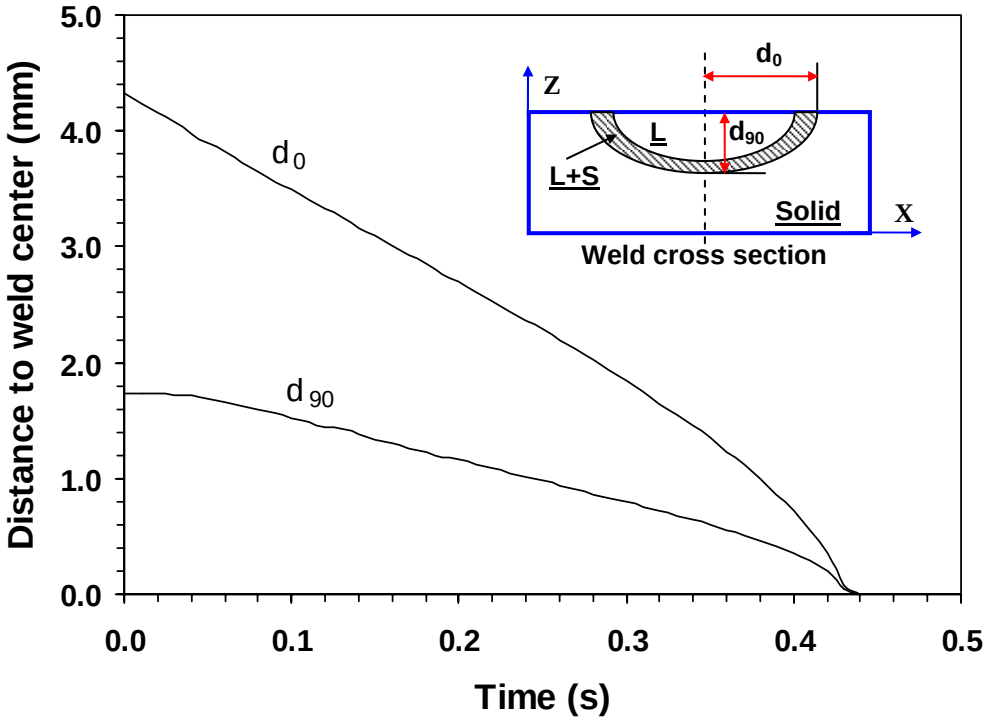

Fig. **3.10**: Distance between the mushy zone/solid front and weld center as a function of solidification time. The distances d_0 and d_{90} are measured along the 0° and 90° planes, respectively, as shown in the inset figure. The time zero corresponds to the time when the arc is switched off at t = 16 s.

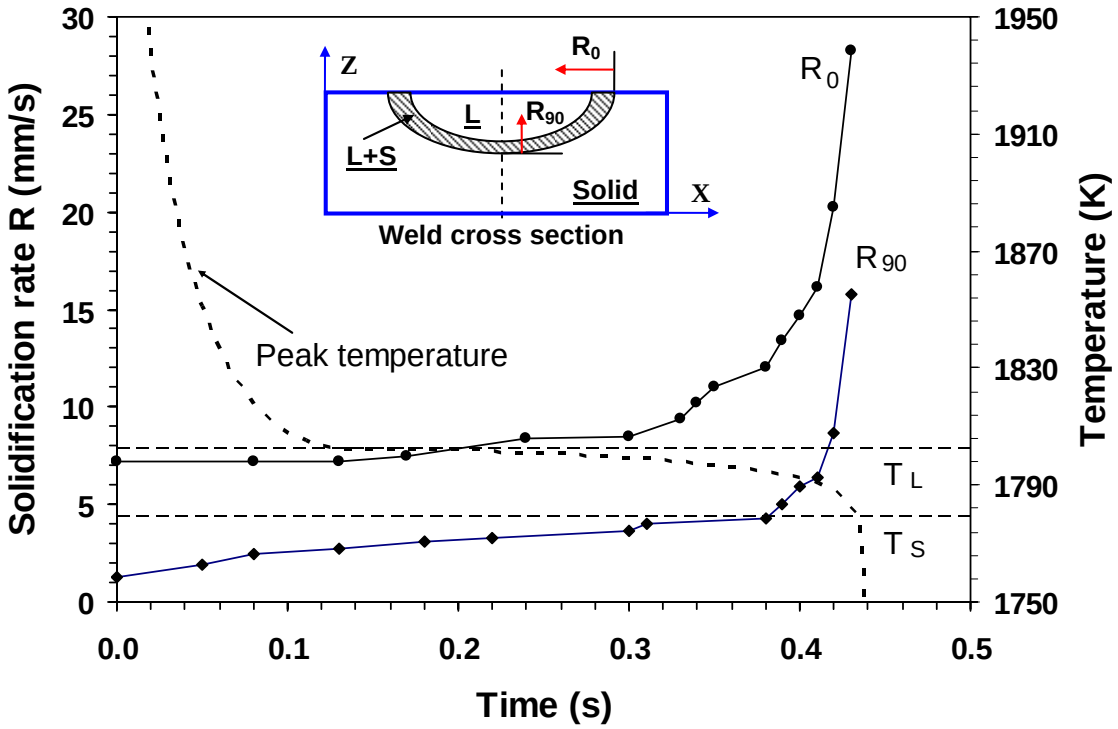

Fig. **3.11**: Solidification rate, R, as a function of time. The growth rates R_0 and R_{90} are calculated along the 0° and 90° planes, respectively, as shown in the inset figure. The superimposed dashed curve indicates the peak temperature at the weld pool center as a function of solidification time.

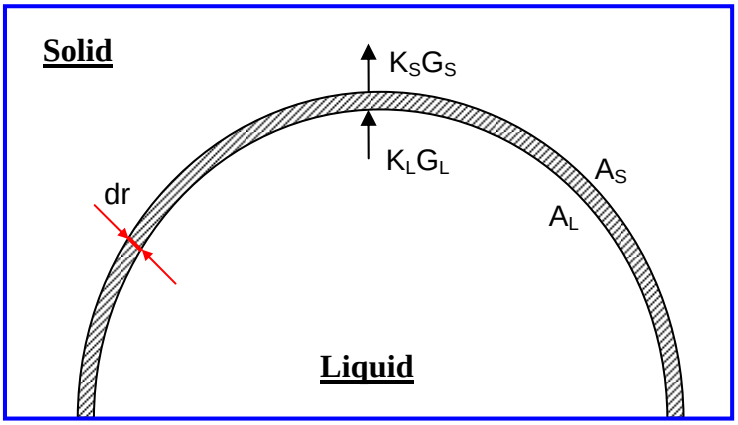

Fig. **3.12**: Schematic plot showing the solidification of a thin liquid shell.

The temperature gradients, G_0 and G_{90}, are evaluated in the mushy zone at the mushy/solid interface along the 0° and 90° planes, respectively. Figure **3.13** shows the plot of temperature gradients as a function of the solidification time. As shown in this figure, G_0 and G_{90} decrease with time.

The solidification rate, R, and temperature gradient, G, are important in the combined forms G/R and GR (cooling rate) as they can be related to the solidification morphology and the scale of the solidification substructure, respectively. Figure **3.14** depicts the solidification parameter G/R at the 0° and 90° planes. As shown in this figure, the solidification parameter G/R decreases, since G decreases while R increases with the solidification time. The maximum value of G/R is of the order of 10^2 K s mm^{-2} at the 90° plane.

Using the solidification parameter G/R, the solidification front stability could be determined. The criterion for constitutional supercooling for plane front instability is given as [**5**]:

$$G / R < \Delta T_E / D_L \qquad (3.23)$$

where ΔT_E is the equilibrium solidification temperature range at a given composition, and D_L is the solute diffusion coefficient in liquid. For 1005 steel, ΔT is equal to 23 K and D_L is taken as the carbon diffusion coefficient in pure liquid iron, 2×10^{-2} mm^2 s^{-1} [**24**]. Thus, $\Delta T/D_L$ is equal to 1.25×10^3 K s mm^{-2} for 1005 steel. Therefore, the plane front is unstable and the weld metal solidification microstructure will be of cellular or dendritic form.

The temporal variation of the solidification parameter G/R shown in Fig. **3.14** may result in changes in solidification structures, since the interface morphology generally varies from cellular, cellular-dendritic to equiaxed-dendritic as the value of G/R decreases [**6**]. Thus, it is expected that a cellular type of microstructure close to the fusion line, an equiaxed-dendritic microstructure at the pool center, and a cellular-dendritic microstructure in between, during the solidification of the spot weld pool. It should be noted that the calculations presented here indicate aspects of solidification in a qualitative manner. Quantitative determination of the solidification microstructure requires not only the parameter G/R, but also the thermodynamics and kinetics of solidification.

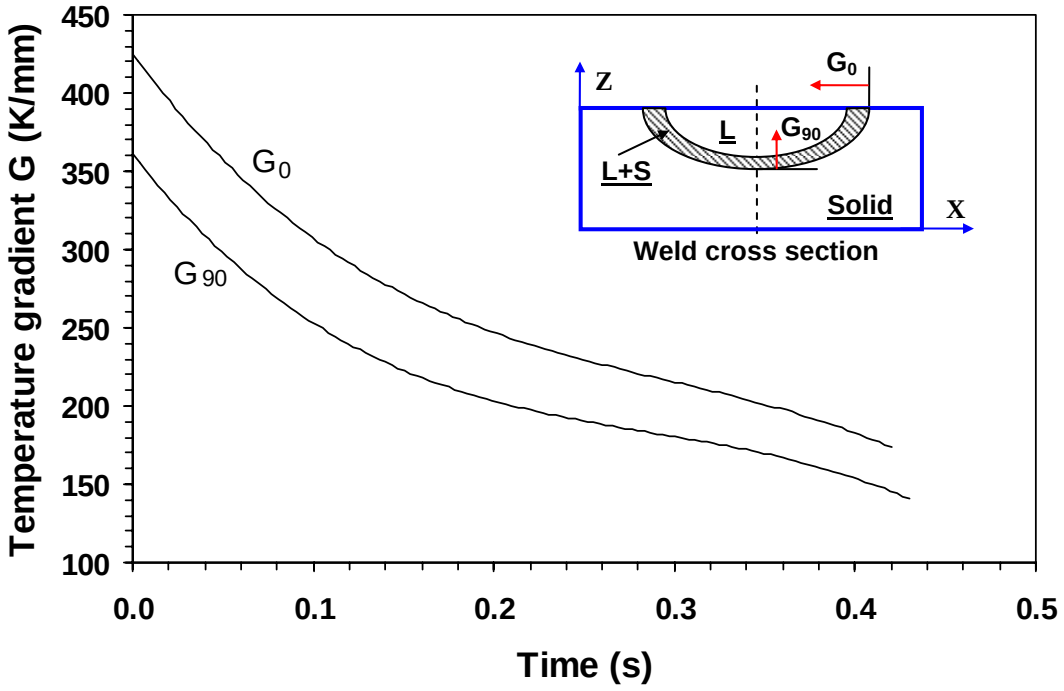

Fig. **3.13**: Evolution of the temperature gradient, G, calculated in the mushy zone at the mushy zone/solid interface at the 0° and 90° planes during solidification.

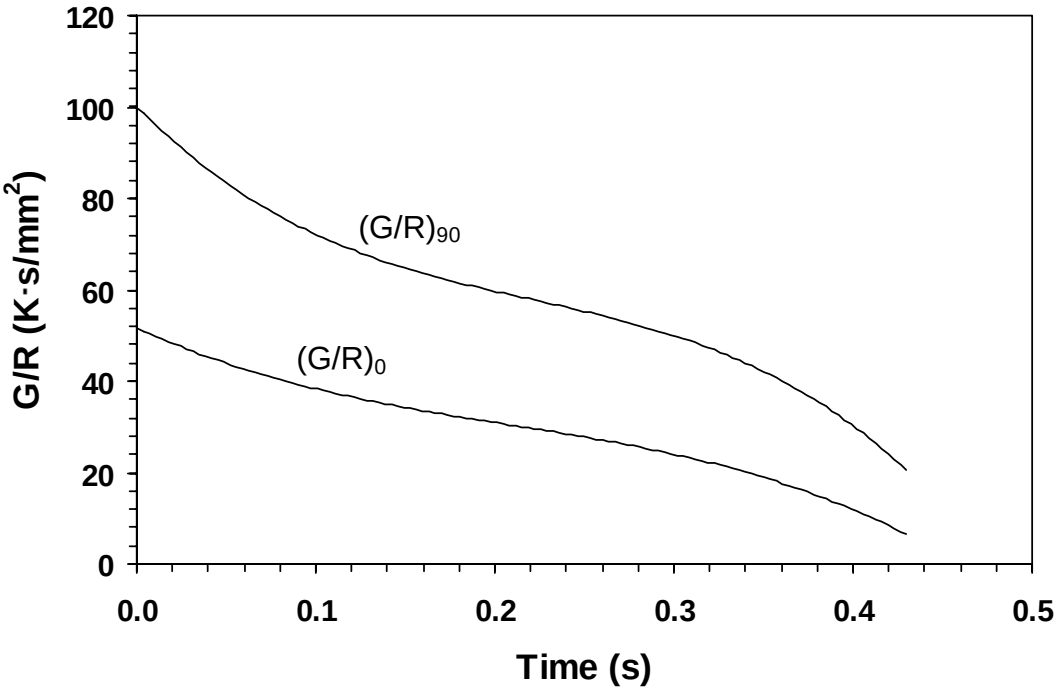

Fig. **3.14**: Calculated solidification parameter G/R at the 0° and 90° planes.

The solidification parameter GR is useful to estimate the scale of the solidified substructure [6]. Figure 3.15 shows computed value of GR as a function of time at the two planes. Since G decreases and R increases with time, the parameter GR does not always change monotonically with time. Depending on how the rates of G and R change with time, the parameter GR can either increase or decrease with time. The average values of GR are 2500 and 900 K/s at the 0° and 90° planes, respectively.

It should be noted that the validation of the transient numerical model was limited to the weld pool geometry and cooling rates. The calculated solidification parameters have not been validated against the corresponding experimental results in 1005 steel spot welds, since the focus here was the examination of the results of the transient heat transfer and fluid flow model. However, the solidification parameters computed using the transient model have been successfully used to predict the solidification structure in other alloy systems [25]. Furthermore, the solidification process investigated in the present model is governed only by the transfer of heat. An accurate prediction of the weld pool solidification will require consideration of both the thermodynamics and kinetics of solidification. In the literature, several solidification models have been developed to predict the solidification morphology and solute segregation pattern in different materials under various processing conditions [26-33]. These models include the Scheil's equation [26], steady-state growth model considering the solid/liquid interface shape [27], phase selection model [28,29], phase field method [30,31], and cellular automata model [32,33]. In the future work, a solidification model will be coupled with the transient thermo-fluid model to better understand the physics of solidification quantitatively.

3.4 Summary and Conclusions

In this chapter, the evolution of temperature and velocity fields during GTA spot welding of 1005 steel was studied using a transient numerical model. The weld thermal cycles, weld pool geometry and various solidification parameters could be quantitatively calculated. The following conclusions can be made from the investigation.

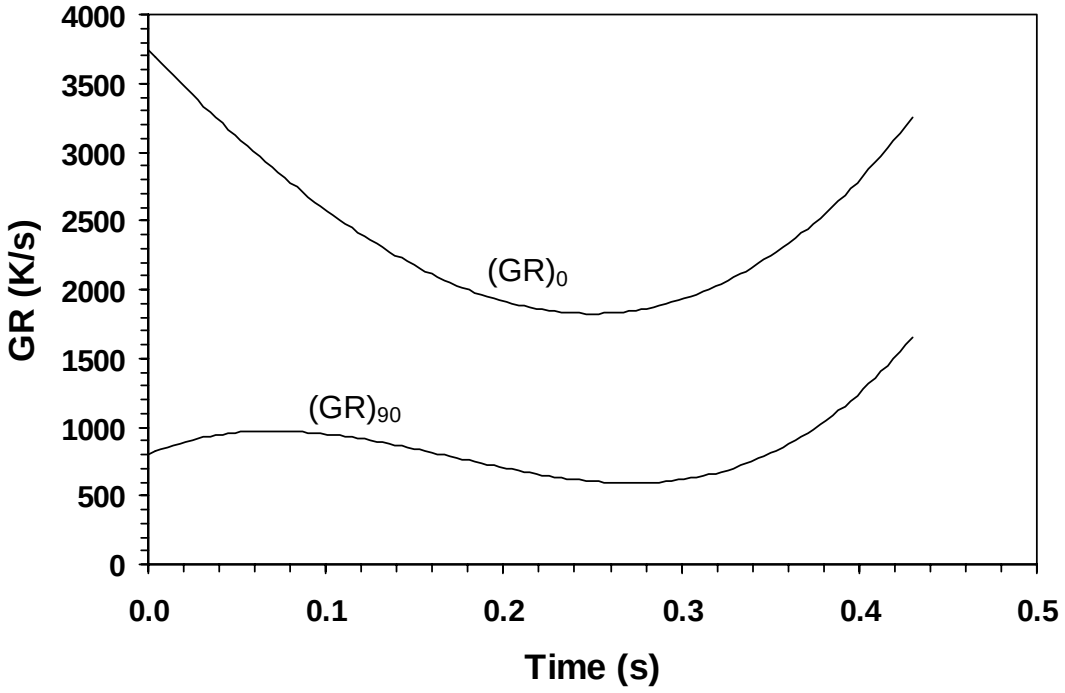

Fig. **3.15**: Calculated solidification parameter GR at the 0° and 90° planes.

(1) The geometry of the FZ and HAZ and weld cooling curves predicted from the transient heat transfer and fluid flow model were in good agreement with the corresponding experimental results. The calculated cooling rates are found to be almost independent of position between the 1073 K and 773 K (800 °C and 500 °C) temperature range.

(2) Liquid metal convection is the dominant mechanism of heat transfer as the weld pool is fully developed, and thus determines the temperature distribution in the liquid pool as well as the pool shape. Heat transfer by conduction is important when the liquid velocity is small at the beginning stage of melting and during pool solidification.

(3) The size of the mushy zone, i.e., liquid + solid two phase region, grows significantly with time during solidification. This behavior can be explained from the heat transfer consideration taking into account the latent heat of fusion.

(4) The temperature gradients (G) in the mushy zone at the mushy zone/solid interface decrease with the solidification time. The solidification rate (R) of the mushy zone/solid interface increases with time as a result of the decrease of the temperature gradient and latent heat content in the weld pool. The solidification parameters G, R, G/R and GR were quantitatively calculated and then used to estimate the solidification morphology and substructure in 1005 steel spot welds. Tracking these solidification parameters with time shows that the weld pool solidifies with decreasing interface stability, i.e., with a higher tendency to form dendrites towards the center of the weld.

The information obtained using the transient heat transfer and fluid flow model is useful to understand the weld characteristics during spot welding including the microstructural evolution in the HAZ, the solidification morphology and the scale of the solidification substructure in the FZ. This work demonstrates that the application of numerical transport phenomena can significantly add to the quantitative knowledge base in welding and help the welding community in solving practical problems.

It should be noted that the system considered in the present transient calculation contains a rectangular workpiece with a flat non-deformable weld pool top surface. Such simple system is valid for the welding conditions studied in this chapter, i.e. GTA welding with low arc currents. However, in many other cases, particularly the gas metal

arc (GMA) fillet welding, the workpiece is not a rectangle and the weld pool top surface is often severely deformed by the arc pressure and droplet transfer. Therefore, the simple system presented in this chapter cannot be used to describe the heat transfer and fluid flow in GMA fillet welding. In the next chapter, a numerical model utilizing the boundary fitted coordinate system was developed to simulate the heat transfer and free surface flow in the complex weld joint geometry.

3.5 References

1. J. W. Elmer: *The Influence of Cooling Rate on the Microstructure of Stainless Steel Alloys*, Ph.D. thesis, Massachusetts Institute of Technology, Sept 1988.

2. J. F. Lancaster: *The Physics of Welding*, 2nd Edition, Pergamon, Oxford, 1986.

3. T. DebRoy and S. Kou: *Heat Flow in Welding*, Chapter 3, Welding Handbook, vol. 1, 9th Edition, American Welding Society, p. 87, 2001.

4. K. Easterling: *Introduction to the Physical Metallurgy of Welding*, 2nd Edition, Butterworth-Heinemann, Oxford, 1992.

5. S. A. David and T. DebRoy: *Science*, **257**, 497 (1992).

6. T. DebRoy and S. A. David: *Rev. Mod. Phys.*, **67**, 85 (1995).

7. S. Kou: *Welding Metallurgy*, 2nd edition, John Wiley & Sons, Hoboken, New Jersey, 2003.

8. Ø. Grong: *Metallurgical Modeling of Welding*, 2nd edition, The Institute of Materials, London, 1997.

9. H. G. Kraus: *Weld. J.*, **68**, 84s (1989).

10. W. Pitscheneder, R. Ebner, T. Hong, T. DebRoy, K. Mundra and R. Benes: in *Mathematical Modelling of Weld Phenomena 4*, edited by H. Cerjak, p. 4, 1998.

11. G. M. Oreper, J. Szekely, and T. W. Eager: *Metall. Trans. B*, **17B**, 735 (1986).

12. G. M. Oreper and J. Szekely: *Metall. Trans. A*, **18A**, 1325 (1987).

13. V. R. Voller and C. Prakash: *Int. J. Heat Mass Transfer*, **30**, 2690 (1987).

14. A. D. Brent, V. R. Voller and K. J. Reid: *Numer. Heat Transfer A*, **13**, 297 (1988).

15. R. B. Bird, W. E. Stewart and E. N. Lightfoot: *Transport Phenomena*, John Wiley & Sons, New York, 1960.

16. S. Kou and D. K. Sun: *Metall. Trans. A*, **16A**, 203 (1985).

17. K. Mundra, T. DebRoy, and K. M. Kelkar: *Numer. Heat Transfer A*, **29**, 115 (1996).

18. S. V. Patankar: *Numerical Heat Transfer and Fluid Flow*, Hemisphere Publishing, New York, 1982.

19. J. W. Elmer, J. Wong, and T. Ressler: *Metall. Mater. Trans. A*, **32A**, 1175 (2001).

20. E. A. Brandes and G. B. Brook: *Smithells Metals Reference Book*, 7th Edition, Butterworth-Heinemann, Oxford, 1992.

21. L. A. Betram: *J. Eng. Mater. Technol.*, **115**, 24 (1993).

22. K. Mundra, T. DebRoy, S. S. Babu, and S. A. David: *Welding J.*, **76**, 163s (1997).

23. J. W. Elmer: *Private Communication*, Lawrence Livermore National Lab, 2002.

24. W. Kurz and D. J. Fisher: *Fundamentals of Solidification*, Trans Tech Publication LTD, Switzerland, 1986.

25. S. S. Babu: *Private Communication*, Oak Ridge National Laboratory, 2002.

26. M. C. Flemings: *Solidification Processing*, McGraw-Hill, New York, 1974.

27. M. Pappaz, S. A. David, J. M. Vitek and L. A. Boatner: *Metall. Trans. A*, **20A**, 1125 (1989).

28. T. Umeda, T. Okane and W. Kurz: *Acta Mater.*, **44**, 4209 (1996).

29. S. Fukumoto and W. Kurz: *ISIJ Inter.*, **38**, 71 (1998).

30. A. Karma and W. Rappel: *J. Phys. Rev.*, **E53**, R3017 (1996).

31. L. Q. Chen: *Ann. Rev. Mater. Res.*, **32**, 113 (2002).

32. M. Rappaz and C. A. Gandin: *Acta Metall. Mater.*, **41**, 345 (1993).

33. C. A. Gandin, J. L. Desbiolles, M. Rappaz and P. Thevoz: *Metall. Mater. Trans. A.*, **30A**, 3153 (1999).

Chapter 4

HEAT AND FLUID FLOW IN COMPLEX JOINTS DURING GAS METAL ARC FILLET WELDING

Gas metal arc (GMA) fillet welding is one of the most important processes for metal joining because of its high productivity and suitability for automation [1,2]. This welding process is highly complex because of the presence of a V-groove joint geometry, the significant deformation of the weld pool free surface, the addition of metal droplets from a consumable electrode, and the simultaneous occurrence of various other important physical processes. These physical processes include the absorption of arc energy, the melting and the formation of the weld pool, the liquid metal circulation in the deformed molten pool, the transport of heat in the entire weldment, and the solidification of the molten metal [1-5]. All these features must be taken into account to accurately model the GMA fillet welding processes. Such modeling of GMA fillet welding process is important in that the improved understanding would lead to better welds.

Although mathematical modeling has provided fundamental and quantitative understanding of various weldment characteristics [6-13], much of previous computer simulation efforts has focused on simple systems. Most of the studies considered rectangular workpiece and ignored any deformation of the weld pool top surface, i.e. a flat top surface is used. These models worked well for gas tungsten arc (GTA) or laser conduction mode welding of butt welds for a wide variety of welding conditions in materials with diverse thermo-physical properties [6-13]. However, such simple models are not readily applicable to widely used GMA fillet welding process because of the complexities in the weld geometry and welding process. A fundamental understanding of heat transfer and fluid flow considering free surface deformation is still evolving. Although significant progresses have been made in the modeling of GMA welding of butt joints with free surface deformation [14-18], a three-dimensional framework for understanding of heat transfer and fluid flow based on scientific principles still remains to be undertaken for GMA welding of fillet joints due to its complexity.

It should be noted that in our earlier work [19], a numerical heat conduction model employing a boundary fitted curvilinear coordinate system was used to study temperature fields in the complex fillet weld considering the deformation of the weld pool surface. The model takes into account several special features during GMA fillet welding, which include complex fillet weld geometry, the significant deformation of the pool surface and the transport of metal droplets into the weld pool which is largely responsible for the finger penetration commonly observed in the fusion zone (FZ). An enhanced thermal conductivity was assigned to the liquid metal to account the convective heat transfer in the weld pool. Although the heat conduction model reasonably predicted the weld bead geometry and cooling rates [19], it was unable to describe the liquid metal convection and the resulting convective heat transfer in the pool. It has been well established that convection is usually the dominant mechanism of heat transfer in the weld pool, and determines the weld temperature distribution and bead shape [3-5]. Recently, the effect of various driving forces on liquid metal convection has been examined. Examples include the liquid flow driven by the surface tension gradient, electromagnetic and buoyancy forces [6-11]. Especially, the surface tension driving flow was found to be very effective in the dissipation of the incident energy flux on the pool surface and often affect the weld pool geometry. For instance, a liquid flow with negative temperature coefficient of surface tension often results in a wide and shallow pool. However, when some surface active elements are present in the material, the temperature coefficient of surface tension may become positive [20] and the liquid flow pattern can be dramatically altered, which results in a narrow and deep pool [21]. Such effect of surface active elements on the weld geometry can be readily modeled considering liquid metal flow, while it poses real difficulty using a heat conduction model with enhanced thermal conductivity of liquid. Hence, the knowledge of liquid convection in the weld pool is essential to comprehensive understanding of the fillet welding processes.

The purpose of the study reported in this chapter is to develop a three-dimensional model for understanding heat transfer and fluid flow during GMA fillet welding based on transport phenomena. The numerical model considers the complex joint geometry, the deformation of the weld pool free surface, the addition of the metal droplets, and the

liquid convection in the weld pool. The numerical model was used to investigate the heat transfer and free surface flow during GMA fillet welding of A-36 mild steel. Dimensional analysis was used to understand the relative importance of heat transfer by convection and conduction and the role of various driving forces on liquid convection in the weld pool. The calculated FZ shape and size, finger penetration and cooling rates were compared with the corresponding experimental results for various welding conditions. The effect of welding parameters on important weld bead characteristics was quantitatively studied using the numerical model.

4.1 Assumptions and Salient Features

Because of the complexity of the GMA fillet welding process, the following simplifying assumptions were made to make the computational work tractable.

(a) The thermal diffusivity and the specific heat of the workpiece material are assumed to be temperature independent. However, the numerical model is capable of easily incorporating temperature dependent thermo-physical properties.

(b) The liquid metal flow is assumed to be incompressible, Newtonian, and laminar. The effect of turbulence flow in the weld pool is taken into account through the use of the enhanced thermal conductivity and viscosity of the liquid metal.

(c) The heat transported from the filler metal droplets is taken into account using a time-averaged volumetric heat source. The dynamic impingement of the droplets on the weld pool surface is considered.

(d) Both the heat and current flux from the arc are assumed to have a Gaussian distribution at the weld top surface. The distribution is unaffected by the top surface deformation.

The heat transfer and fluid flow model takes into account the liquid metal convection in the weld pool, the complex joint geometry of fillet welds, the deformation of the weld pool free surface, additions of the filler metal, and the detailed calculations of

the heat transfer by the droplets. The driving forces for weld pool convection include the surface tension gradient, electromagnetic force and buoyancy (gravitational) force. The output from the model includes temperature and velocity fields, thermal cycles, FZ geometry and the solidified geometry of the weld reinforcement.

4.2 Heat Transfer and Fluid Flow in Joint with Complex Geometry

4.2.1 Governing equations

By using a coordinate system moving with the heat source, the welding problem is assumed to be at steady state. In other words, the heat source is fixed in space and the material enters and leaves the computational domain at the welding speed [8]. Thus, the circulation of liquid metal in the weld pool is represented by the following momentum conservation equation.

$$\rho \frac{\partial \left(u_i u_j\right)}{\partial x_i} = \frac{\partial}{\partial x_i}\left(\mu \frac{\partial u_j}{\partial x_i}\right) + S_j \qquad (4.1)$$

where ρ is the density, x_i is the distance along the i^{th} (i = 1, 2 and 3) direction, u_i and u_j are the velocity components along the i^{th} and j^{th} direction, respectively, μ is the viscosity, and S_j is the source term for the j^{th} momentum equation and is given as:

$$S_j = -\frac{\partial p}{\partial x_j} - \rho U_w \frac{\partial u_j}{\partial x_1} - C\left(\frac{(1-f_l)^2}{f_l^{\,3} + B}\right)u_j + F_j^e + F_j^b \qquad (4.2)$$

where p represents pressure, U_w is the material moving speed (parallel to the positive x direction, i.e., i = 1 direction), and F_j^e and F_j^b correspond to the electromagnetic and buoyancy forces, respectively. In Eq. 4.2, the third term represents the frictional dissipation in the mushy zone according to the Carman-Kozeny equation for flow through a porous media [22,23], where f_l is the liquid fraction, B is very small computational constant introduced to avoid division by zero, and C is a constant accounting for the mushy zone morphology.

The following continuity equation is solved in conjunction with the momentum equation to obtain the pressure field.

$$\frac{\partial u_i}{\partial x_i} = 0 \qquad (4.3)$$

It should be noted that metal droplets carry additional mass into the weld pool. For simplicity, the droplet mass is ignored in Eq. 4.3, whereas it is considered in the calculation of the weld pool free surface profile. Such simplification is reasonable, since the GMA welding process is at steady-state and the addition mass of metal droplets forms weld reinforcement after solidification. In other words, the total mass in the weld pool does not vary with time.

By dividing the total enthalpy into the sensible heat and latent heat content [22,23], the energy conservation equation is given as:

$$\rho\frac{\partial(u_i h)}{\partial x_i} = \frac{\partial}{\partial x_i}\left(\alpha\frac{\partial h}{\partial x_i}\right) - \rho L\frac{\partial(u_i f_l)}{\partial x_i} - \rho U_w\frac{\partial h}{\partial x_1} - \rho U_w L\frac{\partial f_l}{\partial x_1} + S_v \qquad (4.4)$$

where h is the sensible heat, α is the thermal diffusion coefficient (defined as $\alpha = k/C_p$, where k is the thermal conductivity and C_p is the specific heat), L is the latent heat of fusion, and S_v is a source term accounting for the additional heat from metal droplets, which is described in details in a later section. The liquid fraction, f_l, is assumed to vary linearly with temperature [8]:

$$f_l = \begin{cases} 1 & T \geq T_l \\ \dfrac{T - T_s}{T_l - T_s} & T_s < T < T_l \\ 0 & T \leq T_s \end{cases} \qquad (4.5)$$

where T_l and T_s are the liquidus and solidus temperature of the material, respectively.

4.2.2 Coordinate transformation

Accurate solution of heat transfer and fluid flow with a deformable weld pool surface and complex fillet joint geometry requires the use of non-orthogonal deformable

grid to exactly fit the curved surface profile. Therefore, the governing equations are transformed from the Cartesian to curvilinear coordinate system. Figure **4.1** shows the transformation from the L-shape physical domain denoted by (x, y, z) to a simple rectangular computational domain represented by (ξ, η, ζ), where the transformed governing equations were discretized and numerically solved. As shown in this figure, only the z coordinate in the physical domain is transformed into the ζ coordinate in the computational domain, while ξ and η coordinates remain the same as x and y coordinates, respectively. For clarity, subscripts x, y, z, ξ, η and ζ are used to represent corresponding partial derivatives in the following discussion. For example, symbols ξ_x and h_η represent the partial derivatives $\partial\xi/\partial x$ and $\partial h/\partial\eta$, respectively.

The following Chain rule is used for the coordinate transformation [**24**,**25**]:

$$\begin{aligned}\frac{\partial}{\partial x} &= \xi_x\frac{\partial}{\partial\xi}+\eta_x\frac{\partial}{\partial\eta}+\zeta_x\frac{\partial}{\partial\zeta}\\ \frac{\partial}{\partial y} &= \xi_y\frac{\partial}{\partial\xi}+\eta_y\frac{\partial}{\partial\eta}+\zeta_y\frac{\partial}{\partial\zeta}\\ \frac{\partial}{\partial z} &= \xi_z\frac{\partial}{\partial\xi}+\eta_z\frac{\partial}{\partial\eta}+\zeta_z\frac{\partial}{\partial\zeta}\end{aligned} \qquad (4.6)$$

where the transformation coefficients are expressed as [**19**]:

$$\begin{bmatrix}\xi_x & \xi_y & \xi_z\\ \eta_x & \eta_y & \eta_z\\ \zeta_x & \zeta_y & \zeta_z\end{bmatrix}=\begin{bmatrix}1 & 0 & 0\\ 0 & 1 & 0\\ -Jz_\xi & -Jz_\eta & J\end{bmatrix} \qquad (4.7)$$

where J is the Jacobian of the transformation and is given as:

$$J=\frac{1}{z_\zeta} \qquad (4.8)$$

The following relationships could be derived from Eqs. **4.6** to **4.8**:

$$\frac{\partial\phi}{\partial xi}=J\left[\frac{\partial}{\partial\xi}\left(\frac{\xi_{xi}\phi}{J}\right)+\frac{\partial}{\partial\eta}\left(\frac{\eta_{xi}\phi}{J}\right)+\frac{\partial}{\partial\zeta}\left(\frac{\zeta_{xi}\phi}{J}\right)\right] \qquad (4.9)$$

$$\frac{\partial u\phi}{\partial x}+\frac{\partial v\phi}{\partial y}+\frac{\partial w\phi}{\partial z}=J\left[\frac{\partial(U\phi)}{\partial\xi}+\frac{\partial(V\phi)}{\partial\eta}+\frac{\partial(W\phi)}{\partial\zeta}\right] \qquad (4.10)$$

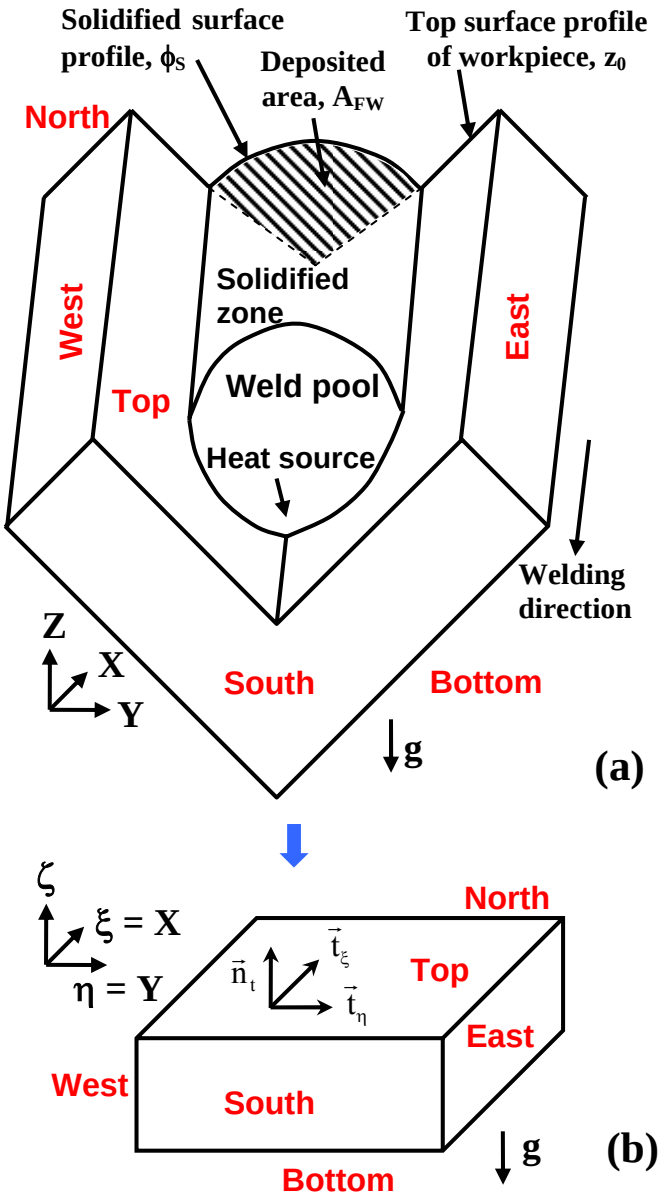

Fig. **4.1**: Schematic plot showing the coordinate transformation from the physical (x, y, z) to the computational domain (ξ, η, ζ). (a) physical domain, and (b) computational domain. Symbols $\vec{n}_t$, $\vec{t}_\xi$ and $\vec{t}_\eta$ are normal and tangential vectors to the top surface. The shadowed area, A_{FW}, is equal to the volume of wire feeding per unit length of the weld.

where ϕ is a general variable, xi is the distance along the i^{th} direction (xi = x, y and z when i = 1, 2 and 3, respectively), u, v and w are Cartesian velocity components along the x, y and z directions, respectively, and U, V and W are the contravariant velocity components in the ξ, η, and ζ directions, respectively, and are defined as:

$$\begin{aligned} U &= \frac{\xi_x u}{J} + \frac{\xi_y v}{J} + \frac{\xi_z w}{J} = z_\zeta u \\ V &= \frac{\eta_x u}{J} + \frac{\eta_y v}{J} + \frac{\eta_z w}{J} = z_\zeta v \\ W &= \frac{\zeta_x u}{J} + \frac{\zeta_y v}{J} + \frac{\zeta_z w}{J} = -z_\xi u - z_\eta v + w \end{aligned} \tag{4.11}$$

4.2.2.1 Transformation of continuity equation

Applying Eq. **4.10**, the continuity equation in the curvilinear coordinate is:

$$\frac{\partial U}{\partial \xi} + \frac{\partial V}{\partial \eta} + \frac{\partial W}{\partial \zeta} = 0 \tag{4.12}$$

4.2.2.2 Transformation of momentum equations

The transformation of x, y and z momentum equations are very similar. Therefore, in the following discussion, only the transformation of the x momentum equation is presented. Using Eqs. **4.9** and **4.10**, the transformed x momentum equation is written as follows:

$$\begin{aligned} &\rho\left[\frac{\partial(Uu)}{\partial\xi} + \frac{\partial(Vu)}{\partial\eta} + \frac{\partial(Wu)}{\partial\zeta}\right] = \frac{\partial}{\partial\xi}\left[\mu(z_\zeta \frac{\partial u}{\partial\xi} - z_\xi \frac{\partial u}{\partial\zeta})\right] + \frac{\partial}{\partial\eta}\left[\mu(z_\zeta \frac{\partial u}{\partial\eta} - z_\eta \frac{\partial u}{\partial\zeta})\right] \\ &+ \frac{\partial}{\partial\zeta}\left[\mu(-z_\xi \frac{\partial u}{\partial\xi} - z_\eta \frac{\partial u}{\partial\eta} + q_{33} \frac{\partial u}{\partial\zeta})\right] - \left(z_\zeta \frac{\partial p}{\partial\xi} - z_\xi \frac{\partial p}{\partial\zeta}\right) \\ &- \rho U_w\left(\frac{\partial(z_\zeta u)}{\partial\xi} - \frac{\partial(z_\xi u)}{\partial\zeta}\right) - C\left(\frac{(1-f_l)^2}{f_l^3 + B}\right) z_\zeta u + z_\zeta F_x^e + z_\zeta F_x^b \end{aligned} \tag{4.13}$$

where coefficient q_{33} is defined as:

$$q_{33} = J(z_\xi^2 + z_\eta^2 + 1) \tag{4.14}$$

4.2.2.3 Transformation of energy conservation equation

Using Eqs. 4.9 and 4.10, the transformed energy equation in the curvilinear coordinate system is given as:

$$\begin{aligned}
&\rho\left[\frac{\partial(Uh)}{\partial\xi}+\frac{\partial(Vh)}{\partial\eta}+\frac{\partial(Wh)}{\partial\zeta}\right]=\frac{\partial}{\partial\xi}\left[\alpha(z_\zeta\frac{\partial h}{\partial\xi}-z_\xi\frac{\partial h}{\partial\zeta})\right]+\frac{\partial}{\partial\eta}\left[\alpha(z_\zeta\frac{\partial h}{\partial\eta}-z_\eta\frac{\partial h}{\partial\zeta})\right]\\
&+\frac{\partial}{\partial\zeta}\left[\alpha(-z_\xi\frac{\partial h}{\partial\xi}-z_\eta\frac{\partial h}{\partial\eta}+q_{33}\frac{\partial h}{\partial\zeta})\right]-\rho U_w\left[\frac{\partial(z_\zeta h)}{\partial\xi}-\frac{\partial(z_\xi h)}{\partial\zeta}\right]\\
&-\rho L\left[\frac{\partial(Uf_1)}{\partial\xi}+\frac{\partial(Vf_1)}{\partial\eta}+\frac{\partial(Wf_1)}{\partial\zeta}\right]-\rho U_w L\left[\frac{\partial(z_\zeta f_1)}{\partial\xi}-\frac{\partial(z_\xi f_1)}{\partial\zeta}\right]+z_\zeta S_v
\end{aligned} \tag{4.15}$$

4.2.3 Driving forces for liquid convection and boundary conditions

4.2.3.1 Driving forces

The driving forces for the liquid metal convection considered in the present study are the electromagnetic force, buoyancy force and shear stress due to the surface tension gradient at the weld pool top surface. The electromagnetic force, $\vec{F}^e$, is given as:

$$\vec{F}^e = \vec{J} \times \vec{B} \tag{4.16}$$

where $\vec{J}$ and $\vec{B}$ are the current flux and magnetic field in the workpiece, respectively. In this study, the electromagnetic force is approximated using equations derived for a rectangular domain [26] to simplify the calculation.

Using the Boussinesq approximation, the buoyancy force, $\vec{F}^b$, is given as:

$$\vec{F}^{b} = -\rho\vec{g}\beta(T - T_{ref}) \qquad (4.17)$$

where $\vec{g}$ is the gravity acceleration and is in the negative z or ζ direction, β is the thermal expansion coefficient, T and T_{ref} are the local and arbitrarily selected reference temperatures, respectively. It should be noted that in the calculation of the buoyancy driven flow, only the difference in buoyancy force at two locations is meaningful and not the absolute values of buoyancy force. For instance, considering two points in the weld pool, A and B, the buoyancy forces at the two locations are given as: $\vec{F}_A^b = -\rho\vec{g}\beta(T_A - T_{ref})$, and $\vec{F}_B^b = -\rho\vec{g}\beta(T_B - T_{ref})$, where T_A and T_B are temperatures at locations A and B, respectively. The difference between $\vec{F}_A^b$ and $\vec{F}_B^b$, which drives the liquid flow, is equal to $\rho\vec{g}\beta(T_B - T_A)$. Therefore, the buoyancy driven flow depends only on the spatial variation of temperatures in the weld pool and not the selection of T_{ref}.

The third driving force for the weld pool convection, i.e. the Marangoni shear stress due to the surface tension gradient, is discussed in the boundary conditions for momentum equations.

4.2.3.2 Boundary conditions for momentum equations

The velocities at the weld pool top surface are given as:

$$\vec{v} \cdot \vec{n}_t = 0 \qquad (4.18a)$$

$$\mu\nabla(\vec{v} \cdot \vec{t}_\xi) \cdot \vec{n}_t = f_l\left(\frac{d\gamma}{dT}\right)\nabla T \cdot \vec{t}_\xi \qquad (4.18b)$$

$$\mu\nabla(\vec{v} \cdot \vec{t}_\eta) \cdot \vec{n}_t = f_l\left(\frac{d\gamma}{dT}\right)\nabla T \cdot \vec{t}_\eta \qquad (4.18c)$$

where $\vec{v}$ is the liquid metal velocity, dγ/dT is the temperature coefficient of surface tension, $\vec{n}_t$ is the local unit normal vector to the top surface, and $\vec{t}_\xi$ and $\vec{t}_\eta$ are local unit tangential vectors to the top surface along the ξ and η directions, respectively. Eq. **4.18a** indicates that the normal velocity to the weld pool top surface is zero, while Eqs. **4.18b**

and **4.18c** represent the Marangoni shear stress at the top surface. As shown in Fig. **4.1(b)**, the normal and tangential vectors to the weld pool top surface are given as:

$$\vec{n}_t = \frac{\zeta_x \vec{i} + \zeta_y \vec{j} + \zeta_z \vec{k}}{\sqrt{\zeta_x^{\,2} + \zeta_y^{\,2} + \zeta_z^{\,2}}},\ \vec{t}_\xi = \frac{x_\xi \vec{i} + y_\xi \vec{j} + z_\xi \vec{k}}{\sqrt{x_\xi^{\,2} + y_\xi^{\,2} + z_\xi^{\,2}}},\ \vec{t}_\eta = \frac{x_\eta \vec{i} + y_\eta \vec{j} + z_\eta \vec{k}}{\sqrt{x_\eta^{\,2} + y_\eta^{\,2} + z_\eta^{\,2}}} \quad (4.19)$$

where $\vec{i}$, $\vec{j}$ and $\vec{k}$ are the unit vectors along x, y and z directions, respectively.

The liquid metal velocity at all other surfaces, i.e., bottom, east, west, south and north surfaces, are equal to zero.

4.2.3.3 Boundary conditions for energy conservation equation

As shown in Fig. **4.1(a)**, the heat flux at the top surface, F_t, is given as:

$$\alpha \nabla h \cdot \vec{n}_t = F_t = \frac{IV\eta}{2\pi r_b^2} \exp\left(-\frac{x_h^{\,2} + y_h^{\,2}}{2r_b^2}\right)(\vec{k} \cdot \vec{n}_t) - \sigma\varepsilon\left(T^4 - T_a^{\,4}\right) - h_c(T - T_a) \quad (4.20)$$

where I is the current, V is the voltage, η is the arc efficiency, r_b is the heat distribution parameter, x_h and y_h are the x and y distances to the arc axis, respectively, σ is the Stefan-Boltzmann constant, ε is the emissivity, h_c is the convective heat transfer coefficient, and T_a is the ambient temperature. In Eq. **4.20**, the first term on the right hand side (RHS) is the heat input from the arc defined by a Gaussian heat distribution. The second and third terms represent the heat loss by radiation and convection, respectively. Since the radiation heat loss represents only a very small fraction of the net heat flux at the top surface, the effect of geometry on radiation is neglected, i.e., the view factor for two perpendicular steel plates is assumed to be unity for simplicity. As shown in Fig. **4.1(b)**, the top surface is defined as ζ = constant. Therefore, Eq. **4.20** is transformed into the following equation in the curvilinear coordinate:

$$\left.\frac{\partial h}{\partial \zeta}\right|_t = \frac{\frac{F_t\left\|\vec{V}_t\right\|}{J\alpha} + \frac{\partial h}{\partial \xi} z_\xi + \frac{\partial h}{\partial \eta} z_\eta}{J(z_\xi^2 + z_\eta^2 + 1)} \tag{4.21}$$

where $\vec{V}_t$ is a normal vector to the top surface defined as $\frac{\partial \zeta}{\partial x}\vec{i} + \frac{\partial \zeta}{\partial y}\vec{j} + \frac{\partial \zeta}{\partial z}\vec{k}$ [25], and $\left\|\vec{V}_t\right\|$ is its norm.

For the bottom surface, the heat flux, F_b, is given as:

$$\alpha \nabla h \cdot \vec{n}_b = F_b = h_c(T - T_a) \tag{4.22}$$

where $\vec{n}_b$ is a unit normal vector to the bottom surface. Similar to the heat flux equation at the top surface, Eq. **4.22** is transformed to the following expression in the curvilinear coordinate system:

$$\left.\frac{\partial h}{\partial \zeta}\right|_b = \frac{\frac{F_b\left\|\vec{V}_b\right\|}{J\alpha} + \frac{\partial h}{\partial \xi} z_\xi + \frac{\partial h}{\partial \eta} z_\eta}{J(z_\xi^2 + z_\eta^2 + 1)} \tag{4.23}$$

where $\left\|\vec{V}_b\right\|$ is the norm of a normal vector to the bottom surface.

The temperatures at other surfaces, i.e., east, west, south, and north surfaces are set to the ambient temperature.

4.2.4 Grid system and discretization of governing equations

The governing equations are discretized using the control volume method [27], where the computational domain is divided into small rectangular control volumes, as shown in Fig. **4.2**. A scalar grid point is located at the center of each control volume, storing the values of scalar quantities such as pressure and enthalpy. Velocity components lie at the control volume faces, staggered with respect to scalar locations. For example, both Cartesian v velocity and contravariant V velocity are placed at the south and north faces of a control volume P, as shown in Fig. **4.2**. Thus, the control volumes for

vectors are different from those for scalars. Such an arrangement is extensively used in orthogonal coordinates preventing unrealistic solution of velocity and pressure fields [27]. Discretized equations for a variable are formulated by integrating the corresponding governing equation over the control volumes in the computational domain. A power-law based scheme [27] is used to describe the convective flux at the control volume faces. The final expression can be written in the following general form as:

$$a_P\phi_P = a_E\phi_E + a_W\phi_W + a_N\phi_N + a_S\phi_S + a_T\phi_T + a_B\phi_B + b \qquad (4.24)$$

where a_E, a_W, etc., denote the combined convection-diffusion coefficients and b includes all the source terms.

4.2.5 Modified SIMPLE algorithm for solving discretized equations

The governing equations, i.e., continuity, momentum and energy conservation equations, need to be solved "simultaneously" to obtain temperature and velocity fields. A modified Semi-Implicit Method for Pressure Linked Equations (SIMPLE) [27] is used to solve the discretized equations. The modification takes into account the main feature in the transformed governing equations in the curvilinear coordinate system, i.e., a mixed Cartesian-contravariant velocity components.

4.2.5.1 Discretized momentum equations

As discussed in previous section, the discretized momentum equations are obtained by integrating the momentum equations over the corresponding control volumes. Figure 4.3 shows a control volume for the v velocity which is staggered in the η direction. The discretized equation for v_n can be seen to be:

$$a_n^v v_n = \sum a_{nb} v_{nb} + b + A_n z_\zeta (p_P - p_N) \qquad (4.25)$$

where subscripts n, p, P, N, etc., indicate the location where a variable is evaluated, and A_n is the area of the north face. Similar equations for Cartesian velocity components u and w can be written.

4.2.5.2 Pressure and velocity corrections

Suppose the velocity field at an intermediate step of the iterative solution procedure is given by u^*, v^* and w^*, corresponding to a guessed pressure field p^*. For example, the "starred" v velocity field results from the solution of the following discretized v momentum equation:

$$a_n^v v_n^* = \sum a_{nb}^v v_{nb}^* + b + A_n z_\zeta (p_P^* - p_N^*) \tag{4.26}$$

The correct pressure and velocity fields can be obtained from:

$$p = p^* + p'; \qquad u = u^* + u'; \qquad v = v^* + v'; \qquad w = w^* + w' \tag{4.27}$$

where p', u', v' and w' are corresponding corrections.

Subtract Eq. 4.26 from Eq. 4.25, we have:

$$a_n^v v_n' = \sum a_{nb}^v v_{nb}' + A_n z_\zeta (p_P' - p_N') \tag{4.28}$$

Ignoring the first term on the RHS of Eq. 4.28, the following v velocity-correction formula is obtained:

$$v_n' = \frac{A_n z_\zeta (p_P' - p_N')}{a_n^v} \tag{4.29}$$

Similarly, the u and w velocity-correction formulas are given as:

$$u_e' = \frac{A_e z_\zeta (p_P' - p_E')}{a_e^u} \tag{4.30}$$

$$w_t' = \frac{A_t (p_P' - p_T')}{a_t^w} \tag{4.31}$$

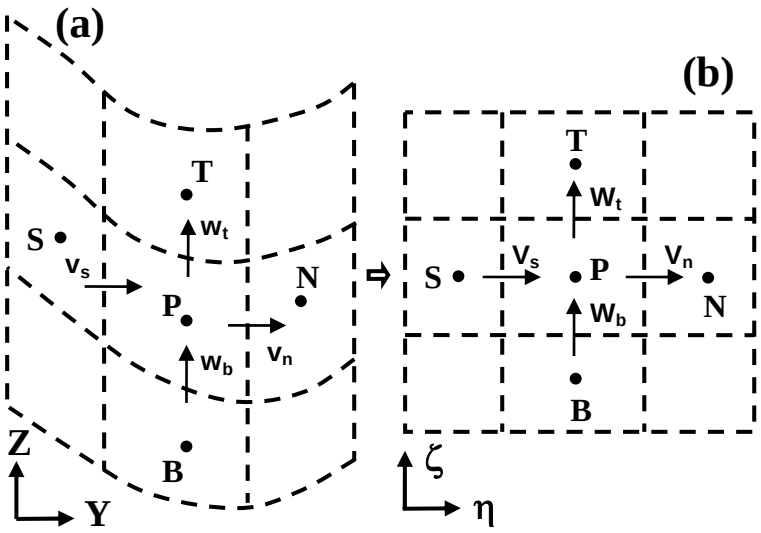

Fig. **4.2**: Grid system in the physical and computational domains. (a) a YZ plane in the physical domain, and (b) the corresponding ηζ plane in the computational domain. Dashed lines represent control volume's interfaces, while solid dots indicate scalar grid points. Symbols W, E, S, N, B, T are the east, west south, north, bottom and top neighbors of the grid point P, respectively, while symbols s, n, b, t are the south, north, bottom and top interfaces of the control volume P.

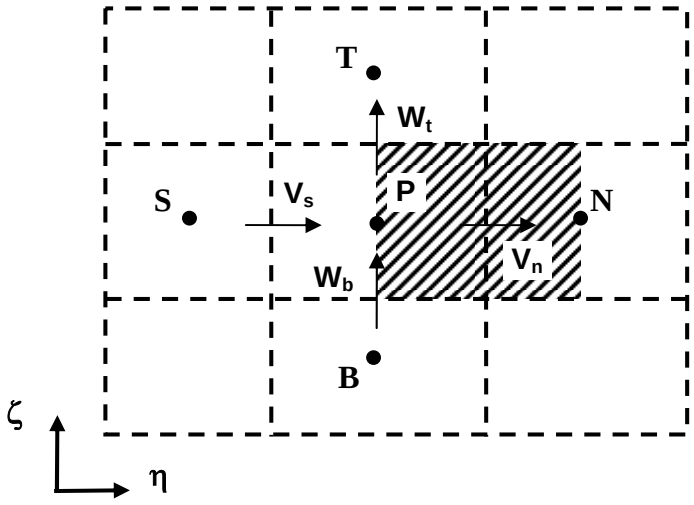

Fig. **4.3**: Control volume for v or V velocity component in the computational domain. For clarity, only the ηζ section is shown.

4.2.5.3 Continuity equation

Substituting Eq. 4.11 into Eq. 4.3, the continuity equation in the curvilinear coordinate can be rewritten as:

$$\frac{\partial(z_\zeta u)}{\partial\xi}+\frac{\partial(z_\zeta v)}{\partial\eta}+\frac{\partial(w-z_\xi u-z_\eta v)}{\partial\zeta}=0 \qquad (4.32)$$

Integrating the above equation over the scalar control volume P shown in Fig. 4.3, the discretized continuity equation is given as:

$$\begin{aligned}&A_e[(z_\zeta u)_e-(z_\zeta u)_w]+A_n[(z_\zeta v)_n-(z_\zeta v)_s]+A_t[w_t-w_b]=\\&A_t[(z_\xi u+z_\eta v)_t-(z_\xi u+z_\eta v)_b]\end{aligned} \qquad (4.33)$$

If we now substitute for all the velocity components the expressions given by the velocity-correction formulas, we obtain, after rearrangement, the following discretized equation for p':

$$a_P p'_P = a_E p'_E + a_W p'_W + a_N p'_N + a_S p'_S + a_T p'_T + a_B p'_B + b_p \qquad (4.34)$$

where

$$a_E = \frac{A_e^2 (z_\zeta)_e^2}{a_e^u} \qquad (4.35a)$$

$$a_W = \frac{A_e^2 (z_\zeta)_w^2}{a_w^u} \qquad (4.35b)$$

$$a_N = \frac{A_n^2 (z_\zeta)_n^2}{a_n^v} \qquad (4.35c)$$

$$a_S = \frac{A_n^2 (z_\zeta)_s^2}{a_s^v} \qquad (4.35d)$$

$$a_T = \frac{A_t^2}{a_t^w} \qquad (4.35e)$$

$$a_B = \frac{A_t^2}{a_b^w} \qquad (4.35f)$$

$$a_P = a_E + a_W + a_N + a_S + a_T + a_B \qquad (4.35g)$$

$$b_p = A_e\left(U_w^* - U_e^*\right) + A_n\left(V_s^* + V_n^*\right) + A_t\left(W_b^* - W_t^*\right) \qquad (4.35h)$$

4.2.5.4 Modified SIMPLE algorithm

The SIMPLE algorithm was originally developed to solve the discretized mass continuity, momentum conservation and energy conservation equations in the rectangular Cartesian domain [27]. In the present study, the SIMPLE algorithm was modified to take into account the mixed Cartesian-contravariant velocity components in the curvilinear coordinate system. The modified SIMPLE algorithm is listed below:

(1) Guess the pressure field p^*.

(2) Solve the discretized momentum equations, such as Eq. **4.25**, to obtain u^*, v^* and w^*. Then, the corresponding contravariant velocity is updated using Eq. **4.11**.

(3) Solve the p' equation, i.e. Eq. **4.34**.

(4) Calculate p using Eq. **4.27** by adding p' to p^*.

(5) Calculate u, v, w from their starred values using the velocity-correction formulas **4.29** to **4.31** and Eq. **4.27**. Then, update contravariant velocity components using Eq. **4.11**.

(6) Solve the discretized energy equation using the latest values of contravariant velocities.

(7) Update the solution domain for the momentum equations and material properties based on the current temperature field.

(8) Treat the corrected pressure p as a new guessed pressure p^*, return to step (2), and repeat the whole procedure until a converged solution is obtained.

4.3 Heat Transfer from Metal Droplets

Molten droplet transfer is one of the characteristics of GMA welding, and it makes the welding process highly productive. There are three basic modes of transferring the molten metal at the feeding wire tip to the weld pool: globular, spray, and short-circuiting [2,28]. Spray transfer mode is often observed at medium and high currents. In this mode, small discrete metal drops travel across the arc gap at high frequency and

speed, which enables highly stable metal transfer and less spatters. For GMA welding of thick workpiece, spray transfer mode is often preferred for its stability and efficiency.

An important feature of the GMA weld bead is the finger penetration mainly caused by the transfer of heat from the superheated metal droplets into the weld pool. For the spray transfer mode, previous research work in butt [29,30] and fillet welding [19] has shown that the droplet heat transfer can be effectively simulated by incorporating a time-averaged volumetric heat source term (S_v) in the energy conservation equation. This approach is also used here, since the welding conditions studied are consistent with those for the spray transfer mode.

4.3.1 Calculation of volumetric heat source

As shown in Fig. 4.4, the volumetric heat source is characterized by its radius (R_v), height (d) and power density (S_v). The height is calculated using the following equation based on kinetic energy balance [2,29]:

$$d = h_v - x_v + D_d \tag{4.36}$$

where h_v is the estimated height of cavity by the impact of metal droplets, x_v is the distance traveled by the center of the slug between the impingement of two successive droplets, and D_d is the droplet diameter. The values of h_v and x_v in Eq. 4.36 are determined as follows [2,29]:

$$h_v = \left(-\frac{2\gamma}{D_d \rho g} + \sqrt{\left[\left(\frac{2\gamma}{D_d \rho g} \right)^2 + \frac{D_d v_d^{\,2}}{6g} \right]} \right) \tag{4.37}$$

$$x_v = \left(h_V + \frac{2\gamma}{D_d \rho g} \right) \left\{ 1 - \cos\left[\left(\frac{g}{h_v} \right)^{1/2} \Delta t \right] \right\} \tag{4.38}$$

where γ is the surface tension of the molten metal, g is the gravitational constant, v_d is the droplet impingement velocity, and Δt is the interval between two successive drops (Δt = 1/f, where f is the droplet transfer frequency).

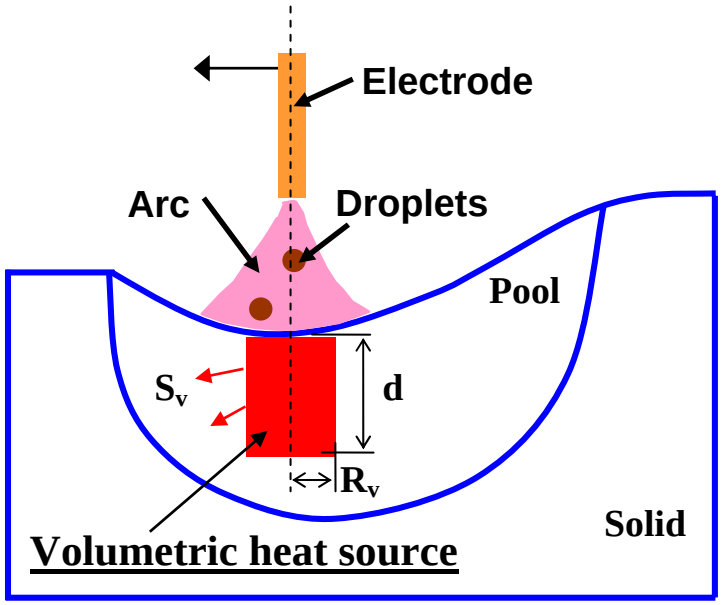

Fig. **4.4**: Schematic plot illustrating the cylindrical volumetric heat source in the weld pool along the longitudinal plane.

The radius of the volumetric heat source is assumed to be twice as the droplet radius [2,29].

The total sensible heat input from the metal droplets, Q_t, is given as:

$$Q_t = \rho \pi r_w^2 w_f H_d \quad (4.39)$$

where ρ is the density, r_w is the radius of the wire, w_f is the wire feeding rate, and H_d is the total enthalpy of the droplets. It should be noted that a portion of Q_t is used to heat the additional metal from the droplets up to liquidus temperature. Therefore, the effective heat of droplets (Q_d) carrying into the weld pool is given as [16]:

$$Q_d = \rho \pi r_w^2 w_f C_{pl} (T_d - T_l) \quad (4.40)$$

where C_{pl} is the specific heat of the liquid metal, T_d is the droplet temperature and is assumed to be 2673 K [31], and T_l is the liquidus temperature. From the computed values of Q_d, D_d and d, the time-averaged power density of the volumetric heat source, S_v, is calculated as following:

$$S_v = \frac{Q_d}{\pi D_d^2 d} \quad (4.41)$$

It should be noted that S_v only applies for scalar grid points within the cylindrical heat source, and the power density is zero outside the cylinder.

As shown in Eqs. 4.36 through 4.38, the calculation of the dimensions of the volumetric heat source requires the knowledge of the droplet transfer frequency, radius and impingement velocity. These parameters are determined from the knowledge base available in the literature for given welding conditions as follows.

4.3.2 Droplet transfer frequency and radius

Rhee [32] and Jones [33] found that the droplet frequency was strongly affected by the welding current under conditions similar to those used in this investigation. The droplet transfer frequency is thus calculated by fitting their experimental results into a

sigmoid function combined with a quadratic function, as shown in Fig. **4.5(a)**. The resulting equation is given as:

$$f = \frac{-243.44}{1+\exp\left(\frac{I-291.086}{6.06437}\right)} + 323.506 - 0.874 \times I + 0.0025 \times I^2 \ \text{(Hz)} \qquad (4.42)$$

where I is the welding current in Ampere.

With the knowledge of the droplet transfer frequency, assuming that the droplets are spherical, the droplet radius r_d is given by:

$$r_d = \sqrt[3]{\frac{3}{4} r_w^{\,2} w_f \Big/ f} \qquad (4.43)$$

where r_w is the radius of the feeding wire, and w_f is the wire feeding rate.

4.3.3 Droplet impingement velocity

The molten droplets detached from electrode wire are accelerated in the arc column mainly by gravity and plasma drag force. If a constant acceleration is assumed, the velocity of droplets impinging the weld pool is given as:

$$v_d = \sqrt{v_0^{\,2} + 2 a_d L_a} \qquad (4.44)$$

where v_0 is the initial droplet velocity, a_d is the droplet acceleration and L_a is the arc length. Eq. **4.44** indicates that the knowledge of v_0, a_d and L_a is required to calculate the droplet impingement velocity. The initial velocity of the droplets is estimated by fitting the experimental results of Lin et al. [**34**] in the following equation:

$$v_0 = \sqrt{-0.33692 + 0.00854\,(I / D_d)} \ \text{(m/s)} \qquad (4.45)$$

where I is the arc current in ampere, and D_d is the droplet diameter in meter.

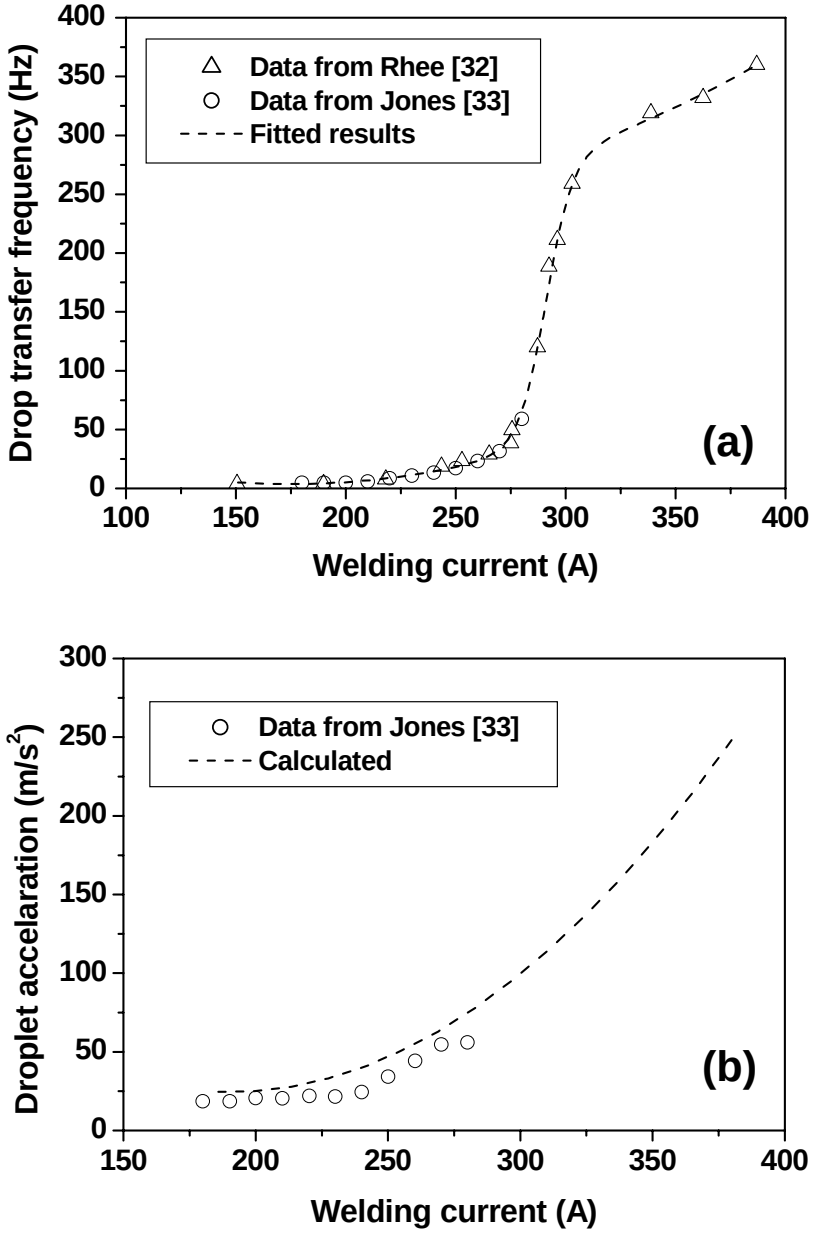

Fig. **4.5**: Calculated droplet characteristics. (a) comparison between the fitted and measured droplet transfer frequency, and (b) comparison between calculated and measured droplet acceleration in the arc column.

In the arc column, the arc plasma flies from the electrode to the workpiece at high speeds [2]. Hence, the droplet in the arc column is pushed by the viscous plasma flow. The droplet is further accelerated by the gravity force. By considering the interaction between the arc plasma and droplet, the acceleration (a_d) due to the plasma drag and gravity forces is expressed as [35]:

$$a_d = \frac{3}{8}\frac{v_g^{\,2}\rho_g}{r_d\rho_m}C_d + g \qquad (4.46)$$

where v_g and ρ_g are the velocity and density of argon plasma, respectively, r_d is the radius of droplet, C_d is the drag coefficient, ρ_m is the density of droplet and g is the gravitational constant. The velocity of argon plasma is calculated using the following equation [2]:

$$v_g = k_1 \times I \qquad (m/s) \qquad (4.47)$$

where k_1 is a constant and a value of 1/4 is used in this study. The other parameters in Eq. **4.46** were calculated using the relationship and data available in the literature [2]. As shown in Fig. **4.5(b)**, the acceleration calculated using Eq. **4.46** is in a good agreement with the corresponding experimental data [33].

The arc length was estimated using the equivalent circuit of GMA welding system. In a steady state, the arc length is given by the following circuit equation [35]:

$$V_{OC} = V_{a0} + (R_S + R_P + R_e + R_a)I + (E_{al} + E_{ai}I)L_a \qquad (4.48)$$

where V_{OC} is the open-circuit voltage, $R_S + R_P$ is the electrical resistance of the welding power source and cable, R_e is the electrical resistance over the electrode extension, V_{a0}, R_a, E_{al} and E_{ai} are coefficients used in Ayrton's equation [35]. These parameters were determined from the data available in the literature [35].

In summary, the impingement velocity is calculated using Eq. **4.44**, with the estimated droplet initial velocity, acceleration and arc length. The droplet impingement velocity, transfer frequency and radius are then used to calculate the dimensions of the cylindrical volumetric heat source, as discussed in the previous section.

4.3.4 Effect of welding parameters on volumetric heat source

The effects of current, voltage and contact tube to workpiece distance (CTWD) on the height of the volumetric heat source are shown in Fig. **4.6(a)**. As shown in this figure, it is found that the height of the heat source arises with both welding current and voltage, while it drops with the increase in CTWD. The influence of current can be understood from its effect on the droplet impingement velocity, which increases with current. The higher impingement velocity, in turn, increases the height of the heat source, as evident from Eq. **4.37**. When the voltage is increased keeping the current constant, both the arc length and the droplet impingement velocity increase. As a result, the height of the volumetric heat source also increases with voltage. With the increase in CTWD the impingement velocity decreases which leads to a reduction of the height of the heat source. This is because the increase in CTWD is accompanied by an increase in the wire feeding rate to maintain a target current. As a consequence, the droplet radius increases and the impingement velocity decreases. It will be shown in the next paragraph that the droplets carry a significant amount of energy into the weld pool for the welding conditions investigated. Under these conditions, the height of the volumetric heat source significantly affects finger penetration, a characteristic of GMA welds.

Fig. **4.6(b)** shows the efficiency of droplet heat transfer (η_d), defined as the ratio of the total sensible heat input owing to metal droplets (Q_t) over the total heat input (IV), i.e., $\eta_d = Q_t/(IV)$. Since the droplet temperature (2673 K) does not change significantly for the welding conditions used in this study [**31**], the droplet heat transfer rate is determined by the wire feeding rate. Therefore, at a given wire feeding rate, the efficiency of droplet heat transfer is inversely proportional to the total heat input, as shown in Fig. **4.6(b)**. On the other hand, the higher the wire feeding rate, the higher the droplet heat transfer efficiency for the same amount of total power input, as evident from Eq. **4.40**. The computed values of the efficiency of droplet heat transfer are found to vary between 28% and 36% for all the cases studied here, which is consistent with the 25±5% value reported in Essers and Walters's experimental measurements [**36**] for similar welding conditions. The entire sensible heat of the droplets is distributed into a small

cylindrical volume directly under the arc, and this distribution of heat is the main reason for the finger penetration observed in the FZ of GMA fillet welds.

4.4 Calculation of Weld Pool Free Surface Profile

At high current, the weld pool surface becomes significantly depressed under the action of arc force [37,38]. In GMA welding, the addition of filler metal by means of metal transfer further displaces the weld pool surface. Therefore, the assumption of a flat pool surface is not appropriate at high currents. A numerical model needs to take into account the depressed surface profile to accurately calculate the heat transfer and fluid flow during GMA fillet welding.

4.4.1 Minimization of total surface energy

At steady state, the top surface profile of the liquid weld pool can be determined using the energy minimization method. The total energy to be minimized includes the surface energy due to the change in area of the pool surface, the potential energy in the gravitational field and the work performed by the arc pressure displacing the pool surface. The following two equations [15,16] are solved to obtain the weld pool surface profile.

$$\gamma\left\{\frac{(1+\phi_y{}^2)\phi_{xx}-2\phi_x\phi_y\phi_{xy}+(1+\phi_x{}^2)\phi_{yy}}{(1+\phi_x{}^2+\phi_y{}^2)^{3/2}}\right\}=\rho g\phi+P_a+\lambda \qquad (4.49)$$

$$\int(\phi_s-z_0)dy-\frac{\pi r_w^2 w_f}{U_w}=0 \qquad (4.50)$$

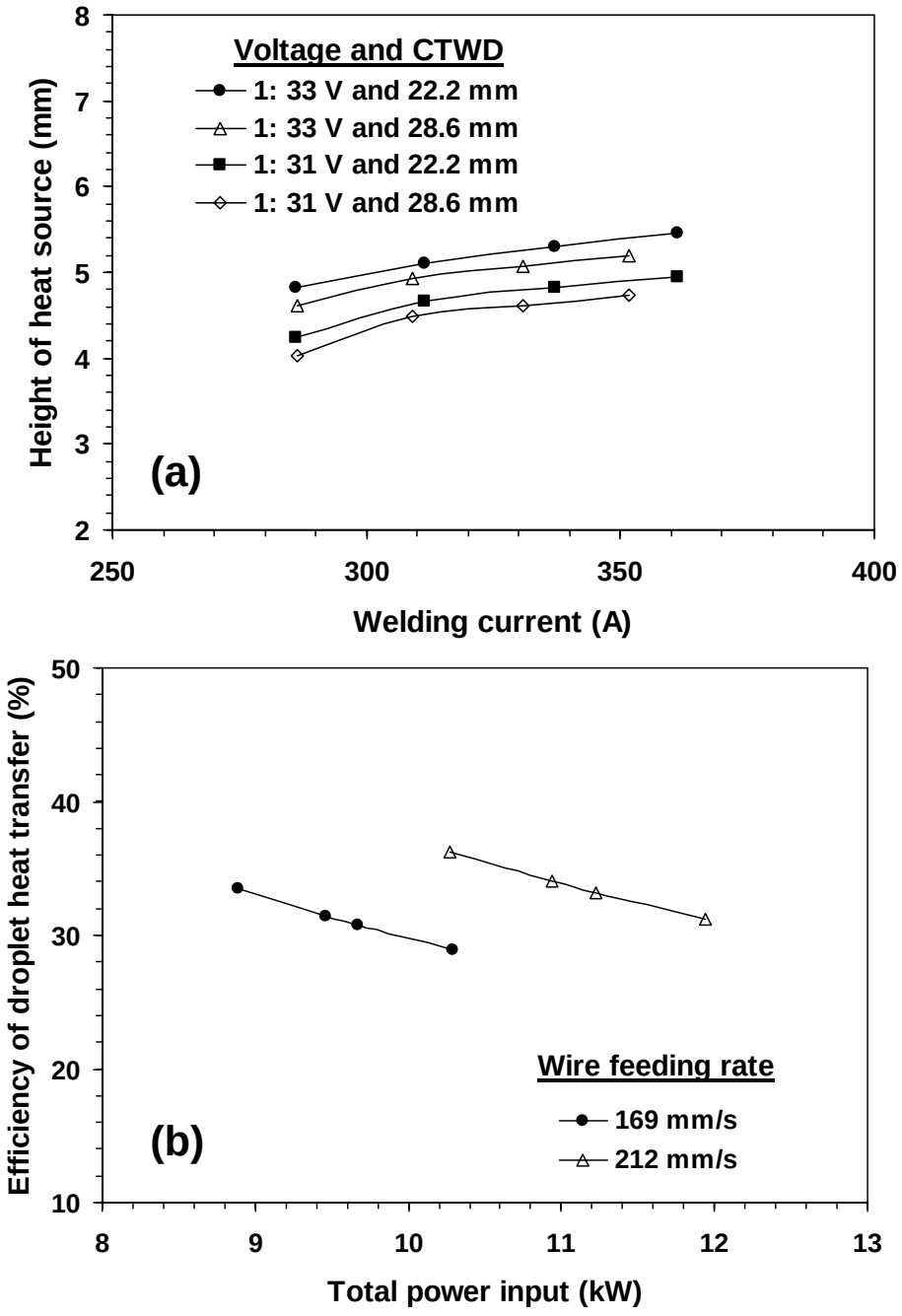

Fig. **4.6**: (a) Calculated height of the volumetric heat source, and (b) calculated efficiency of droplet heat transfer, for various conditions. Symbol CTWD represents the contact tube to workpiece distance. The efficiency of droplet heat transfer is defined as the ratio of the total sensible heat input from metal droplets over the total power input.

In Eq. **4.49**, subscripts x and y represent partial derivatives with respect to x and y, respectively, γ is the surface tension, P_a is the arc pressure distribution at the pool top surface (discussed in the next section), and λ is the Lagrange multiplier. In Eq. **4.50**, r_w, w_f and U_w are the wire radius, wire feeding rate and the welding speed, respectively, and ϕ_s is the solidified surface profile, z_0 is the z location of the workpiece top surface, as shown in Fig. **4.1(a)**. Eq. **4.49** represents the static force balance at the pool top surface, while Eq. **4.50** defines a constraint condition that the deposited area, A_{FW}, at a solidified cross section of the fillet weld is equal to the amount of feeding wire per unit length, as shown in Fig. **4.1(a)**.

The boundary conditions for the free surface equation are given as:

$$\text{At the front pool boundary: } \phi = z_0 \qquad (4.51)$$

$$\text{At the rear pool boundary: } \frac{\partial \phi}{\partial x} = 0 \qquad (4.52)$$

where the front and rear pool boundaries are defined so that the temperature gradient along the x direction (dT/dx) is positive at the front pool boundary and negative at the rear boundary.

To obtain the free surface profile, both Eqs. **4.49** and **4.50** are solved. Eq. **4.49** is discretized using the finite difference method. It is then solved using the Gauss-Seidel point-by-point method [**27**] for an assumed λ with appropriate boundary conditions. The resulting free surface profile is applied to the constraint Eq. **4.50**, and the residual (defined as the left hand side of Eq. **4.50**) is evaluated. The value of λ is determined iteratively using the bisection method [**39**] until both Eqs. **4.49** and **4.50** are satisfied.

4.4.2 Arc pressure distribution

The arc pressure P_a is usually approximated by a Gaussian distribution as [**37**,**38**]:

$$P_a = \frac{F}{2\pi\sigma_p^{\,2}} \exp\left(-\frac{x_h^2 + y_h^2}{2\sigma_p^{\,2}}\right) \qquad (4.53)$$

where F is the total arc force, σ_p is the distribution parameter for arc pressure, and x_h and y_h are the x and y distances to the arc axis, respectively. As shown in Eq. **4.53**, the calculation of arc pressure distribution at the weld pool top surface requires the knowledge of the total force and the distribution parameter. Lin and Eagar [**37**] measured the arc pressure distribution for tungsten electrodes with three different electrode tip angles, i.e. 30°, 60° and 90°. They found that both F and σ_P depended strongly on the welding current. In this study, the relationship of F and σ_P as a function of current was extracted from their experimental data for the three tip angles. For instance, the total arc force was calculated by integrating the measured arc pressure distribution data:

$$F = \int 2\pi r P_a' dr \qquad (4.54)$$

where P_a' is the measured arc pressure at a distance of r from the arc axis. Once the total arc force was obtained, the pressure distribution parameter was then determined by fitting the experimental distribution into Eq. **4.53**.

The calculated total arc force and pressure distribution parameter as a function of welding current (in ampere) are given in the following equations.

$$F = \begin{cases} -0.06049 + 0.0002808 \times I \ (N) & (30^o \text{ tip angle}) \\ -0.04017 + 0.0002553 \times I \ (N) & (60^o \text{ tip angle}) \\ -0.04307 + 0.0001981 \times I \ (N) & (90^o \text{ tip angle}) \end{cases} \qquad (4.55)$$

$$\sigma_P = \begin{cases} 0.7725 + 0.00193 \times I \ (mm) & (30^o \text{ tip angle}) \\ 1.4875 + 0.00123 \times I \ (mm) & (60^o \text{ tip angle}) \\ 1.4043 + 0.00174 \times I \ (mm) & (90^o \text{ tip angle}) \end{cases} \qquad (4.56)$$

These relationships were plotted in Fig. **4.7**, showing that sharp electrode tip results in a concentrated arc pressure distribution. Both total arc force and pressure distribution parameters increase with current. In this study, the calculated σ_P for 60° tip angle was used, while F was taken as the average of those for three tip angles, as follows:

$$F = -0.04791 + 0.0002447 \times I \ (N) \qquad (4.57)$$

$$\sigma_P = 1.4875 + 0.00123 \times I \ (mm) \qquad (4.58)$$

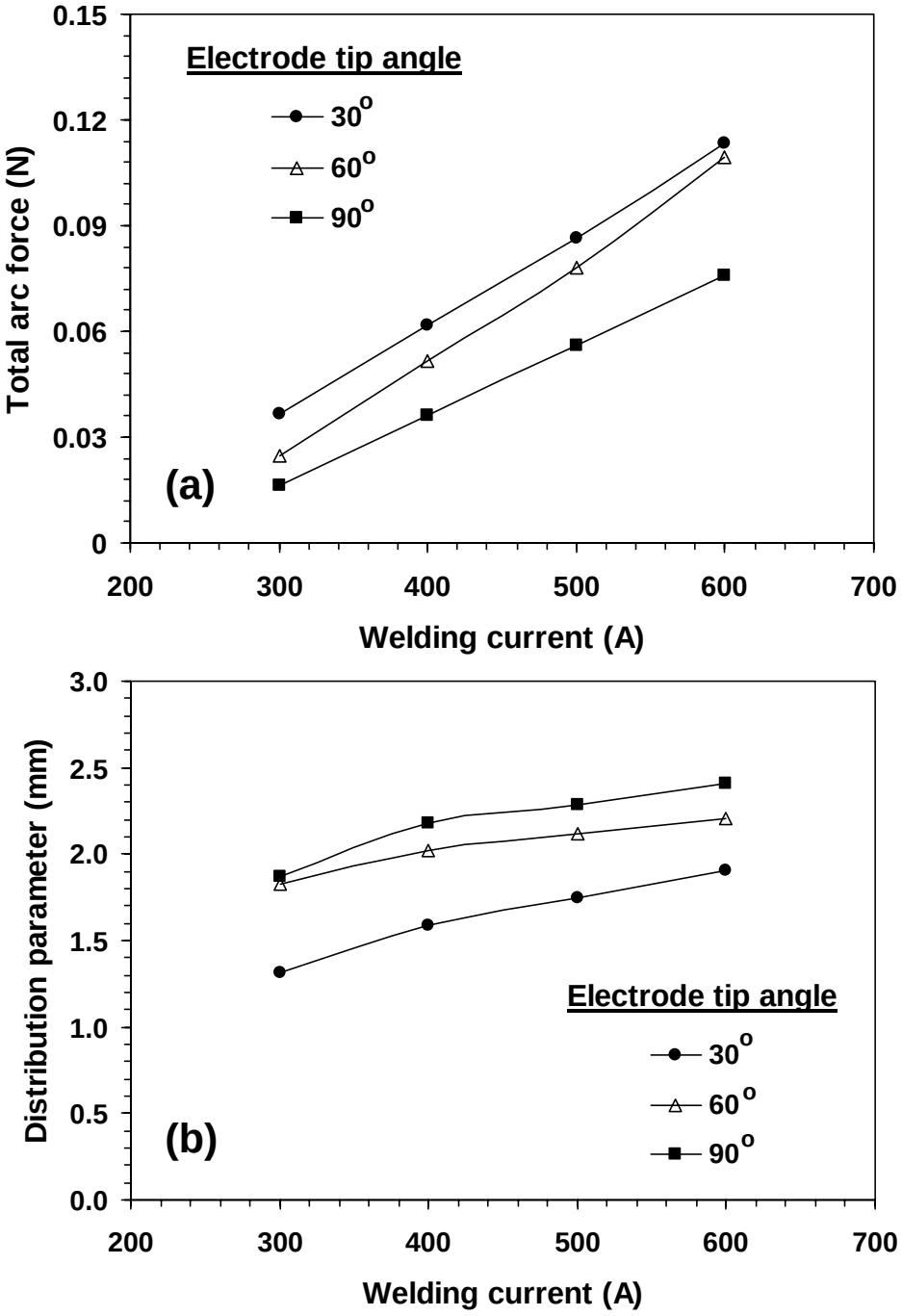

Fig. **4.7**: Calculated (a) total arc force, and (b) arc pressure distribution parameter, as a function of welding current for three different tip angles.

It should be noted that, in the spray transfer model, the droplets impinge on the weld pool surface at high velocities. Such droplet transfer has the following effects. First, the impingement can cause severe deformation of the pool surface. Second, it may result in a downward liquid flow in the center of the weld pool. Finally, the additional heat from the droplets can contribute significantly to the formation of the finger type penetration. In this study, the dynamic impingement of droplets on the weld pool surface is not considered for simplicity. In other words, the computed weld pool surface profile directly under the arc and the liquid convection pattern in the center of the weld pool may not be accurate. However, as it can be shown later, the volumetric heat source can properly simulate the droplet heat transfer, resulting in a good prediction of the FZ geometry.

4.5 Overall Solution Procedure

The governing equations are solved "simultaneously" to obtain the temperature and velocity fields and the free surface profile. Figure **4.8** is a flow chart showing the overall iterative procedure used in the heat transfer and fluid flow model. First, the modified SIMPLE algorithm is used to calculate the temperature and velocity fields. Then, the free surface profile is calculated based on the temperature field obtained in the previous step. After the solution of the free surface profile, the z locations of grids are adjusted to exactly fit the surface profile, and the temperature and velocity fields are then re-calculated in the fitted grid system. The calculation procedure is repeated until converged temperature and velocity fields and free surface profile are obtained.

A 72×66×47 grid system was used and the corresponding solution domain had dimensions of 450 mm in length, 108 mm in width and 18 mm in depth. Spatially non-uniform grids with finer grids near the heat source were used for maximum resolution of variables. The calculations normally converged within 5000 iterations, which took about 30 minutes in a PC with 2.8 GHz Intel P4 CPU and 512 Mb memory. Comparing with the heat transfer model [**19**] which converges in 4000 iterations (about 6 minutes), the heat transfer and fluid flow calculation is much more computationally intensive.

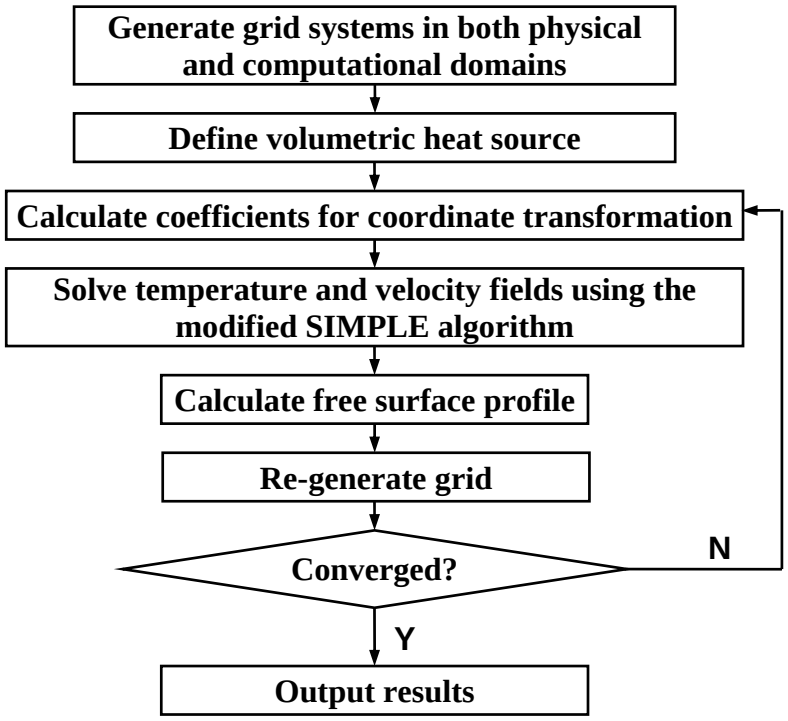

Fig. **4.8**: Schematic diagram showing the overall iterative procedure for the calculation of temperature and velocity fields and surface profile during GMA fillet welding.

4.6 Results and Discussion

The numerical heat transfer and fluid flow model was used for the calculation of temperature and velocity fields for the eight cases listed in Table 4.1. The welding conditions used for these fillet welding experiments are also given in this table. The material properties for the A-36 steel workpiece [40] and the other data used in the calculations are presented in Table 4.2.

Table 4.1: Welding conditions used in the GMA fillet welding experiments.

Case No.	CTWD (mm)	Wire feeding rate (mm/s)	Travel speed (mm/s)	Voltage (V)	Current (A)
1	22.2	169.3	4.2	31	312.0
2	22.2	211.7	6.4	31	362.0
3	22.2	169.3	6.4	33	312.0
4	22.2	211.7	4.2	33	362.0
5	28.6	169.3	6.4	31	286.8
6	28.6	169.3	4.2	33	286.8
7	28.6	211.7	4.2	31	331.4
8	28.6	211.7	6.4	33	331.4

Polarity:	Direct current electrode positive (DCEP)
Joint type:	Fillet joint, flat position, 90° joint angle, and no root gap
Electrode type:	AWS E70S-6, 1.32 mm (0.052 inch) diameter solid wire.
Base metal:	ASTM A-36 mild steel
Shielding gas:	Ar – 10% CO_2
Droplet transfer:	Spray transfer mode

Table 4.2: Physical properties of the A-36 steel [40] and the other data used in the calculation.

Name	Value
Liquidus Temperature, T_l, (K)	1785
Solidus temperature, T_s, (K)	1745
Density of metal, ρ, (kg m^{-3})	7.2×10^{3}
Thermal conductivity of solid, k_s, (J $m^{-1}\cdot s^{-1}\cdot K^{-1}$)	21.0
Enhanced thermal conductivity of liquid, k_l, (J $m^{-1}\cdot s^{-1}\cdot K^{-1}$)	88.2
Enhanced viscosity of liquid metal, μ, (kg m^{-1} s^{-1})	3×10^{-2}
Specific heat of solid, C_{ps}, (J $kg^{-1}\cdot K^{-1}$)	703.4
Specific heat of liquid, C_{pl}, (J $kg^{-1}\cdot K^{-1}$)	808.1
Surface tension of liquid metal at melting point, γ, (N m^{-1})	1.2
Temperature coefficient of surface tension, $d\gamma/dT$, (N $m^{-1}\cdot K^{-1}$)	-3.5×10^{-4}
Magnetic permeability, μ_m, (N A^{-2})	1.26×10^{-6}
Coefficient of thermal expansion, β, (K^{-1})	1.0×10^{-5}
Arc efficiency, η	54%
Arc radius, r_b, (mm)	5.0
Convective heat transfer coefficient, h_c, (W mm^{-2} K^{-1})	42.0
Emissivity, ε	0.7
Ambient temperature, T_a, (K)	298
Constant B in the Carman-Kozeny equation	1.0×10^{-7}
Constant C in the Carman-Kozeny equation	1.6×10^{4}

4.6.1 Convection versus conduction on weld temperature distribution

4.6.1.1 Dimensionless analysis

During welding, the arc energy is transported from the top surface of the weld pool to the surrounding solid region by both heat conduction and liquid metal convection. The rate of the heat flow determines not only the peak temperature and shape of the weld pool but also the temperature distribution in the heat-affected zone (HAZ). Therefore, it is important to understand the effects of conduction and convection on the heat dissipation in the weld pool. The relative importance of convection versus conduction in transferring heat in the pool can be accessed from the value of the Peclet number (Pe), which is given by Eq. 2.19. When Pe is large, which in physical terms means large liquid metal velocity, large weld pool, and poor thermal conductivity, the liquid metal convection significantly affects the heat transfer in the weld pool. In contrast, when Pe is small, say much less than unity, the conduction plays an important role in the heat dissipation in the pool.

Figure **4.9** shows the calculated temperature and velocity fields in a fillet weld. The welding conditions used are those in case #4 (Table **4.1**). For clarity, only half of the workpiece is shown, since the weld is symmetric about the central longitudinal plane containing the welding direction. For the fillet weld shown in Fig. **4.9**, if the average v velocity and the pool width are used as the characteristic velocity and length of the weld pool, respectively, the Peclet number is calculated to be about 120. Since the Peclet number is much larger than unity, the liquid metal convection plays a dominant role in dissipating the heat in the weld pool. In other words, a model, which takes into account only the conduction heat transfer in the pool, is not able to accurately describe the heat transport process in the fillet weld.

4.6.1.2 Convection versus conduction on temperature distribution in weld pool and HAZ

To understand the role of liquid metal convection, weld temperature distributions were calculated using the same welding parameters with and without considering convection. In other words, the effect of convection was ignored in one calculation and considered in the other. Figure **4.10** shows the calculated temperature field at the weld top surface for two cases: one with convection (i.e., heat transfer and fluid flow calculation), and the other without convection (i.e., heat conduction calculation). As shown in Fig. **4.10**, in front of the heat source, the weld pool boundary, represented by the 1745 K isothermal line, expands slightly outward for the case with convection, since the liquid metal flow helps carry heat away from the center to the front boundary. In the solid region ahead of the heat source, the difference in the isothermals between two cases is rather small. This small difference is expected since the isothermals in front of the heat source are largely compressed due to the motion of the heat source (welding speed). As a result, the heating rates are expected to be similar for cases with or without the convection calculation. On the other hand, the isothermals are quite different behind the heat source for the two cases. As shown in Fig. **4.10**, the isothermals are elongated for the case with convection than the one without convection, since the melt convection brings a significant amount of heat energy to the rear part of the weld pool. Therefore, the cooling rates for the case considering convection are expected to be smaller than those without considering convection.

Table **4.3** summarizes some characteristic parameters of the fillet weld pool calculated for various cases. As shown in this table, the peak temperature of the weld pool for the case without convection is 350 K higher than that for the case considering convection. The higher computed peak temperature in the absence of convection is expected, since the liquid metal convection plays a major role in dissipating heat in the weld pool. For the case without convection, the heat dissipation in the pool relies solely on the conduction of heat. Thus, the heat dissipation rate for this case is much slower than the case with convection. Hence, more heat is accumulated in the weld pool and the peak temperature in the weld pool is higher for the case without convection.

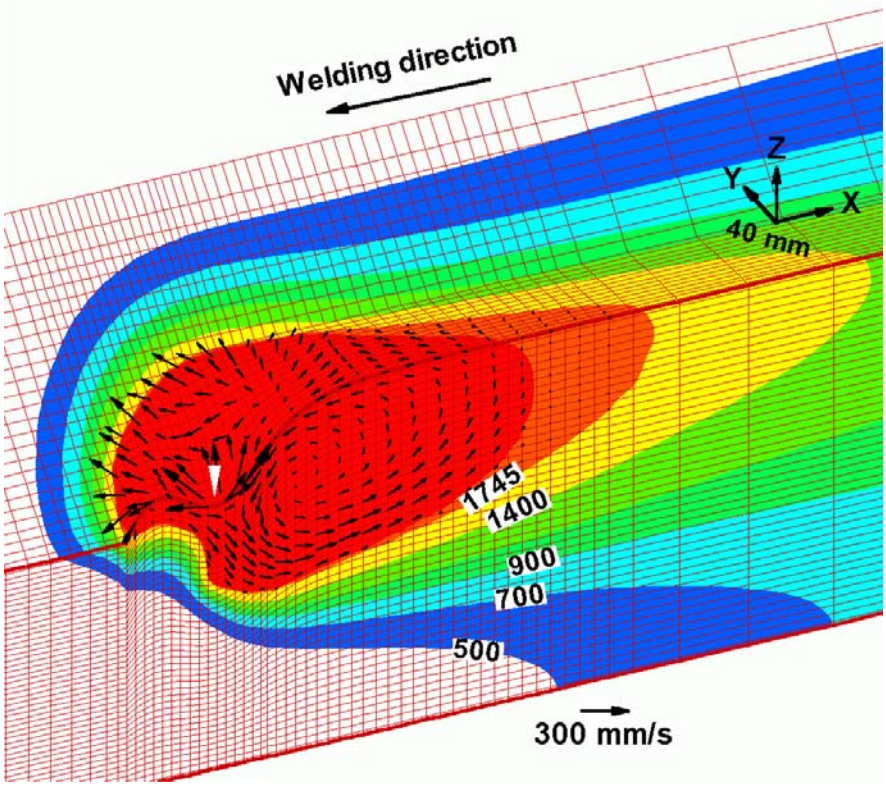

Fig. **4.9**: Calculated temperature and velocity fields in a fillet weld. All the temperatures are given in Kelvin. The white arrow in the middle of the weld pool indicates the location of the heat source. The weld pool boundary is represented by the 1745 K isothermal line. Welding conditions used are those given in case #4 (Table **4.1**).

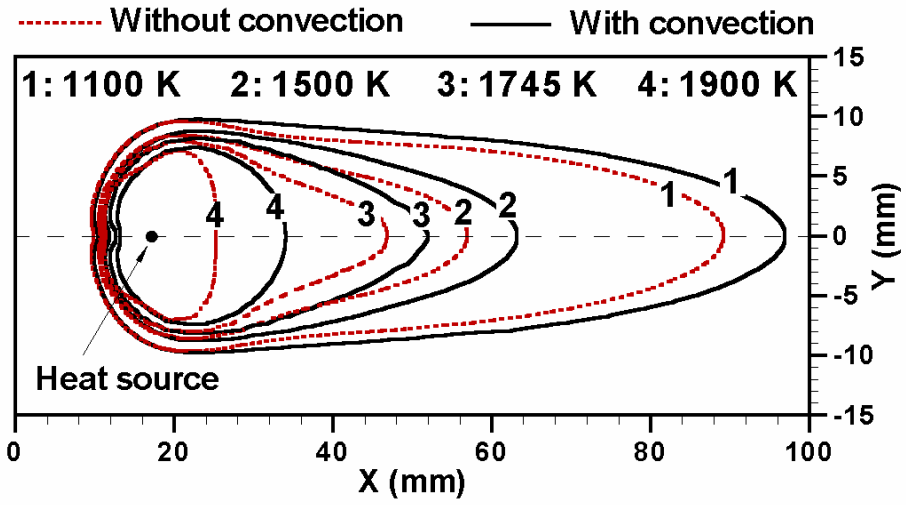

Fig. **4.10**: Calculated temperature distributions at the weld top surface for cases with and without considering convection. Welding conditions are the same as those in Fig. **4.9**.

Table 4.3: Effect of different driving forces on the weld pool characteristics. Symbol T_{peak} represents the peak temperature of the weld pool, while symbols u_{max}, v_{max} and w_{max} represent the maximum velocity (magnitude) in x, y and z directions, respectively.

	T_{peak} (K)	u_{max} (mm/s)	v_{max} (mm/s)	w_{max} (mm/s)	Width (mm)	Depth (mm)
Conduction	2730	0	0	0	17.0	13.2
All three driving forces	2380	352	349	210	17.0	14.0
Marangoni stress	2320	425	382	236	18.3	13.0
Buoyancy force	2700	6.7	6.1	5.7	17.0	13.1
Electromagnetic force	2250	178	177	218	15.4	15.6

4.6.1.3 Convection versus conduction on weld bead shape

Figure 4.11 shows the comparison of the weld bead shape for two cases with and without considering convection. As shown in this figure, the weld bead for case with convection is narrower than that without convection. In other words, the weld bead profile is more rounded for the case without convection, which is due to the fact that the rate of heat conduction is the same in all directions. Figure 4.11 also indicates that the depth of the FZ is deeper for the case with convection. As shown in Fig. 4.9, the liquid metal is driven downwards in the middle of the weld pool by the electromagnetic force. This strong downward flow is responsible for the deeper penetration in the case with convection.

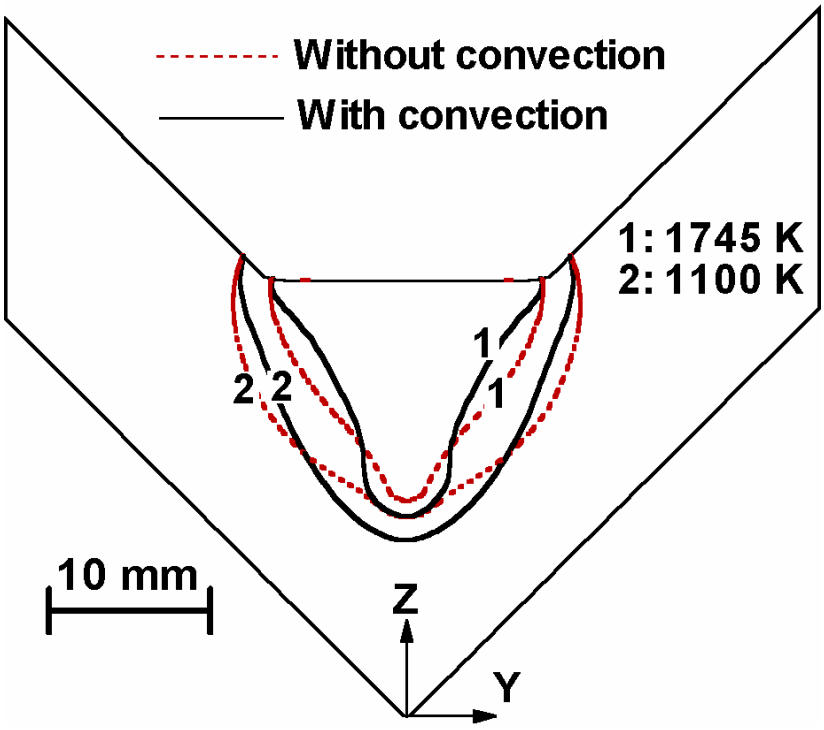

Fig. **4.11**: Comparison of weld bead geometry for cases with and without convection. Welding conditions are the same as those in Fig. **4.9**.

It should be noted that in our previous work [19], we used a heat conduction model, which does not take into account the liquid metal convection, to calculate the weld temperature fields and bead profile. In that heat conduction model, an enhanced thermal conductivity of the liquid metal was used to account for the effect of convection on the heat dissipation in the weld pool. To match the width and depth of the weld bead measured experimentally, the value of the enhanced thermal conductivity used in the calculation was 420 J $m^{-1} \cdot s^{-1} \cdot K^{-1}$ [19]. This value is about 20 times higher than the actual value of the thermal conductivity of liquid metal, which is equal to 21 J $m^{-1} \cdot s^{-1} \cdot K^{-1}$. In our present heat transfer and fluid model, a value of 88.2 J $m^{-1} \cdot s^{-1} \cdot K^{-1}$ was used for the enhanced thermal conductivity. The enhancement is to take into account the effect of turbulence in the weld pool. Figure 4.12 shows the calculated weld bead profiles, which fit the experimental bead profile best, using two models. As shown in this figure, the calculation considering convection (Fig. 4.12(b)) results in a better agreement with the overall experimental bead profile than the one without convection (Fig. 4.12(a)). In other words, although a heat conduction model can simulate the effect of convection by introducing a very high value of thermal conductivity of liquid metal, it is still not possible for it to accurately predict the weld bead geometry. The heat transfer and fluid flow model, although it also relies on the use of the enhanced thermal conductivity to simulate turbulence flow, provides a more realistic description of the physical processes during fillet welding, and thus results in a better prediction of the weld bead profile.

4.6.2 Role of driving forces on liquid metal convection and weld pool shape

During arc welding, more than one type of driving forces act on the liquid metal in the weld pool. Therefore, the fluid flow pattern in the weld pool is a result of a combination of various driving forces. In the present study, three primary driving forces, namely the electromagnetic force, the Marangoni shear stress and the buoyancy force were considered in the calculations.

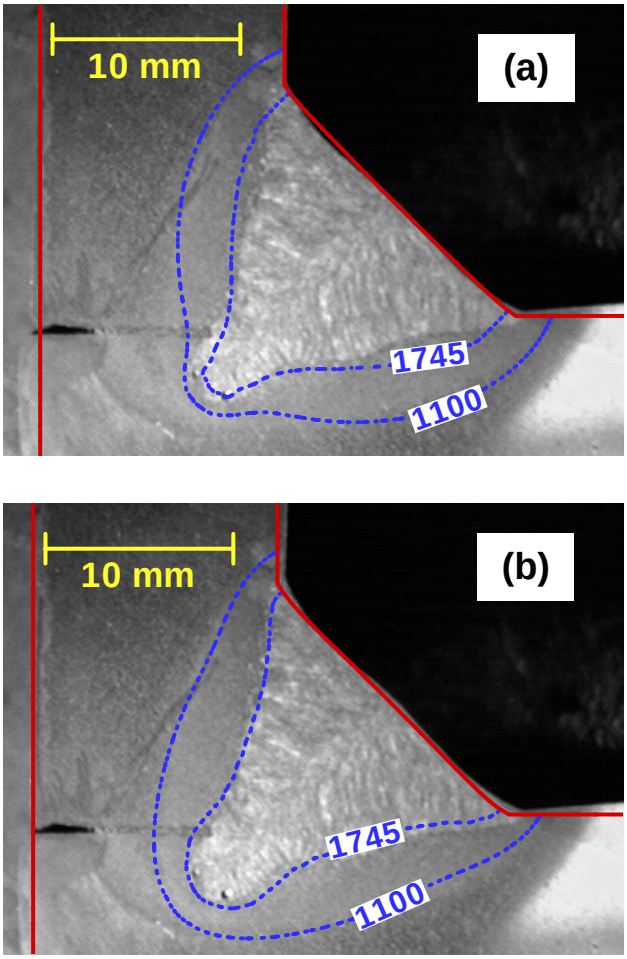

Fig. **4.12**: Comparison between the calculated and measured weld bead profile. (a) Using the heat conduction model with an effective thermal conductivity of 420 J $m^{-1} \cdot s^{-1} \cdot K^{-1}$ [**19**], and (b) using the heat transfer and fluid flow model with an effective thermal conductivity of 88.2 J $m^{-1} \cdot s^{-1} \cdot K^{-1}$. All other input parameters used in the two models are the same. Welding conditions are the same as those in Fig. **4.9**.

The effect of various driving forces on the liquid metal convection and the resulting weld pool shape have been extensively studied for welding of butt joints, i.e., simple rectangular workpiece. However, for welding of fillet joints with complex geometry, the study of the role of the driving forces remains scarce. Since it is rather difficult to separate the effect of the individual driving forces by conducting welding experiments, the numerical heat transfer and fluid flow model and dimensionless analysis were employed to examine their role in fillet welds.

4.6.2.1 Marangoni convection

In butt welds, the Marangoni convection with a negative dγ/dT results in a liquid flow from the center to the periphery at the weld pool top surface and upward flow at the center of the pool [5,21,28]. Figure 4.13 shows the temperature and velocity fields in a fillet weld in the absence of electromagnetic and buoyancy forces. As shown in this figure, the effect of Marangoni shear stress in the fillet weld is similar to that in butt welds. Since the value of dγ/dT is negative for the A-36 steel, the warmer liquid metal has a lower surface tension and vice versa. At the pool top surface, the liquid metal is flowing radically outward, since the warmer liquid metal of lower surface tension near the center of the pool is pulled outward by the cooler metal of higher surface tension at the pool edge. Pushed by the strong outward flow at the top surface, the liquid metal is transported outwards from the middle of the weld pool and arises at the center of the pool. Therefore, along the central longitudinal plane, a clockwise circulation loop is formed behind the heat source while anticlockwise circulation loop exists in front of the heat source, as shown in Fig. 4.13. The anticlockwise circulation is much weaker than the clockwise one behind the heat source. This is because the weld pool is largely compressed in front of the heat source due to the welding speed and the arc pressure, and the liquid flow is significantly restricted there. The compressed weld pool in front of the heat source also constrains the liquid flow resulting from other two driving forces, i.e. the buoyancy and electromagnetic forces, as shown in the following sections.

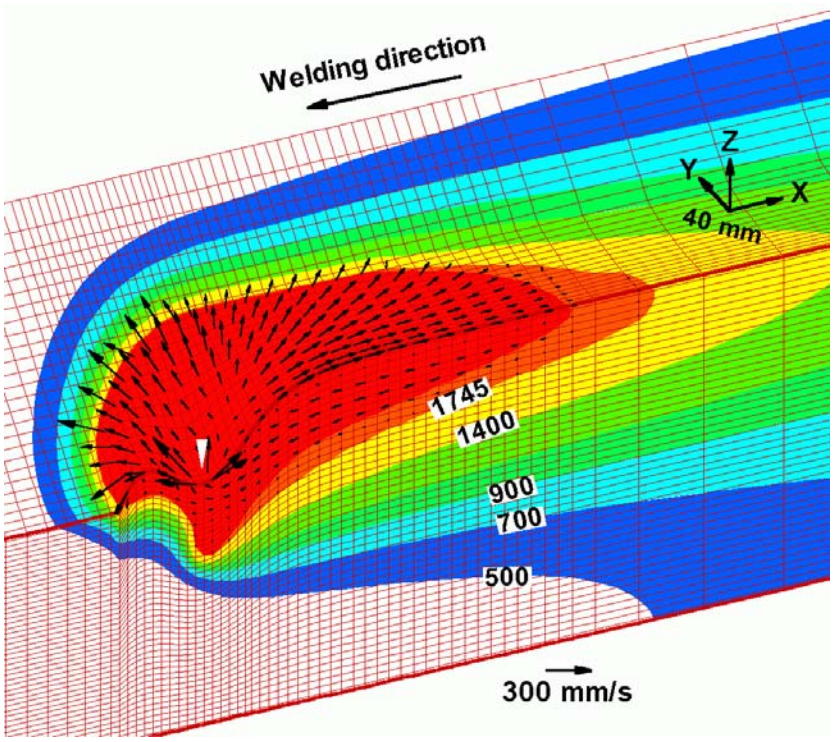

Fig. **4.13**: Marangoni convection with an outward surface flow in a fillet weld pool. The white arrow indicates the location of the heat source. All the temperatures are given in Kelvin. Welding conditions used are those in case #4 (Table **4.1**).

An order of magnitude of the maximum velocity (u_{st}) under Marangoni convection can be estimated by Eq. 2.18 [4]. Using this equation and the physical property data given in Table 4.2, the maximum velocity is estimated to be of the order of 280 mm/s. This value agrees fairly well with that calculated using the heat transfer and fluid flow model, where the maximum velocity was found to be around 420 mm/s. Furthermore, as shown in Fig. 4.13, the maximum velocity is found to be located in front of the heat source at the top surface of the weld pool, since the temperature gradient ahead of the heat source is much higher than that behind it.

Using Eq. 2.19, the Pelect number is found to be around 140 under the effect of Marangoni convection. Therefore, the heat transfer by convection is the dominant mechanism of the heat dissipation in the weld pool, and the convective heat transfer determines the pool shape. Table 4.3 summarizes some weld pool characteristic parameters under the Marangoni convection. As shown in this table, the weld pool is wide and shallow. The depth of the weld pool is even less than that for conduction case. This is because the arc energy input is largely carried away from the center to the periphery of the pool by the strong outward flow at the top surface. The upward flow in the middle of the pool hinders the heat transfer along the depth direction.

4.6.2.2 Buoyancy driven flow

The Boussinesq approximation was used in the calculation of buoyancy driven flow. In other words, the variation in the density of the liquid metal is ignored, except insofar as it gives rise to a buoyancy force, which is also termed as the gravitational force. Figure 4.14 shows the calculated temperature and velocity fields under the buoyancy driven convection. It is found that the flow pattern driven by the buoyancy force in the fillet weld is similar to that in the butt welds. As shown in Fig. 4.14, the liquid metal rises along the pool center with low magnitude and fall along the pool boundary due to the local variation of density. This flow pattern is expected because the liquid metal near the heat source is at a relatively high temperature. It moves upwards because of its relatively low density. On the other hand, the liquid metal near the pool

boundary has relatively low temperature and it flows downward because of its high density [28]. Figure 4.14 clearly indicates a clockwise circulation loop behind the heat source along the central longitudinal plane. The anticlockwise circulation loop in front of the heat source is much weaker due to the constraint of the weld pool there. Overall, the flow pattern resulted from the buoyancy force is similar to that resulted from the Marangoni shear stress, while with a much less magnitude of the flow velocity.

An order of magnitude of the maximum velocity (u_{grv}) under the buoyancy driven flow is given by Eq. 2.16 [41]. Using this equation, the order of the magnitude of the maximum velocity is estimated to be about 30 mm/s. The maximum velocity calculated using heat transfer and fluid flow model is around 7 mm/s, which is about the same order as the value estimated using Eq. 2.16.

For the buoyancy driven flow, the Pelect number calculated using Eq. 2.19 is found to be approximately 0.2. Therefore, the heat transfer by conduction is the dominant mechanism in the heat dissipation in the weld pool. In other words, the convection plays a much less important role in transferring the heat than the conduction does. As shown in Table 4.3, due to the poor heat dissipation in the weld pool, the peak temperature of the pool under gravity driven flow is only slightly smaller than that of the conduction case. The weld pool shape is almost the same as that of the conduction case.

4.6.2.3 Flow driven by electromagnetic force

The electromagnetic force is caused by the electric current field together with the magnetic field it induces in the metal workpiece. Figure 4.15 shows the calculated temperature and velocity fields under electromagnetic convection in a fillet weld. At the center of the weld pool, the liquid metal is driven downwards, whereas at the top surface the melt flows from the periphery to the center of the pool. As a result, a strong anticlockwise circulation loop is formed along the central longitudinal plane of the weld. This flow pattern is expected since the direction of the electromagnetic force is downward and inward. The flow pattern produced by the electromagnetic force is opposite to that induced by the Marangoni shear stress.

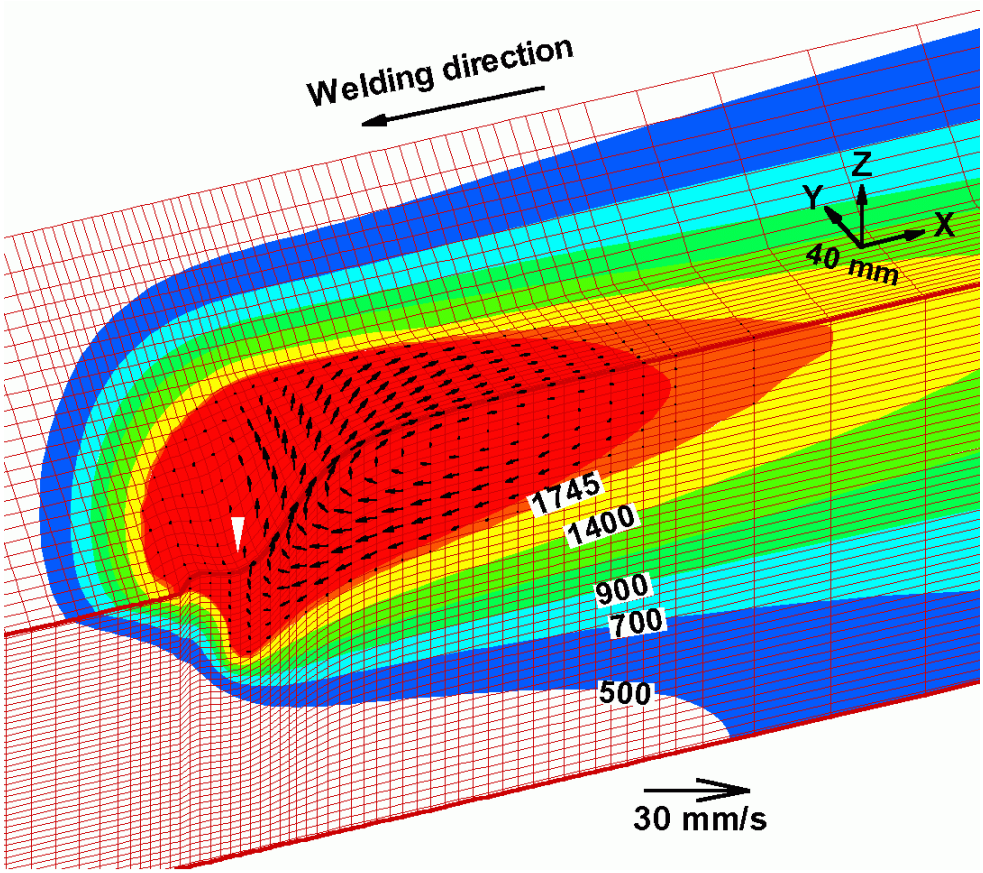

Fig. **4.14**: Calculated temperature and velocity fields under the buoyancy driven convection. Welding conditions are the same as those in Fig. **4.13**.

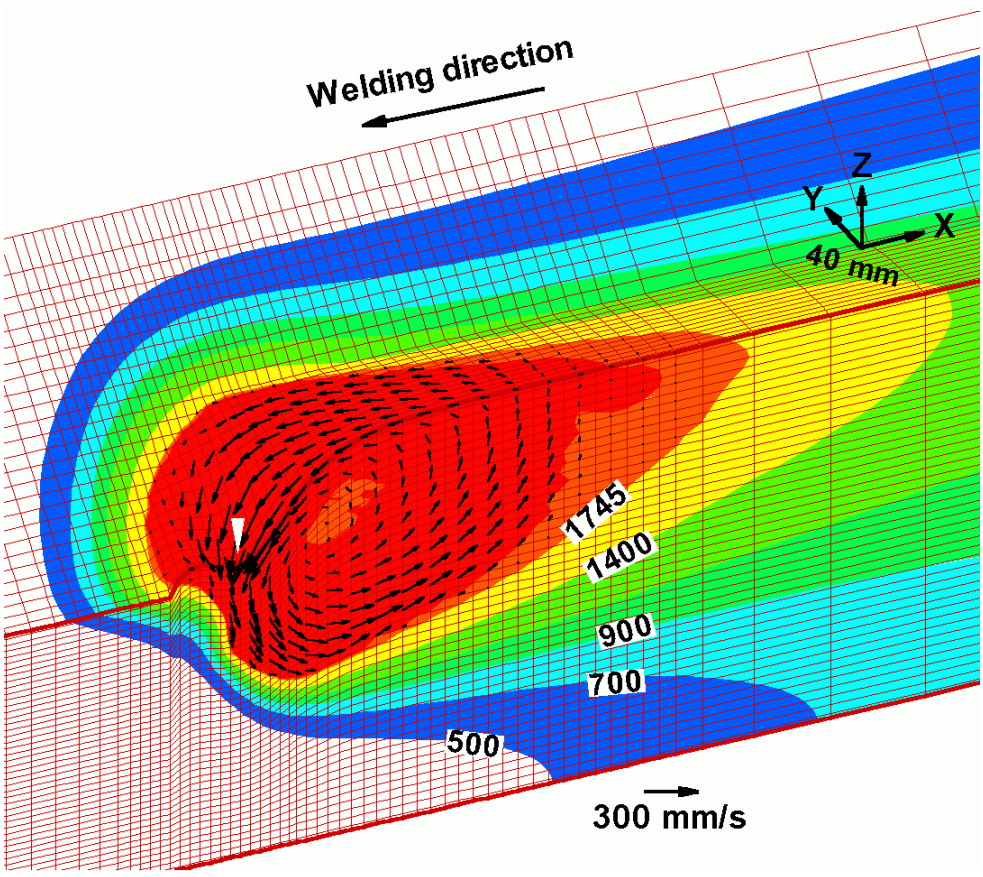

Fig. **4.15**: Calculated temperature and velocity fields under the electromagnetic force driven convection. Welding conditions are the same as those in Fig. **4.13**.

As shown in Fig. **4.15**, the maximum velocity due to the electromagnetic force is located in the middle of the weld pool along the central longitudinal plane. The maximum velocity is found to be 218 mm/s in the fillet weld pool. An order of magnitude calculation of the maximum velocity (u_{emf}) under electromagnetic convection can be done by Eq. 2.17 [**41**]. Using this equation, the magnitude of the maximum velocity is estimated to be around 290 mm/s, which is in a fair agreement with that calculated using the heat transfer and fluid flow model.

The Pelect number for the flow driven by the electromagnetic force is found to be 70 for the fillet weld pool shown in Fig. **4.15**. Therefore, the convection pattern has a strong influence on the heat transfer. The arc energy input is primarily carried from the surface towards the bottom of the weld pool by the downward flow in the middle of the weld pool. The heat energy is then dissipated into the solid region surrounding the weld pool as the flow arises along the pool boundary. Comparing with the weld pool for the Marangoni convection, the width of the pool is decreased while the depth is increased for electromagnetic convection, as shown in Table **4.3**.

4.6.2.4 Relative importance of driving forces

In the foregoing discussion, the role of individual driving forces, i.e. surface tension gradient, electromagnetic and buoyancy forces, is examined. It is also important to know the relative importance of the driving forces on the liquid convection and the weld pool geometry. As discussed in Chapter 2, the relative importance of these driving forces can be estimated using several dimensionless numbers in Eqs. 2.11 to 2.15. Table **4.4** summarizes the computed dimensionless numbers in the GMA fillet weld pool. As shown in this figure, the liquid flow is mainly driven by the electromagnetic and surface tension gradient forces, and to a much less extent, by the buoyancy force. The relative importance of driving forces based on above dimensionless analysis is also consistent with the flow field obtained using the heat transfer and fluid flow model for individual driving forces shown Figs. **4.13**, **4.14**, and **4.15**.

Comparing the dimensionless numbers in the fillet weld pool with those in the GTA spot weld pool shown in Table 3.2 of Chapter 3, the electromagnetic force is found to play more important role in the fillet weld pool, since the welding current used in the GMA fillet welding is much higher than that in GTA spot welding.

Table 4.4: Dimensionless numbers calculated in the GMA fillet weld pool.

Dimensionless number	Description	Value
Gr	Ratio of buoyancy to viscous force	12.0
Rm	Ratio of electromagnetic to viscous force	3.6×10^{4}
Ma	Ratio of surface tension to viscous force	2.9×10^{4}
$R_{M/B}$	Ratio of electromagnetic to buoyancy force	2.9×10^{3}
$R_{S/B}$	Ratio of surface tension to buoyancy force	2.3×10^{3}

4.6.2.5 Combined effect of all the driving forces

The calculated temperature and velocity fields, when all three driving forces are considered, are shown in Fig. 4.9. As shown in this figure, the liquid metal motion is quite complicated due to the combined effects of the driving forces. The electromagnetic force plays a dominant role in driving the liquid metal flow in the weld pool. In the middle of the weld pool, the liquid metal is driven downwards by the electromagnetic force, and a major anticlockwise circulation loop is formed along the central longitudinal plane. In contrast, at the top surface of the weld pool, the Marangoni shear stress drives the melt from the center to the edge of the pool in the region close to the heat source, where the spatial variation of the surface temperature is relatively high. In the rear part of the weld pool, where the temperature gradient is relatively low, the effect of Marangoni

shear stress is less strong than that of electromagnetic force. As a result, the liquid metal flows inward in the rear part of the pool.

4.6.3 Evolution of free surface profile

The free surface profile for case #4 (Table **4.1**) is illustrated in Fig. **4.16**. As shown in this figure, the weld top surface is severely deformed under the arc heat source. The molten metal is pushed to the rear part of the weld pool by the arc force. As a result of the filler metal addition, the solidified weld metal forms pronounced weld reinforcement. The calculated temperature and velocity field and surface profile at various cross sections perpendicular to the welding direction for case #4 is shown in Fig. **4.16**, where the weld pool boundary is represented by the 1745 K solidus isotherm of A-36 steel. Figure **4.16(a)** shows a plane located 6 mm ahead of the heat source, where the base metal has not yet melted. The region directly under the heat source is shown in Fig. **4.16(b)**. The weld pool surface is severely depressed under the effect of the arc pressure, and the liquid metal flows downwards in the middle of the pool driven by the electromagnetic force. As the monitoring location moves away from the heat source, the weld pool surface shows considerably less depression as would be expected from the reduction in arc pressure. Furthermore, the accumulation of the liquid metal in the rear of the weld pool is clearly visible in Figs. **4.16(c)** and **4.16(d)**. This accumulated liquid metal forms the weld reinforcement after solidification. The temperature profile shown in Figs. **4.16(b)** and **4.16(c)** also indicates the fillet weld pool with the characteristic shape of finger penetration during GMA welding.

It should be noted that the liquid metal at the top surface shown in Fig. **4.16(c)** appears to move out of the weld pool. In other words, the normal velocity to the pool top surface seems to be nonzero. This is due to the two-dimensional projection of the three dimensional velocity field is shown. As shown in Fig. **4.9**, the normal velocity is zero at the top surface of the weld pool.

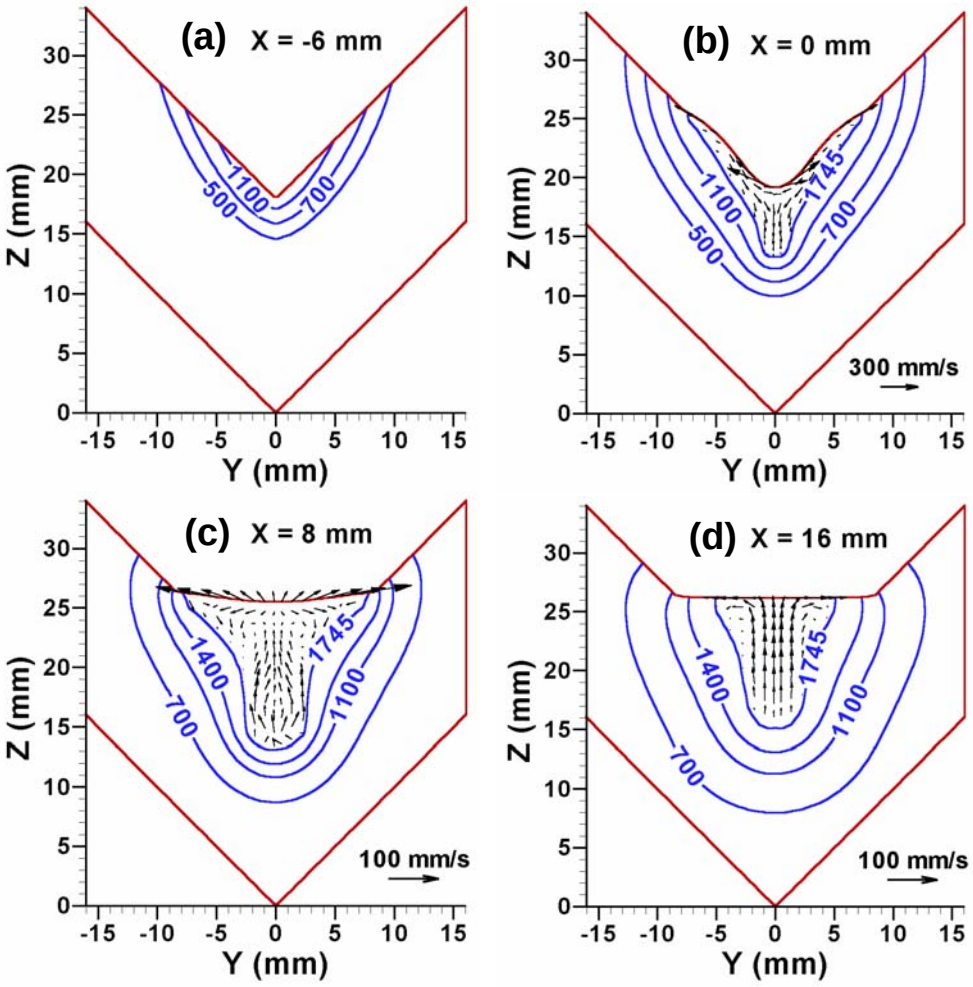

Fig. **4.16**: Calculated temperature field at four cross sections perpendicular to the welding direction. The temperatures are given in Kelvin. The X = 0 plane corresponds to the heat source location. Welding conditions are the same as those in case #4 (Table **4.1**).

4.6.4 Weld thermal cycles

The temperature field obtained from the calculation is at quasi-steady state, since the coordinate system is attached to the heat source moving at a constant welding speed. Therefore, the thermal cycles can be calculated by converting the x distance into time using the welding speed. Figure **4.17** shows the thermal cycles at the top surface of the fillet weld for case #2 (Table **4.1**). Curve 1 is located in the FZ. Curve 2 is located at the fusion boundary. All other curves are located in the HAZ. As shown in Fig. **4.17**, the heating rates are much higher than the cooling rates. This is due to the following two reasons. First, the isotherms in front of the heat source are compressed whereas those behind it are largely elongated due to the high welding speed. Second, the existence of the volumetric heat source also contributes to the high heating rates. As expected, the peak temperatures are higher at locations close to the weld center, and decrease as the monitoring location moves outwards.

In welding of steels, the average cooling rate, $\dot{T}_{8/5}$, from 1073K to 773K (800 °C to 500 °C) is of importance, since it affects the final microstructure of the weld metal for most steels [**42**,**43**]. Figure **4.18** shows the calculated average cooling rates at two monitoring locations, i.e., fusion boundary at the top surface and the joint root, for various welding conditions shown in Table **4.1**. As shown in this figure, the calculated average cooling rate decreases as the heat input per unit length (defined as the total power input / welding speed) increases. The effect of heat input per unit length on $\dot{T}_{8/5}$ can be explained as follows. The average cooling rate $\dot{T}_{8/5}$ is calculated as:

$$\dot{T}_{8/5} = \frac{T_{800} - T_{500}}{t_{8/5}} = \frac{300\, U_w}{\Delta d_{8/5}}$$

where $t_{8/5}$ is the cooling time from 1073K to 773K, U_w is the welding speed and $\Delta d_{8/5}$ is the distance between two points where a line parallel to the x direction intercepts the 1073 K and 773 K isothermal contours.

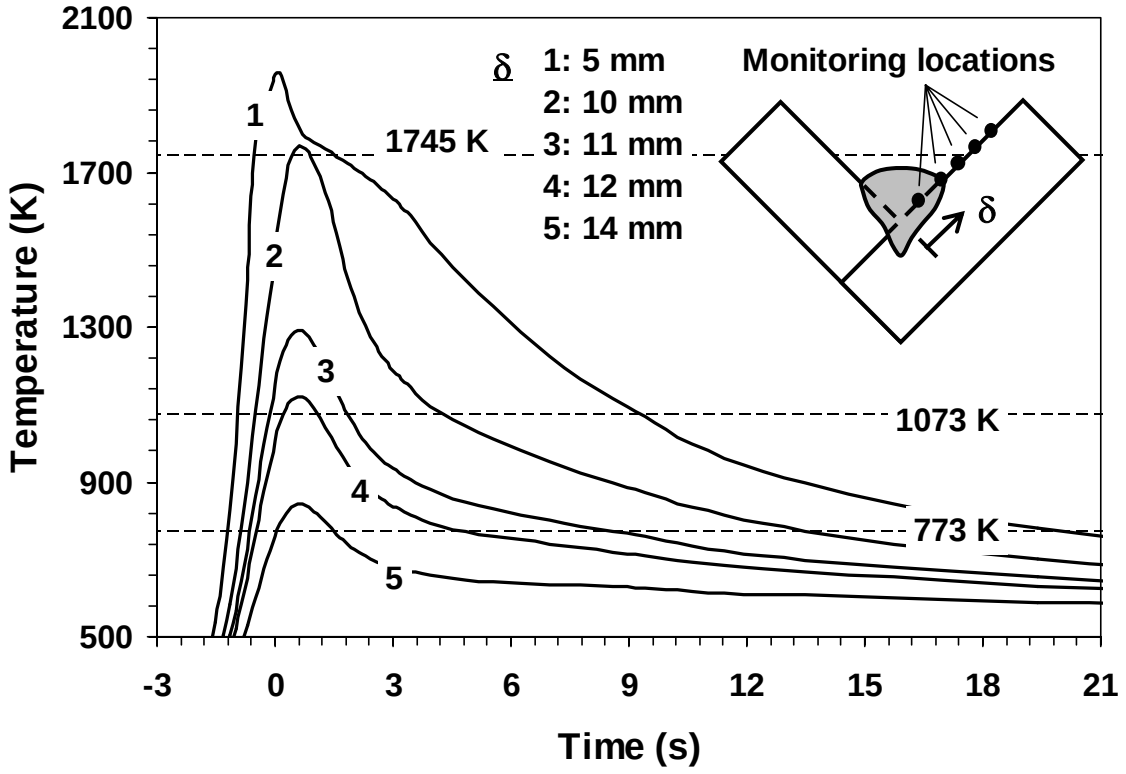

Fig. **4.17**: Calculated thermal cycles in the fillet weld. Symbol δ represents the distance from the joint root to a monitoring location at the top surface, as shown in the small figure. Time zero is arbitrarily set to be correspondent to X = 0 mm location.

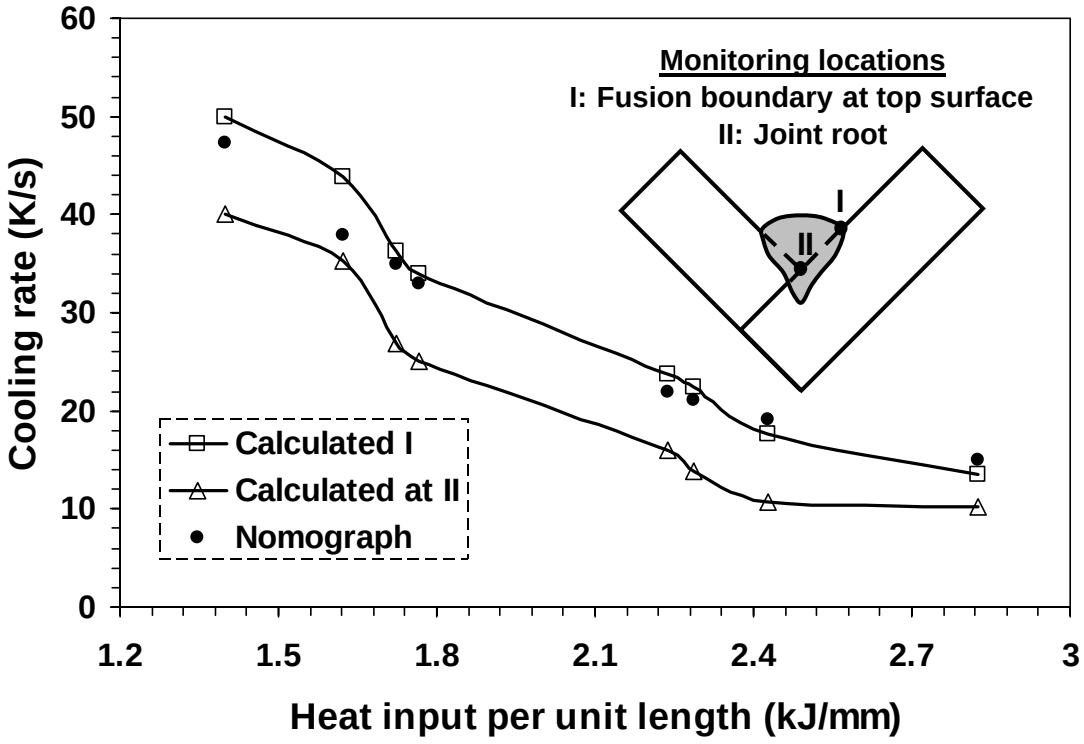

Fig. **4.18**: Calculated average cooling rate $\dot{T}_{8/5}$ at two monitoring locations in the fillet weld for various welding conditions. The solid dots represent the cooling rate estimated using the nomograph available in the literature [**44**].

We can first consider the changes in the cooling rate resulted form an increase in welding speed. As the U_w increases, both the 1073 K and 773 K isothermals expands outwards. However, the distance $\Delta d_{8/5}$ does not change significantly. As a result, the cooling rate increases. Since an increase in U_w is accompanied by a reduction in the heat input per unit length, a reduction in heat input is thus accompanied by an increase in the cooling rate, as observed in Fig. **4.18**. On the other hand, when the welding speed is kept constant and the power input is increased, the isotherms are expanded and $\Delta d_{8/5}$ increases. Hence, the cooling rate decreases with an increase in the power input. Since both a decrease in the welding speed and an increase in the power input result in a decline in the cooling rate, the higher the heat input per unit length, the lower the cooling rate $\dot{T}_{8/5}$.

Figure **4.18** also indicates that the average cooling rates at the joint root are smaller than those at the fusion boundary of the top surface. This is because the heat is conducted more easily at the top surface than at the central plane. In the literature, a cooling rate nomograph [**44**] is commonly used to estimate the average cooling rate $\dot{T}_{8/5}$ for various welding conditions. As shown in Fig. **4.18**, the calculated cooling rates at the fusion boundary agree reasonable well with those estimated using the nomograph. This good agreement indicates the validity of the fillet heat transfer and fluid flow model. Furthermore, the heat transfer and fluid flow model is capable of providing much more information on cooling rates than the nomograph, such as the spatial variation of the cooling rate.

4.6.5 Weld bead geometry and solidified surface profile

Figure **4.19** shows the calculated weld bead shape for all the eight cases listed in Table **4.1**. As shown in this figure, the calculated weld bead geometry for all cases agrees reasonably well with the corresponding experimental results. In particular, the shape of the weld reinforcement and the finger penetration could be satisfactorily predicted by the model. Comparing with the results calculated using the heat transfer model in our previous work [**19**], the present heat transfer and fluid flow model provides a better

agreement with the experimental weld bead profile. It should be noted that some discrepancy between the experimental bead profile and the computed results are observed in Figs. **4.19(c)**, **4.19(g)** and **4.19(h)**. Part of this discrepancy is contributed by the thermal stress induced distortion, as can be evidenced by the gap between the two perpendicular plates.

Since the weld bead geometric characteristics affect the mechanical properties of the fillet weld, the effect of various welding parameters on the weld bead shape were studied. Figure **4.20** shows three important geometrical parameters of the weld bead, i.e. the leg length, penetration and the actual throat as a function of the welding current. As shown in this figure, both the experimental data and the computed results show that the geometrical parameters increase with the current. Furthermore, the computed results and the experimental data show a reduction in all these dimensions with an increase in the welding speed. As shown in Fig. **4.21**, these three geometric parameters are also plotted as a function of heat input per unit length. It is observed that only the leg length increases continuously with the increase in heat input. The data for the penetration and actual throat are segregated into clusters with identifiable welding speeds.

Figures **4.20** and **4.21** indicate that the leg length depends strongly on the heat input per unit length, while the penetration is affected largely by the welding current. The dependence of the leg length and penetration on welding parameters can be explained as follows. For a fillet weld (such as the one shown in Fig. **4.19(a)**,), the arc energy input is primarily responsible for the formation of the top part of the weld bead, whereas the volumetric heat source is largely responsible for the formation of the finger penetration (i.e., lower part of the weld bead). As the heat input per unit length increases, more base metal is melted in the weld cross section and the leg length thus increases. On the other hand, the dimensions and the power density of the volumetric heat source are more sensitive to the welding current. Therefore, as the welding current arises, the penetration also increases. As for the actual throat, it can be approximately determined from a combination of the leg length and penetration based on geometric consideration. Hence, the actual throat results from a combination of the heat input per unit length and current.

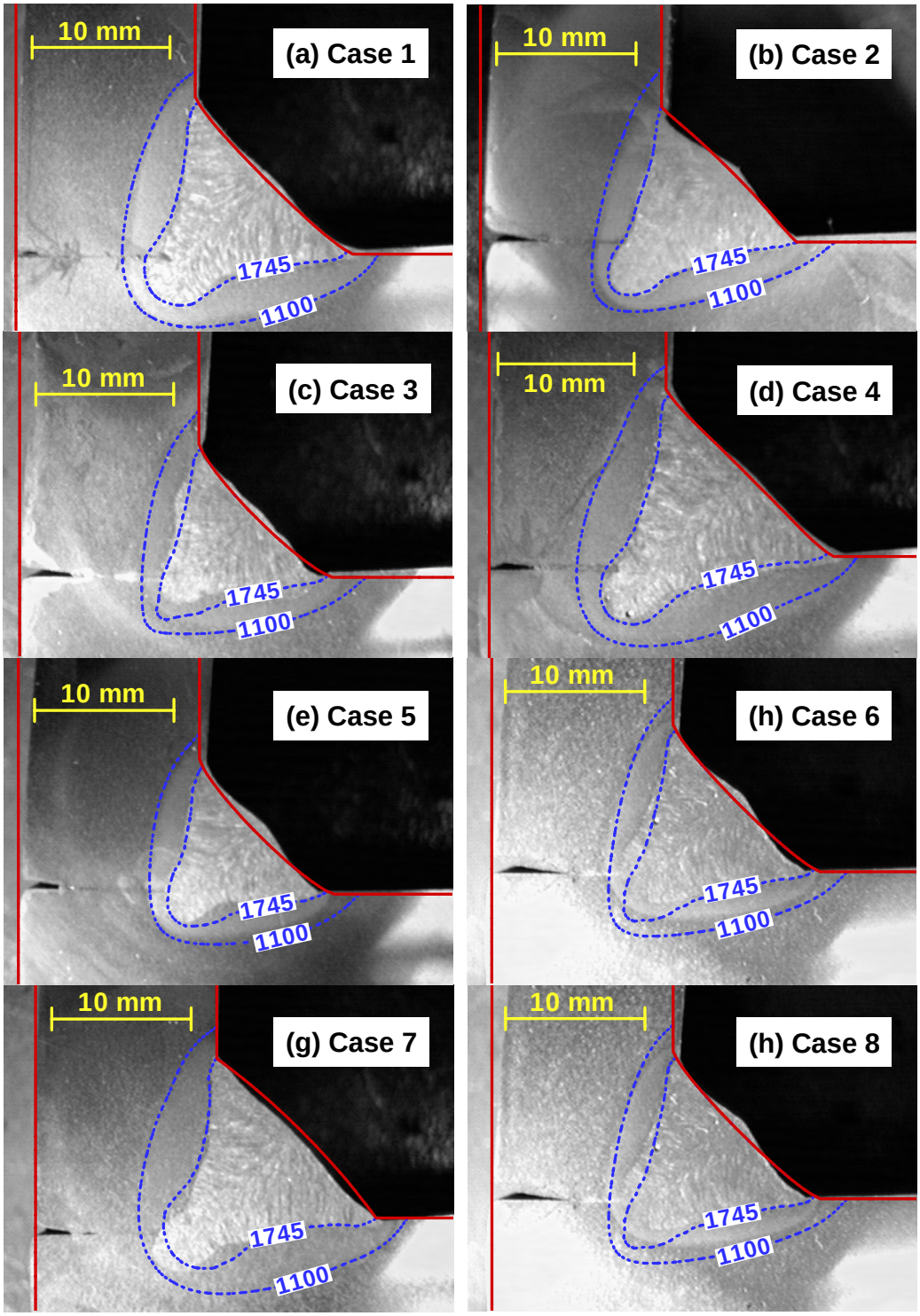

Fig. **4.19**: Comparison between the calculated and experimental weld geometry for different cases given in Table **4.1**. The 1745 K solidus isotherm represents the calculated weld pool boundary.

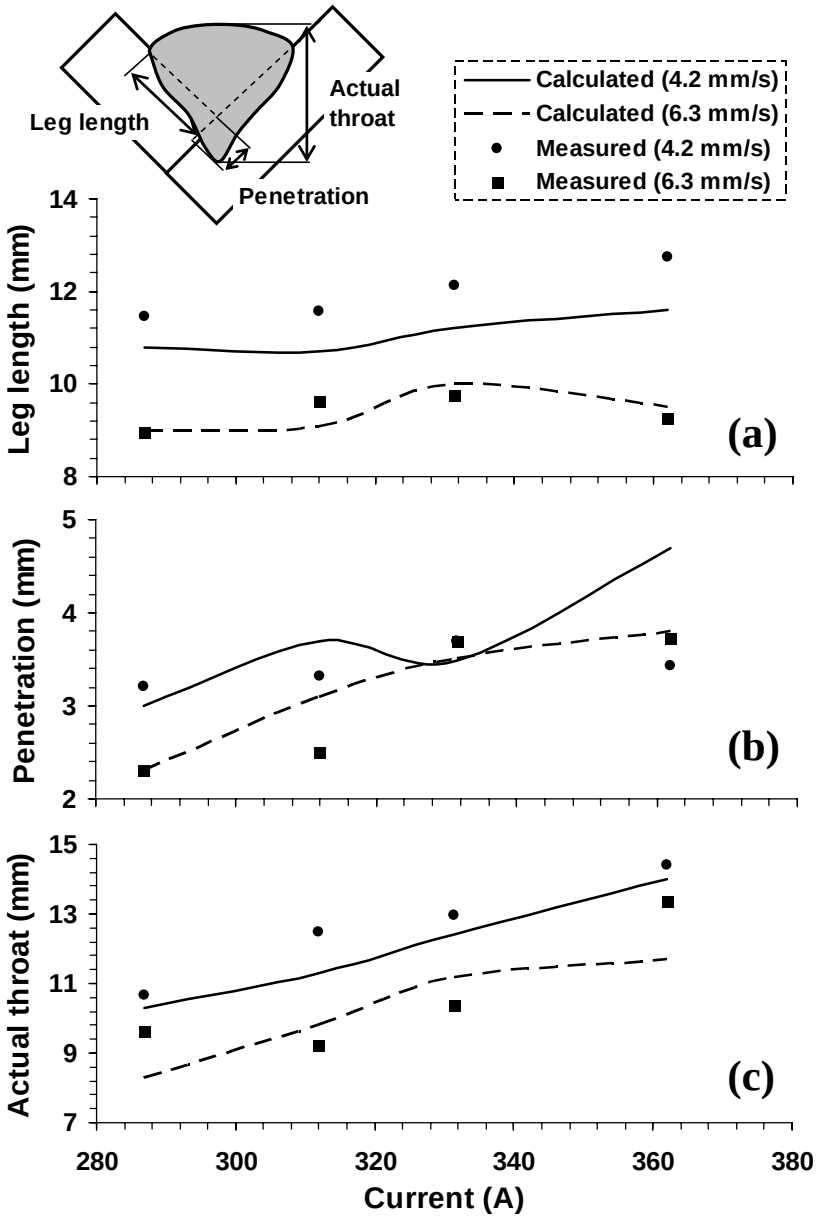

Fig. **4.20**: Weld bead geometric parameters as a function of the current and welding speed: (a) leg length, (b) penetration, and (c) actual throat.

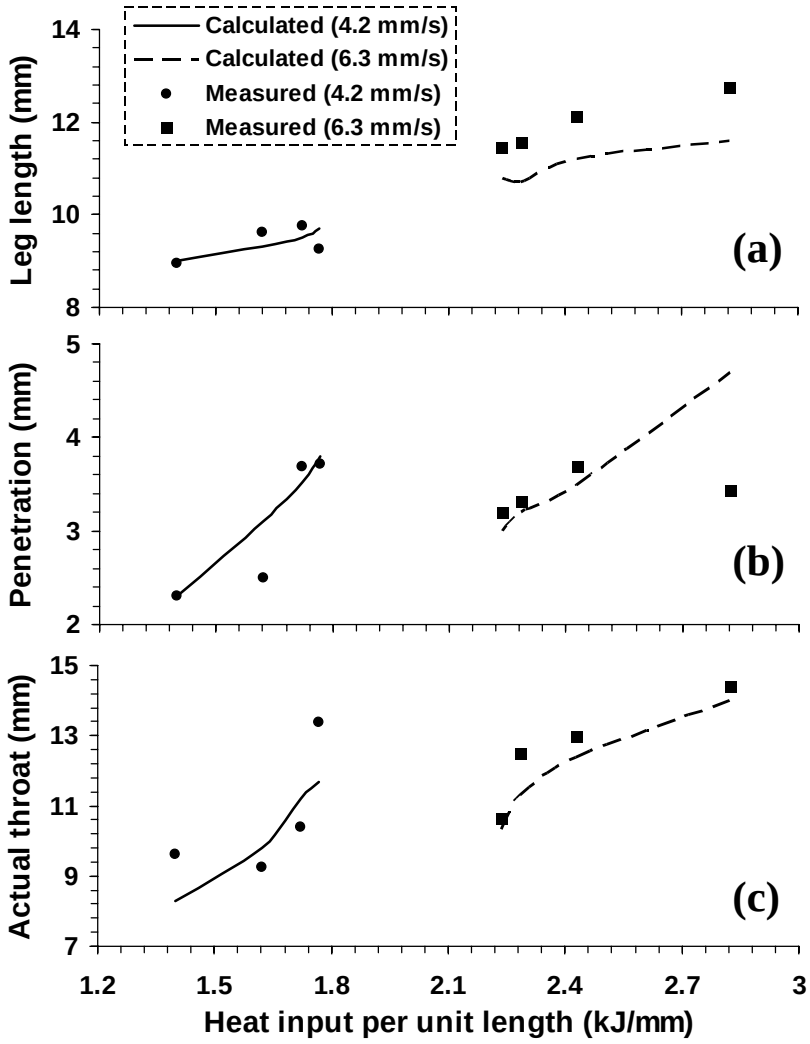

Fig. **4.21**: Weld bead geometric parameters as a function of the heat input per unit length and welding speed: (a) leg length, (b) penetration, and (c) actual throat.

As shown in Fig. **4.20** and **4.21**, the average difference between the calculated and the measured values for the leg length, the penetration and the actual throat were found to be 5.5%, 9.5% and 8.0%, respectively. These numerical values are to be interpreted with caution because of the limited volume of experimental data and lack of any statistically significant index of the quality of the experimental data. In summary, the trends and values of the geometric variables of the fillet weld could be satisfactorily predicted by the numerical heat transfer model within the range of values of the welding variables investigated.

4.7 Summary and Conclusions

A three-dimensional numerical heat transfer and fluid flow model was developed to calculate the temperature profiles, velocity field, weld pool shape and size and the nature of the solidified weld pool reinforcement surface during GMA welding of fillet joints. The numerical model was used to study GMA fillet welding of A-36 steel. The following conclusions can be drawn from the results.

(1) The numerical model solves the continuity, momentum conservation and energy conservation equations in a boundary fitted coordinate system. The governing conservation equations and the corresponding boundary conditions were transformed into the curvilinear coordinate system and then discretized in a simple rectangular computational domain. A modified SIMPLE algorithm was used to simultaneously solve the discretized equations to obtain the temperature and velocity fields.

(2) The liquid metal convection plays dominant role in dissipating the heat in the weld pool. The melt convection determines the temperature distribution and shape of the weld pool. Heat transfer and fluid flow calculation results in not only a more realistic description of the heat transfer process in the weld pool but also provides a better agreement with experimental weld bead profile than the heat transfer calculation alone.

(3) The role of various driving forces for the liquid metal convection was examined using both the dimensionless analysis and the numerical model. It is found that the liquid metal is driven mainly by the electromagnetic force and the Marangoni shear

stress and, to a much less extent, by the buoyancy force. The flow pattern resulted from different driving forces in fillet welds is similar to that in butt welds.

(3) The heat transfer from metal droplets was simulated using a volumetric heat source. A procedure was established to calculate the radius, height and power density of the volumetric heat source based on the experimental data for GMA welding available in the literature. Such procedure took into account the droplet characteristics such as the droplet radius, temperature and impingement velocity.

(4) The weld pool surface profile was calculated by minimizing the total surface energy, which includes the surface tension energy, gravity potential, and work done by arc force. The dynamic impingement of droplets on the weld pool surface was not considered for simplicity. As a result, in the vicinity of the weld pool center, the predicted pool surface profile may be less displaced than that under the influence of droplet impingement. However, at the rear part of the weld pool, the predicted surface profile is expected to be reasonable, since the effect of droplet impingement in that region is small.

(5) Both the experimental results and the model predictions indicate that the average cooling rate between 1073 and 773 K decreased with increase in heat input per unit length. The calculated cooling rates were also in good agreement with independent experimental data.

(6) The numerically computed fusion zone geometry, finger penetration characteristic of the GMA welds and the solidified surface profile of the weld reinforcement were in fair agreement with the experimental results for various welding conditions. The leg length, penetration and actual throat were found to increase with the increase in welding current. All these parameters decreased with the increase in welding speed. The predicted values of these three geometric parameters agreed well with those measured experimentally.

The results reported in this chapter indicate a significant promise for understanding and control of GMA fillet welding processes based on fundamental principles of transport phenomena. The information obtained using the numerical model, such as the weld bead geometry and thermal cycles in the weldment, can be used to

further understand the weld properties and structure. In particular, the microstructure in the FZ and HAZ can be effectively studied by the combination of phase transformation models and computed thermal cycles. Applications of the computed thermal cycles to examine the microstructural evolution in several important steel systems are presented in the Chapters 5 and 6.

4.8 References

1. ASM Handbook: *Welding, Brazing and Soldering*, volume 6, ASM International, Materials Park, OH, 1995.

2. J. F. Lancaster: *The Physics of Welding*, 2nd Edition, Pergamon, Oxford, 1986.

3. S. A. David and T. DebRoy: *Science*, **257**, 497 (1992).

4. T. DebRoy and S. A. David: *Rev. Mod. Phys.*, **67**, 85 (1995).

5. T. DebRoy and S. Kou: *Heat Flow in Welding*, Chapter 3, Welding Handbook, vol. 1, 9th Edition, American Welding Society, p. 87, 2001.

6. M. C. Tsai and S. Kou: *Weld. J.*, **69**, 241s (1990).

7. X. He, P. W. Fuerschbach and T. DebRoy: *J. Phys. D: Appl. Phys.*, **36**, 1388 (2003).

8. K. Mundra, T. DebRoy, and K. Kelkar: *Numer. Heat Transfer A*, **29**, 115 (1996).

9. Z. Yang, J. W. Elmer, J. Wong, and T. DebRoy: *Weld. J.*, **79**, 97s (2000).

10. Z. Yang, S. Sista, J. W. Elmer, and T. DebRoy: *Acta Mater.*, **48**, 4813 (2000).

11. A. Kumar and T. DebRoy: *J. Appl. Phys.*, **94**, 1267 (2003).

12. T. Hong, W. Pitscheneder and T. DebRoy: *Sci. Technol. Weld. Joining*, **3**, 33 (1998).

13. S. Mishra and T. DebRoy: *Acta Mater.*, **52**, 1183 (2004).

14. C. S. Wu and L. Dorn: *Comput. Mater. Sci.*, **2**, 341 (1994).

15. J. W. Kim and S. J. Na: *Weld. J.*, **74**, 141s (1995).

16. Z. N. Cao and P. Dong: *J. Eng. Mater. Technol.*, Trans. ASME, **120**, 313 (1998).

17. H. G. Fan and R. Kovacevic*: J. Phys. D: Appl. Phys.*, **31**, 2929 (1998).

18. Y. Wang and H. L. Tsai: *Metall. Mater. Trans. B*, **32B**, 501 (2001).

19. C.-H. Kim, W. Zhang and T. DebRoy: *J. Appl. Phys.*, **94**, 2667 (2003).

20. P. Sahoo, T. DebRoy and M. J. McNallan: *Metall. Trans. B*, **19B**, 483 (1988).

21. W. Pitscheneder, T. DebRoy, K. Mundra, and R. Ebner: *Welding J.*, **75**, 71s (1996).

22. V. R. Voller and C. Prakash: *Int. J. Heat Mass Transfer*, **30**, 2690 (1987).

23. A. D. Brent, V. R. Voller and K. J. Reid: *Numer. Heat Transfer A*, **13**, 297 (1988).

24. K. A. Hoffmann and S. T. Chiang: *Computational Fluid Dynamics for Engineering – Volume II*, Engineering Education System, Wichita, KS, USA, 1993.

25. J. F. Thompson, Z. U. A. Warsi and C. Wayne Mastin: *Numerical Grid Generation: Fundamentals and Applications*, Elsevier Science, New York, 1985.

26. S. Kou and D. K. Sun: *Metall. Trans. A*, **16A**, 203 (1985).

27. S. V. Patankar: *Numerical Heat Transfer and Fluid Flow*, Hemisphere Publishing, New York, 1982.

28. S. Kou: *Welding Metallurgy*, 2nd edition, John Wiley & Sons, Hoboken, New Jersey, 2003.

29. S. Kumar and S. C. Bhaduri: *Metall. Mater. Trans. B*, **25B**, 435 (1994).

30. Z. Yang and T. DebRoy: *Metall. Mater. Trans. B*, **30B**, 483 (1999).

31. G. Jelmorini, G. W. Tichelaar and G. J. P. M. Van den Heuvel: *IIW Document 212-411-77*, International Institute of Welding, London, 1977.

32. S. Rhee and E. Kannatey-Asibu, Jr.: *Weld. J.*, **71**, 381s (1992).

33. L. A. Jones, T. W. Eagar and J. H. Lang: *J. Phys. D: Appl. Phys.*, **31**, 107 (1998).

34. Q. Lin, X. Li, and S. W. Simpson: *J. Phys. D: Appl. Phys.*, **34**, 347 (2001).

35. C.-H. Kim and S.-J. Na: *Proc. Instn. Mech. Engrs.*, **215B**, 1270 (2001).

36. W. G. Essers and R. Walter: *Weld. J.*, **60**, 37s (1981).

37. M. L. Lin and T. W. Eagar: *Metall. Trans. B*, **17B**, 601 (1986).

38. Y. S. Kim and T.W. Eagar: *Weld. J.*, **70**, 20s (1991).

39. W. H. Press, B. P. Flannery, S. A. Teukolsky and W. T. Vetterling: *Numerical recipes in FORTRAN*, 2nd edition, Cambridge University Press, Cambridge, 1992.

40. E. A. Brandes and G. B. Brook: *Smithells Metals Reference Book*, 7th Edition, Butterworth-Heinemann, Oxford, 1992.

41. G. M. Oreper and J. Szekely: *Metall. Trans. A*, **18A**, 1325 (1987).

42. K. Easterling: *Introduction to the Physical Metallurgy of Welding*, 2nd Edition, Butterworth-Heinemann, Oxford, 1992.

43. Ø. Grong: *Metallurgical Modeling of Welding*, 2nd edition, The Institute of Materials, London, 1997.

44. K. Masubuchi: *Analysis of Welded Structures*, Pergamon, Oxford, 1980.

Chapter 5

MODELING OF PHASE TRANSFORMATIONS IN 1005 STEEL, 1045 STEEL AND TI-6AL-4V ALLOY ARC WELDS

The welding-induced microstructural changes such as grain growth and phase transformation alter the grain size, phase ratios and microstructural morphologies in the welded region [1-4]. The degree to which the microstructure is altered depends on the weld thermal cycle and the kinetics of the various transformations that take place. The loss of material properties can be severe if the microstructure of the base material is significantly changed. Understanding the evolution of microstructure during welding is crucial for obtaining structurally sound welds.

Comprehensive modeling of phase transformations under welding conditions requires the knowledge of phase transformation theory as well as thermal cycles in the weldment. Since experimental measurements of weld temperature history are cumbersome and inaccurate [5,6], a practical recourse is to utilize transport phenomena based models to obtain such information. As discussed in Chapters 3 and 4, the numerical heat transfer and fluid flow models developed at Penn State can be used to accurately calculate the weld geometry and the temperature distribution in the entire weldment under both transient and steady-state conditions. In this chapter, the phase transformation models and computed thermal cycles are used to quantitatively investigate phase transformation kinetics during gas tungsten arc (GTA) welding. Three systems are examined: AISI 1005 low-carbon steel, 1045 medium-carbon steel and Ti-6Al-4V alloy.

In this chapter, the microstructural evolution in the 1005 steel, 1045 steel and Ti-6Al-4V arc welds are studied by a combination of experiments and modeling. The three-dimensional heat transfer and fluid flow model developed at Penn State was used to calculate the temperature and velocity fields, thermal cycles, and the geometry of the fusion zone (FZ). A X-ray diffraction technique using synchrotron radiation was used to map the phases presented at the surface of the welds by Elmer et al [7-10]. The X-ray diffraction data were further analyzed to obtain relative fraction of phases during

important phase transformations. A kinetic model based on the Johnson-Mehl-Avrami (JMA) theory was developed to study the phase transformations controlled by the nucleation and growth mechanism. The JMA model was used to study the kinetics of the α-ferrite→γ-austenite transformation in the 1005 and 1045 steels, and the α-Ti→β-Ti transformation in the Ti-6Al-4V alloy. A set of kinetic parameters used in the JMA equation were determined from the kinetic data measured using the X-ray diffraction technique, which allow quantitative calculation of the rates of phase transformations under different heating conditions.

This chapter is divided into three parts, and each part presents the investigation of phase transformations in one of the three alloy systems. In the first part, the microstructural evolution in the 1005 steel arc welds was examined. In particular, the α-ferrite to γ-austenite transformation during heating, the γ-austenite grain growth, and the reverse γ-austenite to α-ferrite transformation during cooling were studied. The second part focused on the α-ferrite to γ-austenite transformation during heating in the 1045 steel transient arc welds. In the third part, the kinetics of the α-Ti→β-Ti transformation in the Ti-6Al-4V alloy under transient welding conditions were examined.

5.1 Microstructural Evolution during GTA Welding of 1005 Steel

A series of phase transformations take place in both the FZ and the heat affected zone (HAZ) during welding of low carbon steels. The microstructural history of the FZ is α-ferrite→γ-austenite→δ-ferrite→liquid→δ-ferrite→γ-austenite→α-ferrite, while the typical microstructural evolution path in the HAZ is α-ferrite→γ-austenite→α-ferrite. The α→γ transformation during heating is of importance because the grain size, phase fraction and concentration homogeneity of transformed γ phase affect the kinetics of subsequent γ grain growth and phase transformations during cooling [11,12]. On the other hand, the weld integrity and performance are largely affected by the solidification of liquid metal in the weld pool. However, the final microstructure in the weldment is fairly complex because the solid-state γ→α transformation can significantly alter the

solidification microstructure [1-4]. Therefore, during welding of low carbon steels, the $\alpha \rightarrow \gamma$ transformation during heating, the γ grain growth, and the $\gamma \rightarrow \alpha$ transformation during cooling are three important transformation steps.

While the need for better understanding of the transformation kinetics is well recognized, the use of conventional methods, such as dilatometry, to study the phase transformation kinetics during welding is inherently difficult. First, the conventional methods are indirect in that they measure a certain change in the welded sample (e.g. changes in length) and cannot directly determine the phases present during the test [13]. Furthermore, the conventional methods cannot easily resolve the spatial distribution of phases during welding [13]. Because of these problems, progress in this field has been slow and quantitative kinetic data pertaining to phase transformations in important alloy systems under welding conditions still remain scarce.

A recently developed spatially resolved x-ray diffraction (SRXRD) technique using synchrotron radiation can largely overcome those difficulties. During welding of steels, partial and complete transformations to α-ferrite, γ-austenite, and δ-ferrite phase regions have been identified using this technique with sufficient spatial resolution to identify the spatial location of these phases [7,8,13-16]. Thus, this newly developed technique is useful to investigate phase transformations during welding of steels.

The spatial phase distribution map determined by x-ray diffraction technique is specific for a given set of welding conditions. When the welding parameters are changed, a new set of time consuming experiments may need to be undertaken to obtain the phase distribution map. Therefore, for quantitative understanding of the results from the x-ray diffraction experiments, mathematical modeling is needed. The phase distribution map under a given set of welding conditions can be analyzed using mathematical models. Such analysis results in some kinetic parameters, which enable prediction of phase distribution maps under various welding conditions. Mathematical modeling combined with the real-time experimental results is effective in studying the kinetics and mechanisms of phase transformations during welding.

In this study, a combination of experiments and modeling was used to investigate the microstructural evolution during GTA welding of the 1005 steel, particularly the $\alpha \rightarrow \gamma$

transformation during heating, the γ grain growth, and the γ decomposition during cooling. The weld thermo-fluid model was used to compute the thermal cycles, which were then used in the kinetic models to simulate various transformations during both weld heating and cooling. A JMA equation was used to analyze the unique SRXRD kinetic data of the α→γ transformation, and a set of kinetic parameters were determined. These parameters were useful not only to quantitatively describe the α→γ transformation kinetics, but also to provide insights about the mechanism of austenite nucleation from the ferrite matrix. A Monte Carlo (MC) model [17,18] was utilized to calculate the γ grain growth kinetics after the completion of the α→γ transformation in the HAZ. The γ decomposition during cooling has been examined by Bhadeshia et al. [19-22]. For a known cooling rate, their model provides a quantitative description of the final microstructure in the FZ resulting from the γ→α transformation. Using the computed cooling rate from the thermo-fluid model, the final weld microstructure was calculated using their model. The computed volume fractions of allotriomorphic and Widmanstatten ferrites were compared with those determined by the quantitative microscopy.

5.1.1 Experimental procedure

5.1.1.1 Welding

AISI 1005 steel bar of 10.8 cm diameter was used in the GTA welding experiments. The composition of as-received bar was (by wt%): 0.05 C, 0.31 Mn, 0.18 Si, 0.11 Ni, 0.10 Cr, 0.009 P, 0.008 Cu, 0.005 S, <0.005 Al, <0.005 Nb, <0.005 Mo, <0.005 Ti, <0.005 V, and bal. Fe [7]. GTA welds were made on steel bars using a constant power of 1.9 kW (110 A, 17.5 V) with a W-2%Th welding electrode measuring 4.7 mm in diameter. High purity (99.999%) helium was used as both the welding and shielding gases. The steel bar was rotated below the fixed electrode at a constant speed of 0.11 rpm, which corresponds to a surface welding speed of 0.6 mm/s. Additional details about the welding procedure are reported in the literature [7].

5.1.1.2 Spatially resolved x-ray diffraction experiments

The experimental setup of SRXRD technique is illustrated in Fig. **2.15**, and the salient features of the experiments are briefly described here. The SRXRD measurements were performed on the 31-pole wiggler beam line at Stanford Synchrotron Radiation Laboratory (SSRL) with Stanford Positron-Electron Accumulation Ring (SPEAR) operating at an electron energy of 3.0 GeV and an injection current of ~100 mA. The focused monochromatic beam was passed through a 260 μm tungsten pinhole to render a sub-millimeter beam on the sample surface at an incident angle of ~25 degree. The spatially resolved X-ray diffraction patterns were recorded behind the weld using a 50 mm long 2048 element position sensitive Si photodiode array detector. The welding assembly was integrally mounted to a translation stage driven by a stepper motor with 10 μm precision and placed inside an environmentally controlled chamber to minimize oxidation during welding. The x-ray diffraction data were taken while the beam was at a fixed location with respect to the welding electrode, while the bar rotated under the stationary torch at a constant speed. More details on the SRXRD experimental setup are available elsewhere [**7**,**8**,**13**-**16**].

5.1.1.3 Metallographic characterization

As shown in Fig. **5.1**, the welded samples were sectioned transverse to the welding direction to examine the final microstructure in the weldment. Figure **5.2** shows the optical microstructure of base metal, which is composed of ferrite and small regions of pearlite. The HAZ consisted of a partially transformed region, a fine grained region and a coarse grained region [**7**], as shown in Fig. **5.3(a)**. The microstructure in the coarse grained region of the HAZ was mainly composed of allotriomorphic and Widmanstatten ferrites, as shown in Fig. **5.3(b)**. The FZ microstructure was largely composed of allotriomorphic ferrite, Widmanstatten ferrite and small amount of other microconstituents, as shown in Fig. **5.4**. Under a light microscope, allotriomorphic ferrite is usually equiaxed or lenticular in form, and Widmanstatten ferrite has a thin wedge

shape [23]. The point counting method was used following the International Institute of Welding (IIW) guidelines [24] to determine the relative quantities of these two ferrites in the FZ. As shown in Fig. 5.1, various locations within the FZ were examined. At each location, 100 points were counted to determine the volume fractions of various microconstituents. The resulting volume fractions and their standard deviations are summarized in Table 5.1.

The γ grain size prior to the γ→α transformation during cooling (i.e., the prior γ grain size) was necessary information to calculate the final weld microstructure using the austenite decomposition model [19-22]. It should be noted that there were two kinds of prior γ grains: one resulting from the solidified weld metal in the FZ; the other resulting from the γ grain growth in the HAZ. The prior γ grain size in the FZ was experimentally measured along the longitudinal sections of the 1005 weld. On the other hand, experimental measurement of the γ grain size in the HAZ was difficult, since the prior γ grain boundary could not be etched clearly, as shown in Fig. 5.3(b). As a result, the MC grain growth simulation was undertaken to compute the prior γ grain size in the HAZ.

5.1.2 Calculation of weld thermal cycles

Details about the weld thermo-fluid model are available in Chapters 3 and 4. A 77×40×49 grid system was used, representing a solution domain of 163 mm in length, 60 mm in width and 42 mm in depth. The thermo-physical data used in the calculations are given in Table 2.1. After obtaining the steady-state temperature field, the thermal cycle at any given location (x,y,z) is calculated using the following relationship [25].

$$T(x,y,z,t_2) = \frac{T_S(\zeta_2,y,z) - T_S(\zeta_1,y,z)}{\zeta_2 - \zeta_1} U_w (t_2 - t_1) + T(x,y,z,t_1) \qquad (5.1)$$

where $T(x,y,z,t_2)$ and $T(x,y,z,t_1)$ are the temperatures at times t_2 and t_1, respectively, $T_S(\xi_2,y,z)$ and $T_S(\xi_1,y,z)$ are the steady-state temperatures at (ξ_2,y,z) and (ξ_1,y,z), respectively, U_w is the welding speed, and $(\xi_2 - \xi_1)$ is the length welded in time $(t_2 - t_1)$.

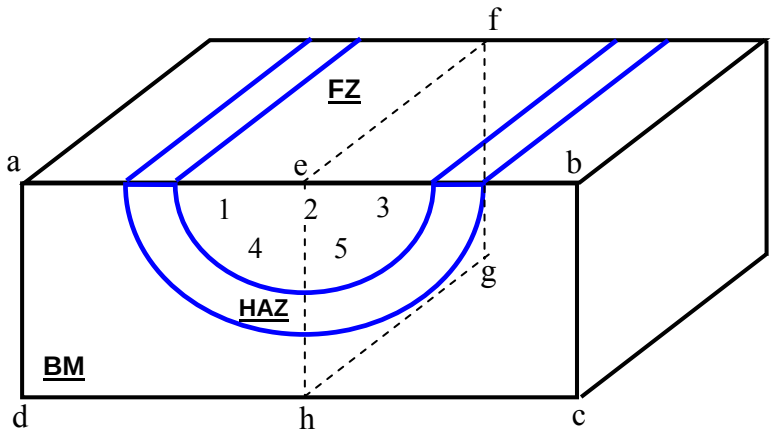

Fig. **5.1**: Schematic diagram showing the two sections where measurements were made. The welding direction is along the line ef. Plane abcd represents the transverse (cross) section, on which the quantitative point counting was carried out at the locations 1 through 5 to determine the volume fractions of final microconstituents in the FZ. Plane efgh is the longitudinal section, on which the prior austenite grain structure in the FZ was examined.

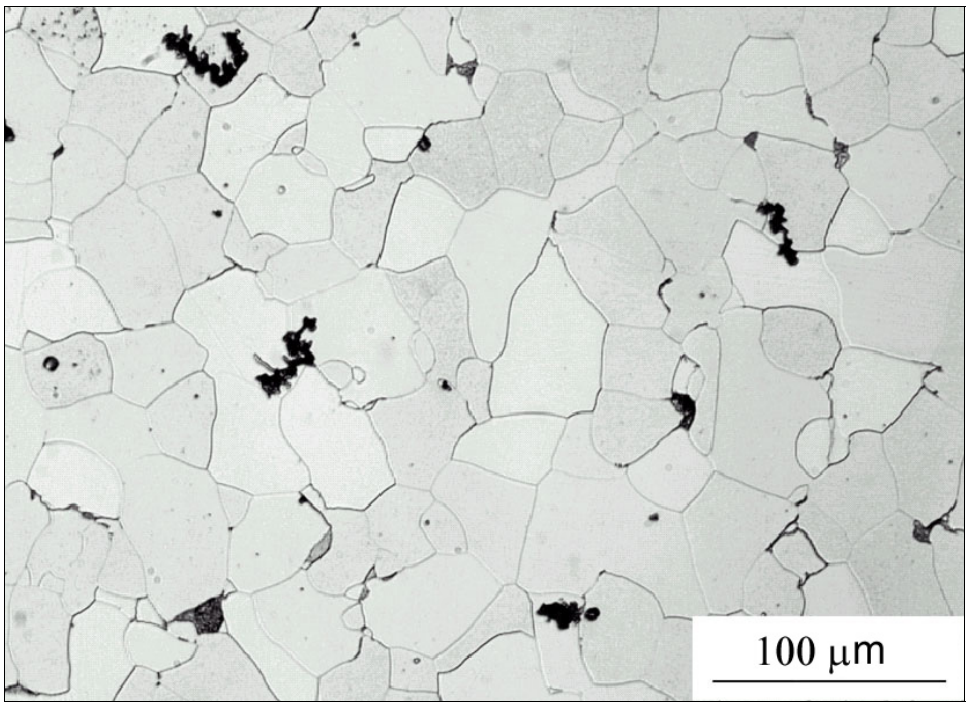

Fig. **5.2**: Optical micrograph of 1005 steel base metal, etched in 2% nital solution.

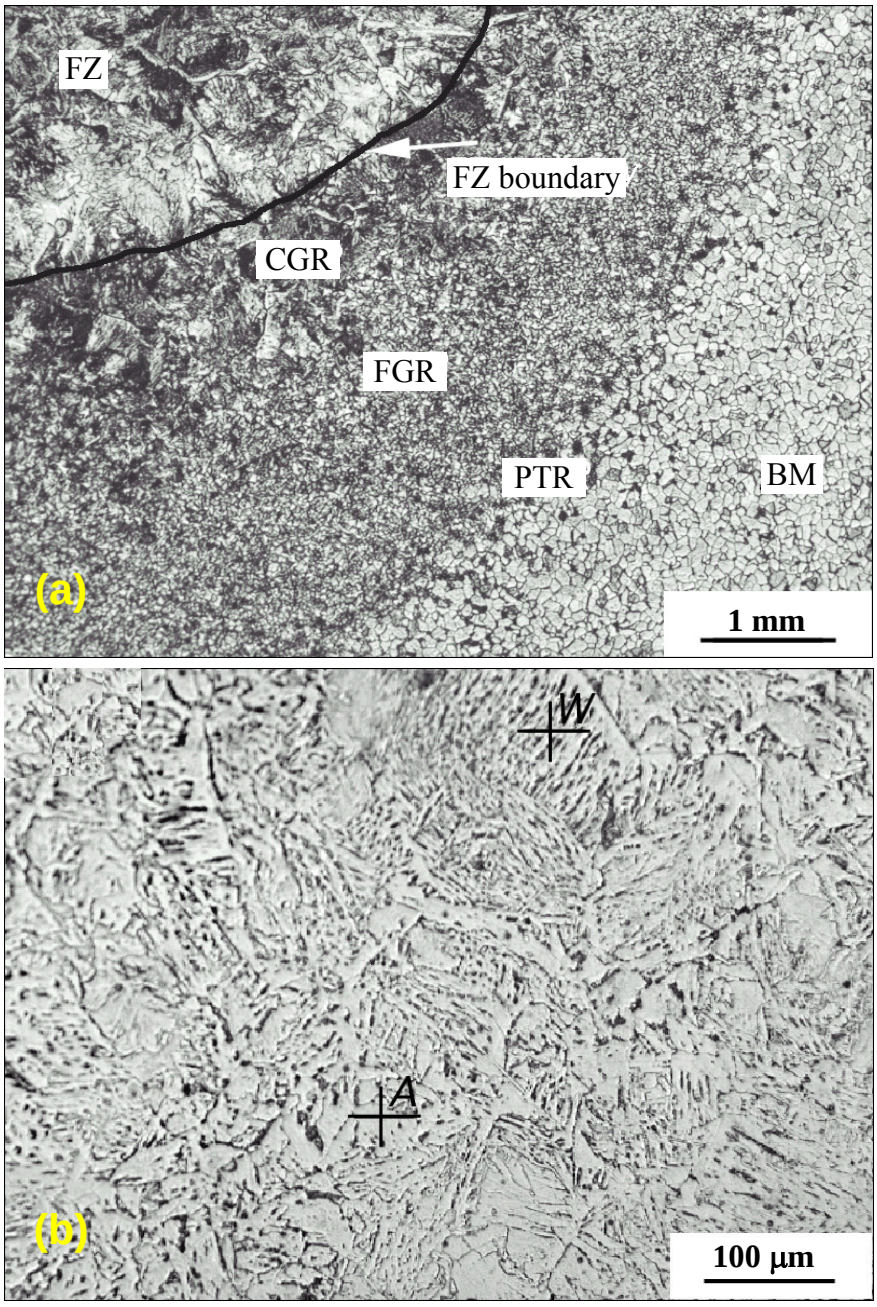

Fig. **5.3**: (a) Macrostructure of the weldment, etched in 2% nital solution, and (b) microstructure of the CGR in the HAZ, etched in saturated picral solution [**23**]. Symbol BM represents base metal, and CGR, FGR and PTR are the coarse grained region, fine grained region and partially transformed region, respectively. The HAZ consisted of the CGR, FGR, and PTR regions. Symbols A and W indicate allotriomorphic ferrite and Widmanstatten ferrite, respectively.

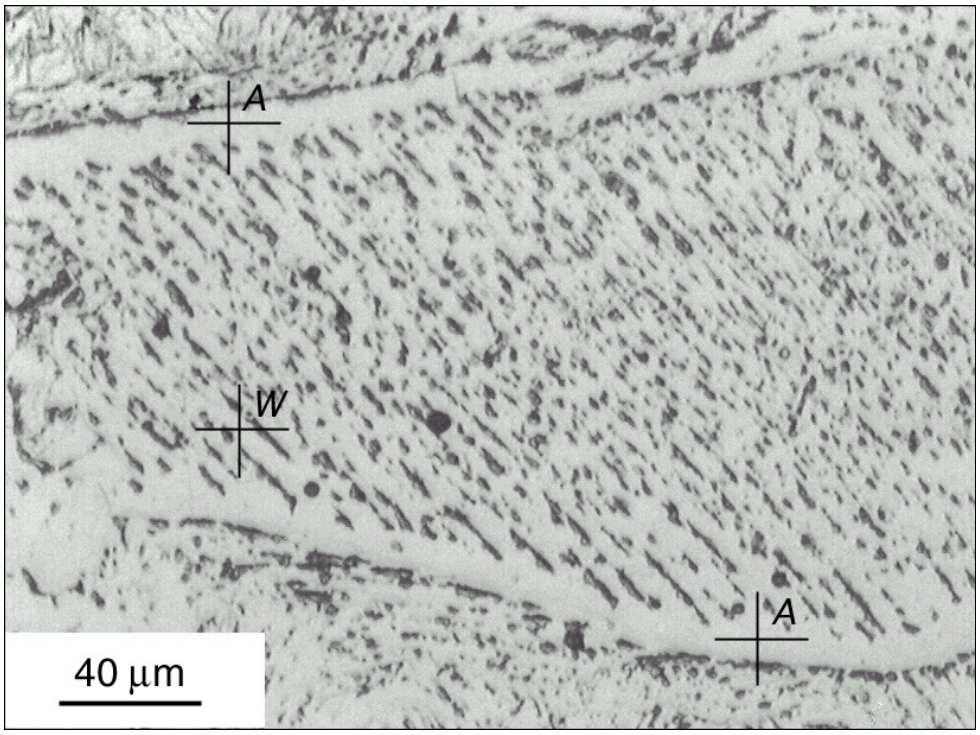

Fig. **5.4**: Microstructure of the FZ, etched in saturated picral solution. Symbols A and W represent the allotriomorphic ferrite and Widmanstatten ferrite, respectively.

Table **5.1**: Experimentally measured volume fractions of microconstituents in the FZ of 1005 arc welds. Locations 1 through 5 are shown in Fig. **5.1**. The symbols V_α, V_W, and V_o represent the volume fractions of allotriomorphic ferrite, Widmanstatten ferrite and other microconstituents, respectively.

	Volume fractions at different monitoring locations (%)					Average volume fractions (%)	Standard deviation (%)
	1	2	3	4	5		
V_α	35	30	37	28	28	31.6	3.7
V_W	57	56	59	62	61	59	2.2
V_o	8	14	4	10	11	9.4	3.3

5.1.3 Modeling of phase transformations

5.1.3.1 Phase equilibria

The calculated pseudo-binary Fe-C diagram [7] for 1005 steel is illustrated in Fig. 5.5. As shown in this figure, on slow heating, the dissolution of carbides and formation of γ take place at 993 K, producing a mixture of α and γ. The α phase transforms completely to γ at 1155 K. The δ phase begins to form at 1705 K and coexists with γ up to 1735 K where γ completely transforms to δ. At 1779 K, δ starts to melt and it is completely converted to liquid at 1802K. On slow cooling, the phase transformations occur in the reverse order.

As a verification of the calculated phase diagram for 1005 steel, dilatometry [26] was performed on a 1005 base metal sample to directly measure the A1 and A3 temperatures, which are both critical to the phase transformations that occur during welding. Specimens measuring 50 mm long and 3 mm in diameter were heated at a rate of 0.05 K/s in a conventional horizontal tube type dilatometer to a peak temperature of 1773 K. The results confirmed the calculated A1 temperature, but the measured A3 temperature was 1204 K, which is higher than the calculated value. It is the A3 temperature measured by dilatometry that is used for calculating the kinetics of the α→γ phase transformation.

5.1.3.2 JMA equation for α→γ transformation during heating

The α→γ phase transformation during heating of low alloy steels normally involves the nucleation of γ phase from the α matrix and the growth of γ phase [27-30]. Therefore, the JMA equation is applicable to describe the α→γ phase transformation in 1005 steel. At a constant temperature, the JMA equation can be expressed as [31]:

$$f_e = 1 - \exp\{-(K\,t)^n\} \qquad (5.2)$$

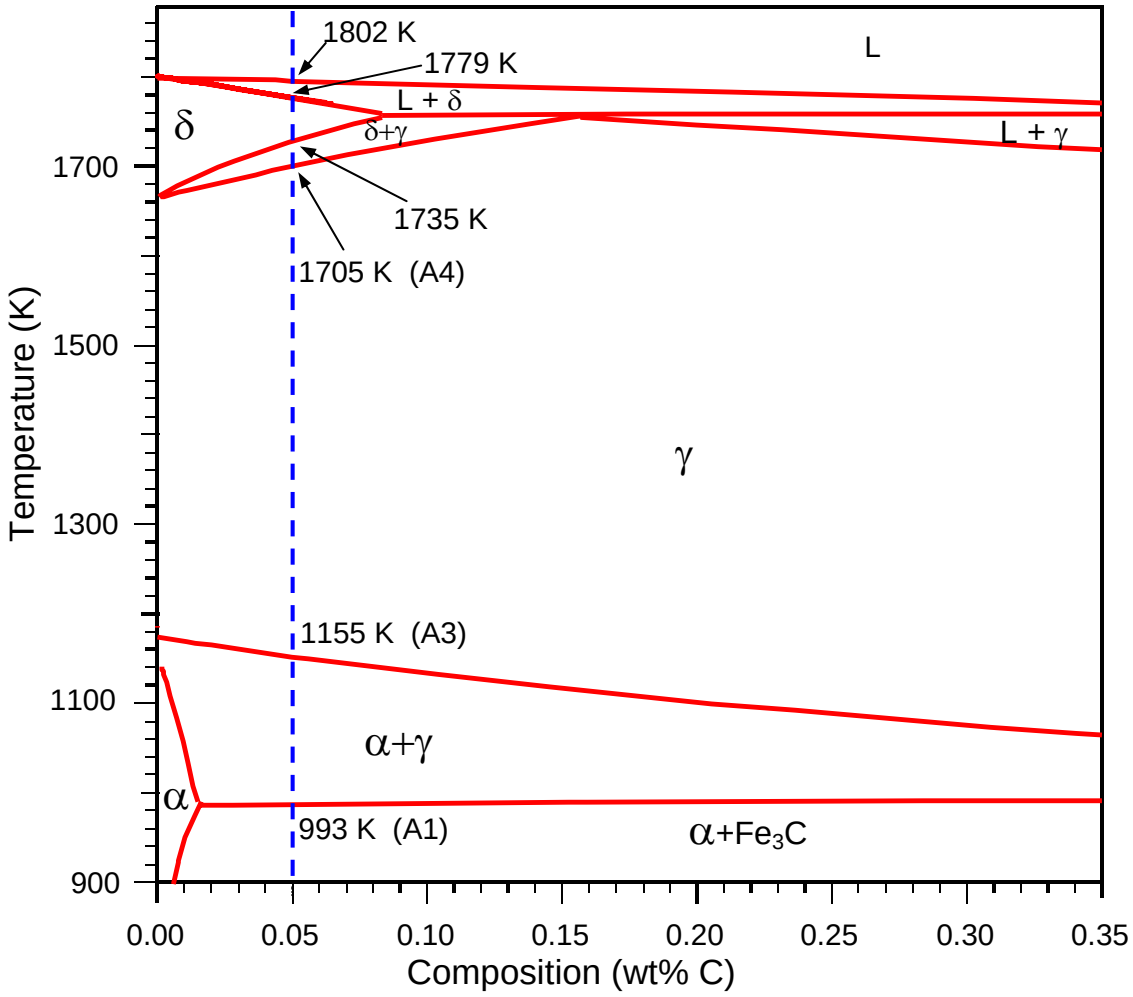

Fig. **5.5**: Calculated pseudo-binary Fe-C phase diagram for 1005 steel. Adapted from reference [**7**].

where f_e stands for the extent of the $\alpha \rightarrow \gamma$ transformation at time t, n is the JMA exponent, which is normally a constant independent of temperature, and K is a rate parameter defined by the following Arrhenius equation [31]:

$$K(T) = k_0 \exp(-\frac{Q}{RT}) \qquad (5.3)$$

where k_0 is a pre-exponential constant, Q is the activation energy of the transformation including the driving forces for both nucleation and growth, R is the universal gas constant, and T is the absolute temperature in Kelvin.

In Eq. 5.2, the extent of the transformation f_e is related to the volume fraction of product phase (f) by the following equation.

$$f_e = \frac{f}{F} \qquad (5.4)$$

where F is the equilibrium fraction of the product phase at temperature T. For transformations of the eutectoid type, i.e., the transformation path involves one phase transforming directly to another at a constant temperature, f_e is identical to f since F is equal to 1. In many instances, such as the α-ferrite to γ-austenite transformation during heating of low alloy steels, the transformation path involves $\alpha \rightarrow (\alpha+\gamma) \rightarrow \gamma$. In the $\alpha+\gamma$ two-phase region, F is not equal to 1 and can be determined from the corresponding phase diagram.

Substituting Eqs. 5.3 and Eq. 5.4 into Eq. 5.2, the isothermal JMA equation is rewritten as:

$$\frac{f}{F} = 1 - \exp[-\{k_0 \times \exp(-\frac{Q}{RT}) \times t\}^n] \qquad (5.5)$$

For eutectoid-type reactions, the non-isothermal solution of the JMA equation has been derived by Krüger [32]. However, Krüger's formulation does no apply to systems where the transformation involves a two-phase region. Here, the JMA equation is extended to deal with such a two-phase region under non-isothermal conditions. In the following derivation, to simplify the problem, we assume that the kinetic parameters Q,

k_0, and n are independent of temperature, i.e. there is no significant change in the nucleation and growth mechanisms during the phase transformation [31].

During a non-isothermal solid-state transformation, the temperature changes continuously with the time, i.e., $T = T(t)$. In the following discussion, the non-isothermal kinetic equation will be derived under continuous heating conditions. The derivation procedure and the resulting equation are the same for continuous cooling conditions. The continuous change of the temperature with time can be approximated by subsequent isothermal steps of the duration Δt. As shown in Fig. 5.6, the temperature-time curve starts at time $t_0 = 0$ and temperature T_1, and finishes at time $t_m = m\Delta t$ and temperature T_{m+1}. It should be noted that time equal to 0 is defined from the instant the sample reaches the isothermal transformation temperature. This continuous curve is discretized into m isothermal steps. For example, the temperature between times t_{i-1} and t_i is equal to T_i, and at the time t_i, the temperature is changed from T_i to T_{i+1}. This temperature (T_{i+1}) prevails between times t_i and t_{i+1}.

The γ fraction converted along the i^{th} isothermal time step $(t_{i-1} \le t \le t_i)$ is expressed as:

$$\frac{f(t)}{F_i} = 1 - \exp\{-[k_0 \times \exp(-\frac{Q}{RT_i}) \times (t - c_i)]^n\} \qquad (5.6)$$

where T_i is the temperature at the i^{th} step, F_i is the equilibrium fraction of the new phase at temperature T_i, and c_i is a time used to account for the pre-converted fraction of new phase at the beginning of i^{th} step. The term c_i ($c_1 = 0$) is determined from the continuity relation that the fraction calculated using Eq. 5.6 at the beginning of the i^{th} time step is equal to that converted at the end of $(i\text{-}1)^{th}$ time step, $f(t_{i-1})$. Substituting $t = t_{i-1} = (i-1)\Delta t$ into Eq. 5.6, we have:

$$c_i = (i-1)\Delta t - \frac{\sqrt[n]{-\ln[1 - \frac{f(t_{i-1})}{F_i}]}}{k_0 \times \exp(-\frac{Q}{RT_i})} \qquad (5.7)$$

where Δt is the time step.

We can define the second term in Eq. 5.7 as another time constant τ_i ($\tau_1 = 0$).

$$\tau_i = \frac{\sqrt[n]{-\ln[1-\frac{f(t_{i-1})}{F_i}]}}{k_0 \times \exp(-\frac{Q}{RT_i})} \qquad (5.8)$$

Thus, we can obtain the fraction of new phase converted at the end of i^{th} step by substituting $t = t_i = i\Delta t$ and $c_i = (i-1)\Delta t - \tau_i$ into Eq. 5.6.

$$\frac{f(t_i)}{F_i} = 1 - \exp\{-[k_0 \times \exp(-\frac{Q}{RT_i}) \times (\Delta t + \tau_i)]^n\} \qquad (1 \le i \le m) \qquad (5.9)$$

Eq. 5.9 is the non-isothermal kinetic equation considering the equilibrium fraction of new phase in two-phase region. This equation was used in the present study to analyze the kinetic data of the $\alpha \rightarrow \gamma$ transformation obtained using the SRXRD technique.

5.1.3.3 MC simulation of γ grain growth

As shown in Fig. 5.5, after the $\alpha \rightarrow \gamma$ transformation during heating, the transformed γ phase is stable over a wide range of temperatures, i.e., from 1155 to 1705 K. At elevated temperatures, the γ grain growth may occur, which significantly affects the subsequent γ decomposition during cooling. In this study, an existing MC model [17,18] was used to simulate the γ grain growth in the HAZ of the 1005 arc welds. Grain growth calculation in the FZ seems unnecessary, since the γ phase eventually becomes liquid upon heating. Details of the MC model have been presented in section 2.4.3.

Table 5.2 summarizes the input data used in the MC calculations. It should be noted that the γ grain growth is significant in the HAZ region where the $\alpha \rightarrow \gamma$ transformation completed during heating, since the un-transformed α may hinder the γ grain growth in the partially transformed region. Such completely transformed region was determined using the JMA equation described in the previous section.

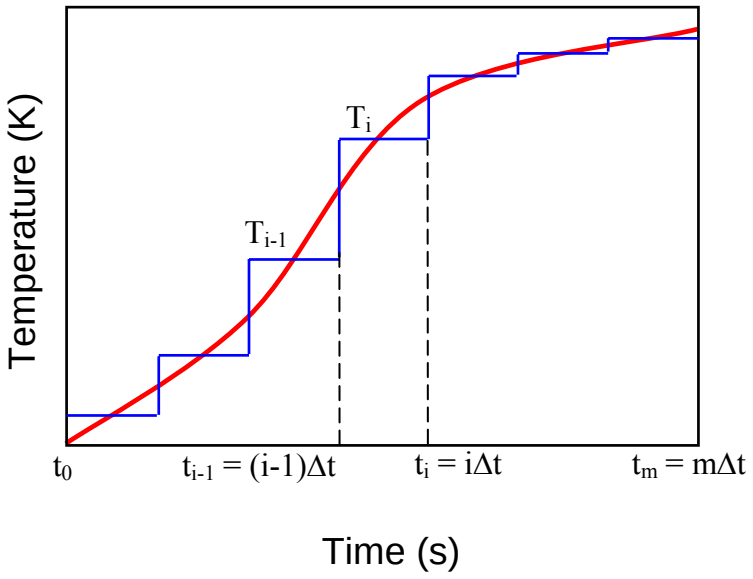

Fig. **5.6**: Discretization of the continuous heating curve.

Table **5.2**: Data used in the MC calculation of γ grain growth in the 1005 steel [**33**].

Property	Value
Thermal conductivity of solid, k_S, (W m^{-1} K^{-1})	36.4
Specific heat per unit volume, ρC_P, (J m^{-3})	5.8×10^{6}
Solidus temperature, T_S, (K)	1779
Activation energy for grain growth (J mol^{-1})	1.8×10^{5}
Experimental grain growth exponent, n	3.17
Pre-exponential factor for grain growth	2.19×10^{-3}
Grain boundary energy (J m^{-2})	1.77
Initial γ grain size (μm)	10.8

5.1.3.4 Modeling γ decomposition during cooling

In low alloy steel welds, allotriomorphic ferrite is the first phase to form from the γ phase during cooling of the weld metal. It nucleates along the γ grain boundaries and grows by diffusion [19-22]. As the temperature decreases, the growth rate of allotriomorphic ferrite decreases, and it finally gives way to the growth of Widmanstatten ferrite. Widmanstatten ferrite nucleates either directly from the austenite grain surfaces or indirectly from allotriomorphic ferrite/austenite interfaces [3,34]. It grows by a combination of carbon diffusion and an invariant-plane strain shape change [3,34]. At even lower temperatures, the remaining austenite transforms into bainite or martensite depending on the cooling rate [19-22]. It should be noted two or more transformations may occur simultaneously at certain temperatures and compete with each other.

Based on thermodynamics and phase transformation kinetics, Bhadeshia et al. [19-22] developed an austenite decomposition mode, which could predict the time-temperature-transformation (TTT) and continuous-cooling-transformation (CCT) diagrams for the $\gamma \rightarrow \alpha$ transformation. Together with the computed cooling rates, their model can also calculate the volume fractions of weld metal microstructure. Details of this model are described in section **2.4.4.1**. It should be noted that the austenite decomposition model was developed for the weld metal in the FZ. For simplicity, it is assumed that this model can also be used to investigate the final microstructure in the HAZ, since our primary objective here is to illustrate that the microstructural evolution during welding could be examined by the combination of various kinetic models and computed thermal cycles. More rigorous study is thus needed in the future to better understand the HAZ microstructure.

5.1.3.5 Coupling of kinetic models

In the previous discussion, three kinetic models have been established for describing each of the three microstructural evolution stages in the 1005 arc welds. The

$\alpha \rightarrow \gamma$ transformation during heating can be calculated using the JMA equation, the γ grain growth at elevated temperatures can be simulated using the MC model [17,18], and the $\gamma \rightarrow \alpha$ transformation during cooling can be computed using the γ decomposition model [19-22]. In this study, a preliminary attempt was made to combine the three kinetic models and computed thermal cycles to investigate the microstructural evolution in both the FZ and HAZ of the 1005 arc weld. The three models were coupled in the following manner.

(a) The JMA model was used to calculate the superheat required for the completion of the $\alpha \rightarrow \gamma$ transformation during heating of the 1005 steel.

(b) The computed temperature, at which the $\alpha \rightarrow \gamma$ transformation completes, was used as the starting point of the γ grain growth in the 1005 steel. Such starting temperature is considered to be more accurate than the equilibrium completion temperature ignoring the superheating.

(c) The prior γ grain sizes, calculated using the MC model, were then used in the austenite decomposition model [19-22] to compute the final microstructure in the HAZ. On the other hand, in the FZ, the measured prior γ grain size was used to compute the weld metal microstructure.

5.1.4 Results and discussion

5.1.4.1 Temperature and velocity fields and weld pool geometry

The computed temperature and velocity fields at the weld top surface and cross section are shown in Figs. **5.7(a)** and **5.7(b)**, respectively. In these figures, the temperature field is indicated by the contour lines and the liquid convection velocities are represented by the arrows. The liquid metal motion in the weld pool is driven mainly by the surface tension gradient and electromagnetic forces and, to a much lesser extent, by the buoyancy force. Because the temperature coefficient of surface tension ($d\gamma/dT$) is

negative for the 1005 liquid metal, the surface tension force drives the liquid metal from the center to the periphery at the top surface of the weld pool. As a result of the strong outward liquid metal flow at the surface, the weld pool is wide and shallow.

Figure **5.7(a)** compares the geometry of the weld pool based on SRXRD [7] and metallographic data at the weld top surface. The FZ and HAZ boundaries, indicated by the horizontal dashed lines in the figure, were measured on the welded samples [7], while the superimposed isotherms were calculated from the heat transfer and fluid flow model. The calculated liquidus isothermal line (1802 K) agrees well with the measured weld pool boundary, and the calculated 993 K (A1 temperature) isotherm matches well with the metallographically determined HAZ boundary. Figure **5.7(b)** shows the comparison between calculated and measured weld pool geometry at the cross section. The fair agreement between the calculated and experimental geometry indicates that the overall features of the FZ and HAZ in the GTA welds can be satisfactorily predicted by the thermo-fluid model. Furthermore, the spatial distribution of peak temperatures, heating rates and cooling rates can be determined from the computed temperature field. Thermal cycles are necessary for understanding the evolution of microstructure in the weldment.

5.1.4.2 Computed thermal cycles

The steady-state spatial distribution of temperatures shown in Fig. **5.7** was converted into thermal cycles using Eq. **5.1**. Considering temperatures along a line parallel to the welding direction (x-direction), the corresponding time values were obtained by dividing the x-distance by the welding speed. This conversion from distance to time coordinates is necessary to understand the welding-induced phase transformations that are affected by both time and temperature. A series of thermal cycles is plotted in Fig. **5.8** for locations at different distances from the weld centerline. In this plot time equal to zero was arbitrarily selected to correspond to the heat source location identified in Fig. **5.7** as x = 0. As shown in Fig. **5.8**, the peak temperatures, heating and cooling rates at various locations decrease with the increasing distance from the welding centerline.

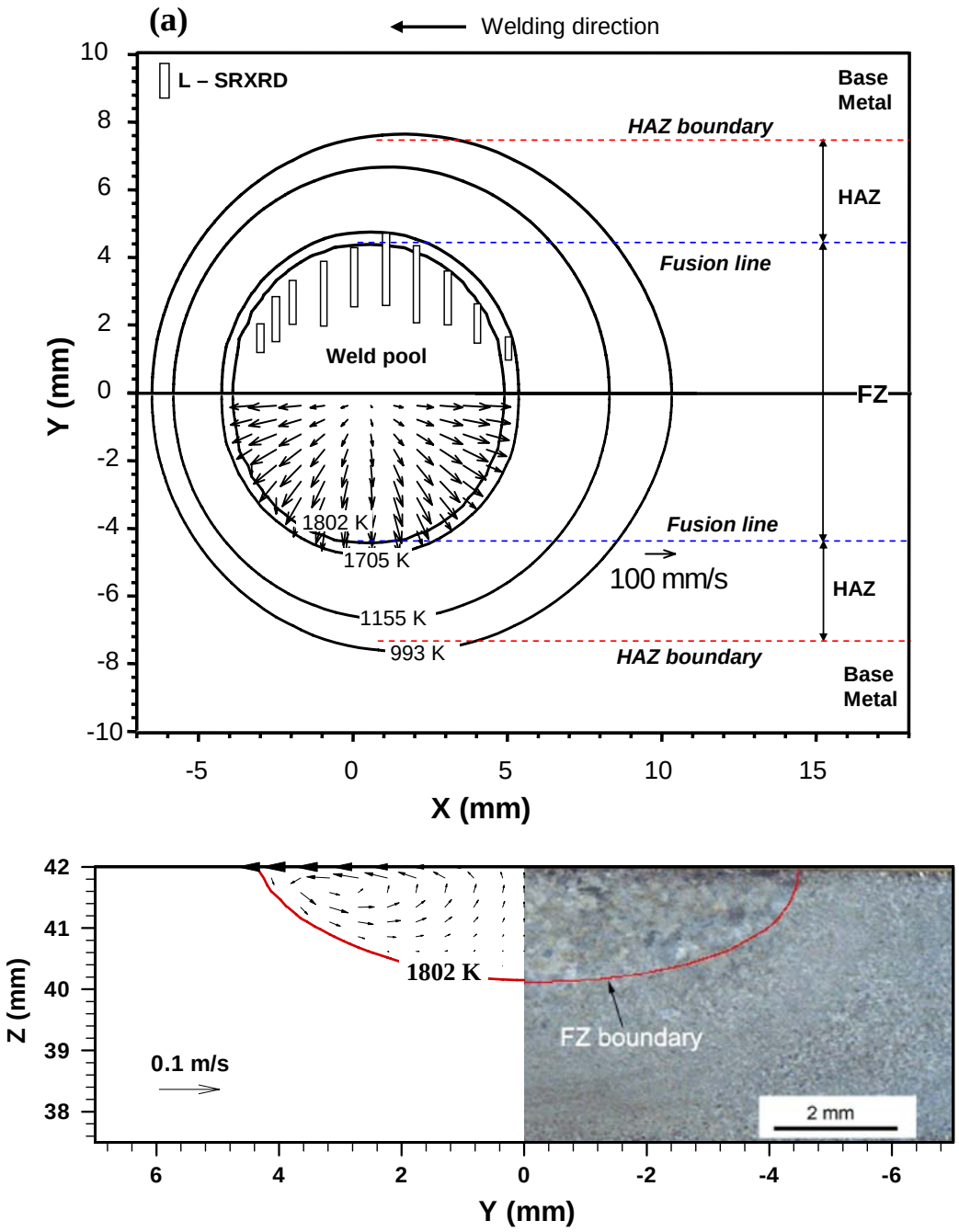

Fig. 5.7: Calculated temperature and velocity fields: (a) top surface, and (b) transverse section. The computed weld pool boundary is represented by the 1802 K isotherm. The liquid phase was plotted from the real-time SRXRD data. The FZ and HAZ boundaries were measured on the metallographically prepared samples. The heat source is positioned at x = y = 0. Welding conditions: GTA, 110 A, 17.5 V and 0.6 mm/s welding speed.

Depending on the local temperatures, different phase transformations may take place in the weldment. For instance, for a location at y = 5 mm, Fig. **5.8** indicates that the peak temperature and the time period over the A3 temperature are relatively large. As a result, this location experiences the complete $\alpha \rightarrow \gamma$ transformation during heating, γ grain growth, and $\gamma \rightarrow \alpha$ transformation during cooling. Further away from the weld centerline, say at y = 8 mm, the peak temperature never reaches the A1 temperature. Therefore, this location does not experience the $\alpha \rightarrow \gamma$ transformation. Between these locations, the $\alpha \rightarrow \gamma$ transformation takes place under different heating rates and peak temperatures, which result in different extents of completion. The extent of the transformed γ affects the subsequent γ grain growth and γ decomposition during cooling.

For low alloy steels, the $\gamma \rightarrow \alpha$ transformation during cooling usually occurs within the temperature range 1073 K to 773 K (800 ^{o}C to 500 ^{o}C) [**35**]. In the FZ, the cooling rates vary with position at high temperatures above the melting point. As the weld metal cools, the spatial variation of cooling rates in the FZ decreases. In the 1073 K to 773 K range the cooling rate in the FZ is almost independent of position, as shown in Fig. **5.9**. This is due to the nearly constant outward heat loss from all locations within the FZ [**35**,**36**]. A consequence of this fact is that the spatial variation of microstructure within the FZ of arc welds is expected to be insignificant. The computed thermal cycles are prerequisite to understand the welding-induced microstructural changes.

5.1.4.3 Spatial distribution of phases at weld top surface

Figure **5.10** plots the phase distribution on the heating side of weld top surface measured using the SRXRD technique. Superimposed is the computed temperature distribution, and the A1 (993 K) and A3 (1204 K) temperatures are shown to identify the equilibrium start and finish locations for the $\alpha \rightarrow \gamma$ transformation. It is observed that the higher the temperature, the larger the extent of $\alpha \rightarrow \gamma$ transformation. Furthermore, higher superheats are required for the transformation at locations closer to the weld center (high heating rates) than those further away from the center.

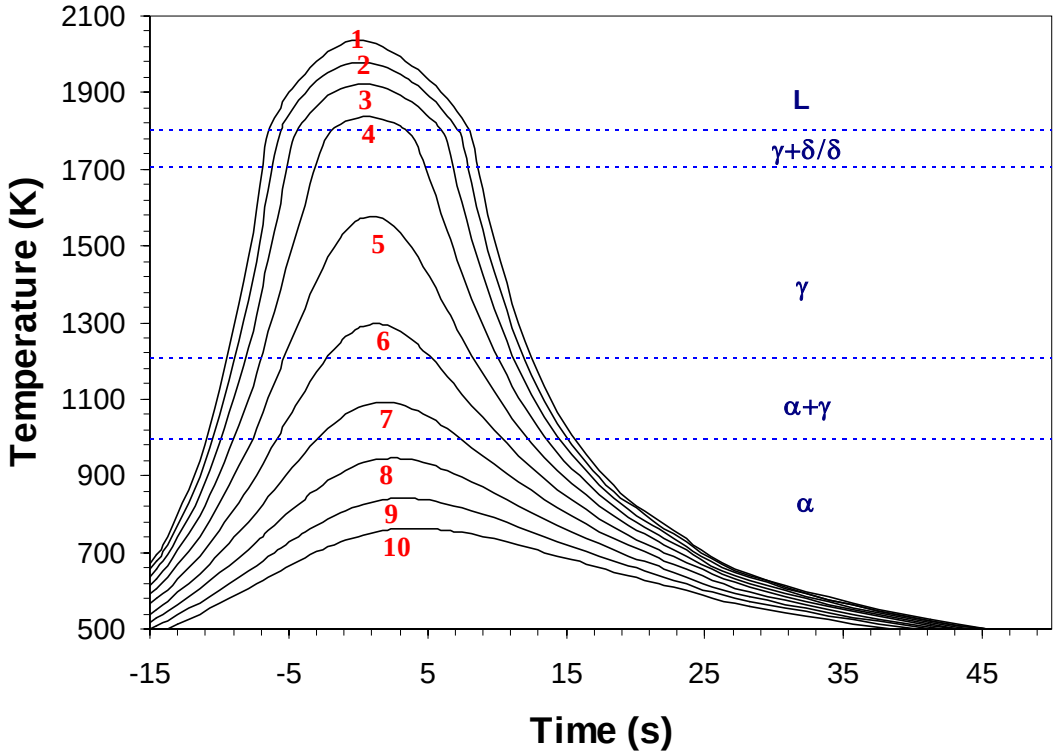

Fig. **5.8**: Computed thermal cycles at various distances from the weld center. 1: 0 mm, 2: 2 mm, 3: 3 mm, 4: 4 mm, 5: 5 mm, 6: 6 mm, 7: 7 mm, 8: 8 mm, 9: 9 mm, and 10: 10 mm.

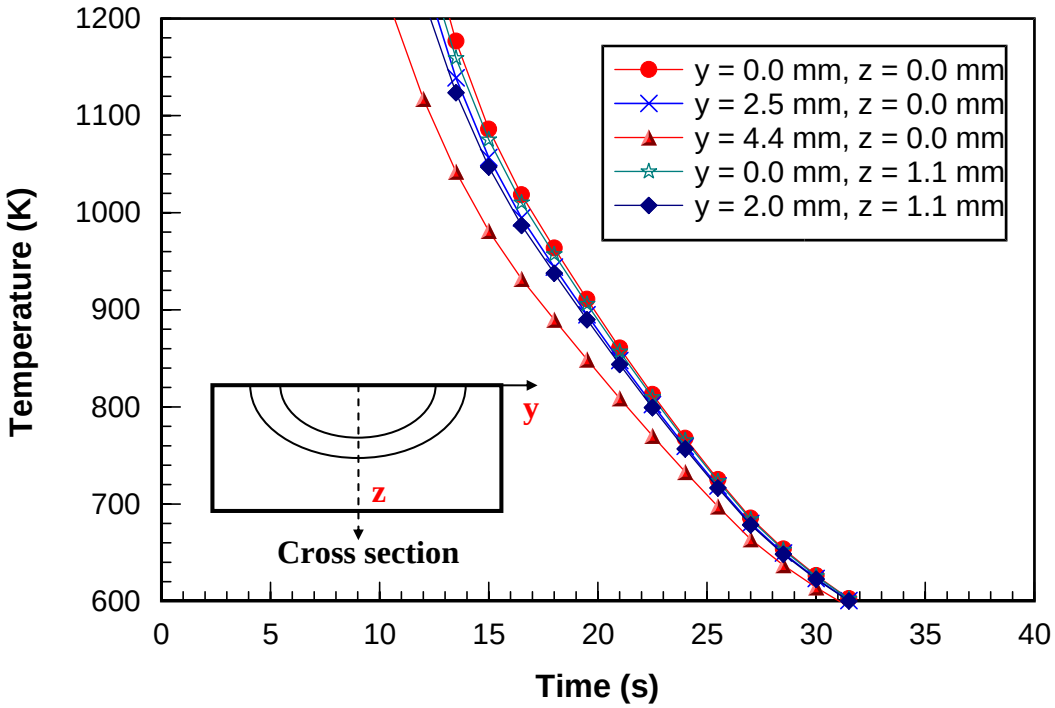

Fig. **5.9**: Calculated cooling curves at different locations. Symbols y and z represent the distance from the weld centerline and the top surface, respectively, as shown in the inset figure. Time zero corresponds to the heat source location at x = 0.

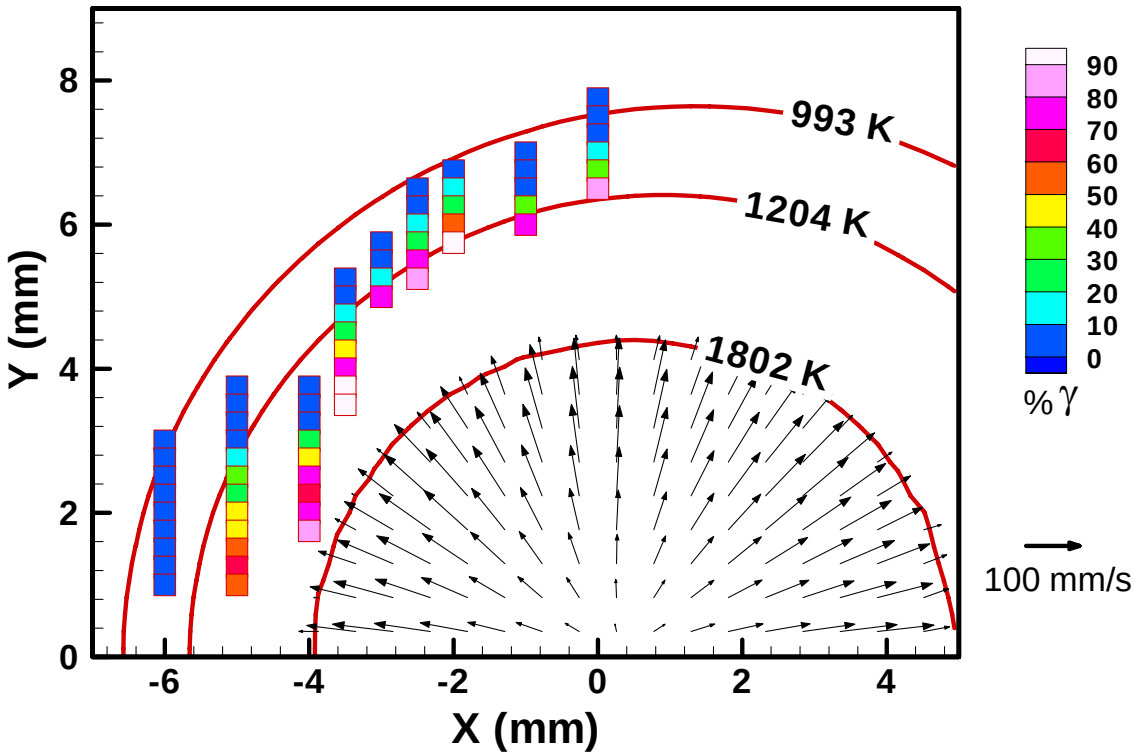

Fig. **5.10**: Spatial distribution of α and γ phases during heating. The stationary heat source is positioned at x = y = 0, while the workpiece moves from left to right along the x direction.

5.1.4.4 Kinetics of α→γ transformation during heating

The rate of the α→γ transformation on heating can be expressed by the JMA equation, since the transformation involves nucleation and growth of the γ phase. Eq. **5.9** indicates that the JMA kinetic parameters (Q, k_0 and n) determine the rate of the α→γ transformation. If the values of these parameters can be specified, the phase transformation rate can be quantitatively described for various thermal cycles. The goal here is to determine these kinetic parameters for the 1005 steel from the SRXRD phase distribution map and the computed temperature field. Apart from providing a quantitative basis for the calculation of the rate of the α→γ transformation in this steel, values of these kinetic parameters can provide insight about the nucleation mode of austenite.

In low alloy steels, the activation energy (Q) for the α→γ transformation is found not to change significantly with the variation of carbon and alloy concentrations [**37**]. The Q value for the α→γ transformation in steels that have similar carbon and alloy concentrations (0.08 C, 0.45 Mn, 0.03 Si, 0.045 S and 0.04 P by wt%) as the 1005 steel has been reported as 117.1 kJ/mol in the literature [**37**]. This activation energy, which incorporates both the effects of nucleation and growth on the transformation kinetics, is lower than the activation energy for the diffusion of carbon in austenite alone, i.e. 135 kJ/mole [**38**]. Such activation energy is consistent with the fact that the growth of γ phase is controlled by the diffusion of carbon atoms in the γ phase, i.e., diffusion-controlled growth [**27-30**,**37**]. In the present investigation, we assume that this value of Q is also valid for α→γ transformation in the 1005 steel.

With the knowledge of Q, the values of k_0 and n were then determined using a fitting program. The program compares the error (Err) between the calculated and experimental γ fractions as a function of k_0 and n.

$$\mathrm{Err}(k_0, n) = \sum_{i=1}^{m} (f_e^i - f_c^i)^2 \qquad (5.10)$$

where f_e^i and f_c^i are the experimental and calculated γ fractions at the i^{th} monitoring location, respectively, and m is the number of data points.

Figure 5.11 shows the error contour plot for the given Q value of 117.1 kJ/mol, where a total number of 39 SRXRD data points were used. As shown in this figure, the optimal JMA parameters correspond to the minimum error on this plot and were found to be ln (k_0) = 12.2 and n = 1.45. The value of n = 1.45 is consistent with diffusion controlled growth under a zero or low nucleation rate [31]. This phase transformation mechanism would further imply that the pre-existing pearlite regions in the base metal provide the majority of the nucleation sites required for the $\alpha \rightarrow \gamma$ transformation, and that these nucleation sites are all active at temperatures close to the A1 temperature where the transformation is first observed. It should be noted that a determination of phase transformation mechanism must await further rigorous study, since the value of n is fairly sensitive to errors in γ-phase fraction data or the computed thermal cycle. The importance of the parameters n and k_0 is that when these values are combined with Q, the set is very useful for quantitative prediction of the transformation kinetics for a wide variety of heating conditions.

The internal consistency of these kinetic parameters was checked by comparing the austenite fraction at the different SRXRD locations to the values calculated using the non-isothermal kinetic Eq. 5.9. Figure 5.12 compares the results from seven different SRXRD locations, denoted in the plot as symbols, with the calculated values, shown as the solid lines. The overall agreement between the experimentally measured data and the calculated data is reasonable, especially when considering the wide range of heating rates experienced at these different HAZ locations.

Knowing these JMA kinetic parameters it is now possible to predict the $\alpha \rightarrow \gamma$ phase transformation rates throughout the HAZ where different heating rates and peak temperatures are observed. In the following section, two important diagrams used for graphical description of the $\alpha \rightarrow \gamma$ in 1005 steel are calculated using the non-isothermal kinetic equation i.e., Eq. 5.9, with the computed kinetic parameters based on the SRXRD results.

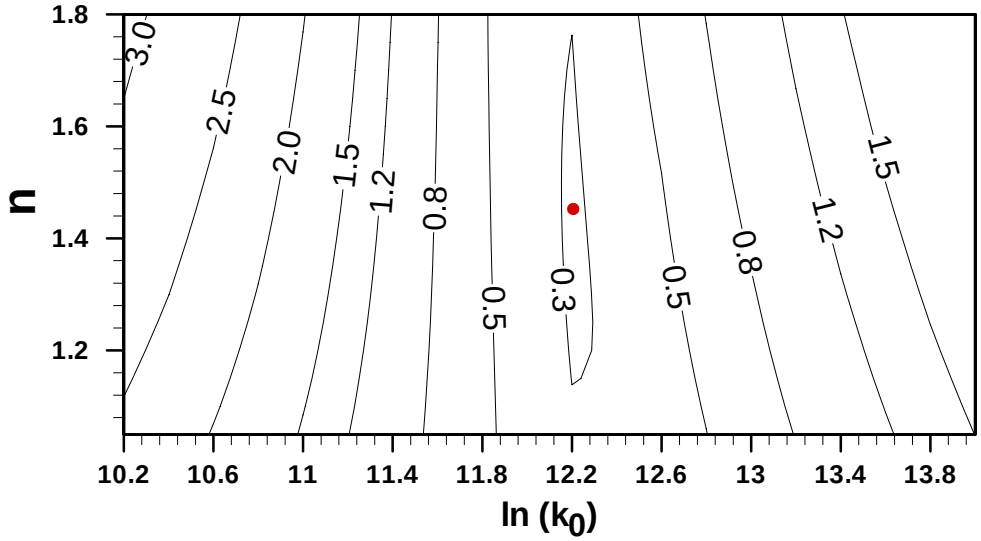

Fig. **5.11**: Calculation of the optimal values of n and k_0 for the Q value of 117.1 kJ/mol. The error field is represented by the contour lines, and the minimum error is indicated by the solid dot.

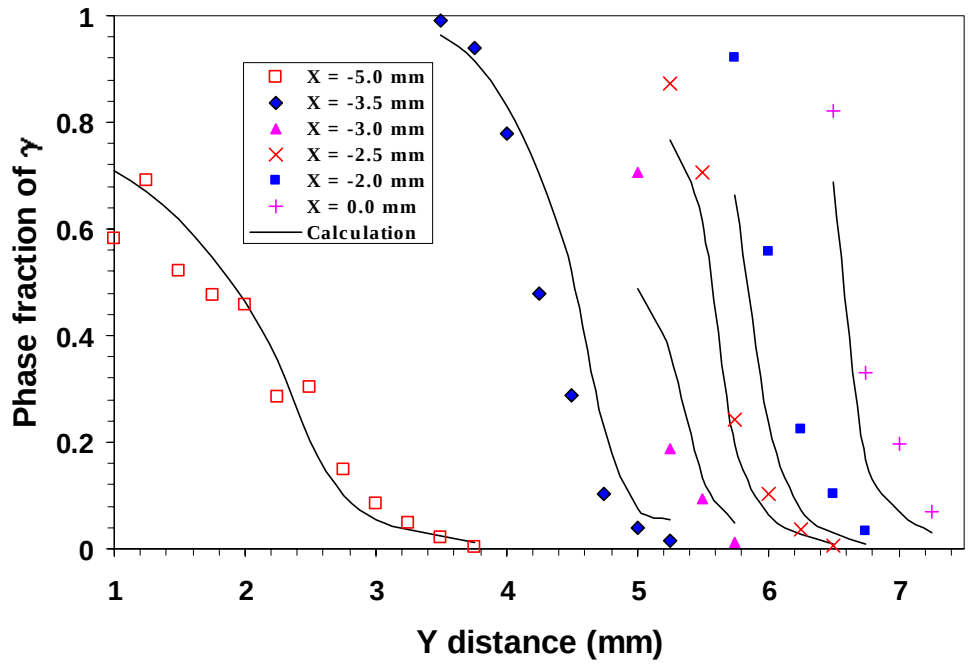

Fig. **5.12**: Comparison between the calculated and SRXRD experimental phase fractions of γ at different monitoring locations.

5.1.4.5 TTT and CHT diagrams for 1005 steel welds during heating

There are two main types of transformation diagrams that are useful in understanding transformation kinetics during welding: continuous-heating-transformation (CHT) and continuous-cooling-transformation (CCT) diagrams. The first type of diagram can be used to predict the transformations that occur on the heating side of the weld and the latter on the cooling side of the weld. Both types of diagrams can be related to the TTT diagrams that are used to measure the rate of the transformation at constant temperatures.

Using the kinetic parameters from the preceding section, TTT and CHT diagrams were constructed for $\alpha \rightarrow \gamma$ transformation in 1005 steel, while the CCT diagram determination is discussed in a later section. For the TTT diagram, the isothermal relationship can be expressed as a function of the temperature above the A1 temperature as follows:

$$T(t) = T_H \qquad (5.11)$$

where T is the temperature at a given time t, and T_H is the constant transformation temperature. Incorporating Eq. **5.11** into Eq. **5.9**, the austenite fraction versus time can be calculated at a given temperature, and the results were used to construct the TTT diagram shown in Fig. **5.13**. In this plot, the constant transformation lines are compared to the A1 and A3 temperatures for this steel. As shown in this figure, the $\alpha \rightarrow \gamma$ transformation rates accelerate rapidly as the temperature increases. The fast rate results from the increase in both the diving force and the diffusivity of carbon in austenite with temperature. Moreover, the transformation can go to completion only at a temperature higher than the A3 temperature. The calculated TTT diagram also indicates that for the isothermal formation of austenite, the transformation start time is usually less than 1 second, while the time for completion is less than 2 seconds.

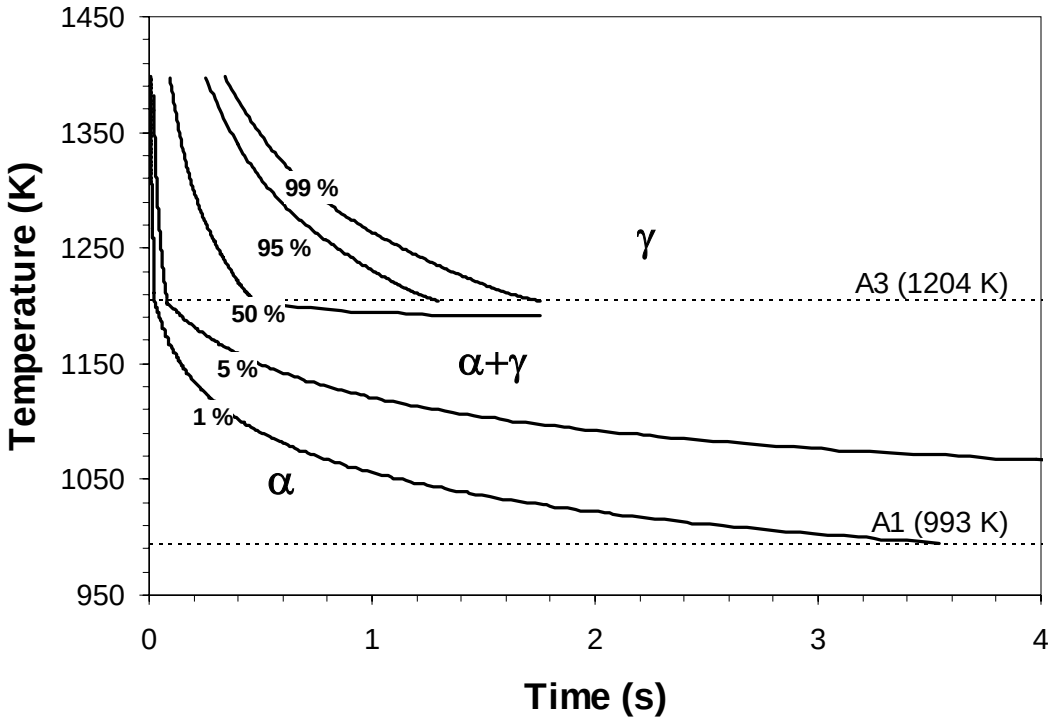

Fig. **5.13**: Calculated TTT diagram for α→γ transformation during heating of 1005 steel. Kinetic parameters used in the non-isothermal JMA equation were based on the SRXRD results.

The CHT diagram was constructed in a similar way as the TTT diagram, but using a constant heating rate as given in equation below:

$$T(t) = T_{A1} + H_T \times t \qquad (5.12)$$

where T_{A1} is the A1 temperature (993 K) and H_T is the heating rate. The non-isothermal transformation kinetics at various heating rates were calculated using Eq. 5.9. The resulting austenite fraction versus time data were then used to construct the CHT diagram, which is shown in Fig. 5.14. The transformation to austenite lines are again compared to the A1 and A3 temperatures for the 1005 steel. As shown in this figure, the transformation rate accelerates rapidly with temperature, and the start and finish temperatures of the transformation both increase with increasing heating rate.

A comparison between Figs. 5.13 and 5.14 shows that for any given temperature, the time to create an equivalent amount of transformation is longer for the CHT conditions than for the TTT conditions. The reason for this is that the total kinetic strength of the transformation is less for the CHT case than for the TTT case, since the CHT conditions integrate the time temperature curves up to the final temperature where the transformation is predicted. The CHT diagram for the 1005 steel indicates that for the isothermal formation of austenite, the transformation start time is usually greater than 1s, while the time for completion is greater than 10 seconds. In addition, it is apparent that some amount of super heating is required to start and complete the phase transformation to austenite under non-isothermal conditions. For example, using a heating rate of 50 K/s, Figure 5.14 predicts the transformation starts (1% austenite) at 70 K above the A1 temperature, while it finishes (99% austenite) at 155 K above the A3 temperature.

It should be noted that two of the kinetic parameters, k_0 and n, depend on the initial microstructure of the base metal. In view of the lack of quantitative kinetic data in the literature, the extent of dependence of the kinetic parameters on the initial microstructure cannot be determined at this time. The lack of kinetic data emphasize the need for quantitative investigations on this topic and suggest that the parameter values obtained in this investigation should be used carefully, paying particular attention to the starting microstructure indicated in Fig. 5.2.

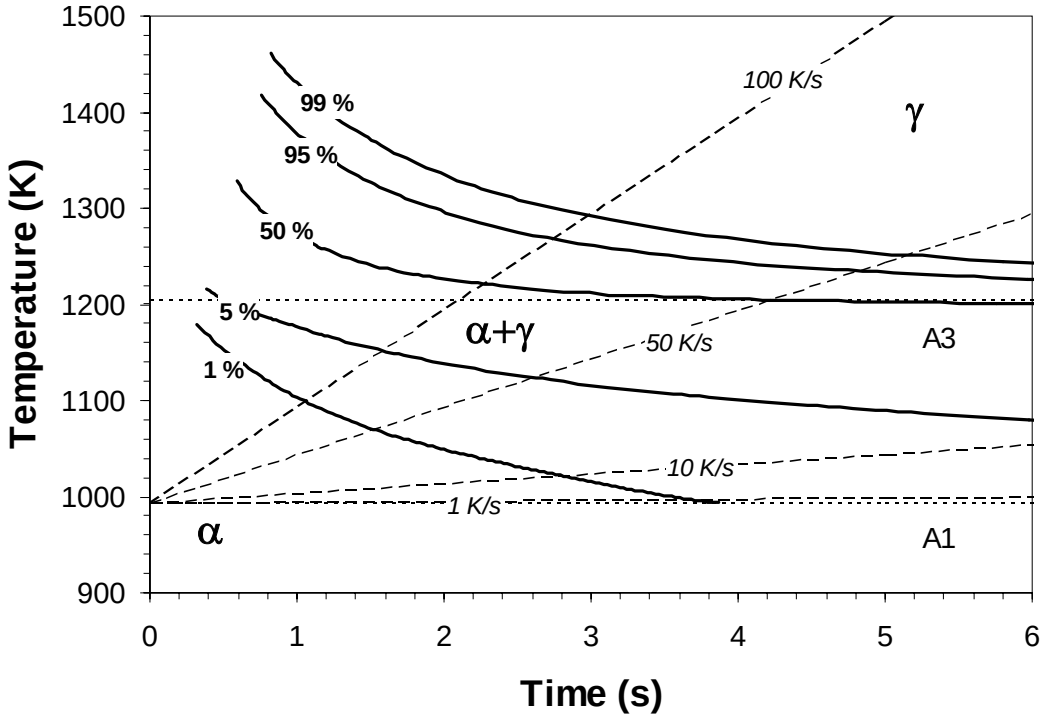

Fig. **5.14**: Calculated CHT diagram for $\alpha \rightarrow \gamma$ transformation during heating of 1005 steel.

5.1.4.6 Kinetics of γ grain growth

The existing MC model [17,18] was used to calculate the γ grain growth kinetics after the completion of the α→γ transformation during heating. As discussed previously, significant γ grain growth only occurs in the regions where the α completely transforms into γ. Hence, a prerequisite of the MC model is the knowledge of the single γ region. In this study, the JMA equation with the kinetic parameters developed in the previous section were used to obtain such information. As shown in Fig. 5.8, the typical heating rate during the α→γ transformation in the HAZ is about 80 K/s. Based on the CHT diagram (Fig. 5.14) computed using the JMA equation, a superheat of about 66 K above the A3 temperature (1204 K) is predicted for the completion of the transformation. Therefore, a temperature of 1270 K was assumed to represent the starting temperature of the γ grain growth in the entire HAZ. It should be noted that the actual completion temperature of the α→γ transformation depends on the local heating rate, and varies in different locations in the HAZ. However, using a constant temperature for representing the start of γ grain growth is reasonable, since the grain growth is a thermal-activated process, and the majority growth takes place at elevated temperatures [17,18].

The γ grain size immediately after the α→γ transformation is another prerequisite to use MC model to simulate γ grain growth. Experimental measurement of this initial γ grain size in the weldment is difficult, since the initial γ structure is altered by the subsequent transformations such as the γ→α transformation during cooling. In this study, the initial γ grain after the α→γ transformation is assumed to have an average size of 10.8 μm, i.e., one half of the average ferrite grain size of the base metal (21.6 μm). This assumption might be reasonable in the 1005 steel arc welds for the following reason. As shown in Fig. 5.2, the base metal of the 1005 steel largely consists of equiaxed α grains. For simplicity, these equiaxed α grains in the base metal are approximated by hexagons in two dimensions [39], as shown in Fig. 5.15(a). As discussed in section 5.1.4.4, the JMA exponent of 1.45 suggested that the α→γ transformation during heating is controlled by growth with zero nucleation rate [31]. In other words, all the possible

nucleation sites are consumed at the beginning of this transformation. Therefore, it is possible to assume that the γ phase nucleates simultaneously at all the ferrite grain boundary triple points (indicated by the solid dots). Such nucleation event consumes all the available nucleation sites, and the nucleated γ grains start growing into the α phase, as shown in Fig. **5.15(b)**. If the above transformation mechanism is true, it is reasonable to assume that the transformed γ grains have an average size equal to a half of that of the parent α grains, as shown in Fig. **5.15(c)**. Hence, such initial γ grain size provides a reasonable starting assumption.

The computed γ grain structure at the weld top surface is shown in Fig. **5.16**. This snapshot was taken just prior to the γ decomposition during cooling. A shown in this figure, spatial gradient of γ grains exists in the HAZ: the closer to the FZ, the larger the grain size; and vice versa. Such spatial grain gradient results from the local variation of heating rates and peak temperatures.

Figure **5.17** plots the calculated mean γ grain size as a function of distance from the FZ boundary. As shown in this figure, severe γ grain growth takes place in the HAZ of the 1005 steel arc weld, particularly in the region close to the FZ. The computed maximum γ grain size is almost eight times higher than the initial size. It is interesting to notice that at a distance about 1.2 mm from the FZ boundary, there is a region with fine γ grains. No significant γ growth occurs in this region because of the relatively low temperature history it undergoes. The average γ grain size is much less than that in the base metal. Hence, the MC simulation used here could capture the fine grain region (FGR) experimentally observed in the 1005 arc weld (Fig. **5.2**). It should be noted that the exact location of the FGR could not be determined by the MC simulation alone, since the γ phase transforms back into the α phase during cooling.

Since the γ grain structure after the grain growth is altered by the γ→α transformation during cooling, it is difficult to experimentally measure the γ grain size in the HAZ of the 1005 steel weld. Hence, the MC predictions have not been compared with experimental results. Further experiments are needed to validate the MC model.

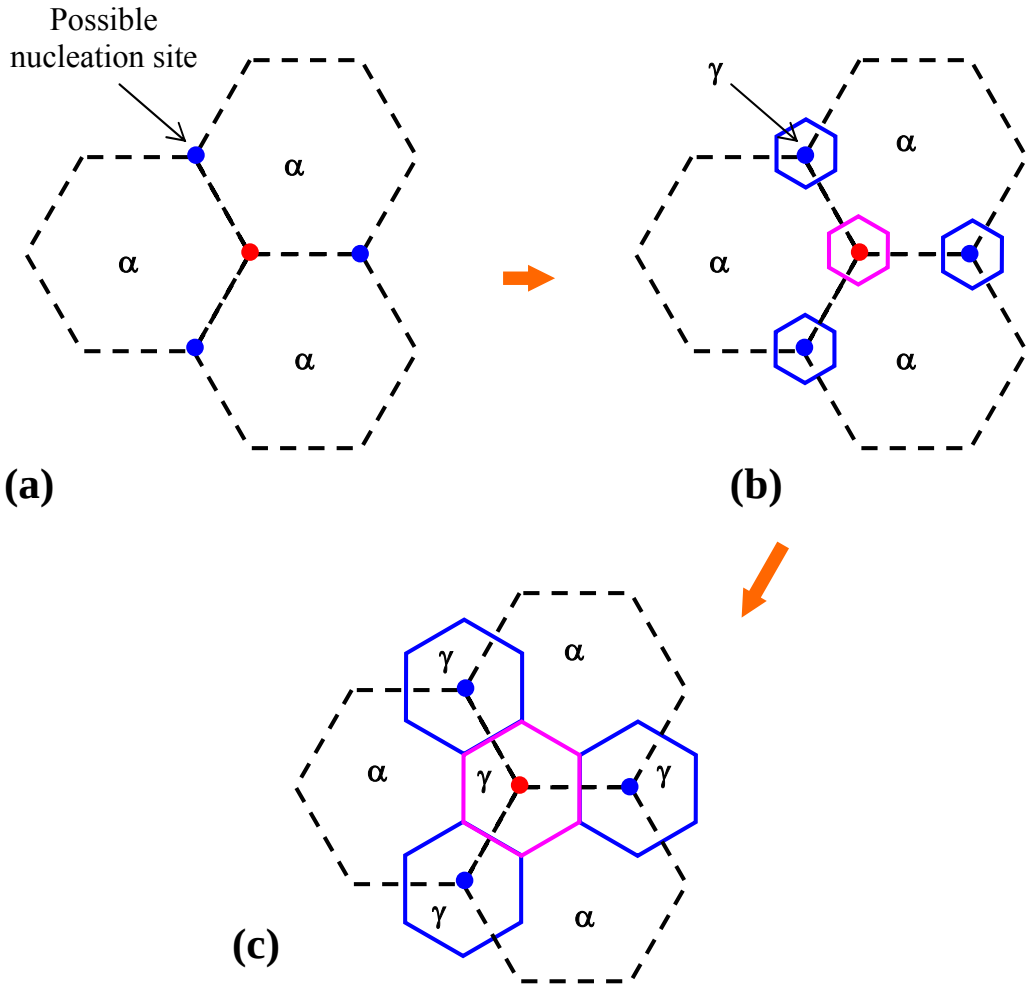

Fig. **5.15**: Schematic plot showing the α→γ transformation sequence during heating. (a) initial α grain structure, (b) nucleation and growth of γ grains, and (c) γ grain structure after the α→γ transformation.

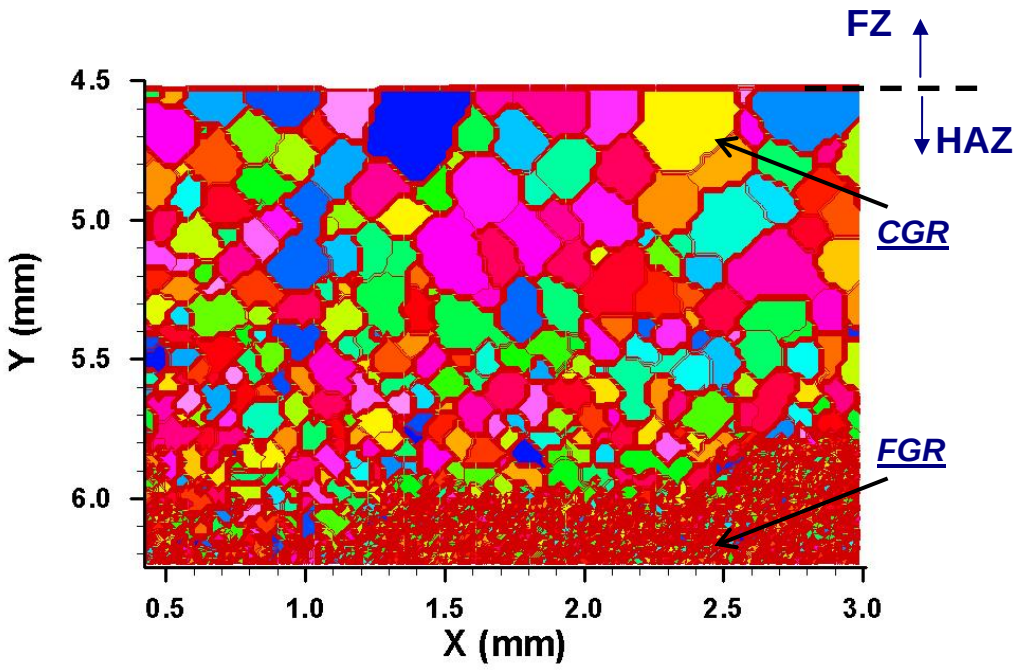

Fig. **5.16**: Computed γ grain structure at the weld top surface prior to the austenite decomposition during cooling. Symbols CGR and FGR represent the coarse grained region and fine grained region after the γ grain growth, respectively.

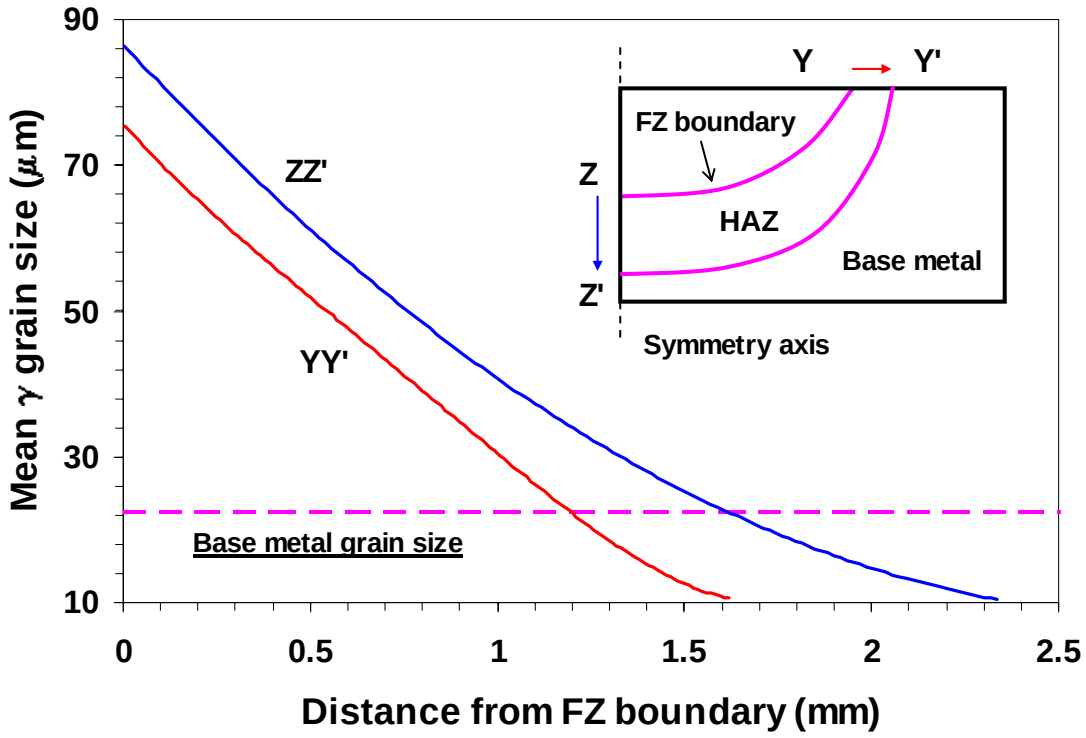

Fig. **5.17**: Calculated mean γ grain size as a function of distance from the FZ boundary using the MC model. Symbols YY' and ZZ' represent the directions along the weld top surface and the vertical symmetry plane, respectively, as shown in the inset figure.

5.1.4.7 Austenite decomposition during cooling

In steel welds, austenite decomposes into various ferrite microconstituents during cooling. The final weldment microstructure is the product of the $\gamma \rightarrow \alpha$ transformation. In this study, a model developed by Bhadeshia et al. [19-22] was used to investigate the austenite decomposition in both the FZ and HAZ of the 1005 steel arc welds. As discussed previously, the knowledge of prior γ grain size is a prerequisite for using the model. In the FZ, it is assumed that the solidification of the liquid metal results in a uniform prior austenite structure [19]. The average prior γ grain size of the FZ was measured along longitudinal sections of the weld, and was found to be about 150 μm. In the HAZ, the prior γ grain structure was calculated using the MC model, which provided quantitative data on the spatial γ grain size gradient.

Using Bhadeshia's model, the computed TTT diagram for the 1005 weld metal is plotted in Fig. 5.18. The TTT diagram consists of two curves. The upper C shaped curve at higher temperatures represents the γ to allotriomorphic ferrite transformation by diffusion, while the one at lower temperatures represents displacive transformations such as the γ to Widmanstatten ferrite and bainite. The $\gamma \rightarrow \alpha$ transformation during cooling exhibits the classical C curve kinetic behavior due to the interaction of two opposing effects: diffusion rates decrease with decreasing temperature, while the chemical driving force for the transformation increases. The martensite transformation is represented by a horizontal line, which indicates that the transformation is almost independent of time. It should be noted that the initially solidified regions in the FZ are depleted of solute such as carbon and manganese. In principle, these regions are first transformed to ferrite. However, due to the low carbon and alloy concentrations in the 1005 steel, the difference between the TTT curves for solute-depleted and bulk regions was fairly small. Hence, only the TTT curve for the bulk region was used. Figure 5.19 shows the CCT diagram computed from the TTT curves based on the Scheil additive rule [40]. The superimposed cooling curve was taken along the thermal cycle 2 in Fig. 5.8. It was found that the cooling curve intercepts both the replacive and displacive curves. Thus, both allotriomorphic and Widmanstatten ferrites are expected to form.

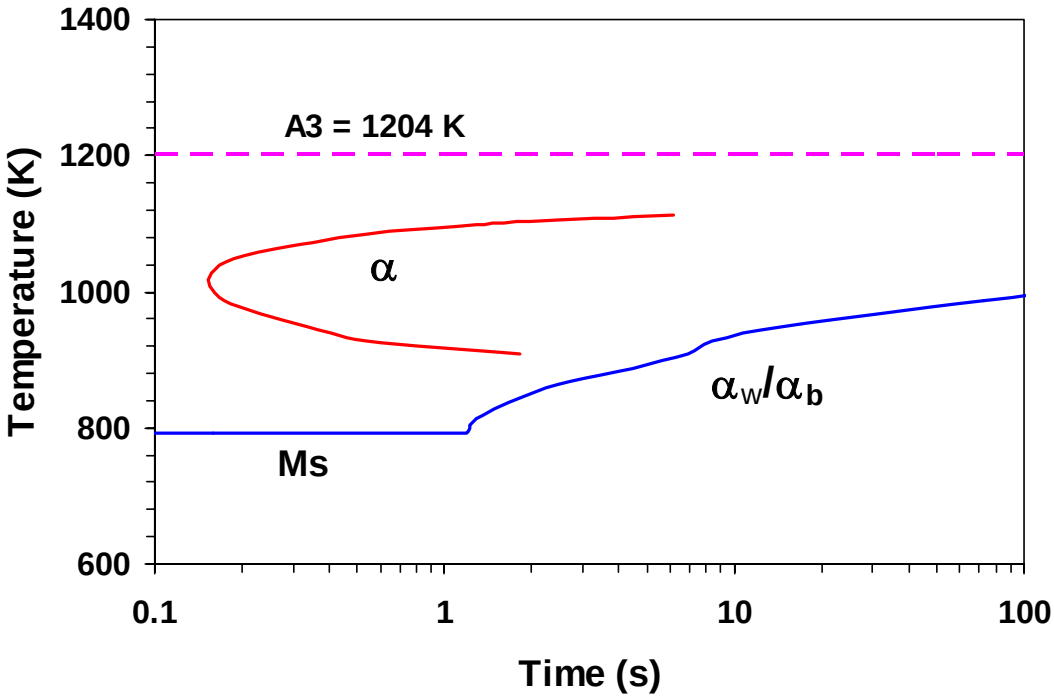

Fig. **5.18**: Calculated TTT diagram for the $\gamma \rightarrow \alpha$ transformation in the 1005 steel welds. Symbols α, α_w, α_b and Ms represent allotriomorphic ferrite, Widmanstatten ferrite, bainite and martensite, respectively. Time equal to zero corresponds to a temperature of 1273 K.

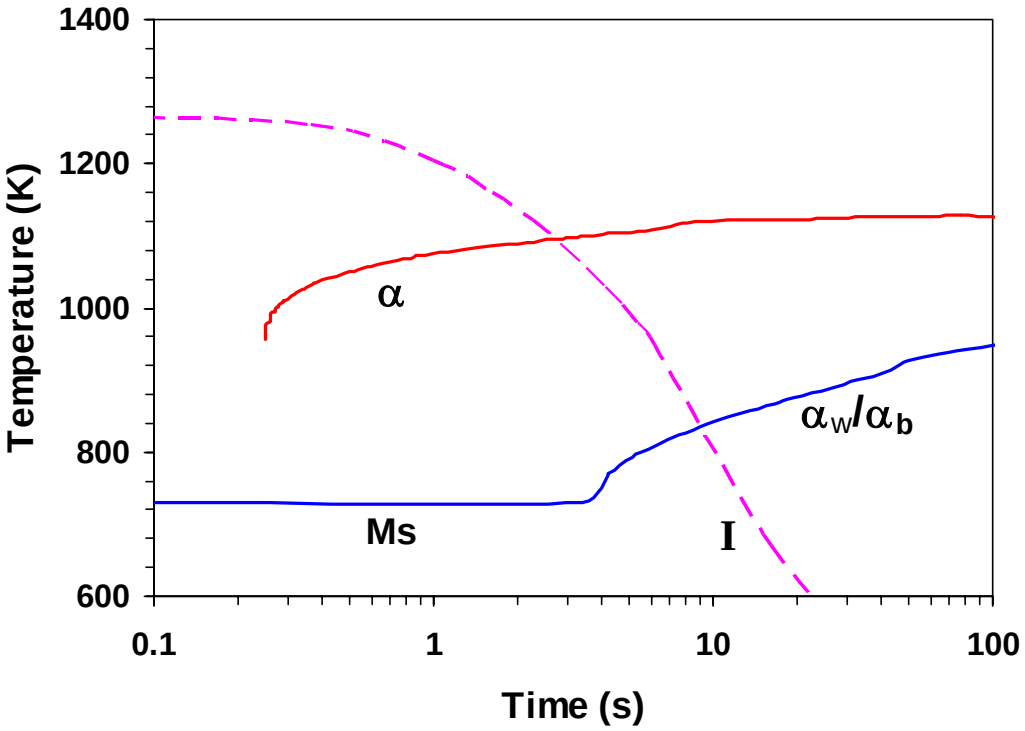

Fig. **5.19**: Calculated CCT diagram for the γ→α transformation in 1005 steel welds. The superimposed cooling curve I corresponds to a location of y = 2 mm in the FZ.

Using the measure prior γ grain size of the FZ and the computed thermal cycle at y = 2 mm, the calculated volume fractions of microconstituents in the FZ are shown in Table 5.3, while the calculated transformation start temperatures are summarized in Table 5.4. From Tables 5.3 and 5.4, it is observed that in the FZ, the γ to allotriomorphic ferrite transformation starts at 1089 K, and 35% of γ transforms into allotriomorphic ferrite. At 863 K, Widmanstatten ferrite transformation begins and an additional 54% of the γ converts into Widmanstatten ferrite. The remaining 11% austenite transforms into bainite and other ferrite microconstituents. Tables 5.3 indicates that good agreement was found between the calculated and the experimental volume fractions of allotriomorphic and Widmanstatten ferrites in the FZ.

Table 5.3: Comparison between the calculated and experimental volume fractions of microconstituents in the FZ. Symbols V_α, V_W, V_o represent the volume fractions of allotriomorphic ferrite, Widmanstatten ferrite and other microconstituents, respectively.

	Experimental volume fraction	Calculated volume fraction
V_α	31.6±3.7%	35%
V_W	59.0±2.2%	54%
V_o	9.4±3.3%	11%

Table 5.4: Calculated start temperatures of austenite to different ferrite microconstituents during cooling in the FZ of 1005 arc welds.

Transformation	Start Temperature (K)
Allotriomorphic ferrite	1089
Widmanstatten ferrite	863
Martensite	724

In the HAZ, the calculated γ grain sizes shown in Fig. **5.17** and the computed cooling rates were used in Bhadeshia's model to calculate the final microstructure at various locations. The results are plotted in Fig. **5.20**, showing the spatial variation of the HAZ microstructure. The allotriomorphic and Widmanstatten ferrites are the dominant microconstituents in the HAZ, which is consistent with the experimental observation shown in Fig. **5.3(b)**. As the distance from the FZ boundary increases, the fraction of the allotriomorphic ferrite increases whereas that of Widmanstatten ferrite decreases. This is due to the spatial variation of the prior γ grain size in the HAZ, which decreases away from the FZ boundary. Eq. **2.32** indicates that the fraction of allotriomorphic ferrite inversely depends on the prior γ size for a given thickening rate. The thickening rate of the allotriomorphic ferrite layer in the HAZ is expected to be roughly constant, since the spatial variations of composition and cooling rates are small. As a result, the larger the prior γ grain size, the less the fraction of allotriomorphic ferrite. Widmanstatten ferrite grows after the completion of the γ to allotriomorphic ferrite transition, and its fraction is thus limited by the remaining γ phase. It is interesting to notice that at a distance about 0.8 mm from the FZ boundary, the prior γ size is small enough so that the γ phase completely transforms into the allotriomorphic ferrite.

The prediction in the HAZ report here has not been verified with the experimental data. Such verification is suggested as a part of the future work.

5.1.5 Summary of phase transformation modeling in 1005 steel welds

Microstructure evolution during GTA welding of AISI 1005 low carbon steel was studied experimentally by the SRXRD technique and modeled using a combination of transport phenomena and phase transformation theory. The following conclusions can be made from this investigation.

(1) A three-dimensional heat transfer and fluid flow model was used to predict the thermal cycles in the entire weldment. The geometry of the FZ and HAZ predicted from the thermo-fluid model were in good agreement with the experimental results.

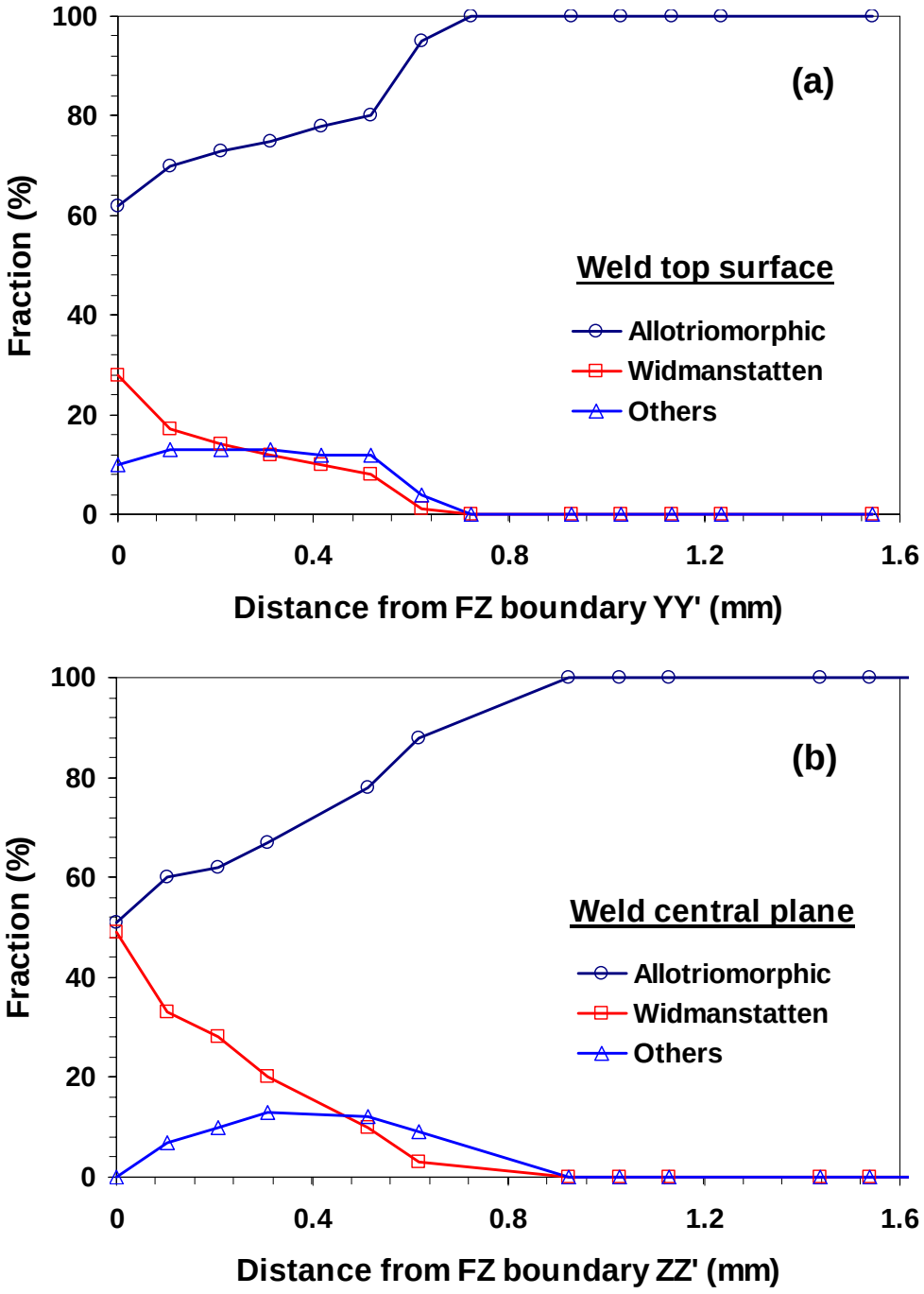

Fig. **5.20**: Spatial variation of the final microstructure in the HAZ. (a) the weld top plane, and (b) the symmetry plane. The YY' and ZZ' directions are shown in the inset plot of Fig. **5.17**.

(2) A JMA analysis considering non-isothermal heating and transformation in the $\alpha+\gamma$ two-phase field was used for the determination of the kinetics of the $\alpha\rightarrow\gamma$ transformation during weld heating. Using the SRXRD experimental data and an activation energy Q = 117.1 kJ/mole, the JMA kinetic parameters for the $\alpha\rightarrow\gamma$ transformation were determined to be ln (k_0) = 12.2, and n = 1.45. These kinetic parameters are consistent with a phase transformation controlled by diffusion of carbon with zero nucleation rate.

(3) TTT and CHT diagrams were calculated for the 1005 steel using the kinetic parameters determined from the SRXRD experiments, providing a graphical means to predict the $\alpha\rightarrow\gamma$ transformation on weld heating for the 1005 steel. These diagrams show that a significant level of superheat is required for the initiation and completion of the phase transformation under the heating rates common to arc welding.

(4) An existing MC model was used to calculate the γ grain growth kinetics in the HAZ. It was found that significant γ grain growth took place in the HAZ, particularly in the vicinity of the FZ. The computed maximum γ grain size is about eight times larger than that of the base metal. The calculated prior γ grain size was then used to understand the final microstructure in the HAZ.

(5) The microstructure of the 1005 steel weld consisted predominantly of allotriomorphic and Widmanstatten ferrites. An existing austenite decomposition model and the computed thermal cycles were used to calculate the volume fractions of microconstituents in both the FZ and HAZ. Good agreement was found between the calculated and the experimental volume fractions of allotriomorphic and Widmanstatten ferrites in the weld metal. The spatial variation of the final microstructure in the HAZ was also quantitatively determined.

Quantitative understanding of the $\alpha\rightarrow\gamma$ transformation during heating, γ grain growth, and $\gamma\rightarrow\alpha$ transformation during cooling represents a contribution to the growing quantitative knowledge base in fusion welding. The results indicate significant promise for understanding microstructure evolution in 1005 steel arc welds by a combination of advanced welding experiments, transport phenomena based calculation of thermal cycles, and phase transformation models. It should be noted that due to the difficulties in the

experiments, the computed γ grain size and the final microstructure in the HAZ were not verified. Further experiments and modeling are needed to better understand the phase transformations during GTA welding of 1005 steel.

5.2 Kinetics of α→γ Transformation in 1045 Steel Spot Arc Welds

It is known that the carbon content in steels has significant influence on the phase transformations, and it plays an important role in the microstructural evolution of steel welds [41,42]. In the previous section, the phase transformations in the 1005 steel, which contains only 0.05 wt% of carbon, were investigated. In particular, the kinetics of α-ferrite→γ-austenite transformation during heating was modeled using the JMA equation, and the kinetic parameters used in the equation were determined from the experimental data. In this section, the α-ferrite→γ-austenite transformation in the 1045 medium-carbon steel arc welds was examined. Comparison of the phase transformation kinetics in the two steels is useful to understand the effect of carbon in the microstructural evolution under welding conditions. The research methodology used here is similar to that used in the 1005 steel arc weld system, i.e., the time resolved x-ray diffraction technique (TRXRD) was used to obtain the real-time phase map and kinetic data during welding, the heat transfer and fluid flow model was used to compute the thermal cycles in the weldment, and the JMA model was used to quantitatively calculate the rates of the α→γ transformation during heating.

5.2.1 Time resolved x-ray diffraction experiments

The TRXRD experiments were done by Elmer et al. of Lawrence Livermore National Laboratory [9]. The 1045 medium-carbon steel containing 0.46 wt% C was rapidly heated and cooled during stationary arc welding. During welding, a synchrotron radiation was used to track the phase transformations that occurred in the HAZ of the weld. These experiments produced a series of x-ray diffraction patterns revealing the

real-time crystal structure of the weld. The experimental setup in TRXRD is very similar to that in SRXRD presented in section **5.1.1.2**. However, in TRXRD experiments, the synchrotron beam was focused on a fix location at the weld top surface, and the diffraction pattern was recorded as a function of time. This is because the weld heats and cools rapidly under the transient welding conditions. Time resolved experiments with resolution on the order of 50 ms were necessary to trace the phase transformations under rapid heating and cooling conditions. In contrast, in SRXRD experiments, the synchrotron beam scanned several regions of the weld top surface, and the spatial variation of the diffraction pattern was recorded. More details on the TRXRD experimental setup are available elsewhere [**9**].

5.2.2 Computed thermal cycles under transient welding conditions

The transient heat transfer and fluid flow model developed in Chapter 3 was used to compute the temperature and velocity fields during GTA spot welding of 1045 steel. The physical properties of the 1045 steel and other data used in the calculation are summarized in Table **5.5**. It should be noted that a common practice in the calculation of weld temperatures for linear welding is to use a constant arc efficiency to represent the amount of arc energy that transfers into the workpiece. This is a reasonable assumption since the temperature field attains quasi-steady state soon after the start of welding. In contrast, for transient spot welding, temperatures change continuously and it takes several seconds for the arc to stabilize. In view of the lack of data on arc efficiency in the literature, a variable arc efficiency, which increases linearly from 0 to 75% in the first 3 seconds, is used to take into account the arc instabilities. A flat plate geometry was used in the transient calculations. No significant error was introduced due to the calculations in the flat geometry, since the dimensions of the weld pool were much smaller than those of the cylindrical 1045 steel bar. The cross sectional shape of the calculated weld pool at its maximum size matched the experimental weld cross section, which had a width just under 10 mm and a maximum depth of 4.2 mm. Such agreement indicated the validity of the transient calculations.

Table 5.5: Physical properties of the 1045 medium-carbon steel [43] and other data used in the transient heat transfer and fluid flow calculations.

Name	Value
Liquidus Temperature, T_L, (K)	1768
Solidus temperature, T_S, (K)	1713
Latent heat of fusion, L, (J kg^{-1})	2.5×10^{5}
Density of liquid metal, ρ, (kg m^{-3})	7.7×10^{3}
Effective viscosity of liquid, μ, (kg m^{-1} s^{-1})	0.16
Thermal conductivity of solid, k_S, (W m^{-1} K^{-1})	36.4
Effective thermal conductivity of liquid, k_L, (W m^{-1} K^{-1})	335
Specific heat of solid, C_{PS}, (J kg^{-1} K^{-1})	586
Specific heat of liquid, C_{PL}, (J kg^{-1} K^{-1})	746
Temperature coefficient of surface tension, dγ/dT, (N m^{-1}·K^{-1})	-4.3×10^{-4}
Coefficient of thermal expansion, β, (K^{-1})	1.51×10^{-5}
Convective heat transfer coefficient, h_c, (W mm^{-2} K^{-1})	159
Sulfur content in the base metal (wt%)	0.02
Arc radius, r_b, (mm)	2.3
Power distribution factor, f_d	0.5
Arc current (A)	153
Arc voltage (V)	17.2
Arc on time (s)	17
Grid system	108×54×59
Computational domain sizes: length, width and depth (mm)	140, 70 and 49
Time step (s)	0.01

Figure 5.21 plots the computed thermal cycles at locations 4.75, 5.0 and 5.5 mm from the weld center. The 5.0 mm location corresponds to the position of the x-ray beam during the TRXRD experiment. Superimposed on this plot are the A1 (985 K) and A3 (1038 K) temperatures of the 1045 steel and two symbols. The open circle and triangle represent the times when the start and finish of the $\alpha \rightarrow \gamma$ transformation on heating, respectively, are observed. The temperature versus time data shown in Fig. 5.21 are prerequisite for analyzing the TRXRD results.

5.2.3 JMA analysis of TRXRD results during heating

The measured γ fraction versus time data at a monitoring location of 5 mm from the weld center (R = 5.0 mm) are plotted in Fig. 5.22. Modeling of these experimentally measured data is useful to understand the mechanisms behind the transformation and to develop parameters useful in the prediction of phase transformation kinetics. Here, the JMA model developed in the previous section was used to describe the $\alpha \rightarrow \gamma$ transformation in the 1045 steel, since it is known that the transformation of the pearlitic microstructure to γ during heating is controlled by the carbon diffusion in γ [44].

The overall activation energy for the $\alpha \rightarrow \gamma$ transformation in the 1045 steel under non-isothermal welding conditions, in which nucleation and growth are operating simultaneously, is not readily available in the literature. However, since the transformation is largely controlled by the carbon diffusion in austenite [44], it may be treated as a growth controlled mechanism, and the activation energy for growth provides a reasonable starting assumption. Therefore, an assumed activation energy of Q = 117.1 kJ/mole [37] was used in the calculations. For the given Q value, a numerical fitting routine was used to determine the minimum error between the JMA calculations and the experimentally determined austenite fraction as a function of ln (k_0) and n. A total of 37 TRXRD data points were used in the calculation, and the optimization results are plotted in Fig. 5.23, showing that the optimal JMA values are n = 0.82 and ln (k_0) = 12.3. Figure 5.22 compares the calculated and measured fractions of austenite as a function of

time. The correlation is reasonable, showing that the JMA best fit to the experimental results adequately represents the data throughout the entire transformation range.

It should be noted that the above JMA kinetic parameters were calculated using the computed temperature versus time data at R = 5.0 mm. Although the distance from a monitoring location to the weld center is exact in the numerical calculation, there are certain errors in the spatial accuracy of the experimental TRXRD data. For the present TRXRD experiments, the uncertainty in the monitoring location of the x-ray beam is about ±0.25 mm. As shown in Fig. **5.21**, such uncertainty of ±0.25 mm in the monitoring location results in an uncertainty of ±70 K in the computed temperatures, which, in turn, contributes to uncertainties in the transformation kinetics. To determine how much the temperature uncertainties affect the kinetic results, the optimization procedure described previously was used to calculate the JMA kinetic parameters for each of the three thermal cycles shown in Fig. **5.21**. Table **5.6** summarizes these results, showing that the correlation for all three thermal cycles is reasonable. Due to the uncertainty in the monitoring location, the uncertainties in the values of n and ln (k_0) were calculated to be about ±0.2 and ±1.0, respectively. Due to the lack of kinetic data in the literature, the calculated JMA kinetic parameters cannot be further verified, and the lack of available data emphasizes the need for additional quantitative investigations on this topic.

It is interesting to compare the kinetics of $\alpha \rightarrow \gamma$ transformation in the 1005 low-carbon and 1045 medium-carbon steels. Such comparison is useful to understand the influence of the carbon content on the weld microstructural evolution. To do this, the JMA parameters for the 1005 steel developed in the previous section were used to predict the fraction austenite for the same time versus temperature profile in the 1045 steel weld, i.e., R = 5.0 mm location. Figure **5.22** shows the comparison of the transformation rates in the two steels, where the dashed line represents the predicted transformation for the 1005 steel, and the solid line for the 1045 steel. As shown in this figure, the two curves start and finish at approximately the same times. However, the transformation rate of the 1045 steel is initially somewhat higher than that of the 1005 steel, but eventually slows down to values less than that of the 1005 steel.

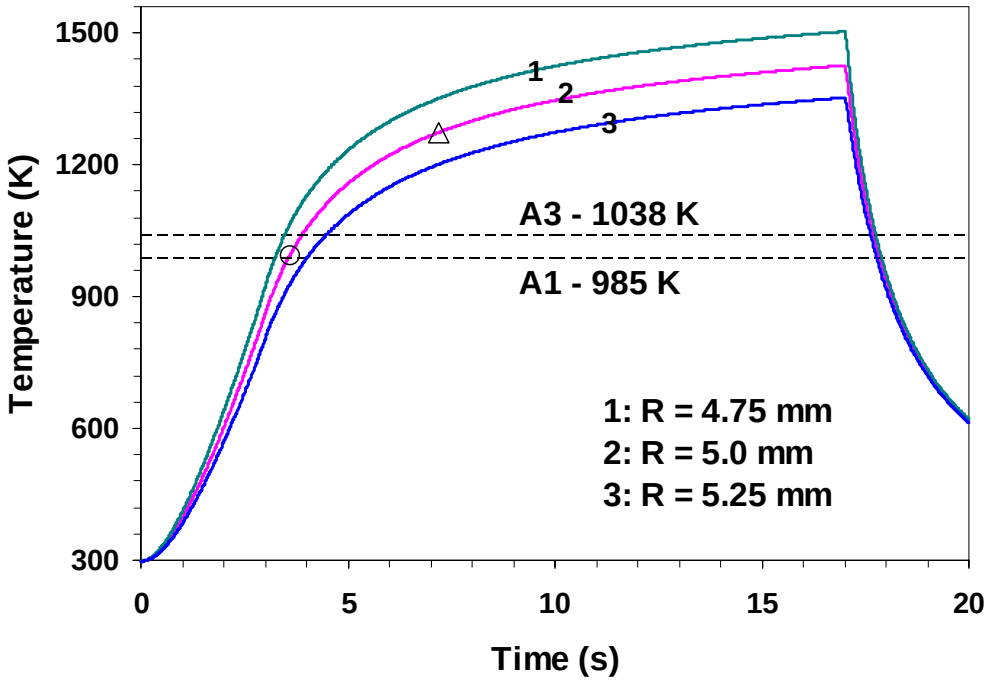

Fig. **5.21**: Calculated weld thermal cycles at three monitoring locations, where R is the distance from a location to the weld center at the top surface. The x-ray beam is located at R = 5.0 mm. The A1 and A3 temperatures for the 1045 steel were calculated using ThermoCalc and the Fe2000 database [**9**].

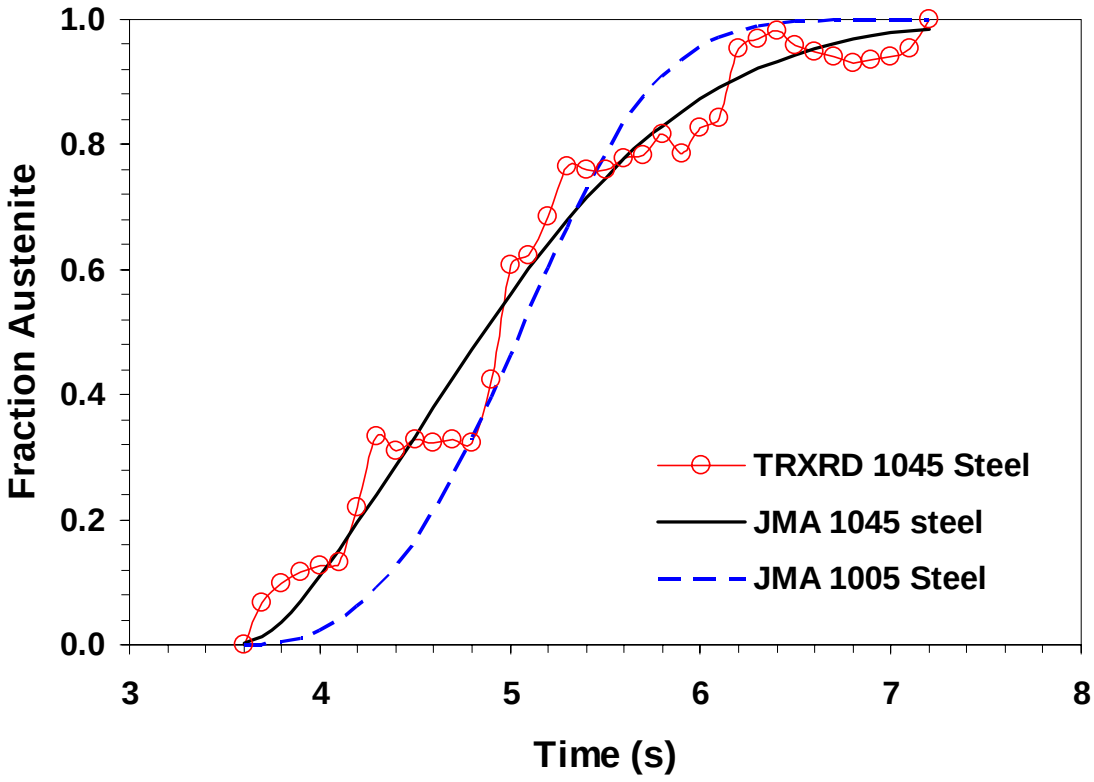

Fig. **5.22**: Kinetics of the ferrite to austenite transformation on weld heating. The TRXRD data for the 1045 steels are given by the solid circles and solid best-fit line, are compared to the JMA parameters for the 1005 steel (dashed line) from the previous study.

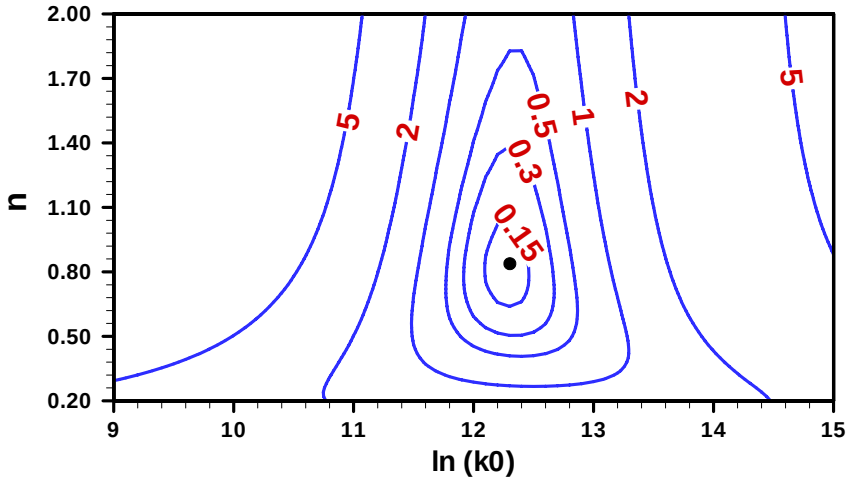

Fig. **5.23**: Error contour plot showing the optimal n and ln (k_0) values for the 1045 steel. An activation energy of Q = 117.1 kJ/mole was assumed, and the solid circle represents the optimal values of the JMA parameters n = 0.82 and ln (k_0) = 12.3.

Table **5.6**: Summary of JMA modeling results on the 1045 steel, and comparison with previous data on the 1005 steel.

Steel	Thermal cycle location	Q (kJ/mole)	n	ln (k_0)	Fitting error
1045	R = 4.75 mm	117.1	0.95	11.4	0.049
1045	R = 5.0 mm	117.1	0.82	12.2	0.052
1045	R = 5.25 mm	117.1	0.60	13.4	0.075
1005	R = 5.0 mm	117.1	1.45	12.3	0.099

The variations in the transformation rates for the two steels can be explained by the different carbon contents of the two steels and the resulting different starting microstructures. The 1005 steel contained less than 10% of pearlite and small pearlite colonies were isolated along the ferrite grain boundaries. In contrast, the 1045 steel contained 88% of pearlite, which occupied the majority of the microstructure. The austenite nucleation rate is higher in pearlite than in ferrite, due to the fine dispersion of cementite in the lamellar pearlitic structure. Therefore, in the early stage of the transformation, it is expected that the 1045 steel, which has the higher fraction of pearlite, would transform to austenite more quickly than the 1005 steel. However, toward the end of the transformation, the available nucleation sites in both steels are consumed completely, and the transformation is then controlled by the diffusion growth. It is known that the transformation rate of diffusion controlled reactions decreases as the grain size gets larger due to the longer diffusion distance [4,31]. Since the grain size for the 1045 steel is four times larger than that for the1005 steel, it might be expected that the total time required to transform the 1045 steel would be longer than that of the 1005 steel.

5.2.4 Summary of phase transformation modeling in 1045 steel welds

TRXRD experiments were performed in the HAZ of the 1045 medium-carbon steel during transient spot arc welding by Elmer et tal. [9]. These experimental observations provided the relative fraction of α and γ phases during rapid weld heating. The transient heat transfer and fluid flow model was used to predict weld temperatures as a function of weld time and location. The model was validated by comparing the predicted and experimentally measured geometry of the FZ. The TRXRD results were analyzed to model the kinetics of the $\alpha \rightarrow \gamma$ transformation during heating of the 1045 steel using the JMA model and the computed weld temperatures. The results yielded kinetic parameters of n = 0.82 and ln (k_0) = 12.3 for the activation energy of Q = 117.1 kJ/mole. The JMA results of the $\alpha \rightarrow \gamma$ transformation of the 1045 steel were then compared with those of the 1005 low-carbon steel calculated in the previous section. It

was found that the initial transformation rate of the 1045 steel is more rapid than that of 1005 steel, but that the transformation rate of the 1045 steel slows down, eventually requiring more time than the 1005 steel to complete the transformation to austenite. The higher fraction of pearlite in the microstructure of the 1045 steel resulted in its initial high transformation rate, but its larger grain size resulted in its longer total transformation time than the 1005 steel.

The JMA kinetic analysis of the TRXRD data adequately describes the transformation kinetics of the 1045 steel, providing a quantitative means for predicting austenite formation in the HAZ of similar carbon content steel welds. Comparisons between the $\alpha \rightarrow \gamma$ transformation kinetics of the 1045 steel and 1005 steel illustrated how the carbon content affects the transformation rate through its affect on the starting microstructure of the base metal. It should be noted that the Q value for the 1005 steel (i.e., 117.1 kJ/mol) was also assumed to be valid in the 1045 steel, due to the lack of kinetic data available in the literature. Hence, the two kinetic parameters, n and k_0, reported in here should be interpreted carefully.

5.3 Kinetics of α-Ti→β-Ti Transformation in Ti-6Al-4V Spot Arc Welds

In this study, the TRXRD method was used to directly observe phase transformations during GTA transient spot welding of Ti-6Al-4V alloy by Elmer et al. [10]. One location in the FZ and two locations in the HAZ of the weld were examined. At these different locations, the α-Ti→β-Ti transformation proceeded under different heating rates to different peak temperatures, resulting in different microstructures. Transient heat transfer and fluid flow modeling was used to calculate weld temperatures as a function of time and location. By combining the computed temperatures and TRXRD data, kinetics of the $\alpha \rightarrow \beta$ transformation in the Ti-6Al-4V alloy were determined using the JMA analysis. Such analysis of the weld heating kinetics produced a set of parameters that allowed the prediction of the $\alpha \rightarrow \beta$ transformation rate under different heating conditions.

5.3.1 Experimental procedures

The composition of the Ti-6Al-4V ELI (extra low interstitial) alloy used in the experiments were as follows (by wt%): 6.0 Al, 4.2 V, 0.11 O, 0.17 Fe, 0.014 C, 0.009 N, 0.03 Si, and bal. Ti. GTA spot welds were made on the Ti-6Al-4V samples by striking a stationary arc, maintaining this arc for a fixed amount of time, and then extinguishing the arc to let the weld cool. TRXRD data were gathered at three different locations at the weld top surface: 4.5 mm, 5.0 mm and 5.5 mm from the weld center. The welding parameters used were 100 amperes and 19 volts with an arc on time of 17 s to 20 s, resulting weld pools with a diameter just less than 10 mm. Additional details about the TRXRD experiments are available in the literature [**10**].

5.3.2 Computed thermal cycles

Similar to the study in 1045 spot arc welds reported in the previous section, the transient heat transfer and fluid flow model was also used to compute the temperature and velocity fields during GTA transient spot welding of Ti-6Al-4V alloy. The physical properties of the Ti-6Al-4V alloy and other data used in the calculation are summarized in Table **5.7**. For the accurate calculation of weld temperature distribution, the thermal conductivity (k_S) of solid Ti-6Al-4V is taken as temperature dependent based on the data available in the literature [**45**]. A variable arc efficiency was used for the first 2 seconds of the arc on time, as the arc establishes itself.

The calculated weld time versus temperature plots for each of the three x-ray locations are shown in Fig. **5.24**. It is clear that the monitoring location closest to the center of the weld heated the fastest, and was the only location of the three to reach the liquidus temperature. The other two x-ray locations had temperatures that exceeded the β transus temperature (1248 K) and were held above this temperature for times in excess of 10 s prior to extinguishing the arc.

Table 5.7: Physical properties of Ti-6Al-4V alloy [45,46] and other data used in the weld heat flow calculations.

Name	Value
Liquidus Temperature, T_L, (K)	1928
Solidus temperature, T_S, (K)	1878
Density of liquid metal, ρ, (kg m^{-3})	3.89×10^{3}
Effective viscosity of liquid, μ, (kg m^{-1} s^{-1})	0.049
Thermal conductivity of solid, k_S, (W m^{-1} K^{-1})	8.3 to 24.2
Effective thermal conductivity of liquid, k_L, (W m^{-1} K^{-1})	32.5
Specific heat of solid, C_{PS}, (J kg^{-1} K^{-1})	725
Specific heat of liquid, C_{PL}, (J kg^{-1} K^{-1})	872
Temperature coefficient of surface tension, $d\gamma/dT$, (N $m^{-1}\cdot K^{-1}$)	-2.8×10^{-4}
Coefficient of thermal expansion, β, (K^{-1})	1.1×10^{-5}
Convective heat transfer coefficient, h_c, (W mm^{-2} K^{-1})	159
Arc efficiency, η (%)	0 to 74.1
Arc radius, r_b, (mm)	3.75
Power distribution factor, f_d	0.5
Arc current (A)	100
Arc voltage (V)	19
Arc on time (s)	17 to 20
Grid system	110×55×48
Computational domain sizes: length, width and depth (mm)	92, 46 and 32
Time step (s)	0.1

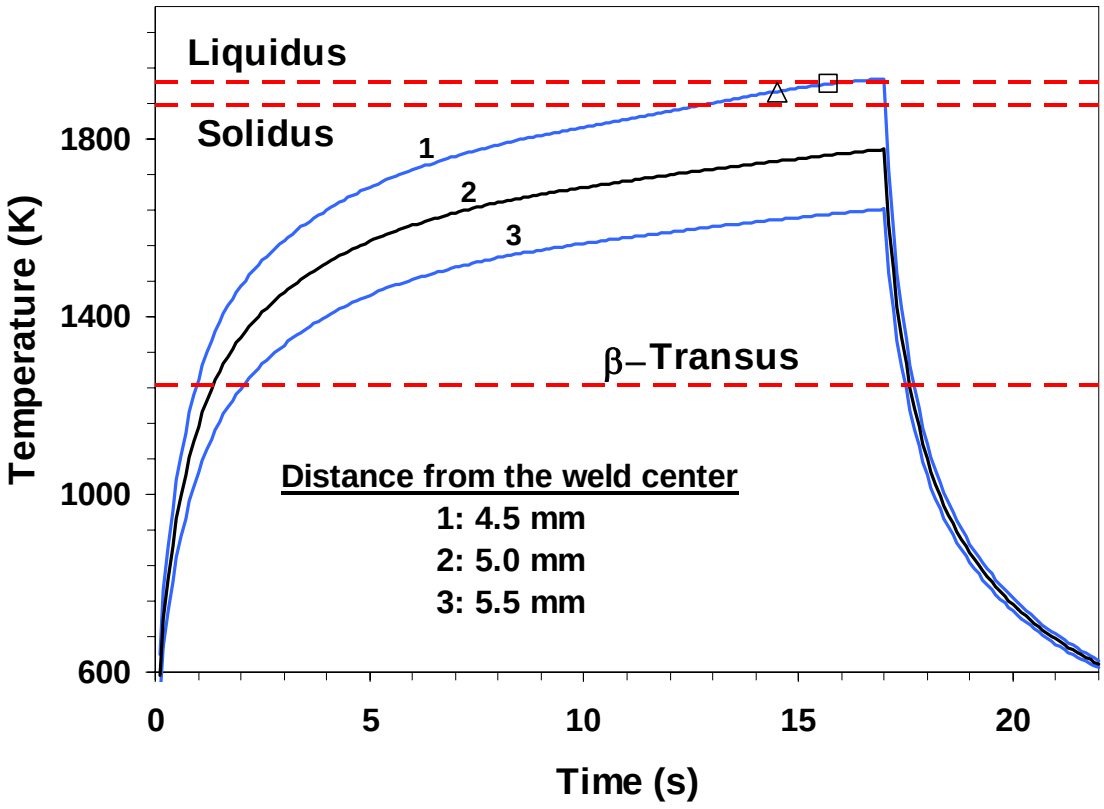

Fig. **5.24**: Calculated weld thermal cycles at the three x-ray locations. The open triangle marks the TRXRD time where melting was observed to begin, and the open square where melting was observed to be complete.

5.3.3 Analysis of TRXRD data

Figure 5.25 shows the experimentally measured β fraction as a function of time at three monitoring locations during weld heating, showing that the transformation followed a general sigmoid shape curve at each location. More rapid heating and higher transformation rates occurred at the locations closest to the weld center. The kinetics of the α→β transformation at each location were modeled using the JMA approach to develop a set of parameters that could be used to predict the extent of the phase transformation for different weld heating rates.

As discussed previously, the activation energy (Q) in the JMA equation includes the contributions from both nucleation and growth. The activation energy for the α→β transformation in Ti-6Al-4V alloy is not readily available in the literature. In the present study, the values of Q and k_0 were determined from the TRXRD experimental data for an assumed n value of 4. The n value of 4 implies an interface controlled growth with a constant nucleation [23]. In other words, it is assumed that the nucleation and growth occur simultaneously during the α→β transformation. The computed optimal kinetic parameters (Q and k_0) at each of the three monitoring locations are summarized in Table 5.8. The average error between the fitted and experimental data points is reasonably small at all three locations. It is found that the ln (k_0) value varied from 8.2 to 12.0, and the Q value changed from 144 to 188 kJ/mole, both increasing with the distance from the weld center. Table 5.8 also shows the optimal JMA parameters determined when all the TRXRD data at the three locations were used. This set of kinetic parameter was then used to calculate the transformation kinetics at the three locations. The results are superimposed as the solid lines over the measured β fraction versus time plots shown in Fig. 5.25, illustrating a fair agreement in all three cases.

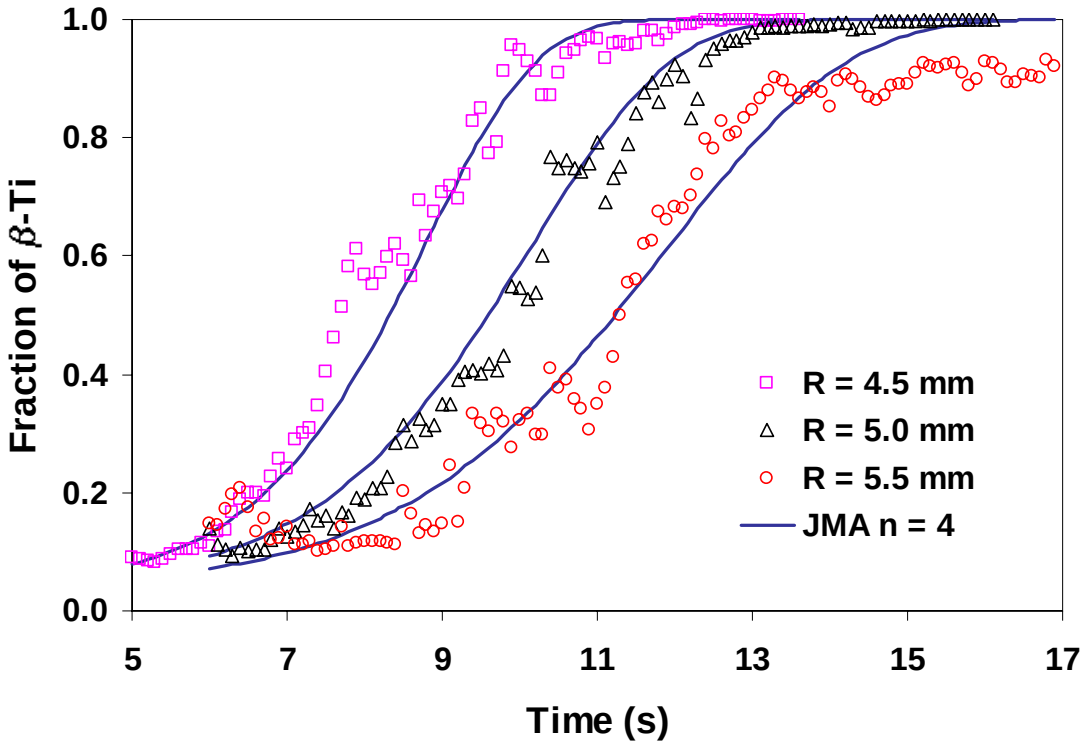

Fig. **5.25**: TRXRD results showing the fraction of β-Ti as a function of weld time during heating at three monitoring locations. The solid lines are computed using the following set of JMA kinetic parameters: n = 4, Q = 189 kJ/mol and ln (k_0) = 11.4.

Table 5.8: Summary of the calculated JMA parameters Q and k_0 for each of the weld locations, using an assumed n value of 4. The JMA kinetic parameters for the α→β transformation in the commercially pure titanium [17] are also listed.

Location	n	ln (k_0)	Q (kJ/mol)	Average error
R = 4.5 mm	4	8.2	144	0.043
R = 5.0 mm	4	11.2	186	0.064
R = 5.5 mm	4	12.0	188	0.063
All data	4	11.4	189	0.055
Pure titanium	3	14.6	153	

In the literature, the α→β transformation in the commercially pure titanium has been reported to be controlled by the titanium atom short range diffusion with zero nucleation rate [17]. The JMA kinetic parameters in the pure titanium are also summarized in Table 5.8. Comparing the parameters for the commercially pure titanium and the Ti-6Al-4V alloy, the activation energy is quite similar in both systems. This may suggest that the α→β transformation during heating of Ti-6Al-4V is also controlled by the α/β interface movement, while the nucleation of β phase plays an important role in the overall transformation kinetics.

5.3.4 Summary of phase transformation modeling in Ti-6Al-4V alloy welds

TRXRD experiments employing synchrotron x-ray radiation were performed in-situ on transient GTA welds on the Ti-6Al-4V alloy, providing real-time observations of the α→β transformation in both the weld FZ and HAZ [10]. The transient numerical model was used to predict the weld temperature distribution. The kinetics of the α→β transformation on heating were modeled using the JMA approach. Such analysis produced a set of JMA kinetic parameters (i.e., n = 4, Q = 189 kJ/mole, and ln (k_0) = 11.4) for the prediction of the transformation rate under various heating conditions.

It should be noted that although the JMA modeling approach successfully produced sets of parameters that allow the weld heating transformation rate to be predicted, the transformation mechanism was not definitively established. The difficulties associated with using the JMA approach to determine activation energies for transformations involving nucleation and growth have been observed by other investigators [47], and additional studies will be required to provide more conclusive evidence for the transformation mechanism during weld heating of Ti-6Al-4V.

5.4 Summary and Conclusions

In this chapter, the phase transformations during GTA welding of the 1005 low-carbon steel, 1045 medium carbon steel, and Ti-6Al-4V alloy were investigated by a combination of experiments and modeling. The experiments involved the real-time phase mapping using the x-ray diffraction technique. Numerical heat transfer and fluid flow calculations were used to obtain the weld temperature distribution, heating and cooling rates under both linear and transient spot welding conditions. The computed FZ geometries using the thermo-fluid model were compared with the experimental results. A kinetic model based on the JMA theory was developed to describe the kinetics of phase transformations controlled by the nucleation and growth mechanism. The JMA kinetic parameters were computed from the x-ray diffraction data, allowing the rates of phase transformations to be predicted under various heating conditions. In particular, the kinetic parameters were determined for the α-ferrite to γ-austenite transformation in the 1005 low-carbon and 1045 medium carbon steels, and the α-Ti to β-Ti transformation in the Ti-6Al-4V alloy under welding conditions. The consistence of the computed JMA parameters was validated by comparing the JMA predictions with the experimental results obtained using the x-ray diffraction technique.

It should be noted that the JMA kinetic parameters depend strongly on the starting microstructure of the base material. The dependence of the parameters on the initial microstructure cannot be easily determined at this time due to the lack of quantitative

kinetic data in the literature. The lack of kinetic data emphasizes the importance of quantitative study of the microstructural evolution during welding, and the kinetic parameters reported in this chapter should be used carefully. In the next chapter, a numerical diffusion model is developed to describe the γ-austenite→δ-ferrite transformation in the 2205 duplex stainless steel arc weld. The effect of the staring microstructure on the transformation rates is investigated using the diffusion model.

5.5 References

1. K. Easterling: *Introduction to the Physical Metallurgy of Welding*, 2nd Edition, Butterworth-Heinemann, Oxford, 1992.

2. S. Kou: *Welding Metallurgy*, 2nd edition, John Wiley & Sons, New Jersey, Hoboken, 2003.

3. L. E. Svensson: *Control of Microstructures and Properties in Steel Arc Welds*, CRC Press, 1994.

4. Ø. Grong: *Metallurgical Modeling of Welding*, 2nd edition, The Institute of Materials, London, 1997.

5. W. Pitscheneder, R. Ebner, T. Hong, T. DebRoy, K. Mundra and R. Benes: in *Mathematical Modelling of Weld Phenomena 4*, edited by H. Cerjak, p. 4, 1998.

6. T. DebRoy and S. Kou: *Heat Flow in Welding*, Chapter 3, Welding Handbook, vol. 1, 9th Edition, American Welding Society, p. 87, 2001.

7. J. W. Elmer, J. Wong and T. Ressler: *Metall. Mater. Trans. A*, **32A**, 175 (2001).

8. T. A. Palmer, J. W. Elmer and J. Wong: *Sci. Technol. Weld. Joining*, **7**, 159 (2002).

9. J. W. Elmer, T. A. Palmer, S. S. Babu, W. Zhang and T. DebRoy: *In-Situ Observations of Austenite, Bainite and Martensite Formation During Arc Welding of 1045 Steel*, submitted to Welding Journal, February 2004.

10. J. W. Elmer, T. A. Palmer, S. S. Babu, W. Zhang and T. DebRoy: *J. Appl. Phys.*, in press, April 2004.

11. R. Mancini and C. Budde: *Acta Mater.*, **47**, 2907 (1999).

12. R. C. Reed, T. Akbay and Z. Shen: *Mater. Sci. Eng. A*, **256**, 152 (1998).

13. J. W. Elmer, J. Wong, M. Fröba, P. A. Waide and E. M. Larson: *Metall. Mater. Trans. A*, **27A**, 775 (1996).

14. J. Wong, M. Fröba, J. W. Elmer, P. A. Waide and E. M. Larson: *J. Mat. Sci.*, **32**, 1493, (1997).

15. J. W. Elmer, J. Wong and T. Ressler: *Metall. Mater. Trans. A*, **29A**, 2761, (1998).

16. J. W. Elmer, J. Wong and T. Ressler: *Scripta Mater.*, **43**, 751 (2000).

17. Z. Yang, J. W. Elmer, J. Wong, and T. DebRoy: *Weld. J.*, **79**, 97s (2000).

18. S. Mishra and T. DebRoy: *Acta Mater.*, **52**, 1183 (2004).

19. H. K. D. H. Bhadeshia and L. E. Svensson: in *Mathematical Modeling of Weld Phenomena*, edited by H. Cerjak et al., Institute of Materials, London, p. 109 (1993).

20. H. K. D. H. Bhadeshia, L. E. Svensson and B. Gretoft: *Acta metall.*, **33**, 1271 (1985).

21. H. K. D. H. Bhadeshia: *Bainite in Steels*, 2nd Edition, Institute of Materials, London, 2001.

22. H. K. D. H. Bhadeshia: *Metal Sci.*, **16**, 159 (1982).

23. L. E. Samuels: *Light Microscopy of Carbon Steels*, ASM International, Materials Park, OH, 1999.

24. IIW: Guide to the Light Microscope Examination of Ferritic Steel Weld Metals, *Weld. World*, **29**, 160 (1991).

25. K. Mundra, T. DebRoy, and K. Kelkar: *Numer. Heat Transfer A*, **29**, 115 (1996).

26. J. W. Elmer, T. A. Palmer, W. Zhang, B. Wood and T. DebRoy: *Acta Mater*, **51**, p. 3333 (2003).

27. T. Akbay, R.C. Reed and C. Atkinson: *Acta Metall. Mater.*, **47**, 1469 (1994).

28. M. Hillert, K. Nilsson and L.-E. Törndahl: *J. Iron Steel Inst.*, **209**, 49 (1971).

29. A. Roósz, Z. Gácsi and E. G. Fuchs: *Acta Metall.*, **31**, 509 (1983).

30. F. G. Caballero, C. Capdevila and C. García de Andrés: *Metall. Mater. Trans. A*, **32A**, 1283 (2001).

31. J. W. Christian: *The Theory of Transformations in Metals and Alloys*, 2nd Edition, Part I, Pergamon, Oxford, U.K, 1975.

32. P. Krüger: *J. Phys. Chem. Solids*, **54**, 1549 (1993).

33. R. M. Miranda and M. A. Fortes: *Mater. Sci. Eng. A*, **108**, 1 (1989).

34. S. J. Jones and H. K. D. H. Bhadeshia: *Acta Mater.*, **45**, 2911 (1997).

35. L. E. Svensson, B. Gretoft and H. K. D. H. Bheadeshia: *Scand. J. Metall.*, **15**, 97 (1986).

36. Z. Yang and T. DebRoy: *Metall. Mater. Trans. B*, **30**, 483 (1999).

37. S. K. Nath, S. Ray and V. N. S. Mathur: *ISIJ Inter.*, **34**, 191 (1994).

38. J. Askill: *Tracer Diffusion Data for Metals, Alloys and Simple Oxides*, IFI Plenum Press, 1970.

39. D. A. Porter and K. E. Easterling: *Phase Transformation in Metals and Alloys*, Van Nostrand Reinhold Co. Ltd., Berkshire, England, 1981.

40. M. Takahashi and H. K. D. H. Bhadeshia: *Mater. Trans.*, **32**, 689 (1991).

41. R. W. K. Honeycomb and H. K. D. H. Bhadeshia: *Steels: Microstructure and Properties*, 2nd edition, Halsted Press, New York, 1996.

42. H. K. D. H. Bhadeshia: *Bainite in Steels*, 2nd edition, Institute of Materials, London, 2001.

43. F. Cverna: *Thermal properties of metals*, ASM International, Materials Park, OH, 2002.

44. G. R. Speich, V. A. Demarest and R. L. Miller: *Metall. Trans. A*, **12A**, 1419 (1981).

45. K. C. Mills: *Recommended values of thermophysical properties for selected commercial alloys*, ASM International, Materials Park, OH, 2002.

46. C. J. Smithells, E. A. Brandes and G. B. Brook: *Smithells Metal Reference Book*, 7th edition, Butterworth-Heinemann Ltd., Oxford, United Kingdom, 1992.

47. M. B. Berkenpas, J. A. Barnard, R. V. Ramanujan and H. I. Aaronson: *Scripta Metall.*, 20, 323 (1986).

Chapter 6

MODELING OF AUSTENITE TO FERRITE TRANSFORMATION DURING GAS TUNGSTEN ARC WELDING OF 2205 DUPLEX STAINLESS STEEL

Duplex stainless steels (DSS) are two-phase alloys comprising approximately equal proportions of ferrite (δ) and austenite (γ) phases in their microstructures. This balanced microstructure offers a combination of high toughness, good weldability, satisfactory corrosion resistance, and high strength. The combination of these desirable properties can not be easily achieved by either austenitic or ferritic stainless steels [1,2]. The performance of DSS can be significantly affected by welding. The welding-induced microstructural changes such as annealing, grain growth, and phase transformation alter the grain size, phase ratios and microstructural morphologies in the welded region [1,2]. The degree to which the microstructure is altered depends on thermal cycles and the kinetics of the various transformations that are taking place during welding. If the balanced microstructure of the base metal is significantly altered, the loss of material properties can be acute. Understanding the evolution of microstructure during welding of DSS has been an important goal in contemporary welding research.

As an initial effort to understand the microstructural evolution during welding of a 2205 DSS, the γ-austenite to δ-ferrite (γ→δ) transformation during heating was considered for the following reasons. First, the γ→δ transformation is important because the grain size, phase fraction and concentration homogeneity of transformed δ phase affect the kinetics of subsequent δ grain growth and phase transformations during cooling [1-3]. Second, an X-ray diffraction technique [4-8] was used to obtain the real-time kinetic data of the γ→δ transformation under welding conditions. Such kinetic data are fairly unique and are very difficult to obtain by conventional experimental methods, since the microstructure that forms during heating is subsequently altered by the transformations during cooling.

The research work reported in this chapter involved a combination of welding experiments using the X-ray diffraction technique and numerical modeling based on principles of transport phenomena and phase transformation theory. The kinetic data of the γ→δ transformation were determined using the Spatially Resolved X-ray Diffraction (SRXRD) technique by Palmer et al. [7]. The thermal cycles under which the γ→δ transformation took place were computed using the numerical heat transfer and fluid flow model. A numerical diffusion model considering the diffusion of nitrogen in both γ and δ phases was developed to calculate the rates of the γ→δ transformation during heating. The calculated data were compared with the SRXRD results. The numerical diffusion model was then used to calculate the Time-Temperature-Transformation (TTT) and Continuous-Heating-Transformation (CHT) diagrams for the 2205 DSS. The effect of the starting microstructure on the transformation kinetics was also examined.

It should be noted that in the previous chapter, a kinetic model based on the Johnson-Mehl-Avrami (JMA) theory was developed to quantitatively describe the phase transformations during weld heating. A set of kinetic parameters used in the JMA equation were determined from the kinetic data measured using the X-ray diffraction technique, which allow quantitative calculation of the rates of phase transformations under different heating conditions. This approach can also be used to study the kinetics of the γ→δ transformation in the 2205 DSS. However, the computed JMA kinetic parameters are valid for a specific starting microstructure, and the dependence of the parameters on the starting microstructure can not be easily determined. Furthermore, the γ→δ transformation is often considered to be controlled by growth. Since the starting microstructure of the 2205 DSS consists of a two-phase structure, the nucleation of the δ phase is not necessary. Therefore, a numerical diffusion model was developed here to study the γ→δ transformation in the 2205 DSS, particularly the effect of starting microstructure on the phase transformation rates.

6.1 Direct Observation of Phase Transformations during Welding

The in-situ x-ray diffraction experiments during GTA welding were done by Palmer et al. [7] of Lawrence Livermore National Laboratory. The chemical composition of the 2205 DSS is the following (by wt%): 22.43 Cr, 4.88 Ni, 3.13 Mo, 1.40 Mn, 0.18 N, 0.023 C, 0.004 S, 0.67 Si and bal. Fe. The as received 2205 DSS was solution annealed at 1338 K for 2.5 hours followed by water quenching to ambient temperatures. The microstructure of the heat-treated 2205 DSS is shown in Fig. **6.1**. The base metal of the 2205 DSS consists of alternative layers of δ-ferrite and γ-austenite phases that exist in nearly equal amounts (54% of ferrite and 46% of austenite). It should be noted that the starting microstructure of the 2205 DSS, resulted from the high temperature heat treatment followed by the water quenching, is metastable and non-homogeneous.

Gas tungsten arc (GTA) welds were made on the 2205 DSS cylindrical bar samples, which had dimensions of 102 mm in diameter and 80 mm in length. During GTA welding, the surface of the 2205 sample was irradiated with a high-intensity synchrotron beam, and the diffracted beam was collected to determine spatial variation of crystal structure. The results were then used to construct a phase map of the HAZ on the top surface of the weldment. The spatial distribution of the regions consisting of γ-austenite, δ-ferrite and liquid phases, and the boundaries between these regions were qualitatively identified in the phase map. The diffraction data were further analyzed using a curve fitting routine to determine the peak area in each of diffraction patterns. This analysis was used to provide a semi-quantitative measure of the relative fractions of γ and δ during the γ→δ transformation upon weld heating. Additional details of the SRXRD experiments are available elsewhere [7].

Figure **6.1** also shows the microstructure in the heat affected zone (HAZ) and fusion zone (FZ) of the 2205 DSS weld. The microstructure in both the HAZ and FZ is dominated by large δ grains, which have been partially transformed to intra-granular and grain boundary γ during cooling. Figure **6.1** clearly illustrates the welding-inducing microstructure change and the spatial variation of microstructure.

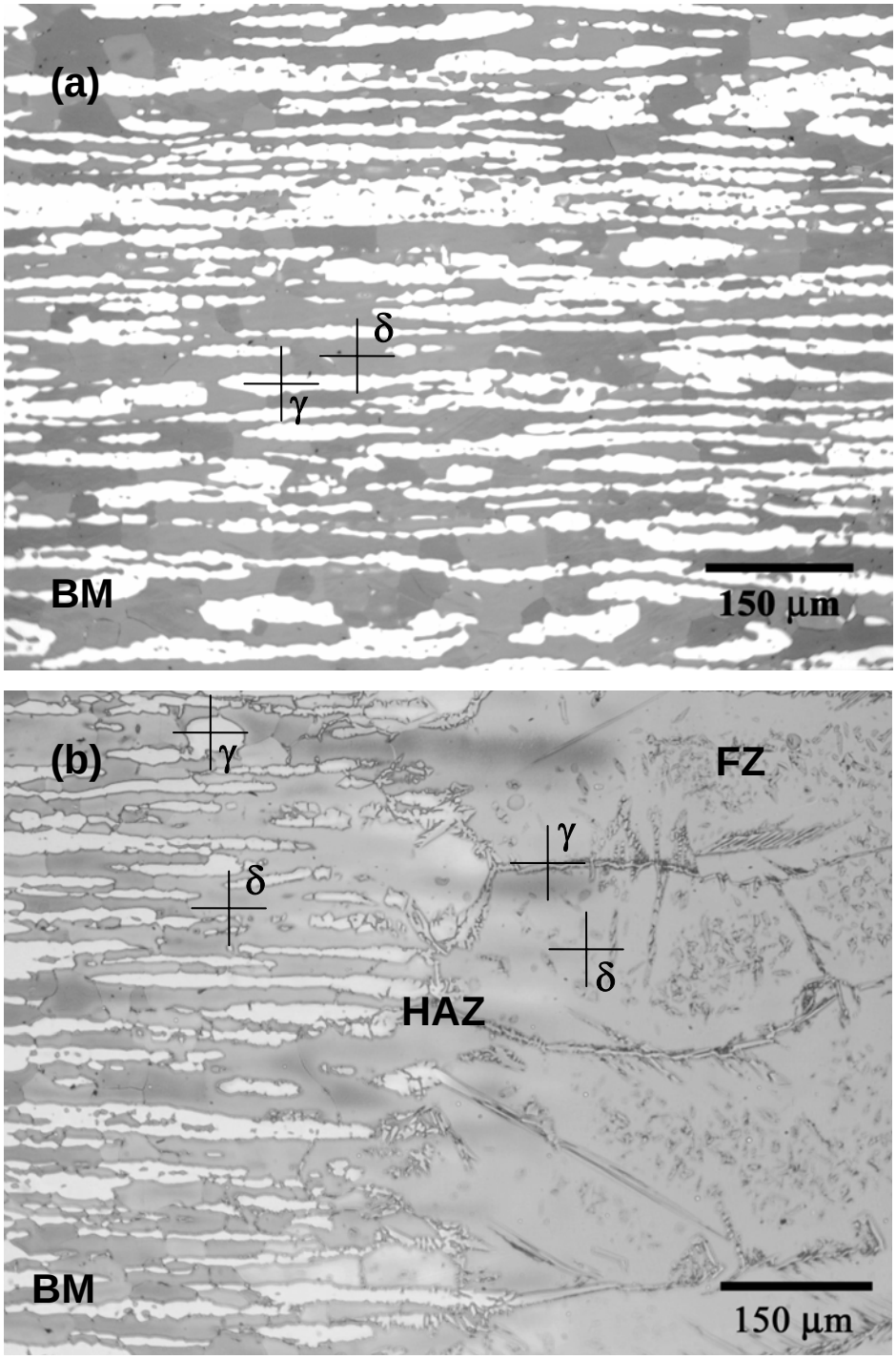

Fig. **6.1**: Optical microstructure of the 2205 DSS weld: (a) base metal, and (b) weldment. Symbols BM, HAZ, and FZ represent base metal, heat affected zone and fusion zone, respectively. The γ-austenite appears light and the δ-ferrite appears dark. Adapted from Palmer et al. [7].

6.2 Mathematical Background

Much of previous research on diffusion problems considers systems which consist of grains with average sizes [9-12]. For instance, for the γ→δ transformation problem studied here, a system consisting of one γ grain and one δ grain with respective average sizes can be used [3]. Such a system implies a uniform starting microstructure, where all γ and δ grains have constant sizes specific to the phase. However, a uniform starting microstructure rarely exists in engineering materials. Hence, it is important to evaluate the effect of the starting microstructure on the rates of phase transformations. For the clarity and simplicity of the presentation, in the following discussion, the diffusion problem is first formulated in a system consisting of one γ grain and one δ grain with average sizes. A more complex system consisting of several grains is then used to simulate the effect of non-uniform starting microstructure.

6.2.1 Governing equations of diffusion

The starting microstructure of the 2205 DSS shown in Fig. **6.1** is assumed to be represented by plates of δ-ferrite and γ-austenite that are infinite in two directions. Figure **6.2(a)** is a schematic plot showing a δ plate and a γ plate and their interface, where W_δ and W_γ represent the thicknesses of the δ and γ plates, respectively. In the present investigation, the γ→δ phase transformation is assumed to be controlled by the diffusion of nitrogen [3,13]. Local equilibrium of nitrogen is attained at the δ/γ interface, and the partitioning of the other alloying elements are assumed to be negligible during the γ→δ transformation. Such a para-equilibrium approximation is reasonable under the rapid heating conditions encountered during welding, since the available time scale for the phase change is short and there may not be sufficient time for substitutional elements to redistribute within phases.

Nitrogen is a strong austenite stabilizer, and the γ phase is richer in nitrogen than the δ phase. Since the 2205 DSS was solution treated at an elevated temperature, it is

assumed that the nitrogen distributes evenly in the starting microstructure. Figure **6.2(b)** shows a schematic concentration profile of nitrogen along the X direction in the base plate, where $N_{\delta,0}$ and $N_{\gamma,0}$ represent the initial concentrations of nitrogen in the δ and γ phases, respectively.

Figure **6.3** shows the nitrogen concentration profile during the γ→δ transformation, where M is the δ/γ interface location, and $N_{\delta,M}$ and $N_{\gamma,M}$ are the concentrations of nitrogen in the δ and γ phases at the δ/γ interface, respectively. The nitrogen concentration as a function of time (t) and distance (x) is given by the following Fick's second law for diffusion [**14**].

$$\begin{aligned} \frac{\partial N}{\partial t} &= D_\delta \frac{\partial^2 N}{\partial x^2} && \text{in } \delta \ (0 < x < M) \\ \frac{\partial N}{\partial t} &= D_\gamma \frac{\partial^2 N}{\partial x^2} && \text{in } \gamma \ (M < x < x_\gamma) \end{aligned} \qquad (6.1)$$

where N is the nitrogen concentration, t is time, and D_δ and D_γ are the diffusion coefficients of nitrogen in δ and γ phases, respectively. For simplicity, in Eq. **6.1**, D_δ and D_γ are assumed to be constant in δ and γ phases [**3**,**9**,**10**].

The initial conditions (at t = 0) are given as:

$$\begin{aligned} N &= N_{\delta,0} && 0 \le x \le M \\ N &= N_{\gamma,0} && M \le x \le x_\gamma \\ M &= x_\delta \end{aligned} \qquad (6.2)$$

The boundary conditions are given as:

$$\begin{aligned} \frac{\partial N}{\partial x} &= 0 && x = 0 \text{ and } x = x_\gamma \\ N &= N_{\delta,M} && x = M^- \\ N &= N_{\gamma,M} && x = M^+ \end{aligned} \qquad (6.3)$$

where M^- and M^+ are the location in δ and γ phases at the δ/γ interface, respectively. Eq. **6.3** indicates there is no mass flux of nitrogen across the two boundary surfaces at x = 0 and x_γ, and the nitrogen concentrations in δ and γ phases are in local equilibrium at the δ/γ interface.

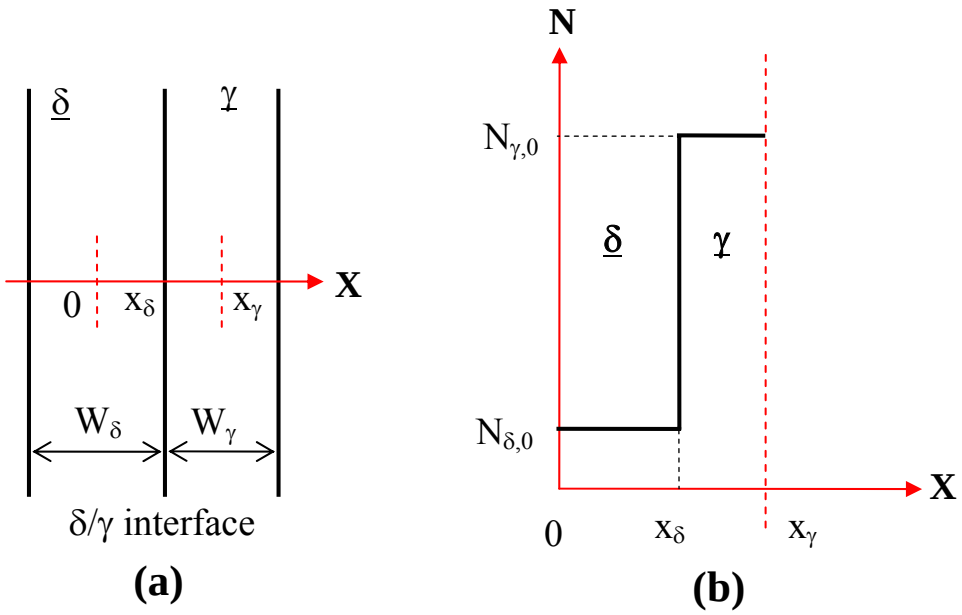

Fig. **6.2**: Schematic representation of (a) the starting microstructure, and (b) the initial nitrogen concentration profile in the δ and γ phases.

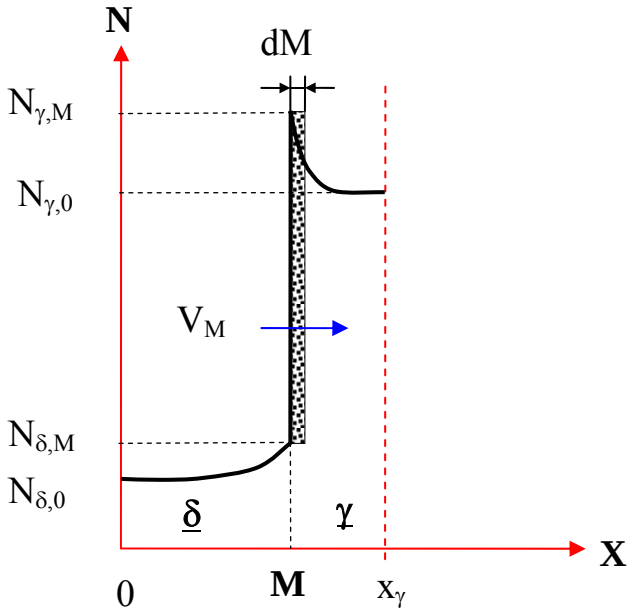

Fig. **6.3**: Schematic plot showing the nitrogen concentration during transformation.

Since the δ/γ interface is moving during the transformation, its location (M) needs to be determined in order to solve Eqs. **6.1** to **6.3**. As shown in Fig. **6.3**, in order for the interface to advance a distance of dM in a short time period of dt, an equivalent amount of nitrogen in the shadowed area needs to be diffused away. Therefore, the interface location as a function of time is given as:

$$\begin{aligned} &\left(N_{\gamma,M} - N_{\delta,M}\right)dM = \left(D_\delta \left.\frac{\partial N}{\partial x}\right|_{M-} - D_\gamma \left.\frac{\partial N}{\partial x}\right|_{M+} \right)dt \\ &\text{or, } \left(N_{\gamma,M} - N_{\delta,M}\right)\frac{dM}{dt} = D_\delta \left.\frac{\partial N}{\partial x}\right|_{M-} - D_\gamma \left.\frac{\partial N}{\partial x}\right|_{M+} \end{aligned} \qquad (6.4)$$

where $\frac{dM}{dt}$ is the interface moving velocity (V_M), $\left(N_{\gamma,M} - N_{\delta,M}\right)dM$ represents the nitrogen content in the shadowed area, and terms $D_\delta \left.\frac{\partial N}{\partial x}\right|_{M-}$ and $-D_\gamma \left.\frac{\partial N}{\partial x}\right|_{M+}$ are the nitrogen fluxes diffused into the δ and γ phases at the δ/γ interface, respectively. Eq. **6.4** indicates that the total mass of nitrogen in the system is conserved. In other words, as the thin γ layer with thickness of dM is dissolved, the nitrogen mass in this layer diffuses into the bulk regions of δ and γ. As a result, the nitrogen concentrations at the two symmetric boundaries, i.e., x = 0 and x = x_γ, increase.

6.2.2 Numerical solution

To solve Eqs. **6.1** to **6.4**, a widely-used numerical method developed by Murray and Landis [**15**,**16**] is employed. As shown in Fig. **6.4**, the solution domain from x = 0 to x_γ is discretized into n grid points. The δ/γ interface M lies on a particular grid point (m), which moves with the interface. For instance, the grid locations at time t are shown in Fig. **6.4**. If the interface advances to a new location at time t+Δt, all the interior grids proportionally move right so that the interface still lies on grid point m. As a result, the spatial intervals of the grids are a function of time. For the moving grid system shown in Fig. **6.4**, Eq. **6.1** is transformed into [**15**,**16**]:

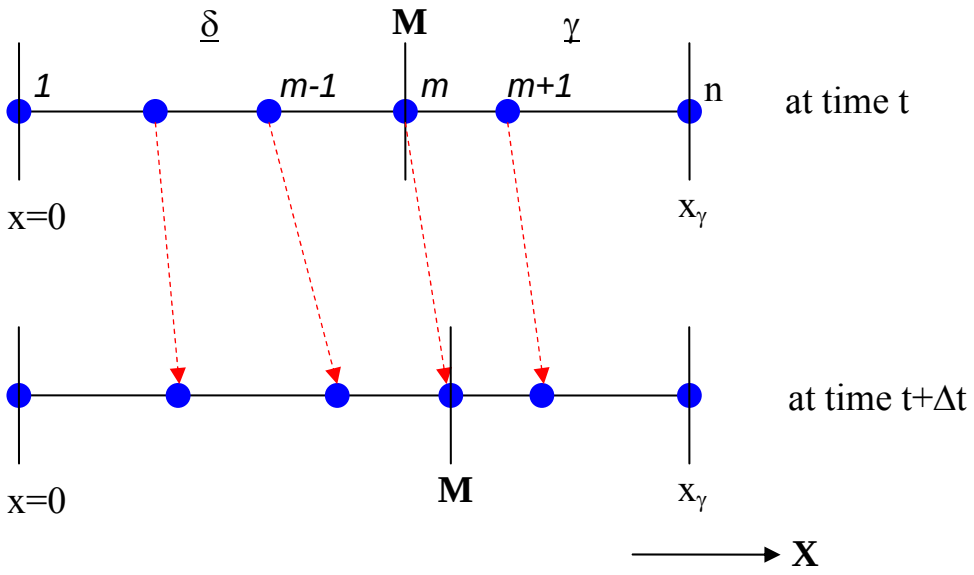

Fig. **6.4**: Schematic representation of grids used in the numerical solution at time t and t+Δt.

$$\left.\frac{\partial N}{\partial t}\right|_i = D_\delta \frac{\partial^2 N}{\partial x^2} + \frac{x_i}{M} V_M \frac{\partial N}{\partial x} \qquad \text{in } \delta \ (0 < x < M)$$
$$\left.\frac{\partial N}{\partial t}\right|_j = D_\gamma \frac{\partial^2 N}{\partial x^2} + \frac{x_j}{M} V_M \frac{\partial N}{\partial x} \qquad \text{in } \gamma \ (M < x < x_\gamma) \qquad (6.5)$$

where x_i and x_j are the locations of the i-th and j-th grid points, respectively, and $\left.\frac{\partial N}{\partial t}\right|_i$ and $\left.\frac{\partial N}{\partial t}\right|_j$ represent the change of nitrogen concentration with time at i-th and j-th grid points, respectively. Comparing this equation with Eq. **6.1**, the right most terms in Eq. **6.5** are used to account for the spatial movements of the grid nodes.

Eq. **6.5** is discretized using the finite difference method with a fully-implicit scheme. The general discretized equation at grid i is given as:

$$a_P N_i = a_W N_{i-1} + a_E N_{i+1} + a_P^0 N_i^0 + Sc_i \qquad (6.6)$$

where N_i^0 is the nitrogen concentration at time t and all other concentrations are evaluated at time t+Δt (fully-implicit). Symbols a_P, a_W, a_E, a_P^0 and Sc_i are coefficients formulated using the finite difference scheme [**17**].

The interface moving velocity is given as:

$$\left(N_{\gamma,M} - N_{\delta,M}\right) V_M = D_\delta \frac{N_m - N_{m-1}}{x_m - x_{m-1}} - D_\gamma \frac{N_{m+1} - N_m}{x_{m+1} - x_m} \qquad (6.7)$$

where m is the particular grid point where the interface is attached, and all the concentrations are evaluated at time t+Δt.

Once the interface moving velocity is obtained, the spatial locations of the grids (x_i) at time t+Δt are updated using the following equation.

$$x_i = x_i^0 + \frac{x_i^0}{M^0} V_M \Delta t \qquad (6.8)$$

where Δt is the time step, and x_i^0 and M^0 are the locations of the i-th grid point and interface at time t, respectively.

The overall solution procedure is shown in Fig. **6.5**. As shown in this figure, there are two loops in the calculation procedure. The outer loop is the time marching loop, whereas the inner loop is used for the iterative solution of Eqs. **6.6** and **6.7**. In other words, at a given time t, these two equations are solved iteratively until a converged solution of nitrogen concentration profile and interface position are obtained. The calculation then advances a time step Δt, and the solution at time t is used as the old values for solution at time $t+\Delta t$.

6.2.3 Verification of numerical diffusion model

Although the numerical diffusion model discussed in the previous section is developed specially for the $\gamma \rightarrow \delta$ transformation in the 2205 DSS, it can be easily used for solving other diffusion problems with appropriate initial and boundary conditions and material properties. Here, we chose to apply our numerical diffusion model to solve a diffusion problem where the analytical solution is available. Therefore, the numerical model can be validated by comparing its results with the analytical solution. The numerical diffusion model can then be applied to more complicated problems.

Considering the following decarburization problem, one end of a semi-infinite rod containing only γ-austenite is brought into contact with a decarburizing gas [**18**]. This is a common technique used in steel treatment, and has been thoroughly studied in the past so reliable thermodynamic and kinetic data are available. As a result, α-ferrite is nucleated on the surface of the rod and grows into the bulk of the rod. The surface concentration of carbon is held constant at C_s, and the initial carbon concentration in γ is equal to C_i. Carbon equilibrium is assumed to be maintained at the α/γ interface and the concentration profile of carbon in the rod at time t is shown in Fig. **6.6**. The analytical solution for the interface moving velocity is derived as [**18**]:

$$\frac{dM}{dt} = V_M = \phi\sqrt{\frac{D_\gamma}{t}} \qquad (6.9)$$

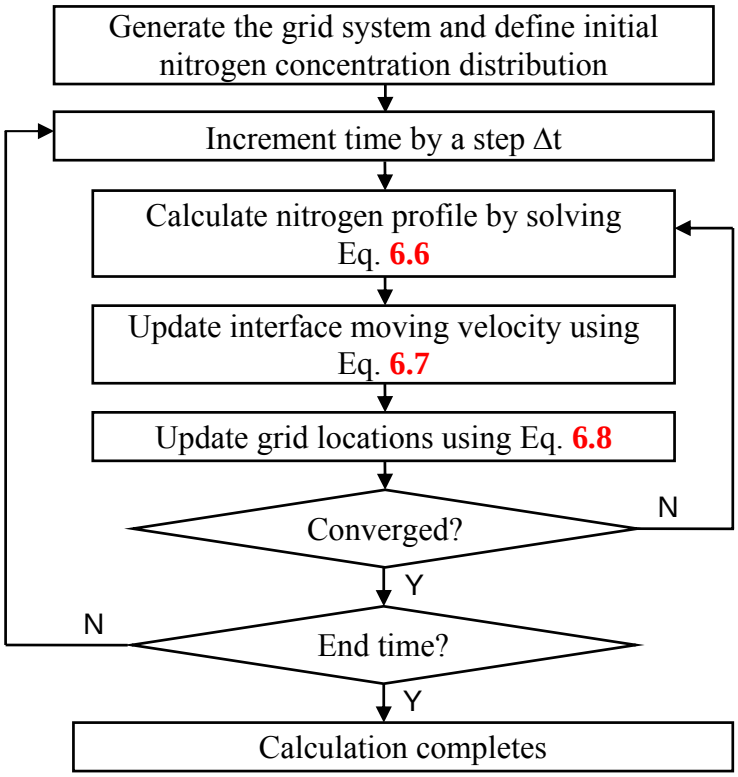

Fig. 6.5: Schematic diagram showing the overall iterative procedure for the calculation of nitrogen concentration profile during γ→δ transformation.

where D_γ is the diffusivity of carbon in γ, and ϕ is obtained from the following equation.

$$C_{\gamma,M} - C_{\alpha,M} = \frac{C_{\gamma,M} - C_i}{\sqrt{\pi}\,\phi\exp(\phi^2)\,\mathrm{erfc}(\phi)} + \frac{C_{\alpha,M} - C_s}{\sqrt{\pi}\,\phi a\exp\{(\phi a)^2\}\,\mathrm{erfc}(\phi a)} \qquad (6.10)$$

where $C_{\alpha,M}$ and $C_{\gamma,M}$ are the concentrations of carbon in α and γ phases at the α/γ interface, respectively, $a = \sqrt{D_\gamma / D_\alpha}$, and D_α is the diffusivity of carbon in α phase.

For our purpose, let us consider the decarburization of a steel with an initial carbon content of 3 atom percent (at %) at 1023 K by a decarburizing gas maintaining a carbon content of 0.05 at %, i.e., $C_i = 3.0$ at % and $C_s = 0.05$ at %. The carbon contents of the α and γ phases at the interface, $C_{\alpha,M}$ and $C_{\gamma,M}$, are 0.09 and 2.7 at %, respectively. At 1023 K, $D_\alpha = 5\times10^{-5}$ mm^2/s and $D_\gamma = 1.1\times10^{-6}$ mm^2/s [18]. Substituting these data into Eq. 6.10, we have:

$$\sqrt{\pi}(2.7 - 0.09) = \frac{2.7 - 3.0}{\phi\exp(\phi^2)\,\mathrm{erfc}(\phi)} + \frac{0.09 - 0.05}{0.148\phi\exp\{(0.148\phi)^2\}\,\mathrm{erfc}(0.148\phi)}$$

$$\text{or, } 4.63 + \frac{0.3}{\phi\exp(\phi^2)\,\mathrm{erfc}(\phi)} - \frac{0.04}{0.148\phi\exp\{(0.148\phi)^2\}\,\mathrm{erfc}(0.148\phi)} = 0$$

The left hand side (LHS) of this equation depends only on ϕ. If we use f(ϕ) to represent the LHS, the problem is thus equivalent to finding the root of the function f. Such root finding can be done by using standard iterative procedures such as Newton-Raphson Method [19] or simply by plotting the LHS as a function of ϕ, and then graphically determining the ϕ value where f(ϕ) = 0. The solution is obtained as ϕ = 0.54. Therefore, from Eq. 6.9, the rate of advance of the interface is:

$$\frac{dM}{dt} = \frac{5.66\times10^{-7}}{\sqrt{t}} \qquad \text{(m/s)}$$

Figure 6.7 shows the interface location M as a function of time calculated using the above analytical solution and the numerical model. As shown in this figure, the good agreement between the interface locations obtained from the numerical model and analytical solution indicates the validity of the numerical diffusion model.

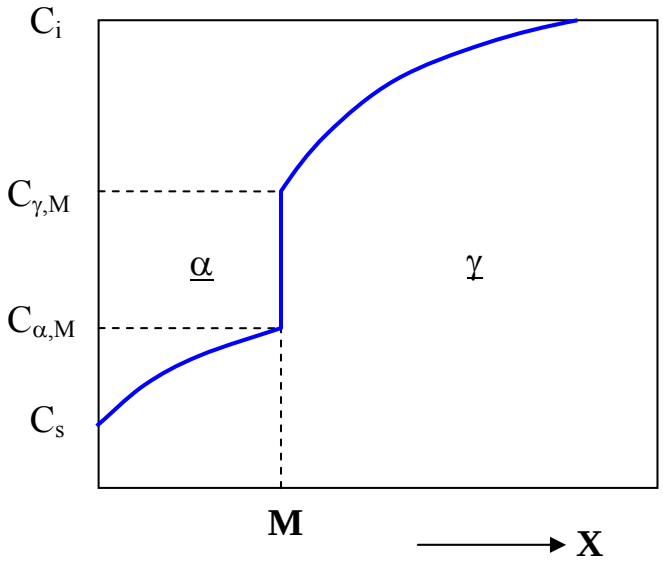

Fig. **6.6**: Schematic representation of the concentration profile of carbon in the iron rod during decarburization of γ-austenite.

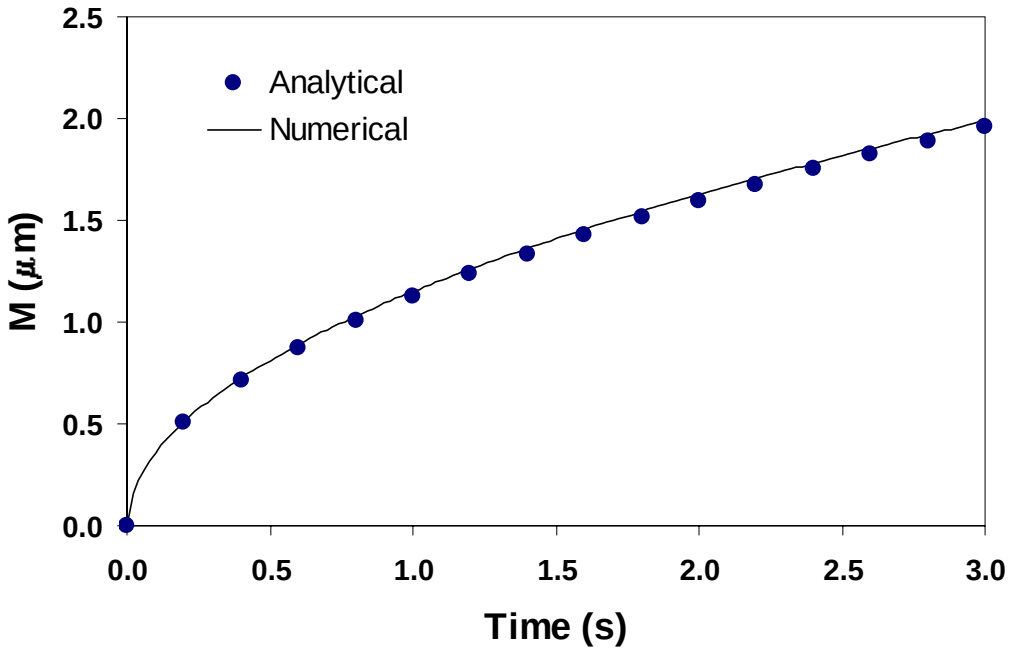

Fig. **6.7**: Comparison of the α/γ interface location (M) as a function of time using numerical and analytical solutions.

6.2.4 Input data used in diffusion calculations

A prerequisite for using the numerical diffusion model to calculate transformation kinetics is that reliable thermodynamic and kinetic data are available for the 2205 DSS. Hertzman et al. [13] evaluated the nitrogen concentrations in the δ and γ phases of a 2205 DSS under the para-equilibrium condition using ThermoCalc, which are given as follows.

$$N_{\delta,M} = 10^{0.002703\times T - 5.04964} \quad (wt\%) \tag{6.11}$$

$$N_{\gamma,M} = 0.48 + 10^{0.002257\times T - 3.99984} \quad (wt\%) \tag{6.12}$$

where $N_{\delta,M}$ is the nitrogen concentration in the δ phase, which is in para-equilibrium with γ, $N_{\gamma,M}$ is the nitrogen concentration in the γ phase, which is in para-equilibrium with δ, and T is temperature in Kelvin. The equilibrium fraction of γ (f_γ) can then be determined by the following lever rule.

$$f_\gamma = \frac{N_C - N_{\delta,M}}{N_{\gamma,M} - N_{\delta,M}} \tag{6.13}$$

where N_C is the nitrogen concentration in the 2205 DSS.

Eqs. 6.11 to 6.13 indicate that f_γ = 0.26 at 1338 K, which is much less than the metallographically measured f_γ = 0.46 in the 2205 DSS base metal used in this study [7,8]. Such inconsistence may result from the composition of the base metal, the thermodynamic database, and the number of alloying elements considered in Hertzman's ThermoCalc calculations. Recent thermodynamic studies [7] indicated f_γ = 0.45 at 1338 K, which is in a very good agreement with the experimental value. Since the main objective here is to develop the numerical diffusion model, for simplicity, the equations based on Hertzman's calculations are used. However, the para-equilibrium nitrogen concentration in the γ phase was adjusted so that the calculated f_γ is 0.46 at 1338 K.

$$N_{\gamma,M} = 0.255 + 10^{0.002257\times T - 3.99984} \quad (wt\%) \tag{6.14}$$

In the literature, the f_γ value as a function of temperature and steel composition has been determined experimentally, and is expressed by the following relationship [20].

$$f_\gamma = 0.01\begin{bmatrix} 75 - 6.8\times10^{-15}\times T^5 + 190(C_C - 0.03) + 6(22 - Cr_C) \\ +9(Ni_C - 5) + 6.5(3 - Mo_C) + 160(N_C - 0.15) \end{bmatrix} \qquad (6.15)$$

where C_C is the carbon concentration, Cr_C is the chromium concentration, Ni_C is the nickel concentration, and Mo_C is the molybdenum concentration. Substituting the composition of the 2205 DSS into Eq. **6.15**, the f_γ versus temperature data are calculated, and these data are plotted in Fig. **6.8**. Superimposed are the f_γ versus temperature data computed using Eqs. **6.11** and **6.14**. As shown in this figure, the correlation between two curves is reasonable.

Eqs. **6.11** and **6.14** indicate that for the 2205 DSS used in the present study, f_γ approaches zero when the temperature is higher than 1592 K. In other words, the equilibrium completion temperature of the $\gamma\rightarrow\delta$ transformation is 1592 K. On the other hand, the start temperature of the $\gamma\rightarrow\delta$ transformation is assumed to be 1338 K, since the 2205 DSS used in the SRXRD experiments was solution annealed at this temperature for 2.5 hours followed by the water quenching to ambient temperatures [**7**]. It should be noted that at temperatures lower than the 1338 K [**7**,**8**], nitrogen can also diffuse, which may result in the formation of sigma phase. In this study, the nitrogen diffusion below the 1338 K was ignored, since the goal here is to study the $\gamma\rightarrow\delta$ transformation, which is one of the most important phase changes during heating. Hence, the 1338 K is only a nominal starting temperature, and not the equilibrium start temperature of the $\gamma\rightarrow\delta$ transition.

The diffusion coefficient of nitrogen in the δ phase as a function of temperature for the 2205 DSS is given as [**13**]:

$$D_\delta = 0.464\ \exp(-10223.7/T) \qquad (mm^2/s) \qquad (6.16)$$

The diffusion coefficient of nitrogen in γ for the 2205 DSS is not readily available in the literature. Hence, the diffusion coefficient of nitrogen in the pure γ-Fe is used [**21**].

$$D_\gamma = 36.0\ \exp(-18883.8/T) \qquad (mm^2/s) \qquad (6.17)$$

The initial thicknesses, phase fractions and nitrogen concentrations of the δ and γ plates are summarized in Table **6.1** [**7**,**8**].

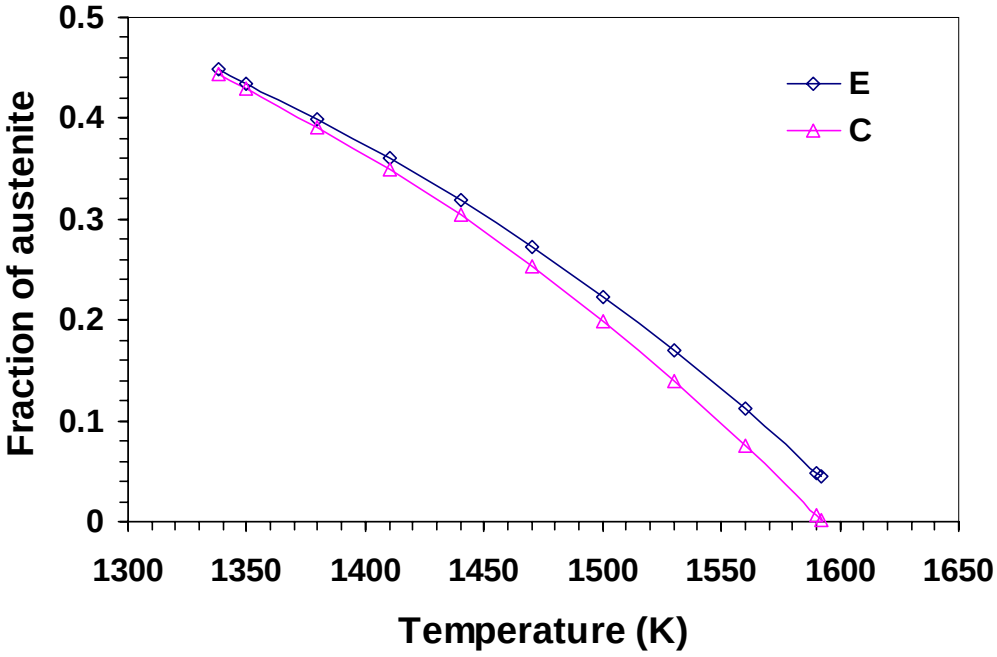

Fig. **6.8**: The equilibrium fraction of γ (f_γ) as a function of temperature in the 2205 DSS. Curve E was computed using the relationship given in Eq. **6.15**, which was obtained experimentally. Curve C was calculated using Eqs. **6.11** and Eq. **6.14**.

Table **6.1**: Initial microstructure of 2205 DSS [**7**,**8**].

Phase	Average grain thickness (μm)	Volume fraction	Nitrogen concentration (wt%)
δ-ferrite	22.3	0.54	0.03
γ-austenite	19.0	0.46	0.356

6.2.5 Grid spacing and time step

Spatially non-uniform grids were used to maximize the resolution of the variables. Finer grid spacing was used in the vicinity of the δ/γ interface, since the concentration gradient of nitrogen in this region is the highest. A number of 201 grid points were used in the δ phase with an initial thickness of 11.15 μm, whereas 151 grid points were used in the γ phase having an initial thickness of 9.5 μm. The time step used in the calculation was 0.1 ms. Such fine grid spacing and small time step were necessary to ensure the accuracy of numerical calculations, as discussed in the following.

The accuracy of the numerical calculations can be evaluated by checking the overall nitrogen mass conservation in the system. In other words, for an accurate numerical solution, the total mass of nitrogen in the system should remain constant. In the present study, the overall mass conservation is defined as:

$$e_N = \frac{N_{cal} - N_{ini}}{N_{ini}} \times 100\% \qquad (6.18)$$

where e_N is an error representing the nitrogen mass conversation, N_{cal} is the calculated total mass of nitrogen at each time step, and N_{ini} is the initial mass of nitrogen in the system. An accurate solution requires that e_N approaches zero.

In the present study, different grid numbers and time step values were tested. It was found that the value of e_N decreased to some fixed value, as the values of grid spacing and time step reduced to a certain level. Further reducing of the values of grid spacing and time step did not change the final results, while making the solution process much more computationally intensive. For the grid system and time step discussed above, the value of e_N was found to be fairly small, i.e. about 0.01%.

6.2.6 Calculation of weld heat transfer and fluid flow

Accurate knowledge of the weld pool geometry and thermal cycles in the weldment is necessary to understand the phase transformation kinetics during welding. In

the present research, the three-dimensional heat transfer and fluid flow model [22] was used to calculate the weld temperature and velocity fields, since the measurement of temperatures is problematic during welding. Details of this model are presented in previous chapters.

For computational accuracy, the numerical model used a very fine grid system consisting of 77×47×50 grid points, and the corresponding computational domain had dimensions of 96 mm long, 69 mm wide and 67 mm deep. Spatially non-uniform grids were used for maximum resolution of the variables. Finer grids were used near the heat source where the temperature gradients are the highest. The thermo-physical properties used to represent the 2205 DSS in the calculations are given in Table 6.2 [7,8,23]. Since the 2205 DSS contains 0.004 wt% sulfur, the effect of sulfur on changing the surface tension was included in the calculation. In addition, at the weld top surface, the heat loss due to the helium shielding gas is considered by using Newton's law of cooling.

Table 6.2: Data used in the heat transfer and fluid flow calculation [7,8,23].

Name	Value
Liquidus Temperature (K)	1718.0
Solidus temperature (K)	1658.0
Density of metal (kg m^{-3})	7200
Surface tension of liquid metal (N m^{-1})	Eq. 6.19
Thermal conductivity of solid (J $m^{-1}\cdot s^{-1}\cdot K^{-1}$)	20.0
Enhanced thermal conductivity of liquid (J $m^{-1}\cdot s^{-1}\cdot K^{-1}$)	146.3
Enhanced viscosity of liquid metal (kg m^{-1} s^{-1})	8×10^{-2}
Specific heat of solid (J $kg^{-1}\cdot K^{-1}$)	560.1
Specific heat of liquid (J $kg^{-1}\cdot K^{-1}$)	806.7
Coefficient of thermal expansion (K^{-1})	1.4×10^{-5}
Arc efficiency	57.2%
Arc radius (mm)	2.8
Heat transfer coefficient at weld top surface (W m^{-2} K^{-1})	1.59×10^{3}

It should be noted that a rectangular solution domain was used to calculate the heat transfer and fluid flow in the cylindrical welding sample (80 mm long and 102 mm diameter) [7]. Since the weld pool dimensions (10 mm wide and 4 mm deep) were much smaller than those of the cylindrical specimen, no significant error was introduced by calculations being performed in a flat geometry.

6.3 Results and Discussion

6.3.1 Heat transfer and fluid flow in the weldment

The computed three-dimensional temperature and velocity fields are shown in Fig. 6.9, where the temperatures are indicated by the contour lines and the melt velocities are represented by the arrows. Since the weld is symmetric about the y = 0 plane, only half of the weld is shown for clarity. As shown in Fig. 6.9, the convection pattern in the pool is complex due to the combined effect of surface tension gradient, electromagnetic and buoyancy forces. The 2205 DSS contains 0.004 wt% of sulfur, which is enough to significantly affect the surface tension (γ) of the liquid metal. The effect of sulfur on the surface tension is calculated using the following equation for the Fe-S binary system [24].

$$\gamma = 1.943 - 4.3\times10^{-4}\,(T-1809) - 1.3\times10^{-8} \\ RT\ln\left[1 + 0.00318\,a_S\exp\left(\frac{1.66\times10^5}{RT}\right)\right] \qquad (6.19)$$

where T is temperature in Kelvin, R is the universal gas constant (8.314 J mol^{-1}), and a_S is the activity of sulfur which is assumed to be equal to its concentration. Eq. 6.19 indicates the surface tension reaches a maximum value at 1860 K. In other words, the temperature coefficient of surface tension ($d\gamma/dT$) is greater than zero when temperature is less than 1860 K, and vice versa. As a result, the liquid metal is pulled from the periphery to the 1860 K isotherm around the pool boundary, whereas the melt flows outward in the center of the pool, as shown in Fig. 6.9. The downward flow in the middle of the pool is driven by the electromagnetic force.

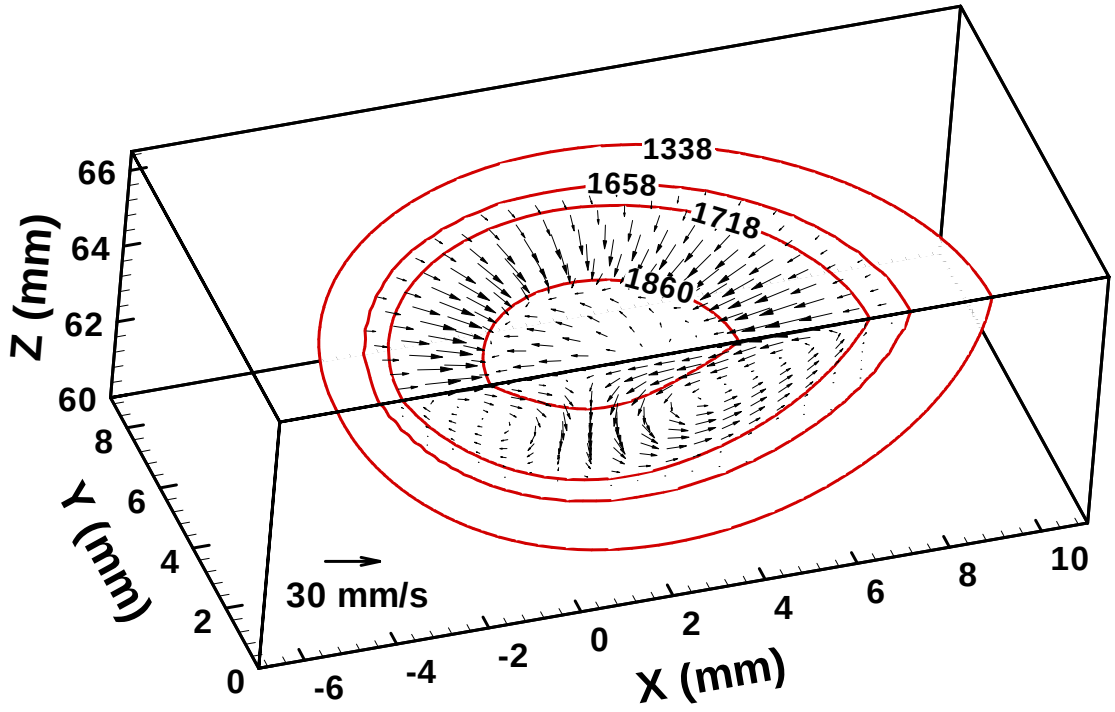

Fig. **6.9**: Calculated temperature and velocity fields in three-dimension. All temperatures are given in Kelvin.

Figure **6.10** shows the comparison between the calculated and metallographically measured fusion zone (FZ) geometry. The calculated FZ boundary is represented by the 1658 K solidus isotherm. As shown in this figure, the calculated width and depth of the FZ agree reasonably well with those measured experimentally. Such good agreement indicates the validity of the heat transfer and fluid flow model.

The knowledge of thermal profiles in the weldment is a prerequisite for understanding the phase transformation kinetics during welding. Figure **6.11** shows the computed thermal cycles at various locations, which are calculated by converting the x distance into time using the welding speed. Due to the motion of the heat source, the temperature field is slightly compressed in front of the heat source and elongated behind the heat source. As a result, the heating rates are higher than the cooling rates. As shown in Fig. **6.11**, the peak temperatures and the heating and cooling rates decrease with increasing distance from the welding centerline. Depending on the local temperatures, different phase transformations take place in the weldment. For instance, at location 1 and 2, the microstructural evolution sequence is the $\gamma \rightarrow \delta$ transformation, melting, solidification and $\delta \rightarrow \gamma$ transformation. At location 3, only $\gamma \rightarrow \delta$ transformation during heating and $\delta \rightarrow \gamma$ transformation during cooling may take place. Further away from the weld center, the temperatures are not high enough to initiate the $\gamma \rightarrow \delta$ transformation. The spatial variation of temperatures results in the spatial variation of microstructure in the weldment.

6.3.2 Kinetics of $\gamma \rightarrow \delta$ transformation during heating

Using the numerical diffusion model and computed thermal cycles, the kinetics of the $\gamma \rightarrow \delta$ transformation at various locations were calculated. Figure **6.12** shows the calculated nitrogen concentration profile as a function of time at a monitoring location of Y = 3.5 mm. At t = 0 s, the γ phase is in equilibrium with the δ phase, and the nitrogen concentration in the γ phase is higher than that in the δ phase. Within each phase, the nitrogen concentration is uniformly distributed. As the temperature increases, the

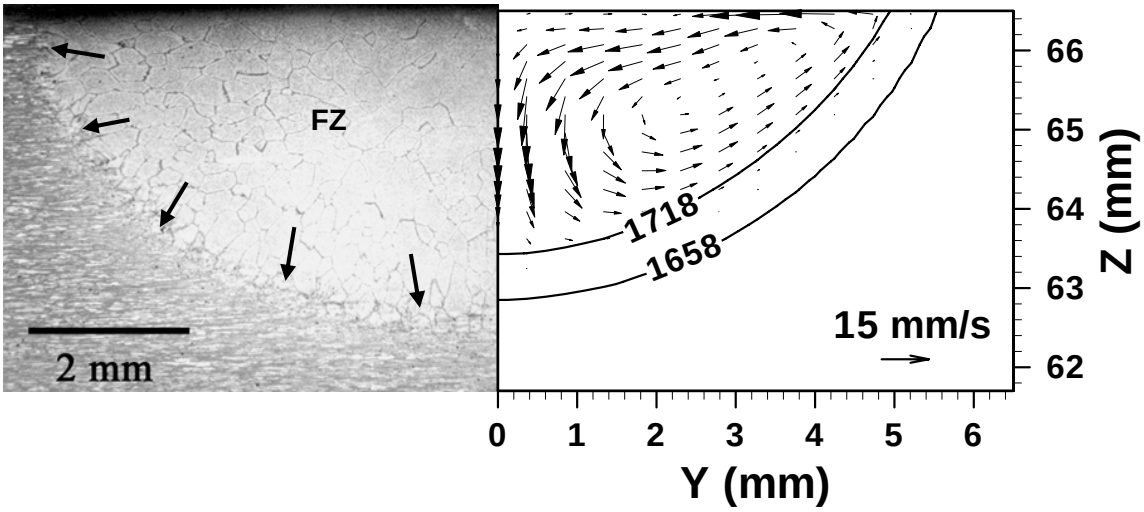

Fig. **6.10**: Comparison between experimental (left) and calculated (right) weld pool cross sections. Temperatures are given in Kelvin.

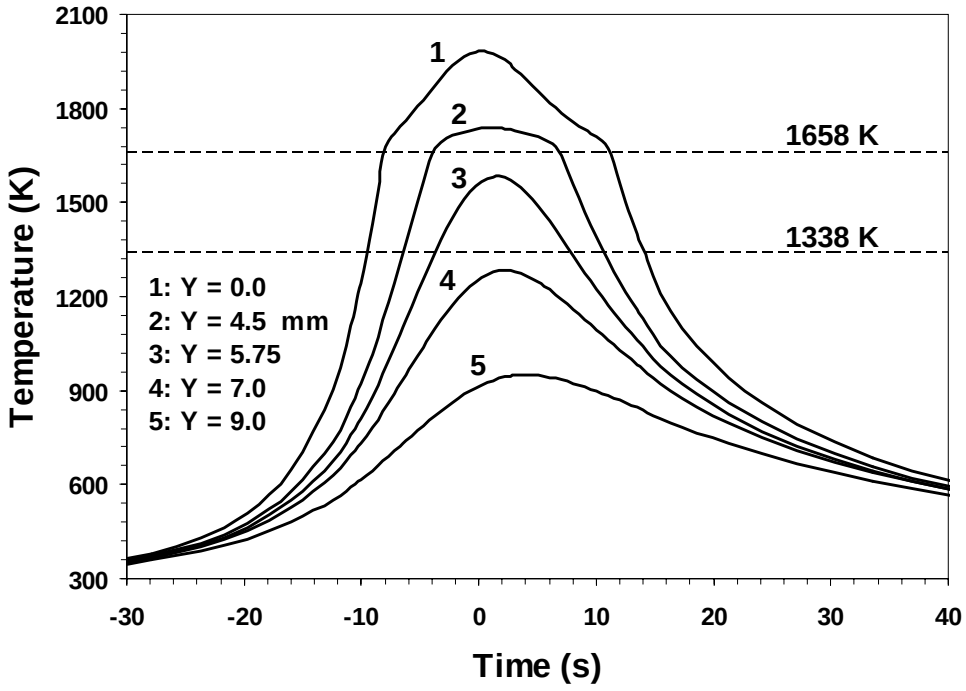

Fig. **6.11**: Calculated thermal cycles at various locations. Time zero corresponds to the X = 0 mm location. Locations 1 and 2 are in the FZ while locations 3, 4 and 5 are in the HAZ.

equilibrium between δ and γ phases can no longer be maintained as the nitrogen solubility in each phase changes with temperature. The nitrogen concentration at the interface then rises to values higher than those in the bulk of either phase. As a result, a concentration gradient develops, causing the nitrogen to diffuse and the interface to move. Figure **6.12** also indicates that at the end of the transformation, the concentration gradients in both phases are small. At the Y = 3.5 mm monitoring location, the temperature is high enough to complete the γ→δ transformation.

Figure **6.13** shows the comparison between the calculated and SRXRD data at various locations. The agreement between the calculated and measured data seems somewhat reasonable, considering the scatter in the measured data points. The overall good agreement indicates the validity of the numerical diffusion model and computed thermal cycles.

The calculated δ fraction versus time profiles in Fig. **6.13** resemble S-shape (sigmoidal) curves. It should be noted that such behavior results from the non-isothermal heating conditions, and not from the nucleation and growth mechanism. For isothermal transformation controlled by diffusion (such as the γ→δ transformation studied here), it has been well established that the growth kinetics vary parabolically with time, i.e., the fraction converted is proportional to the square root of time [**14**,**16**]. In other words, the transformation kinetics are fastest at the beginning and decrease gradually as the transformation approaches completion. However, under the non-isothermal heating conditions, the transformation kinetics are slow initially, since both the temperature and diffusivity of nitrogen are low at the beginning of the transformation. As the transformation proceeds, the temperature and the diffusivity of nitrogen, which depends exponentially on the temperature, increase, thus enhancing the transformation rate. Toward the end of the transformation, the increase in the nitrogen diffusivity no longer plays a dominant role, and the small concentration gradients and longer diffusion distances in the δ plate slow down the transformation.

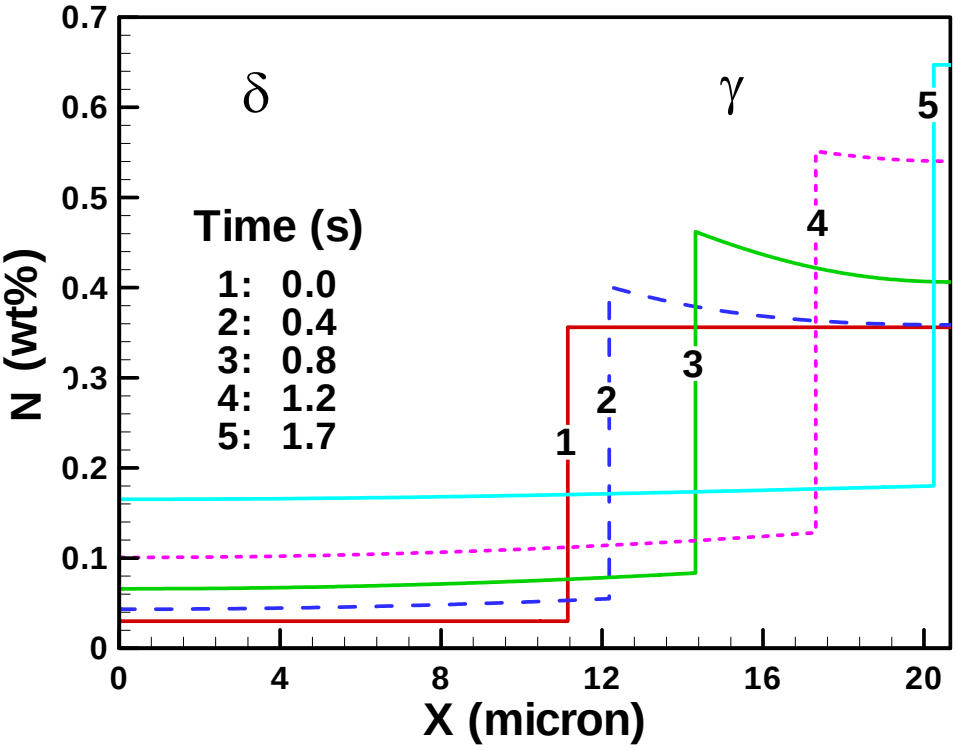

Fig. **6.12**: Calculated nitrogen concentration profile as a function of time at y = 3.5 mm location.

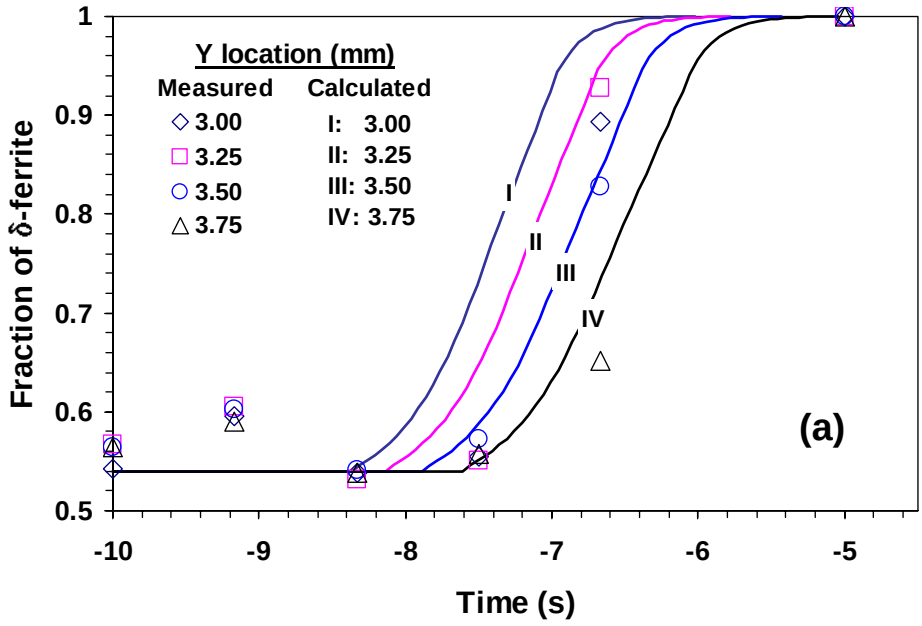

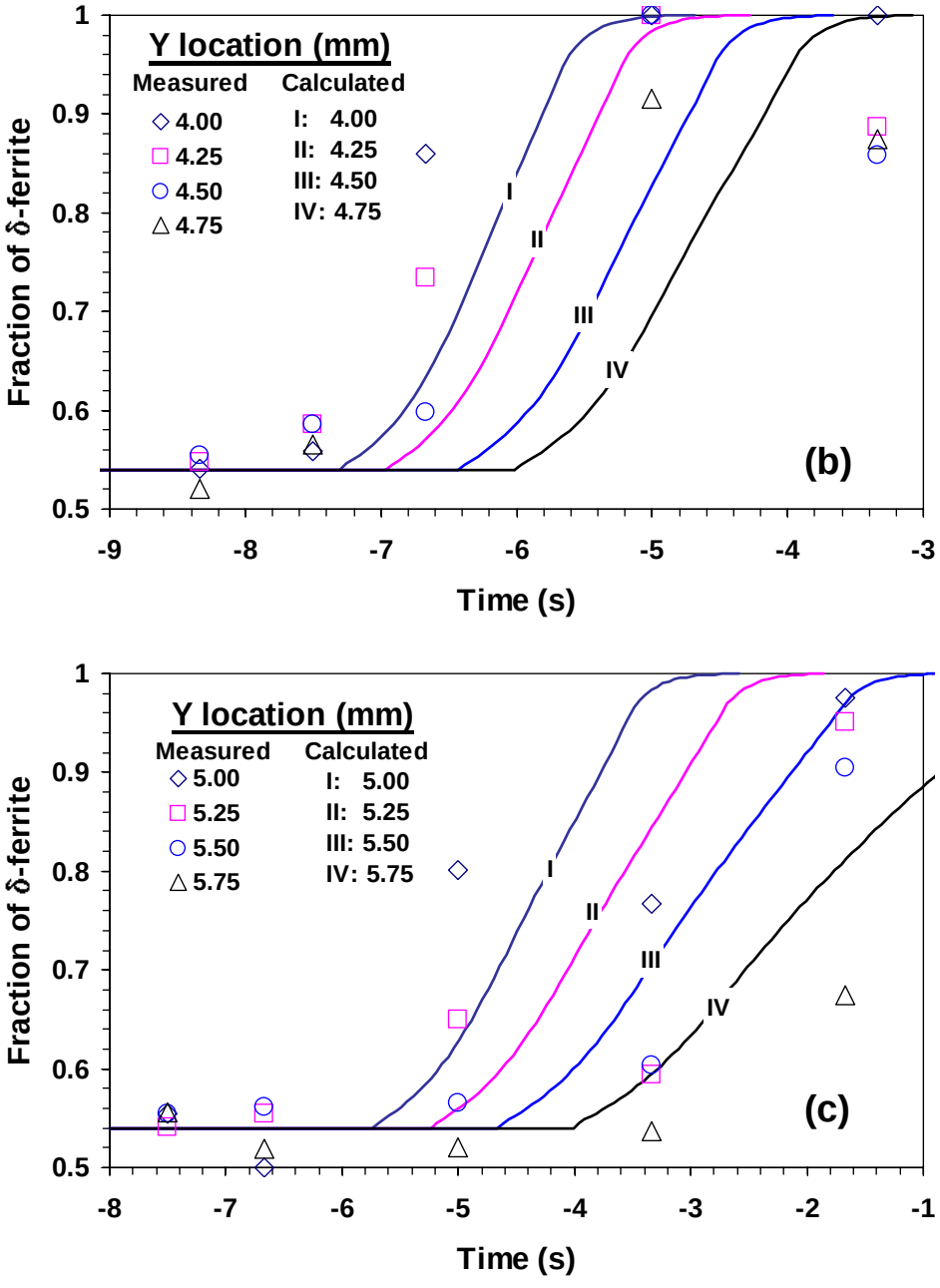

Fig. **6.13**: Comparison of calculated and measured kinetic data at various locations.

6.3.3 TTT and CHT diagrams

There are two main types of transformation diagrams that provide useful graphical representation of the transformation kinetics: TTT and CHT diagrams. The former type predicts isothermal transformation kinetics, whereas the latter type indicates non-isothermal transformation kinetics. Using the numerical diffusion model, TTT and CHT diagrams were developed for the γ→δ transformation in the 2205 DSS.

For the TTT diagram, various constant temperatures above 1338 K, i.e., the nominal start temperature of the transformation, were used. At each constant temperature, the δ fraction as a function of time was calculated, and the results were used to construct the TTT diagram shown in Fig. **6.14**. The 55% and 99% curves are assumed to represent the start and completion of the γ→δ transformation. As shown in this figure, the rates of the γ disolution rapidly accelerate as the temperature increases. The fast rate results from the increase in the diffusivity of nitrogen in the γ and δ with temperature. In addition, the interface concentration of nitrogen increases with temperature, and the driving force for diffusion is consequently increased. Figure **6.14** shows the transformation can go to completion only at temperatures higher than the equilibrium completion temperature (1592 K). The calculated TTT diagram also indicates that for the isothermal formation of δ-ferrite, the transformation start time is usually less than 0.2 s, while the time for completion is less than 0.9 s.

In the CHT diagram, the time temperature relationship is expressed as: $T(t) = 1338 + H_T \times t$, where H_T is the heating rate, and t is the time. The non-isothermal transformation kinetics at various heating rates were calculated using the numerical diffusion model, and the resulting δ fraction versus time data were then used to construct the CHT diagram. Figure **6.15** shows the computed CHT diagram for the γ→δ transformation, where time zero represents the moment when the 1338 K temperature is reached. Superimposed in this figure are the SRXRD experimental data points, at which the completion of the γ→δ transformation is observed. These data points were plotted using the average heating rates during this transformation at respective monitoring locations. The SRXRD data points scattered in the area where the heating rates vary from

75 K/s to 200 K/s. The 99% δ profile, which represents the completion of the transformation, correlates with the SRXRD data fairly, although the model predicts faster transformation rates than experiments.

As shown in Fig. **6.15**, the transformation rate accelerates rapidly with temperature, and both the start and finish temperatures of the transformation increase with increasing heating rate. A comparison between Figs. **6.14** and **6.15** shows that the time required for an equivalent amount of δ formation is longer under the non-isothermal conditions than that under the isothermal conditions. The reason for this behavior is that the total kinetic strength of the transformation is less for the CHT case than for the TTT case, since the time temperature curves are integrated up to the final temperature where the transformation is predicted in the CHT conditions. The CHT diagram for the 2205 DSS indicates that for the non-isothermal formation of δ-ferrite, the transformation start time is usually greater than 0.2 s, while the time for completion is greater than 6 s.

Figure **6.15** also indicates that only a small amount of superheat is required to complete the phase transformation under non-isothermal heating conditions in the 2205 DSS, comparing with those in 1005 steel and Ti-6Al-4V alloy welds reported in the previous chapter. For heating rates of 50 K/s and 100 K/s, Fig. **6.15** predicts the transformation finishes at 6 K and 26 K above the equilibrium completion temperature (i.e. 1592 K), respectively. Such small superheat may be explained by the following two reasons. First, the thicknesses of the γ and δ plates are small. Table **6.1** indicates the half thicknesses of γ and δ plates are only 9.5 and 11.15 μm, respectively. Hence, the distance of nitrogen diffusion is small. Second, at elevated temperatures, the diffusivities of nitrogen in both γ and δ plates are fairly high. Since the γ→δ transformation is assumed to be controlled by nitrogen diffusion, the high nitrogen diffusivity and small diffusion distance result in quick completion of the transformation.

It should be noted that the above TTT and CHT diagrams assume a start temperature of 1338 K. In other words, the nitrogen diffusion below this temperature is ignored. Therefore, strictly speaking, the TTT and CHT diagrams are valid under the rapid heating conditions during welding. Application of them to study the γ→δ transformation in the 2205 DSS under low heating conditions should be careful.

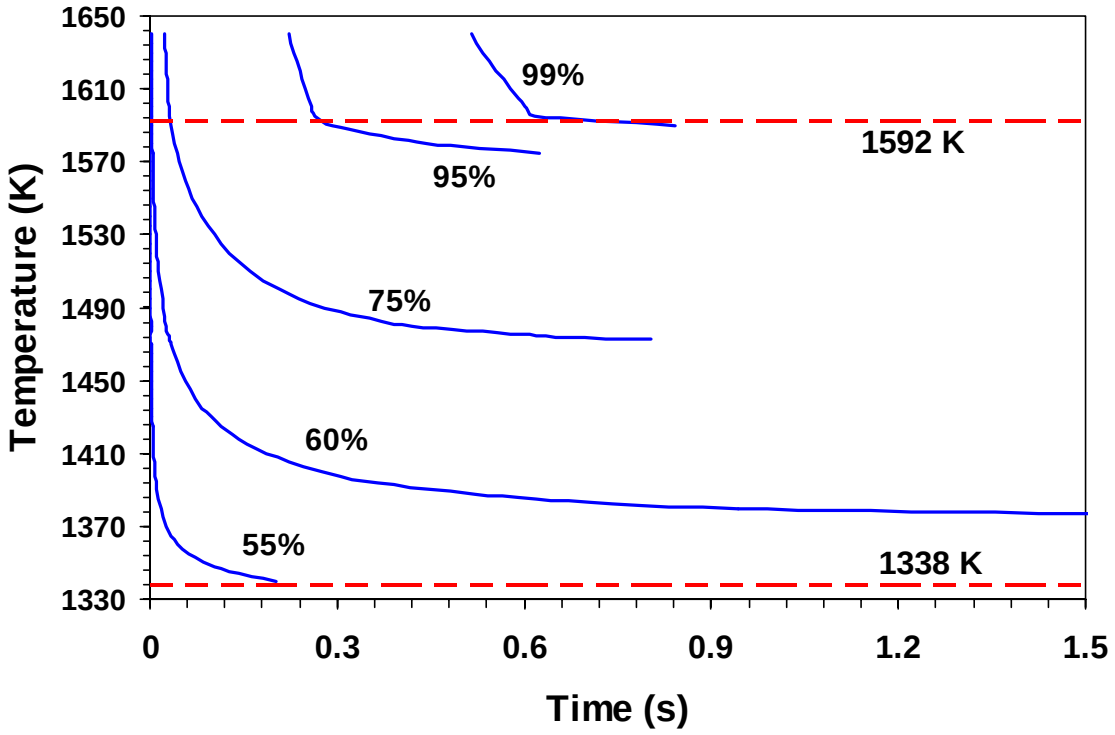

Fig. **6.14**: Calculated TTT diagram for the $\gamma \rightarrow \delta$ transformation during heating of the 2205 DSS. The 1338 K is the nominal starting temperature of the transformation.

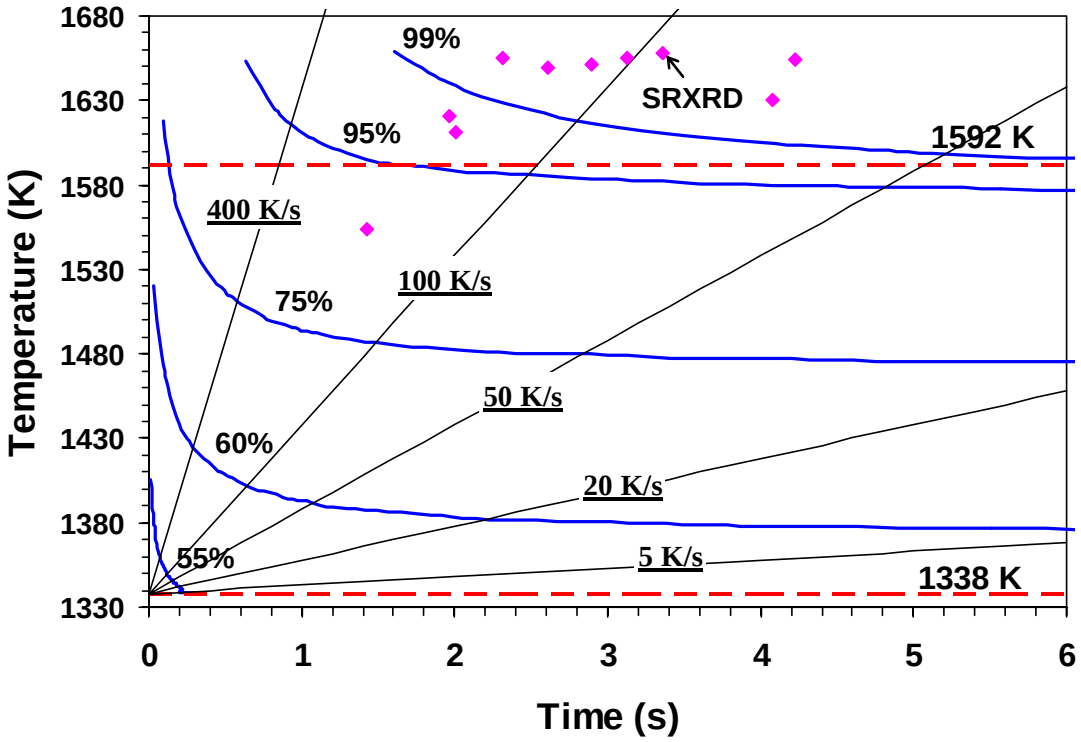

Fig. **6.15**: Calculated CHT diagram for the γ→δ transformation during heating of the 2205 DSS. Solid diamonds represent the experimental data points at which the completion of the transformation is observed.

6.3.4 Effect of starting microstructure

In the preceding discussion, the starting microstructure of the 2205 DSS is assumed to be represented by a pair of δ and γ grains with a uniform starting grain structure. Although this assumption has been widely used in the literature [3,9-12], an actual material rarely contains a uniform grain size. A recent study based on the Avrami theory indicates that the overall transformation rate is fastest when the starting grain structure is uniform [25]. In other words, non-uniform grain structure slows down the transformation kinetics. In the present study, a preliminary attempt was made to understand the effect of the non-uniform grain structure on the kinetics of the γ→δ transformation based on the numerical diffusion model. For simplicity, a unit system consisting of two δ grains and two γ grains with different thicknesses was used to represent the starting microstructure of the 2205 DSS. Although still fairly simple, such a system allows the study of the interactions between neighboring grains, particularly the overlapping of diffusion fields (soft impingement) and existing grain boundaries (hard impingement).

Figure 6.16(a) shows four alternating plates of δ and γ grains. The unit system used in the calculation consists of a half of δ1, one γ1, one δ2, and a half of γ2. In other words, the left half of δ1 and the right half of γ2 are not included in the unit system. Such unit system is used to simplify the numerical calculation, since only three moving interfaces (M1, M2 and M3) are required to be solved in the system. For instance, if the complete δ1 grain is included in the unit system, the leftmost δ/γ interface (M_L) needs to be determined. Similarly, the rightmost δ/γ interface (M_R) is required to be calculated, if the complete γ2 grain is considered. Tracing multiple moving interfaces increases the complexity of the numerical diffusion calculation, since the calculation needs to handle the situation where the interfaces impinge or disappear. As it will be shown later, the unit system shown in Fig. 6.16(a) allows the investigation of the interaction between neighboring grains, which is one of the characteristics of the non-uniform microstructure. Therefore, the unit system consisting of one and a half δ grains, one and a half γ grains, and three moving δ/γ interfaces is used in the diffusion calculation for its simplicity.

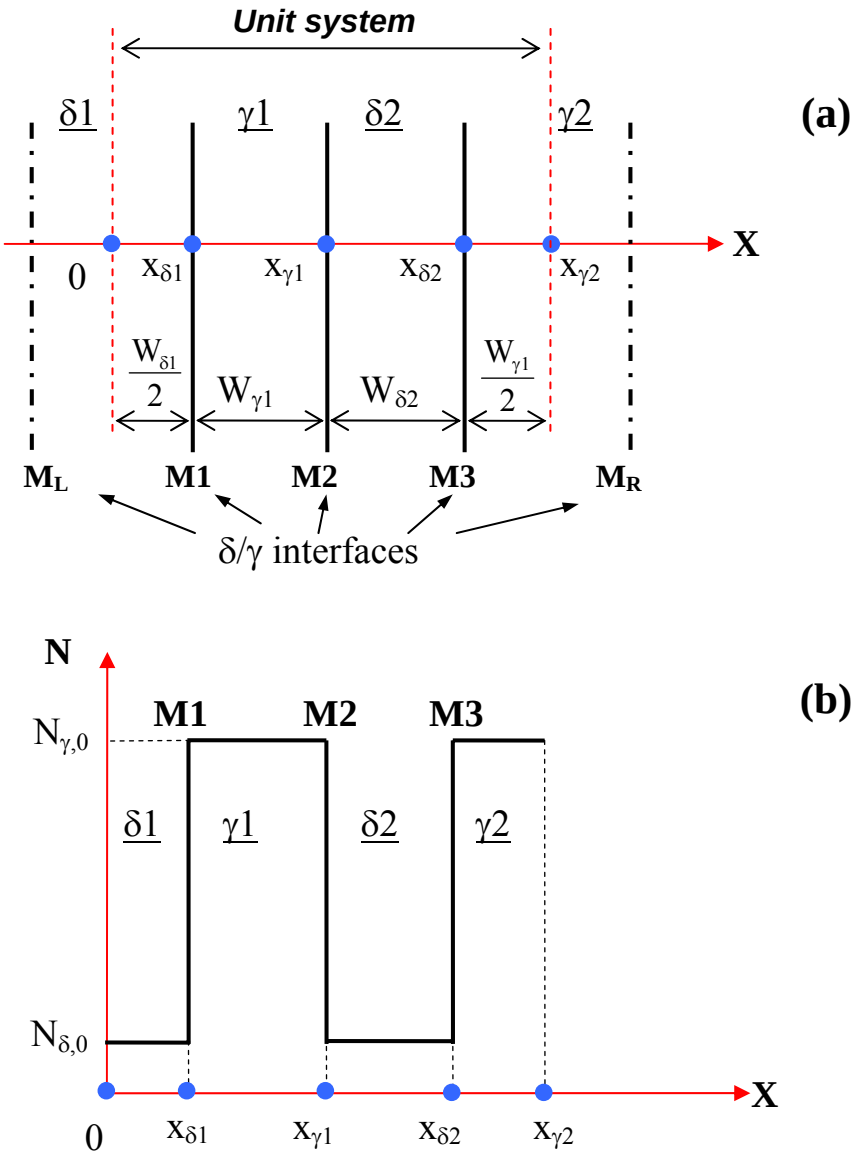

Fig. **6.16**: Initial microstructure of the 2205 DSS with non-uniform grain structure. (a) four γ and δ grains, and (b) the initial nitrogen concentration profile in γ and δ phases. Symbol W represents the thickness of various grains.

For the system shown in Fig. **6.16**, the governing diffusion equations are given as follows:

$$\begin{aligned}
&\frac{\partial N}{\partial t} = D_{\delta}\frac{\partial^2 N}{\partial x^2} && \text{in } \delta 1 \ (0 < x < M1)\\
&\frac{\partial N}{\partial t} = D_{\gamma}\frac{\partial^2 N}{\partial x^2} && \text{in } \gamma 1 \ (M1 < x < M2)\\
&\frac{\partial N}{\partial t} = D_{\delta}\frac{\partial^2 N}{\partial x^2} && \text{in } \delta 2 \ (M2 < x < M3)\\
&\frac{\partial N}{\partial t} = D_{\gamma}\frac{\partial^2 N}{\partial x^2} && \text{in } \gamma 2 \ (M3 < x < x_{\gamma 2})
\end{aligned} \qquad (6.20)$$

where N is the nitrogen concentration, t is the time, D_{δ} and D_{γ} are the diffusivities of nitrogen in the δ and γ phases, respectively, and M1, M2 and M3 are interfaces between δ1 and γ1, γ1 and δ2, and δ2 and γ2, respectively.

Figure **6.16(b)** plots the assumed initial concentration profile of nitrogen in the four grains along the X direction. Hence, the initial conditions are given as:

$$\begin{aligned}
&N = N_{\delta,0} && 0 \le x \le M1 \text{ and } M2 \le x \le M3\\
&N = N_{\gamma,0} && M1 \le x \le M2 \text{ and } M3 \le x \le x_{\gamma 2}\\
&M1 = x_{\delta 1}, && M2 = x_{\gamma 1}, \qquad M3 = x_{\delta 2}
\end{aligned} \qquad (6.21)$$

The boundary conditions are given as:

$$\begin{aligned}
&\delta 1: && \frac{\partial N}{\partial x} = 0 \text{ at } x = 0, && N = N_{\delta,M} \text{ at } x = M1^{-}\\
&\gamma 1: && N = N_{\gamma,M} \text{ at } x = M1^{+}, && N = N_{\gamma,M} \text{ at } x = M2^{-}\\
&\delta 2: && N = N_{\delta,M} \text{ at } x = M2^{+}, && N = N_{\delta,M} \text{ at } x = M3^{-}\\
&\gamma 2: && N = N_{\gamma,M} \text{ at } x = M3^{+}, && \frac{\partial N}{\partial x} = 0 \text{ at } x = x_{\gamma 2}
\end{aligned} \qquad (6.22)$$

where the minus and plus signs represent the left and right sides of a δ/γ interface, respectively. Eq. **6.22** indicates that symmetric boundary conditions are used at x = 0 and $x = x_{\gamma 2}$. In other words, there is no net nitrogen flux across either of the two boundary surfaces, and the total nitrogen content in the unit system is conserved.

Considering the nitrogen mass conservation in the system, the three moving interfaces, i.e. M1, M2 and M3, are traced using the following equation.

$$\begin{aligned}
&\text{M1}: \quad \left(N_{\gamma,M} - N_{\delta,M}\right)\frac{dM1}{dt} = D_{\delta}\left.\frac{\partial N}{\partial x}\right|_{M1-} - D_{\gamma}\left.\frac{\partial N}{\partial x}\right|_{M1+} \\
&\text{M2}: \quad \left(N_{\delta,M} - N_{\gamma,M}\right)\frac{dM2}{dt} = D_{\gamma}\left.\frac{\partial N}{\partial x}\right|_{M2-} - D_{\delta}\left.\frac{\partial N}{\partial x}\right|_{M2+} \qquad (6.23) \\
&\text{M3}: \quad \left(N_{\gamma,M} - N_{\delta,M}\right)\frac{dM3}{dt} = D_{\delta}\left.\frac{\partial N}{\partial x}\right|_{M3-} - D_{\gamma}\left.\frac{\partial N}{\partial x}\right|_{M3+}
\end{aligned}$$

One of the characteristics of the non-uniform microstructure is the interaction between neighboring grains. For instance, when a γ grain completely dissolves, the two neighboring δ grains impinge on each other. For the unit system shown in Fig. **6.16(a)**, there are two possible circumstances of the γ dissolution: γ1 may dissolve completely before γ2; and vice versa. Such change needs to be considered in order to accurately simulate the γ→δ transformation in a non-uniform starting microstructure.

In this study, the impingement is taken into account through the proper adjustment of the boundary conditions (Eq. **6.22**) and interface locations (Eq. **6.23**). Figures **6.17(a)** and **(b)** shows the nitrogen concentration profile for the two circumstances: (a) γ1 dissolves completely before γ2, and (b) γ2 dissolves completely before γ1. When γ1 dissolves first, δ1 and δ2 impinge on each other (hard impingement). It is assumed that the grain boundary between two δ grains is stationary after impingement. Therefore, interfaces M1 and M2 vanish after the impingement, and no boundary condition is needed at the δ1/δ2 grain boundary. In the case that γ2 dissolves completely before γ1, as shown in Fig. **6.17(b)**, interface M3 is removed from the system. The boundary conditions for δ2 are changed to the following equation.

$$\delta 2: \quad N = N_{\delta,M} \text{ at } x = M2^{+}, \qquad \frac{\partial N}{\partial x} = 0 \text{ at } x = x_{\gamma 2} \qquad (6.24)$$

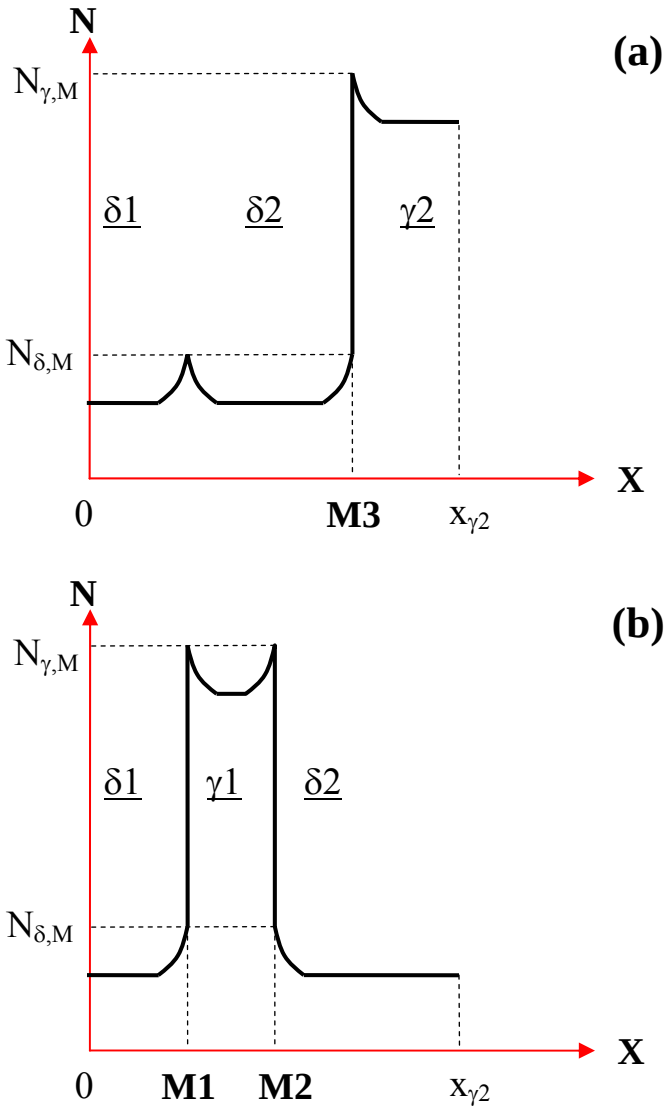

Fig. **6.17**: Schematic plot showing the nitrogen concentration profile for the two circumstances: (a) γ1 dissolves completely before γ2, and (b) γ2 dissolves completely before γ1.

Using the system described above, the effect of the starting microstructure on the phase transformation rates was studied by assigning the four grains with different thicknesses. Table **6.3** shows the five types of starting microstructures considered. In type #0, the average thicknesses for the γ and δ grains were used, i.e., $W_{\delta 1} = W_{\delta 2} = 22.3$ μm, and $W_{\gamma 1} = W_{\gamma 2} = 19.0$ μm.

Table **6.3**: Different types of starting microstructure for the γ→δ transformation in the 2205 DSS.

Type	$\frac{W_{\delta 1}}{2}$ (μm)	$W_{\gamma 1}$ (μm)	$W_{\delta 2}$ (μm)	$\frac{W_{\gamma 2}}{2}$ (μm)
0	11.15	19.0	22.3	9.5
1	11.15	5.0	22.3	23.5
2	11.15	23.5	22.3	5.0
3	5.15	19.0	28.3	9.5
4	28.3	19.0	5.15	9.5

For types #1 through #4 in Table **6.3**, the grain thicknesses are so chosen that the average grain thicknesses in the system are equal to those in the 2205 DSS base metal. In other words, the thicknesses of δ1, γ1, δ2, γ2 grains satisfy the following relationship.

$$\frac{0.5\,W_{\delta 1} + W_{\delta 2}}{1.5} = 22.3\ \mu m$$
$$\frac{W_{\gamma 1} + 0.5\,W_{\gamma 2}}{1.5} = 19.0\ \mu m \qquad (6.25)$$

where the coefficients of 0.5 and 1.5 are used to account for the actual number of grains in the system. As shown in Fig. **6.16(b)**, the system contains one and a half δ grains (i.e., half of δ1 plus δ2), and one and a half γ grains (i.e., γ1 plus half of γ2). The average thickness of a phase is defined as the total thickness of that phase by the number of grains. For the system shown in Fig. **6.16(b)**, the total thickness of the δ grains is $\frac{W_{\delta 1}}{2} + W_{\delta 2}$, whereas the δ grain number is $\frac{3}{2}$. Therefore, the average δ grain thickness in

the system is $\frac{0.5\,W_{\delta 1} + W_{\delta 2}}{1.5}$. Similarly, the average γ grain thickness is $\frac{W_{\gamma 1} + 0.5\,W_{\gamma 2}}{1.5}$, as given by Eq. **6.25**.

Figure **6.18** plots the calculated nitrogen concentration profile versus time for type #1 in Table **6.3**. For this type of starting microstructure, the γ1 grain has a small thickness, which is 5 μm. The γ1 grain dissolves completely at a time slightly after 0.9 s. As a result, the δ1 and δ2 grains impinge on each other, and interfaces M1 and M2 no longer exist. After the dissolution of the γ1 grain, the transformation is controlled only by the movement of interface M3. The calculated nitrogen concentration profile versus time for type #2 (Table **6.3**) is shown in Fig. **6.19**, where γ2 has a smaller thickness than γ1. As shown in this figure, the γ2 grain dissolves completely before γ1, and interface M1 vanishes. Both interface M1 and M2 continue to move until the γ1 grain dissolves completely.

Figure **6.20** shows the comparison of phase transformation rates at y = 3.5 mm location for various types of starting microstructures given in Table **6.3**. As shown in this figure, the transformation rates are fastest for type #0, where the average grain thicknesses of the δ and γ are used. Non-uniform starting structures slow down the transformation kinetics, particularly toward the end of the transformation. Figure **6.20** indicates that for type #0, the γ→δ transformation starts at t = -7.9 s and completes at t = -5.4 s. For all other four types, the transformation starts also at t = -7.9 s but completes at a much later time, i.e. t > -4 s.

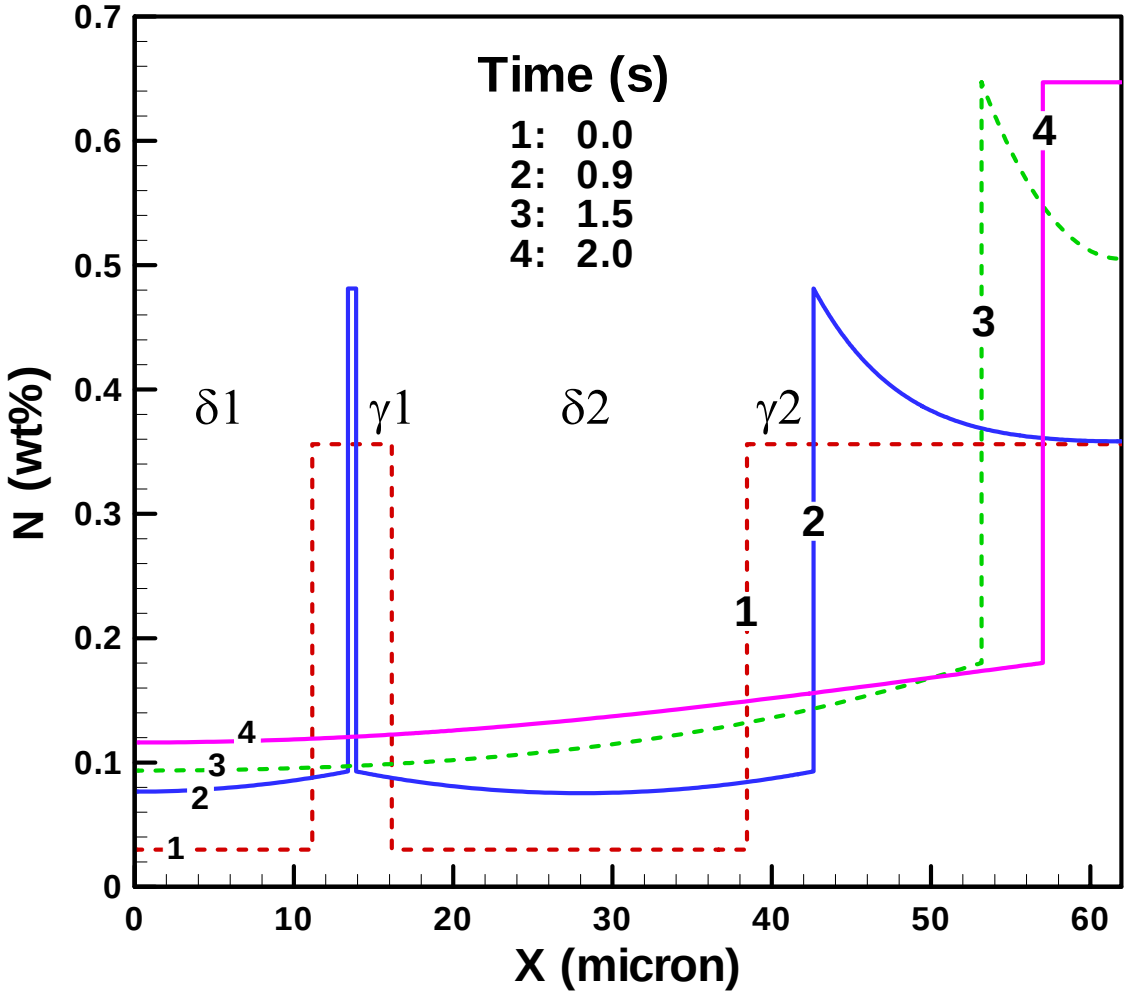

Fig. **6.18**: Calculated nitrogen concentration profile as a function of time for type #1 starting microstructure in Table **6.3**. The thermal cycle at y = 3.5 mm was used in the calculation. Time zero corresponds to the moment when the 1338 K temperature is reached at the y = 3.5 mm location.

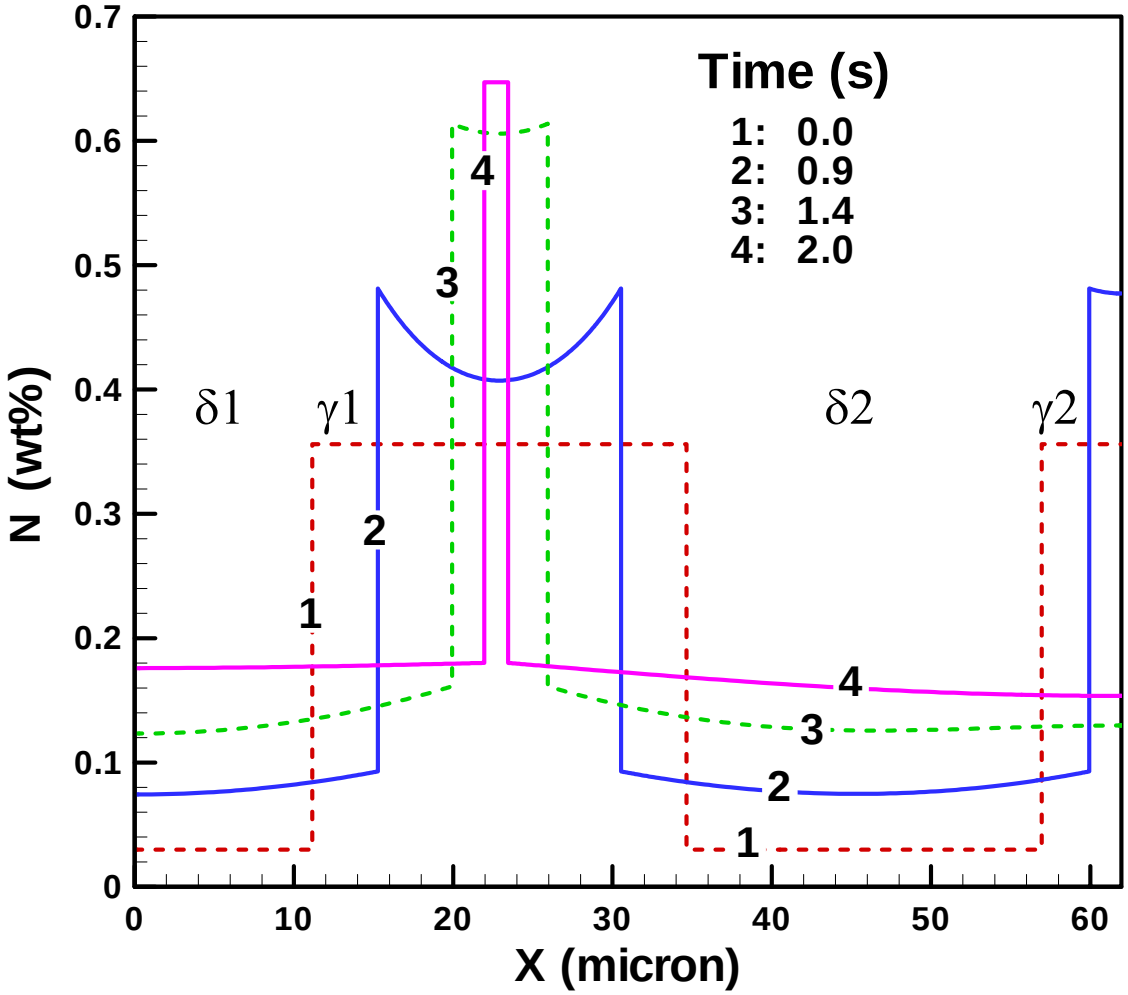

Fig. **6.19**: Calculated nitrogen concentration profile as a function of time for type #2 starting microstructure in Table **6.3**.

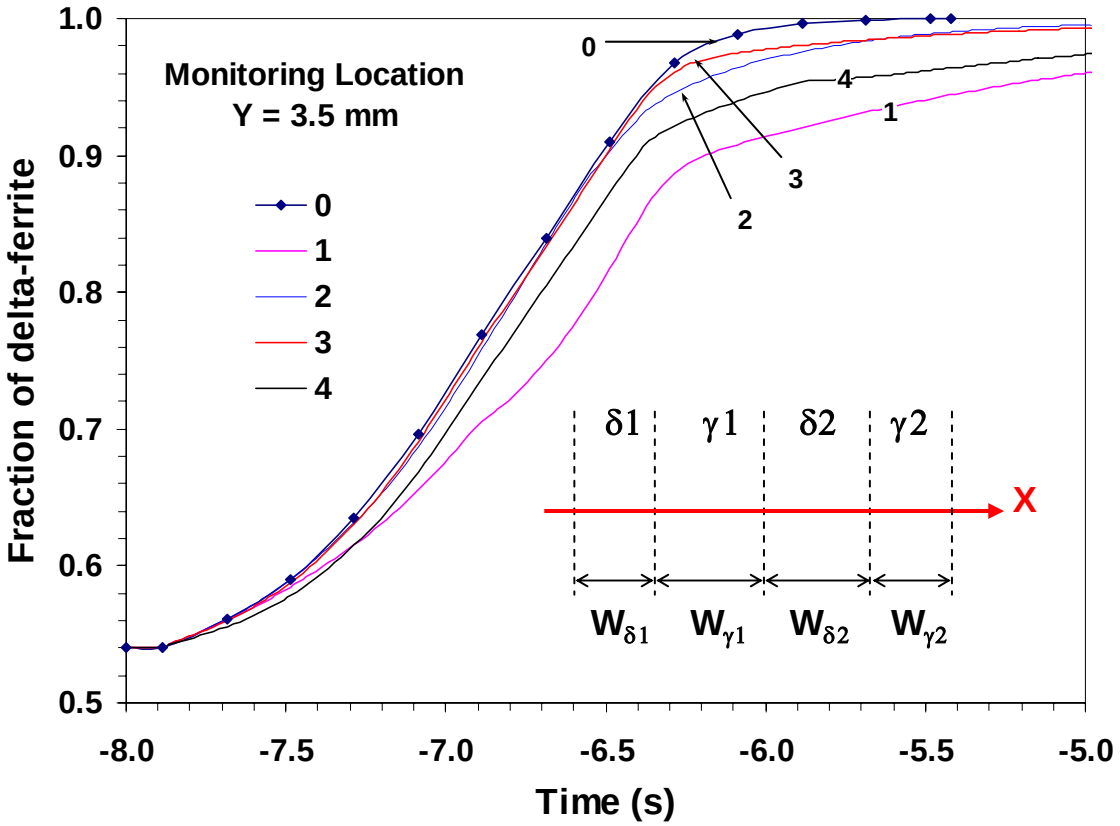

Fig. **6.20**: Ferrite fraction versus time plot for the five types of starting microstructures shown in Table **6.3**.

Types #0, #1 and #2 in Fig. **6.20** compare the effect of the variation in the γ grain thickness on the transformation kinetics. In type #0, both γ grains have the same thickness (19.0 μm), whereas in type #1, the system consists of a very small γ grain (5.0 μm) and a fairly large γ grain (47.0 μm). The γ grain thicknesses for type #2 lie in between those in type #0 and type #1: the large γ grain has a thickness of 23.5 μm and the small one has a thickness of 10.0 μm.

Figure **6.20** shows that the larger the deviation from the average γ thickness, the slower the transformation rate. This is because the small γ grain dissolves completely at first, and the transformation kinetics are then controlled by the nitrogen diffusion in the large γ grain. Figure **6.20** further indicates that the existence of a small γ grain does not speed up the transformation rate at the beginning of the reaction. This is due to the following reason. The γ→δ transformation is assumed to be controlled by nitrogen diffusion. The interface moving velocity, which determines the overall transformation kinetics, depends mostly on the rate at which the nitrogen diffuses away from the δ/γ interface into the δ phase. Therefore, the γ grain thickness may not significantly affect the interfacing moving velocity, and the transformation rates for all three cases are similar at the beginning of the reaction. However, toward the end of the transformation, the small γ grain completely dissolves before the large one. As a result, only one δ/γ interface is still moving, and the other two interfaces impinge on each other, as illustrated in Fig. **6.18**. Hence, the overall transformation rates slow considerably.

The effect of the variation in the δ grain thickness on the transformation kinetics is shown in types #0, #3 and #4 of Fig. **6.20**. It is found that the larger the deviation from the average δ thickness, the slower the transformation rate. However, it seems that the variation in the δ grain thicknesses has a less significant effect on the transformation rates than that in the γ thicknesses. This behavior is expected because of the following. The two γ grains in the system have the same thickness, and they completely dissolve only at the end of the transformation. Three moving δ/γ interfaces exist in the system through the majority of the transformation. In other words, the interface area, in which the γ phase is

in contact with the δ phase, has not changed. As a result, the transformation rates are not significantly affected by the δ grain thicknesses.

It is also interesting to investigate the effect of the starting microstructure on the TTT and CHT diagrams, which are two useful graphical representations of the transformation rates. Figure **6.21** shows the effect of the starting structure on the isothermal transformation kinetics. The uniform and non-uniform microstructures correspond to type #0 and #2 in Table **6.3**, respectively. As shown in this figure, the 55% and 75% δ profiles are unaffected by the starting microstructure, whereas the 99% profile for the non-uniform structure is significantly delayed than that for the uniform one. This phenomenon could be explained by the following. At the initial stage of the transformation, both γ grains dissolve, and the δ/γ interface area is the same for both structures. Since the interface moving velocities are not significantly affected by the grain thickness, the transformation rates for both uniform and non-uniform structures are similar. In contrast, toward the end of the transformation, the small γ grain dissolves before the large one in the non-uniform structure. Hence, the δ/γ interface area is reduced. As a result, the transformation rates for the non-uniform structure slow down, and it takes about 1 second more for the non-uniform structure to complete the transformation than the uniform one.

Figure **6.22** plots the computed CHT diagram for the uniform and non-uniform starting microstructures. Superimposed are the experimental data points where the completion of the γ→δ transformation was observed using the SRXRD technique. Similar to those shown in the TTT diagram, the 55% and 75% δ profiles are unaffected by the starting structure. On the other hand, the non-uniform structure significantly delays the completion of the transformation. The SRXRD experimental data lie in between the two 99% profiles for the uniform and non-uniform structures. A comparison between Figs. **6.21** and **6.22** indicates the effect of the starting microstructure is similar for the γ→δ transformation under isothermal and non-isothermal conditions.

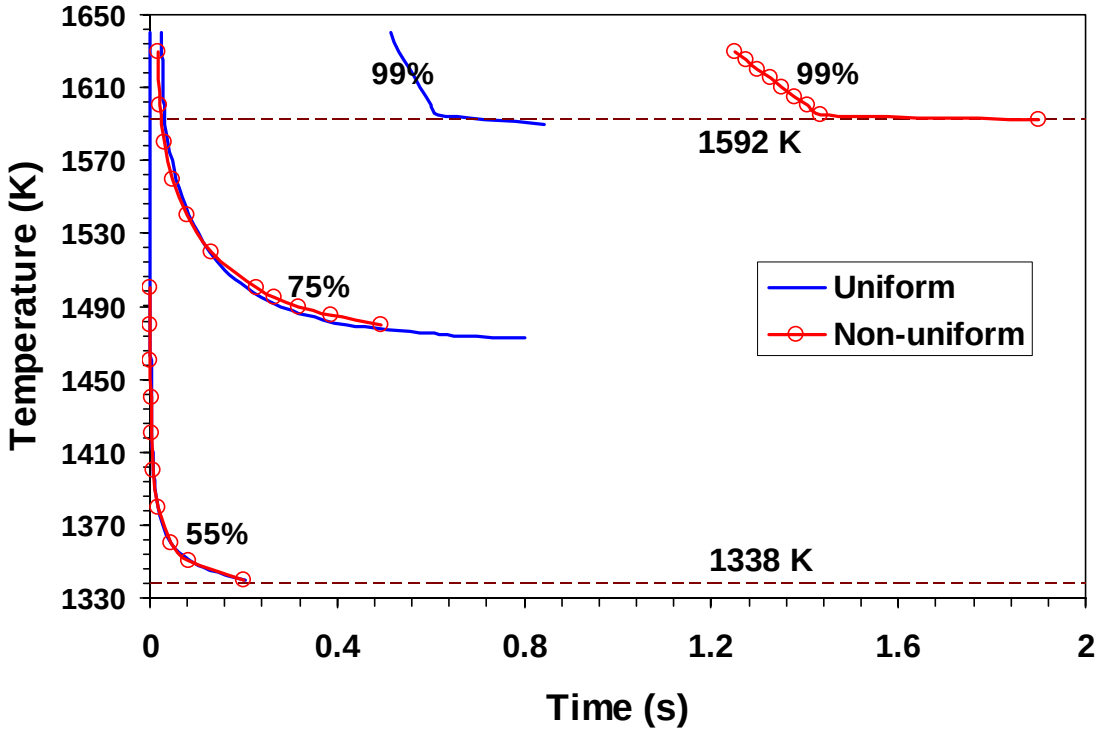

Fig. **6.21**: Effect of the starting microstructure on the computed TTT diagram for the γ→δ transformation in the 2205 DSS.

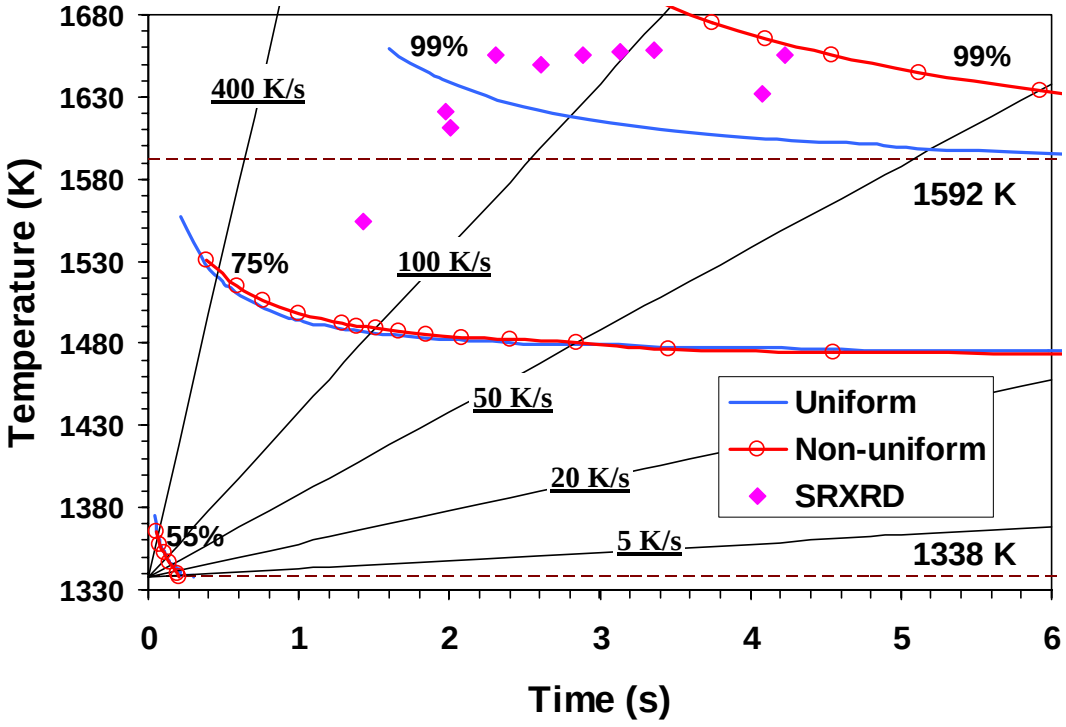

Fig. **6.22**: Effect of the starting microstructure on the computed CHT diagram for the γ→δ transformation in the 2205 DSS.

The following issues should be noted in the interpretation of the results computed using the numerical diffusion model.

First, the system considered here is a constrained one in which the interfacial boundary area is held constant. In a real material, the non-uniformity in the microstructure may also result in the variation of the interfacial area. If the interfacial area for a non-uniform structure is higher than that of the uniform structure, the overall transformation rate for the non-uniform structure may be faster than that of uniform structure at the beginning of the transformation. However, toward the end of the transformation, the non-uniform structure is also expected to slow down the overall transformation rate.

Second, the system used here has a one-dimensional geometry, which provides a reasonable approximation of the microstructure in the 2205 DSS. However, the microstructure in the real material usually has a three-dimensional shape. Hence, it will be interesting to investigate the effect of non-uniformity on the transformation kinetics in the three-dimensional system. Using the moving interface approach to simulate the diffusion problem in three dimensions is difficult [**16**], and other techniques such as phase field method [**26**] may be utilized. However, a recent study [**25**] based on the Avrami theory, considering the nucleation and growth in three dimensions, suggested similar trends as those predicted using the one-dimensional diffusion model. In other words, it is also found that the initial transformation rate is not prominently affected by the non-uniform structure, whereas the completion of the transformation is significantly delayed.

Finally, it should be noted that the system used here consists of only four grains. A more comprehensive study is necessary to accurately predict the transformation kinetics in 2205 DSS. Such study needs to take into account the actual distribution of grain thicknesses in the starting microstructure and the diffusion of nitrogen as well as other alloying elements in multiple grains. This work is left for a future study.

6.4 Summary and conclusions

Kinetics of the γ-austenite to δ-ferrite transformation during GTA welding of 2205 DSS was studied experimentally by the SRXRD technique and simulated using a combination of thermo-fluid and diffusion models. The following conclusions can be made from the present investigation.

(1) A three-dimensional heat transfer and fluid flow model was used to calculate the temperature and velocity fields during GTA welding of 2205 DSS. Because of the presence of sulfur in the base metal, the liquid metal flows inward around the periphery and moves outward at the center of the weld pool. As a result, a rounded weld pool is formed. The calculated FZ geometry correlates fairly well with the experimental FZ geometry. The thermal cycles in the entire weldment were predicted using the thermo-fluid flow model, and were then used in the kinetic calculations.

(2) A numerical diffusion model employing a moving grid system to trace the moving interface was developed to calculate the kinetics of γ→δ transformation during heating of the 2205 DSS. The predicted transformation kinetics agree reasonable well with those measured using the SRXRD technique at various monitoring locations in the weldment. The calculated fraction converted curve exhibits an S-shaped profile as a result of the non-isothermal heating.

(3) The TTT and CHT diagrams were calculated for the 2205 DSS using the numerical diffusion model, providing a graphical means to predict the kinetics of the γ→δ transformation. Both TTT and CHT diagrams show that the transformation rate increases with temperature.

(4) A preliminary study of the effect of non-uniform starting microstructure on the transformation rate was carried out considering a system with two γ grains and two δ grains. It is found that the overall transformation rate is fastest when the starting structure is uniform. The non-uniform starting structure slows down the transformation rate, particularly towards the end of the transformation, because the small γ grains dissolve at the initial stage of the transformation, thereby reducing the δ/γ interface area. The overall reaction rate is then controlled by the dissolution of large γ grains. The variation of γ

grain thickness has a more profound effect on retarding the transformation kinetics than that of δ grain thickness.

6.5 References

1. *Metals Handbook: Properties and Selection: Iron, Steels, and High Performance Alloys*, 10th edition., vol. 1, Materials Park, OH, ASM International, 1990.

2. R. N. Gunn: *Duplex Stainless Steels: Microstructure, properties and applications*, Abington Publishing, Cambridge, 1997.

3. H. Hemmer and Ø. Grong: *Metall. Mater. Trans. A*, **30A**, 2915 (1999).

4. J. W. Elmer, J. Wong, M. Fröba, P. A. Waide and E. M. Larson: *Metall. Mater. Trans. A*, **27A**, 775 (1996).

5. J. W. Elmer, J. Wong and T. Ressler: *Metall. Mater. Trans. A*, **29A**, 2761, (1998).

6. J. W. Elmer, J. Wong and T. Ressler: *Metall. Mater. Trans. A*, **32A**, 175 (2001).

7. T. A. Palmer, J. W. Elmer and J. Wong: *Sci. Technol. Weld. Joining*, **7**, 159 (2002).

8. T. A. Palmer, J. W. Elmer and S. S. Babu: *Mater. Sci. Eng. A*, in press, May 2004.

9. T. Akbay, R. C. Reed and C. Atkinson: *Acta Metall. Mater.*, **47**, 1469 (1994).

10. C. Atkinson, T. Akbay and R. C. Reed: *Acta Metall. Mater.*, **43**, 2013 (1995).

11. J. Årgon: *Acta Mater.*, **30**, 841 (1982).

12. J. R. Yang and H. K. D. H. Bhadeshia: *Mater. Sci. Eng. A*, **131**, 99 (1991).

13. S. Hertzman, P. J. Ferreira and B. Brolund: *Metall. Mater. Trans. A*, **28A**, 277 (1997).

14. P. Shewmon: *Diffusion in Solids*, 2nd edition, TMS, Warrendale, PA, 1989.

15. W. D. Murray and F. Landis: *Journal of Heat Transfer*, Transactions of the ASME, **81**, 106 (1959).

16. J. Crank: *The mathematics of Diffusion*, 2nd edition, Clarendon Press, Oxford, 1975.

17. S. V. Patankar: *Numerical Heat Transfer and Fluid Flow*, McGraw-Hill, New York, 1980.

18. S. Kou: *Transport phenomena and materials processing*, John Wiley, New York, 1996.

19. W. H. Press, B. P. Flannery, S. A. Teukolsky and W. T. Vetterling: *Numerical recipes in FORTRAN*, 2nd edition, Cambridge University Press, Cambridge, 1992.

20. S. Hertzman, W. Roberts and M. Lindenmo: in *Proceedings of Duplex Stainless Steels 86*, 1986, Hague, Netherlands, p. 257.

21. B. Rhee, S. Roh and D. Kim: *Mater. Trans.*, The Japan Institute of Metals, **44**, 1014 (2003).

22. K. Mundra, T. DebRoy and K. M. Kelkar: *Numer. Heat Transfer A*, **29**, 115 (1996).

23. F. Cverna: *Thermal properties of metals*, ASM International, Materials Park, OH, 2002.

24. P. Sahoo, T. DebRoy and M. J. McNallan: *Metall. Trans. B*, **19B**, 483 (1988).

25. H. Matsuda and H. K. D. H. Bhadeshia: *Mate. Sci. Technol.*, **19**, 1330 (2003).

26. L. Q. Chen: *Ann. Rev. Mater. Res.*, **32**, 113 (2002).

Chapter 7

CONCLUDING REMARKS

7.1 Summary and Conclusions

In the present thesis research, the heat transfer, fluid flow and microstructural evolution during fusion welding were investigated based on the fundamentals of transport phenomena and phase transformation theory. Numerical heat transfer and fluid flow calculations were used to predict the liquid metal convection in the weld pool, the temperature distribution in the entire weldment, and the shape and size of the fusion zone (FZ) and heat affected zone (HAZ). An x-ray diffraction technique was used to obtain real-time phase maps under welding conditions by Dr. John W. Elmer of Lawrence Livermore National Laboratory. Phase transformation models and computed thermal cycles were then used to analyze the unique kinetic data obtained by the x-ray diffraction technique. Such analysis was useful to quantitatively understand the kinetics and mechanisms of phase transformations during fusion welding.

The numerical models used in the present thesis work included the follows. (1) An existing transient heat transfer and fluid flow model was utilized for the calculation of the evolution of temperature and velocity fields during spot welding. This transient model was developed by Dr. DebRoy's group at Penn State. (2) A three-dimensional heat transfer and free surface flow model was developed by the author and Dr. Cheolhee Kim for the gas metal arc (GMA) fillet welding considering the complex weld joint geometry. (3) A kinetic model based on the Johnson-Mehl-Avrami (JMA) theory was developed by the author for the calculation of phase transformation kinetics. (4) An existing Monte Carlo model, developed at Dr. DebRoy's group, was used to simulate the grain growth. (5) An existing austenite decomposition model was used to compute the weld final microstructure. This model was developed by Dr. Bhadeshia et al. of Cambridge University. (6) A one-dimensional numerical diffusion model considering multiple

moving interfaces was used to understand phase transformations in a duplex stainless steel (DSS). This diffusion model was developed by the author.

These numerical models together with advanced welding experiments were applied to study the heat transfer, fluid flow and microstructural evolution during fusion welding of several important alloys. The subjects studied in this thesis included: (a) the transient heat transfer and fluid flow during gas tungsten arc (GTA) spot welding of 1005 steel, (b) the heat transfer and free surface flow during GMA fillet welding of A-36 steel, (c) the microstructural evolution during GTA linear welding of 1005 steel, (d) the α-ferrite to γ-austenite phase transformation in 1045 spot arc welds, (e) the α-Ti to β-Ti phase transformation in Ti-6Al-4V spot arc welds, and (f) the γ-austenite to δ-ferrite phase transformation during GTA linear welding of 2205 DSS. The models were validated by comparing the predictions with the experimental results for various conditions.

At the end of Chapter 2, a selection of unanswered questions in the subject of heat transfer, fluid flow and microstructural evolution during fusion welding were identified. Those unanswered questions were investigated during the course of the present thesis research. The current understandings of those questions based on the present study are summarized as follows:

I. Heat transfer and fluid flow during transient spot welding

A transient numerical model was used to understand the evolution of temperature and velocity fields during GTA spot welding of 1005 steel. The thermal cycles, weld pool geometry and various solidification parameters could be quantitatively calculated.

(a) The geometry of the FZ and HAZ and weld cooling curves predicted from the transient thermo-fluid model were in good agreement with the corresponding experimental results. The calculated critical cooling rates between the 1073 K and 773 K temperature range are found to be almost independent of position.

(b) Liquid metal convection is the dominant mechanism of heat transfer as the weld

pool is fully developed, and thus determines the temperature distribution in the liquid pool as well as the pool shape and size. Heat transfer by conduction is important when the liquid velocity is small at the beginning stage of melting and during pool solidification.

(c) The size of the mushy zone, i.e., liquid + solid two phase region, grows significantly with time during solidification. This behavior can be explained from the heat transfer consideration taking into account the latent heat of fusion.

(d) The temperature gradients in the mushy zone at the mushy zone/solid interface decrease with the solidification time, whereas the solidification rate of the mushy zone/solid interface increases with time. The computed solidification parameters were then used to estimate the solidification morphology and substructure in the 1005 steel spot welds. It is found that the weld pool solidifies with decreasing interface stability, i.e., with a higher tendency to form dendrites towards the center of the weld.

The transient heat transfer and fluid flow reported here serves as a basis for investigation microstructure under rapid heating and cooling conditions. In particular, the calculated temperature history is useful information to understand the microstructural evolution in the HAZ, while the computed solidification parameters are important in studying the solidified microstructure in the weld pool.

II. Heat transfer and free surface flow in complex weld joints

A three-dimensional numerical heat transfer and free surface flow model was developed to calculate the temperature profiles, velocity field, weld pool shape and size and the nature of the solidified weld pool reinforcement surface during GMA welding of fillet joints. The numerical model was used to study GMA fillet welding of A-36 steel.

(a) The numerical model solves the mass, momentum and energy conservation equations in a boundary fitted coordinate system. The governing conservation equations and the corresponding boundary conditions were transformed into the

curvilinear coordinate system, and then discretized and solved in a simple rectangular computational domain.

(b) The liquid metal convection plays dominant role in dissipating the heat in the weld pool. The melt convection determines the temperature distribution and shape of the weld pool. Heat transfer and fluid flow calculation results in not only a more realistic description of the heat transfer process in the weld pool, but also provides a better agreement with experimental weld bead profile than the heat transfer calculation alone.

(c) The role of various driving forces for the liquid metal convection was examined using both the dimensionless analysis and the numerical model. It is found that the liquid metal is driven mainly by the electromagnetic force and the Marangoni shear stress and, to a much less extent, by the buoyancy force. The flow pattern resulted from different driving forces in fillet welds is similar to that in butt welds.

(d) The heat transfer from metal droplets was simulated using a volumetric heat source. A procedure was established to calculate the radius, height and power density of the volumetric heat source based on the experimental data for GMA welding available in the literature.

(e) The weld pool surface profile was calculated by minimizing the total surface energy, which includes the surface tension energy, gravity potential, and work done by arc force.

(f) Both the experimental results and the model predictions indicate that the critical cooling rate between 1073 and 773 K decreased with increase in heat input per unit length. The calculated cooling rates were also in good agreement with independent experimental data.

(g) The numerically computed fusion zone geometry, finger penetration characteristic of the GMA welds and the solidified surface profile of the weld reinforcement were in fair agreement with the experimental results for various welding conditions. The leg length, penetration and actual throat were found to increase with the increase in welding current. All these parameters decreased with the increase in welding speed.

The heat transfer and free surface flow takes into account the characteristics of the complex GMA fillet welding process such as the complex joint geometry and metal droplet transfer. It can be used to optimize the fillet joint geometry and structure based on scientific principles.

III. Microstructural evolution during GTA welding of 1005 low-carbon steel

Microstructure evolution in the 1005 steel arc weld was studied experimentally by the x-ray diffraction technique and modeled using a combination of transport phenomena and phase transformation theory.

(a) A three-dimensional heat transfer and fluid flow model was used to predict the thermal cycles in the entire weldment. The geometry of the FZ and HAZ predicted from the thermo-fluid model were in good agreement with the corresponding experimental results.

(b) A JMA analysis that takes into account non-uniform weld heating and transformation in the $\alpha+\gamma$ two-phase field was used for the determination of the kinetics of the $\alpha\rightarrow\gamma$ transformation during weld heating. Using the SRXRD experimental data, the JMA kinetic parameters for the $\alpha\rightarrow\gamma$ phase transformation were determined. These kinetic parameters are consistent with a phase transformation controlled by diffusion of carbon with zero nucleation rate.

(c) TTT and CHT diagrams were calculated for the 1005 steel using the kinetic data determined from the SRXRD experiments, providing a graphical means to predict the $\alpha\rightarrow\gamma$ transformation on weld heating for the 1005 steel. These diagrams show that a significant level of superheat is required for the initiation and completion of the phase transformation under the heating rates common to arc welding.

(d) An existing MC model was used to calculate the γ grain growth kinetics in the HAZ. It was found that significant γ grain growth took place in the HAZ, particularly in the vicinity of the FZ.

(e) The microstructure of the 1005 steel weld consisted predominantly of

allotriomorphic and Widmanstatten ferrites. An existing austenite decomposition model and the computed cooling rates were used to calculate the volume fractions of microconstituents in both the FZ and HAZ. Good agreement was found between the calculated and the experimental volume fractions of allotriomorphic and Widmanstatten ferrites in the weld metal. The spatial variation of the final microstructure in the HAZ was quantitatively determined.

Three kinetic models and the computed weld thermal cycles were successfully coupled together to provide a complete picture of the microstructural evolution in the HAZ of the 1005 steel arc welds. The results indicated significant promise to understand the weldment microstructure based on phase transformation theory.

IV. Phase transformation kinetics in 1045 steel and Ti-6Al-4V alloy arc welds

In this investigation, the time resolved x-ray diffraction experiments were performed during transient spot arc welding of 1045 steel and Ti-6Al-4V alloy. The transient heat transfer and fluid flow model was used to predict weld temperatures as a function of weld time and location. The model was validated by comparing the predicted and experimentally measured geometry of the FZ. The TRXRD results were analyzed to model the kinetics of the α-ferrite$\rightarrow\gamma$-austenite transformation in the 1045 steel and the α-Ti to β-Ti transformation in the Ti-6Al-4V, using the JMA model and the computed weld temperatures. The JMA kinetic analysis of the TRXRD data provided a set of kinetic parameters, allowing a quantitative means for predicting phase transformation rates under different heating conditions.

V. Phase transformation kinetics in 2205 DSS arc welds

Kinetics of the γ-austenite to δ-ferrite transformation during GTA welding of 2205 DSS was studied experimentally by the x-ray diffraction technique and simulated using a combination of thermo-fluid and diffusion models.

(a) A heat transfer and fluid flow model was used to calculate the temperature and

velocity fields during GTA welding of 2205 DSS. Because of the presence of sulfur in the base metal, the liquid metal flows inward around the periphery and moves outward at the center of the weld pool. As a result, a rounded weld pool is formed. The calculated FZ geometry correlates fairly well with the experimental FZ geometry. The thermal cycles in the entire weldment were predicted using the thermo-fluid flow model, and were then used in the kinetic calculations.

(b) A numerical diffusion model employing a moving grid system to trace multiple moving interfaces was developed to calculate the kinetics of $\gamma \rightarrow \delta$ transformation during heating of the 2205 DSS. The predicted transformation kinetics agree somewhat reasonably with those measured using the SRXRD technique at various monitoring locations in the weldment. The calculated fraction converted curve exhibits an S-shaped profile as a result of the non-isothermal heating.

(c) The TTT and CHT diagrams were calculated for the 2205 DSS using the numerical diffusion model, providing a graphical means to predict the kinetics of the $\gamma \rightarrow \delta$ transformation. Both TTT and CHT diagrams show that the transformation rate increases with temperature.

(d) A preliminary study of the effect of non-uniform starting microstructure on the transformation rate was carried out considering a unit system with two γ grains and two δ grains. It is found that the overall transformation rate is fastest when the starting structure is uniform. The non-uniform starting structure slows down the transformation rate, particularly towards the end of the transformation.

The numerical diffusion model is useful to understand the effect of the non-uniform structure on the transformation kinetics, indicating a significant promise to better simulate phase transformations in engineering materials.

The most important feature of this study is its usefulness in understanding the heat transfer, fluid flow and microstructural evolution during fusion welding based on the fundamentals of transport phenomena and phase transformation theory. The prediction of the FZ geometry, temperature distribution, and phase transformation kinetics could only

be achieved by the combination of experiments and modeling. This work demonstrates that the application of numerical transport phenomena can significantly add to the quantitative knowledge base in welding.

7.2 Future Work

During the course of this research, a number of areas were identified that required further investigation.

First, in Chapter 3, a transient heat transfer and fluid flow model was used to calculate the solidification parameters particularly the solidification rate and temperature gradient in the spot weld pool. Such calculation was based on the transfer of heat only, ignoring the thermodynamics and kinetics of solidification. A comprehensive understanding of the weld pool solidification process requires the knowledge of the thermodynamics of the material, kinetics of the solidification, heat transfer and liquid flow. Incorporating a solidification model with the transient thermo-fluid model is an effective approach to better understand the solidification process and solidified material in the weld pool.

Second, in Chapter 4, a numerical heat transfer and free surface flow model was developed for the GMA fillet welding. Due to the complexities of this welding process, several assumptions and simplifications were made to make the computational work traceable. In the future work, it may be useful to relax the following simplifying assumptions used in the present research and address more realistic situations. (a) The droplet heat transfer is currently modeled using a volumetric heat source in the weld pool. Such volumetric heat source approach is only valid for the spray transfer mode, and may not be accurate for the other transfer modes such as the globular transfer. Therefore, appropriate calculations of the droplet heat transfer under different modes will be a useful undertaken. (b) The present model considers the V-shaped fillet joint geometry, where two metal plates perpendicular to each other is welded. It will be useful to consider the other types of weld joint such as a butt or lap joint.

Third, in Chapter 5, a phase transformation model based on the JMA theory was used to quantitatively calculate the rates of phase transformations during weld heating. Although the JMA analysis provided a set of kinetic parameters used in the JMA equation, the transformation mechanism was not definitely determined in several cases. A number of future experiments can be conducted in order to both verify the computed JMA kinetic parameters and to better understand the phase transformation mechanisms and kinetics under welding conditions.

Fourth, in Chapter 6, a numerical diffusion model was developed to describe the kinetics of γ-austenite to δ-ferrite during weld heating of 2205 DSS. This model takes into account only the diffusion of nitrogen. At elevated temperatures, the diffusion of the substitutional alloying elements such as Cr may be important. A more realistic simulation may need to consider the multi-component diffusion process.

Finally, in Chapters 5 and 6, a number of kinetic models were used to describe various transformations during heating. These models included the JMA equation, grain growth model, and austenite decomposition model. In Chapter 5, an investigation was made to combine all the kinetic models together to provide a complete microstructural evolution map during welding of the 1005 steel. In the future work, it is useful to investigate the microstructural evolution in more complex and useful systems such as the 2205 DSS.

It is hoped that the forementioned areas can be addressed in the future work to better understand the heat transfer, fluid flow and microstructural evolution during fusion welding.

VITA

Wei Zhang

Wei Zhang was born in Jiangxi Province, China, on February 1, 1977. In September 1993, he enrolled in the department of Materials Science and Engineering, Huazhong University of Science and Technology (HUST), Wuhan, majored in Welding Technics and Equipment, where he was awarded the degree of Bachelor of Engineering in July 1997. After that, he began graduate study in the department of Materials Science and Engineering, HUST, majored in Materials Processing Engineering, and he was awarded the degree of Master of Engineering in June 2000. In the fall of 2000, he joined the Pennsylvania State University to pursue doctoral study in Materials Science and Engineering under the guidance of Professor T. DebRoy.

The author is a member of American Welding Society (AWS).